

MINISTRY OF EDUCATION, RESEARCH AND INNOVATION

UNIVERSITY OF CRAIOVA

ANNALS

MECHANICAL Series

CRAIOVA

Nr. 1/2009

ISSN 1223-5296

Scientific committee:

Associate Professor Dan Marghitu PhD, Auburn University USA

Associate Professor Dan Stoianovici PhD, JHU University, Baltimore USA

Prof. univ. dr. ing. Dan Băgnaru, University of Craiova

Prof. univ. dr. ing. Marin Bică, University of Craiova

Prof. univ. dr. ing. Nicolae Dumitru, University of Craiova

Prof. univ. dr. ing. Gheorghe Nanu, University of Craiova

Prof. univ. dr. Adriana Burlea Şchiopoiu, University of Craiova

Conf. univ. dr. ing. Nicolae Crăciunoiu, University of Craiova

Editors:

Conf. dr. ing. Adrian Sorin ROŞCA

Asist.univ.ing. Andrei Gheorghe NANU

CONTENT

1.	ILINCIOIU Dan, MIRIȚOIU Cosmin	Corelation Strength-Rigidity for A Metallic Structure	3
2.	MALCIU Raluca, CĂLBUREANU Mădălina, Lucian SEPCU	Experimentally Results About the Vibrations of a Linear Viscoelastic Cinematic Element of a Crank And Connecting Rod Assembly Working at Higher Speeds	17
3.	ROȘCA Vâlcu, CRĂCIUNOIU Nicolae	Numerical Evaluations and Experimental Tests in The Study of The Crack Growth	25
4.	BĂGNARU Dan Gheorghe, NANU Andrei Gheorghe, NANU Gheorghe	The Computational Analysis of the Influence of Vibrations on the Speed and Acceleration Fields of the Linear Elastic Rod of an R (Rrt) Mechanism	31
5.	BĂGNARU Dan Gheorghe, NANU Andrei Gheorghe, NANU Gheorghe	The Computational Analysis of the Influence of Vibrations on the Speed And Acceleration Fields of a Thin Plane Plate Which is a Constitutive Element of a Kinematic Chain	43
6.	SINGH Rajesh, KUMAR Mukesh, CHAUDHARY Manoj K., SMARANDACHE Florentin	Estimation of Mean In Presence of Non Response Using Exponential Estimator	53
7.	MIRIȚOIU Cosmin	Analysis Methods of a Circular Pull Broach Strength	63
8.	CĂLBUREANU Mădălina, MALCIU Raluca, Lucian SEPCU	Contributions About Handling Thermal Bridges for Civil Buildings	75
9.	ȚĂLU Ștefan, ȚĂLU Mihai	Some Considerations Concerning Incompressible Fluid Flow Through Inhomogeneous Porous Media	79
10.	TUTUNEA Dragos, GHERGHINA George, POPA Dragos	The Performance of Biodiesel From Animal Fats in Diesel Engines	83
11.	ȚĂLU Mihai, ȚĂLU Ștefan	Some Considerations Concerning Compressible Fluid Flow Through Inhomogeneous Porous Media With Constant Porosity	89
12.	BICĂ Marin, ENACHE Marian, CERNĂIANU Corina	The Influences of Gas Combustion Parameters on Running Electro-Filters	93
13.	ZAMFIRACHE Marius, STANIMIR Alexandru	Research regarding the roughness of the surfaces titanium alloys (TiAl5 Fe2.5) turning	107
14.	SEPCU Lucian, LUNGU Mihai, CĂLBUREANU Mădălina	Thermic Calculus of Aircraft's Cabin	113
15.	ȚĂLU Ștefan, ȚĂLU Mihai, SIPOS Aurelian, BOKOR Levente	On a Solution for Plane-Radial Flow of a Compressible Fluid Through Inhomogeneous Porous Media	117

16.	FILIP Dumitru, TARNIȚĂ Daniela	Types of Locomotion Systems	123
17.	ȚĂLU Ștefan	An Overview of the Design and Implementation of Visual Prosthesis	131
18.	TUDOR Viorel	Modern Concepts in the Construction of High Power Energy Boilers with Operating on Coal	135
19.	MARGINE Alexandru, CATRINA Gheorghe, GEONEA Ionuț	Kinematics and Dynamic Modelling of a Plane Manipulator	147
20.	SHAH Rajiv, ȚĂLU Ștefan	On the Models Used in Geometrical Representation of Human Extraocular Muscles	155
21.	ZAMFIRACHE Marius	Research Regarding the Roughness of the Surfaces at Stainless Steel Grinding	161
22.	STĂNCIOIU Dumitru	Using the Effect of Thermocooling at the Sedimenting of Dust Particles Inside the Industrial Electrofilters	165
23.	SEPCU Lucian, LUNGU Mihai, MALCIU Raluca	Mathematical Model of the Cabin and the Bottom of the Coating Cabin's Heat Calculus	173
24.	SHAH Rajiv, ȚĂLU Ștefan	A Balancing Forces Model for the Human Extraocular Muscles	177
25.	AȘTEFANEI Ioan, STĂNCIOIU Dumitru	The Study of the Physic Processes of Separating the Fases of the Combustion Gas Mix – Dust Particles in Suspension Through Sedimentation	181
26.	ZAMFIRACHE Marius, LAZAR Luminita	Studies and Research Regarding the Roughness of the Surfaces Got By Milling the Refractar Steel	191
27.	TUTUNEA Dragos, BICA Marin, CERNAIANU Corina, STANCUT Adriana, DIMA Alexandru	Life Cycle Assesment for Rapeseed Methyl Ester and Biodiesel	197
28.	AȘTEFANEI Ioan, STĂNCIOIU Dumitru	The Modelling of the Sedimentation Process of the Dust Particles of the Flue Gasses	205
29.	SHAH Rajiv, ȚĂLU Ștefan	A Mathematical Model of Human Retina	213
30.	SHAH Rajiv, ȚĂLU Ștefan	On the Application of Laminography to the Human Eye	217
31.	STĂNCIOIU Dumitru	The Transport of the Electrostatically Charged Particles from The Filtration Space – to the Depositing Electrodes	221

CORELATION STRENGTH-RIGIDITY FOR A METALLIC STRUCTURE

Dan ILINCIOIU¹, Cosmin MIRIȚOIU²

^{1,2}*University of Craiova, Faculty of Mechanics*

Abstract: It is studied the degree schematization (approximation) effect over the strength calculus of a structural element from a metallic construction. There are analysed the effect of different conditioning used in strength calculus of a beam for classifying in the importance order. It is especially followed the isignation of recommended calculus hypothesis used in designing the component beams of metallic structures. There are defined some appreciation criteria of the applied hypothesis effect in the calculus strength schemes of metallic structures.

Keywords: mechanical structure, strength, calculus hypothesis, schematizations.

1. INTRODUCTION

A metallic structure, that has a main strength role in the construction ensemble, is designed to sustain effective loadings. Mostly, the strains are ignored or a coarse checking is made, based on arbitrary restrictions. Also there are often made simplifications that situate us, in strength calculus, far away from the real phenomenon.

It is proposed the strength analysis of a static defined beam for distinguishing the quantitative effect of various simplifying assumptions. It will be researched the neglecting effect of own mass and elasticity (deformability) of supports; it is followed the effect of support idealization and the real mechanical phenomenon of coupling with the rest of the structure remainder.

Mechanical quantification effect of various simplifying assumptions will be made by referring to the main phenomenon which is the mechanical stress produced in the material. The mechanical stress will be correlated with strain; it will be revealed the effect on the material quantity correctly used at building the structure.

For simplifying the following of main loading phenomena, it will be used the beams with circular section, the main phenomenon won't be

accustomed by this simplification because, initially, the sections are involved by are, inertia moments and axial strength modulus which gives generality to the present study.

For effect quantification of different simplifying assumptions it will be considered as reference model the simple supported beam on an ideal-rigid structure. The supports will be ideal and will introduce only a reaction-force normal on the beam. The other situations (with own weight, elastic supports etc.) will be referred to this situation considered as a reference one.

2. SIMPLE SUPPORTED BEAM

The calculus scheme is presented in fig. 1.a, the reactions and moments are:

$$V_1 = \frac{Fb - Qc}{a + b}, V_2 = F + Q - V_1, M_{23} = V_1x - F(x - a),$$

$$M_{43} = -Qx. \quad (1)$$

Maximum moments are:

$$M_2 = V_1a, M_3 = -Qc. \quad (2)$$

The moment diagram for balanced lengths and loadings (with appropriate values) is presented in fig. 1.b.

If we impose an admissible stress σ_a and an admissible deflection f_a , we will have two sizings (from the strength and rigidity condition). The strength condition will lead to a necessary modulus W_n and a diameter d_n :

$$W_2 = \frac{M_2}{\sigma_a}, \quad W_3 = \frac{|M_3|}{\sigma_a},$$

$$W_n = \text{MAX}(W_2, W_3), \quad d_n = \sqrt[3]{\frac{32W_n}{\pi}} \quad (3)$$

To impose the strain condition, it will be used the Mohr-Maxwell method for strain calculus, considering only the bending moment. Having the loading schemes with the unitary force from fig 1.c and 1.d, the moment equations on beam's spaces are:

$$m_{12_1} = \frac{b}{a + b} \cdot x, \quad m_{23_1} = -\frac{ax}{a + b} + a, \quad m_{43_1} = 0,$$

$$m_{12_2} = -\frac{c}{a + b} \cdot x, \quad m_{23_2} = -\frac{c}{a + b} \cdot x, \quad m_{43_2} = -x. \quad (4)$$

The deflections in the two sections are:

$$f_2 = \frac{1}{EI} \cdot \int Mm_1 dx = \frac{1}{EI} \cdot \left(\int_0^a (V_1 x) m_{12_1} dx + \int_a^{a+b} [V_1 x - F(x-a)] m_{23_1} dx \right),$$

$$f_2 = \frac{ab}{6(a+b)} \cdot \frac{2Fab - Qc(2a+b)}{EI_2}, \quad (5)$$

$$f_3 = \frac{1}{EI} \cdot \int Mm_2 dx = \frac{1}{EI} \cdot \left(\int_0^a M_{12} m_{12_2} dx + \int_a^{a+b} M_{23} m_{23_2} dx + \int_0^c M_{43} m_{43_2} dx \right)$$

$$f_3 = -\frac{c}{6(a+b)} \cdot \frac{Fab(2a+b) - 2Qc(a+b)(a+b+c)}{EI_3}.$$

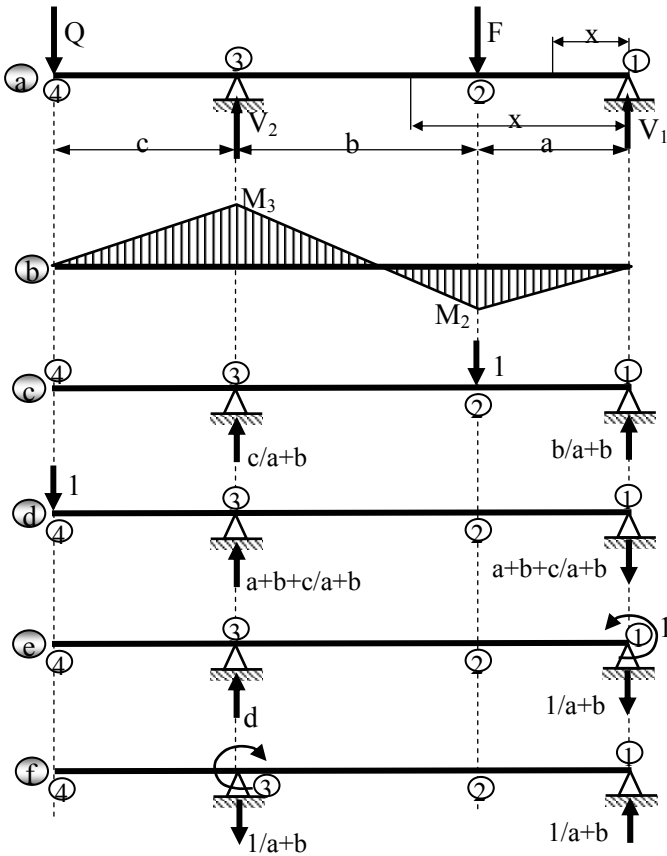


Fig. 1.

If the admissible deflection is imposed f_a , the necessary moment of inertia will be:

$$I_2 = \frac{ab}{6(a+b)} \cdot \frac{2Fab - Qc(2a+b)}{E \cdot f_a},$$

$$I_3 = -\frac{c}{6(a+b)} \cdot \frac{Fab(2a+b) - 2Qc(a+b)(a+b+c)}{E \cdot f_a}, \quad (6)$$

$$I_n = \text{MAX}(I_2, |I_3|).$$

The necessary diameter d_{ns} , from the deflection condition will be:

$$d_{ns} = \sqrt[4]{\frac{64I_n}{\pi}}. \quad (7)$$

Usually the strength condition leads to a higher section: $d_{ns} > d_n$.

To demonstrate the calculus viability, this modeling will be used for a particular case defined in this way:

$$Q = 2000daN, \quad F = 4000daN, \quad a = b = c = 200cm,$$

$$\sigma_a = 2000 \frac{daN}{cm^2}, \quad E = 2 \cdot 10^6 \frac{daN}{cm^2}, \quad f_a = \frac{a+b}{500} = 0,8cm.$$

The results are:

$$W_2 = 100cm^3, \quad W_3 = 200cm^3, \quad W_n = W_3, \quad d_n = 12,7cm,$$

$$I_2 = 833cm^4, \quad I_3 = 5000cm^4, \quad I_n = I_3, \quad d_{ns} = 17,8cm.$$

For an economical comparison, we will ratio the beam masses:

$$m_n = \frac{\pi d_n^2}{4} \cdot (a+b+c) \cdot \rho, \quad m_{ns} = \frac{\pi \cdot d_{ns}^2}{4} \cdot (a+b+c) \cdot \rho,$$

$$e = \frac{m_{ns}}{m_n} \cdot 100 = \left(\frac{d_{ns}}{d_n} \right)^2 \cdot 100. \quad (8)$$

In the particular case, we have the economy parameter $e=198,6\%$, this shows that, if we keep the section constant on all the beam length, its mass is doubled because of rigidity condition.

To observe the rigidity condition, we will compare the effective deflections with the admissible deflection, the beam having the section that satisfies the strength condition:

$$\varepsilon = \frac{f}{f_a} \cdot 100, \quad f = \frac{1}{EI_0} \cdot \int mMdx, \quad I_0 = \frac{\pi d_n^4}{64}. \quad (9)$$

In the chosen particular case we have (if $d = d_n = 12,7\text{cm}$):

$$f_2 = 0,5\text{cm}, \quad f_3 = 3,1\text{cm}, \quad f_a = 0,8\text{cm}, \quad \varepsilon_2 = 66\%, \quad \varepsilon_3 = 395\%.$$

It is observed that the admissible deflection is exceeded 4 times in the case where the strength condition is only used.

The beam rigidity is additionally defined by the spin angle of transversal section. For later analysis of rigidity, will be necessary the angle strains of the two supports. Using Mohr-Maxwell, φ_1 and φ_3 angles are calculated. Using the loading schemes with unitary moments from fig.1.e and 1.f, we will have the moment equations:

$$\begin{aligned} m_{12_3} &= 1 - \frac{x}{a+b}, & m_{23_3} &= 1 - \frac{x}{a+b}, & m_{43_3} &= 0 \\ m_{12_4} &= \frac{x}{a+b}, & m_{23_4} &= \frac{x}{a+b}, & m_{43_4} &= 0. \end{aligned} \quad (9.a)$$

The strain angles on 1 and 3 supports are:

$$\begin{aligned} \varphi_1 &= \frac{1}{EI} \cdot \int Mm_3 dx, \quad \varphi_3 = \frac{1}{EI} \cdot \int Mm_4 dx, \\ \varphi_1 &= \frac{1}{6(a+b) \cdot EI} [Fab(a+2b) - Qc(a+b)^2] = \varphi_3 \end{aligned} \quad (9.b)$$

For the defined calculus example we will have (considering the calculus diameter obtained from the strength condition): $\varphi_1 = \varphi_3 = 2,56 \cdot 10^{-3} \text{rad}$.

3. SIMPLE SUPPORTED BEAM WITH OWN WEIGHT

The calculus scheme is presented in fig.2, the reactions and moment equations are:

$$\begin{aligned} V_1 &= \frac{Fb - Qc - 0,5(a+b+c)(a+b-c)}{a+b}, \\ V_2 &= F + Q + q(a+b+c) - V_1, \\ M_{12} &= V_1 x - 0,5qx^2, \quad M_{23} = V_1 x - 0,5qx^2 - F(x-a), \\ M_{43} &= -QX - 0,5qx^2. \end{aligned} \quad (10)$$

Own weight q is calculated taking into account the necessary diameter obtained from the initial strength condition (with own weight) in this way:

$$q = 0,25d_n^2 \cdot \rho \cdot g , \quad (11)$$

where ρ is the steel density, $g=10 \text{ m/s}^2$. It will be made an iterative calculus until finding the necessary diameter obtained with relation (3); the necessary calculated diameter will be noted with d_{nl} .

The moment equations (10),(14) are used, the imposed deflections allow us to determine the necessary inertia moments:

$$I_2 = \frac{1}{Ef_a} \cdot \int Mm_1 dx , I_3 = \frac{1}{Ef_a} \cdot \int Mm_2 dx , I_n = \text{MAX}(I_2, I_3) \quad (12)$$

The necessary diameter from the rigidity condition d_{n5} , it is calculated with relation (7) and noted with d_{nl} .

The obtained diameter from the rigidity condition is imposed, the own weight is calculated with relation (11) and the section calculus resumed from the admissible deflection condition; the operation is repeated (an iterative calculus is made) until the obtained section won't modify through a dimensioning cycle. The final diameter will be noted with d_{nsl} .

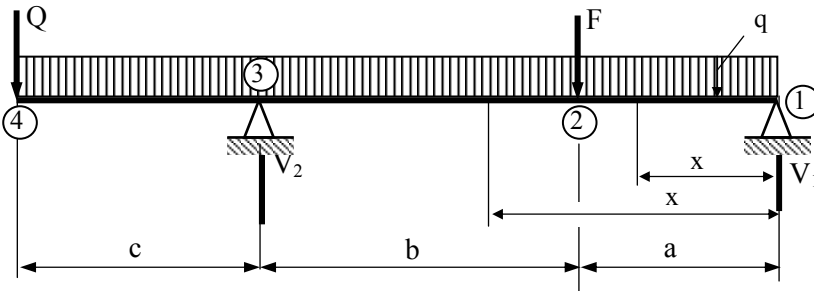


Fig. 2

The beams masses are compared in variant with own weight:

$$e_l = \left(\frac{d_{nsl}}{d_{nl}} \right)^2 , e_{l0} = \left(\frac{d_{nsl}}{d_{ns}} \right) . \quad (13)$$

The effective deflections are compared, in variant where the section fulfills the strength condition (the variant with own weight), with the admissible deflection; the relations (9) are used, where $d_n = d_{nl}$.

$$W_n = 225\text{cm}^3, \quad d_{nl} = 12,9\text{cm}, \quad I_n = 7820\text{cm}^4, \quad d_{nsl} = 20\text{cm}, \\ e_l = 240\%, \quad e_{l0} = 125\%, \quad \varepsilon_2 = 7,5\%, \quad \varepsilon_3 = 576\% .$$

4. BEAM ON ELASTIC SUPPORTS

4.1. STRAINING SUPPORTS

It is considered that the supports suffer a displacement “ δ ”, constant and vertically like in scheme 3. According to strength, there aren't any influences of vertical support displacement, the calculus is made with relations (10),(11) and (3), and the diameter previously obtained, noted with d_{nl} remains valid.

If we impose the admissible deflection, f_a , relations (12) become:

$$I_2 = \frac{1}{E(f_a - \delta)} \cdot \int Mm_1 dx, \quad I_3 = \frac{1}{E(f_a - \delta)} \cdot \int Mm_2 dx, \quad (14)$$

$$I_n = \text{MAX}(I_2, I_3), \quad d_{nsl} = \sqrt[4]{\frac{64I_n}{\pi}} .$$

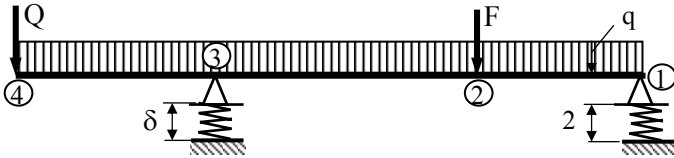


Fig. 3

The beam masses are compared in this variant with the reference one (beam without own weight, variant 0) and variant I (beam with own weight):

$$e_{II} = \left(\frac{d_{nsl}}{d_{nII}} \right)^2, \quad e_{II0} = \left(\frac{d_{nsl}}{d_{ns}} \right)^2. \quad (15)$$

Also, it is calculated the modifying multipliers of effective deflection according to (9).

In the chosen case, next results are obtained (for $\delta=0,3\text{cm}$):

$$W_n = 242\text{cm}^3, \quad d_{nII} = 13,5\text{cm}, \quad I_n = 22440\text{cm}^4, \quad d_{nsl} = 26\text{cm} \\ e_{II} = 370\%, \quad e_{II0} = 212\%, \quad \varepsilon_2 = 122\%, \quad \varepsilon_3 = 856\% .$$

4.2. FIXED ELASTIC SUPPORTS

The calculus scheme is presented in fig. 4.a, it is observed that the beam is twice static indefinite for the support moment we have more mechanical equilibrium conditions. It is used the strain method for solving the indefinite problem, considering only bending. The base system is shown in fig. 4.b, the indefinite static parameters X_1 and X_2 are the support moments (according to fig.4.b).

It is considered that, because of the real constructive solution of supporting, the spin on the supports is prevented in some way. This phenomenon of prevented mobility is quantified by imposing a strain on the supports depending on the initial free spin (the ideal-supported beam) in this way:

$$\varphi_1^* = k\varphi_1, \quad \varphi_3^* = k\varphi_3 \quad (16)$$

where: k -subunit constant that estimates the spinning obstruction degree; φ - the free spin on the supports; φ^* - effective spin on supports.

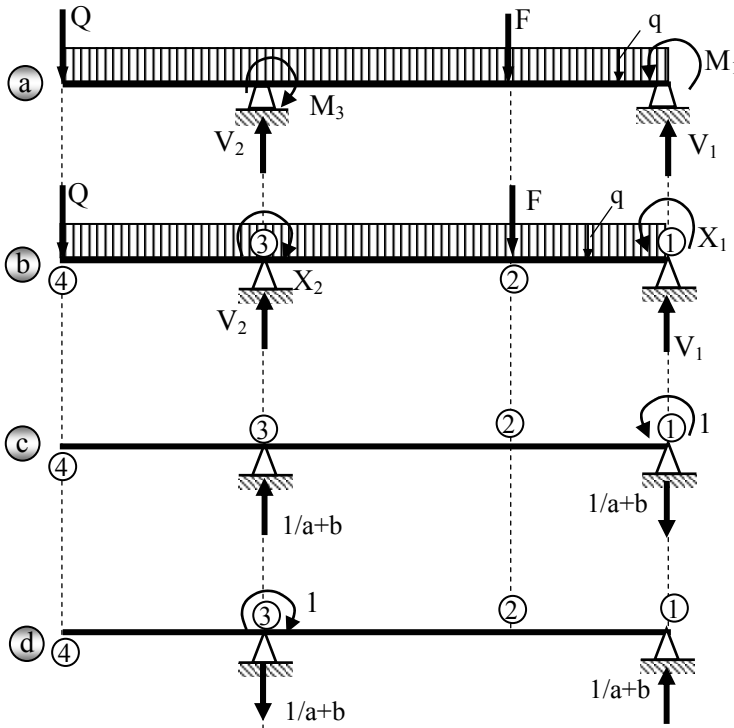


Fig. 4

The moment equations due to the effective loadings in the base system are given with relation (10); moment equations produced by the unitary moments (according to fig.4.c and d) are:

$$m_{12_1} = 1 - \frac{x}{a+b} = m_{23_1}; m_{12_2} = -\frac{x}{a+b} = m_{23_2} \quad (17)$$

The multipliers of canonical equations are:

$$\begin{aligned} d_{11} &= \int m_1^2 dx = \frac{a+b}{3}, & d_{12} &= \int m_1 m_2 dx = -\frac{a+b}{6}, & d_{22} &= d_{11}, \\ d_{10} &= \int m_1 M_0 dx = -\frac{1}{24} \left\{ -4abF \cdot \frac{a+2b}{a+b} + 4cQ(a+b) + \right. \\ & \quad \left. + q(a+b)[2c^2 - (a+b)^2] \right\}, & & & (18) \\ d_{20} &= \int m_2 M_0 dx = \frac{1}{24} \left\{ -4abF \frac{2a+b}{a+b} + 8Qc(a+b) - \right. \\ & \quad \left. - q(a+b)[(a+b)^2 - 4c^2] \right\} \end{aligned}$$

The system of canonical equations is:

$$\begin{cases} d_{11}X_1 + d_{12}X_2 = -d_{10} + k\varphi_1 \\ d_{12}X_1 + d_{22}X_2 = -d_{20} + k\varphi_2 \end{cases} \quad (19)$$

The free spin angles on the supports are:

$$\varphi_1 = \int m_1 M_0 dx = d_{10}, \quad \varphi_2 = \int m_2 M_0 dx = d_{20}. \quad (20)$$

The system determinants are:

$$\begin{aligned} D_1 &= \begin{vmatrix} k\varphi_1 - d_{10} & d_{12} \\ k\varphi_2 - d_{20} & d_{22} \end{vmatrix} = \frac{k-1}{144} [12ab^2 + q(a+b)^4], & (21) \\ D_2 &= \begin{vmatrix} d_{11} & k\varphi_1 - d_{10} \\ d_{12} & k\varphi_2 - d_{20} \end{vmatrix} = \\ &= \frac{k-1}{144} \left\{ -12ab^2F + 12cQ(a+b)^2 - q(a+b)^2[(a+b)^2 - 6c^2] \right\}, \\ D_0 &= \begin{vmatrix} d_{11} & d_{12} \\ d_{12} & d_{22} \end{vmatrix} = \frac{(a+b)^2}{12}. \end{aligned}$$

The system solutions are:

$$X_1 = \frac{D_1}{D_0} = \frac{K-1}{12} \left[\frac{12ab^2F}{(a+b)^2} + q(a+b)^2 \right], \quad (22)$$

$$X_2 = \frac{D_2}{D_0} = \frac{k-1}{12} \left\{ \frac{-12a^2bF}{(a+b)^2} + 12cQ - q[(a+b)^2 - 6c^2] \right\}.$$

The real bending moments on the beam spaces are:

$$M_{12} = V_1x - 0,5qx^2 + \left(1 - \frac{x}{a+b}\right)X_1 - \frac{x}{a+b}X_2, \quad (23)$$

$$M_{23} = V_1x - 0,5qx^2 - F(x-a) + \left(1 - \frac{x}{a+b}\right)X_1 - \frac{x}{a+b}X_2,$$

$$M_{43} = -Qx - 0,5qx^2.$$

The V_1 reaction is obtained with (10). The moment diagram has the form from the fig.4.e.

To calculate the deflection in the application points of F and Q forces are used unitary loadings that produce moments calculated with (4) and (23) in this way:

$$f_2 = \frac{1}{EI} \int m_1 M dx, \quad f_3 = \frac{1}{EI} \int m_2 M dx. \quad (24)$$

$$f_2 = \frac{4ab}{24EI} \left[-\frac{b^2F}{a+b} + (2a+b)V_1 + \frac{(a+2b)X_1}{a+b} - \frac{(2a+b)X_2}{a+b} - 0,25(3a^2 + 3ab + b^2)q \right] = \frac{f_{2a}}{EI},$$

$$f_3 = \frac{4c}{24EI} \left[\frac{(3a+2b)b^2F}{a+b} + 2c^2Q - 2(a+b)^2V_1 - (a+b)X_1 + 2(a+b)X_2 + 0,75(a+b+c)[(a+b)^2 - (a+b)c + c^2] \right] = \frac{f_{3a}}{EI}$$

The beam is dimensioned from the strength condition, if the moment M_3 remains the highest (force and the cantilever length remain high) then the strength condition will not change de diameter, remaining valid the previous one (d_{nII})(the high rigidity of supports influences only the moment on the spaces 1-2-3, moment M_3 being independent from these).

From the strain condition, depending on the highest condition, the necessary diameter will be calculated with (7), and it is noted by d_{nsII} . The beam masses are compared using the parameter “e” calculated with relations:

$$e_{III} = \left(\frac{d_{nsIII}}{d_{nIII}} \right)^2, \quad e_{III0} = \left(\frac{d_{nsIII}}{d_{ns}} \right)^2. \quad (25)$$

The effective deflections are compared with relations (9), obtaining the multipliers ε_1 and ε_3 (the beam satisfies only the strength condition). If it is applied the model previously defined (for two values of k):

$$k = 0,5: \quad d_n = 12,9cm, \quad d_{ns} = 17,3cm, \quad e = 180\%, \quad e_0 = 94\%,$$

$$\varepsilon_2 = 70\%, \quad \varepsilon_2 = 324\%;$$

$$k = 0: \quad d_n = 12,9cm, \quad d_{ns} = 16,4cm, \quad e = 162\%, \quad e_0 = 84\%,$$

$$\varepsilon_2 = 67\%, \quad \varepsilon_2 = 261\%.$$

5. CONCLUSIONS

The constructive solution of the supporting element influences decisively its strain, and, the section dimensions (“its thickness”). That’s why it must be studied the correlations that appear between loadings and supports for every supporting element type (constructive type). In this study, it has been approached a representative case for metallic construction and enough complex by the cantilever existence; also by customizing (the cantilever length is zero $c=0$), it is obtained the most usually applied case (beam supported at both ends with concentrated loading).

The accomplished study, especially in the private case, allows pointing many mechanical phenomena issues of loading that have general application and are useful for the metallic structures designer. The study conclusions, which we consider that have implications with general aspect or crucially influence the designing conception will be presented below.

First of all, it can be said that imposing a rigidity condition leads, mostly, to higher dimensions than the ones obtained from the strength condition. This fact is known and that’s why it is proceeded to strength structure conditioning with some corrections from strain checking.

The loadings values and the beam length (the spaces on the beam) crucially influences the strength calculus and do not permit generalizations not even in the same constructive type. It can be also said, that, in the strength case on the cantilever, this area tends to

become dominant for the strength analysis, giving the section dimensions. That's why it can't be recommended using same additional constructive solutions that unload partially the cantilever, otherwise this will impose using excess of material. The cantilever existence imposes referring to the variable section solution of the beam, at least from one section to another.

If the loading values are in the usual domain, then the own weight has negligible influence. That is why it can be negligible the own weight of the beam if it is loaded by other loadings, especially if these are concentrated.

The supports rigidity has a big importance. The additional displacements it supports produce additional high loadings that impose higher sections. This thing recommends discharging of disallowed displacements (later functioning uncontrolled compaction).

The support stiffening makes the beam loading to decrease, leading to section decrease (material saving). Moreover, the rigidity condition leads to section dimensions more closer to the ones given by the strength condition. Material saving must not be taken "straight meaning" because the stiffening involve additional materials usage that diminishes the positive effect; nevertheless it must be underlined that the stiffening on the supports are a solution of increasing the beams strength, the more so as the stiffening solution are more rational and do not lead to sections increasings of adjacent structure elements.

Those stated before are sustained with numerically values by applying to the calculus model defined for a real constructive solution ($F=4000$ daN, $Q=2000$ daN, $a=b=c=200$ cm, $\sigma_a=2000$ daN/cm², $f_a=0,8$ cm). The results obtained with an automatic calculus programme is presented in table 1.

The loads meaning is: q -the distributed loading (own weight); δ -imposed displacements on supports; k - a constant (between 0 and 1) which allows limits spin on supports ($k \cdot \varphi$ - allowed spin; φ - free spin on support); m_{ns} - the beam mass with the section obtained from the maximum imposed deflection condition (the rigidity condition); m_n - the beam mass with the section obtained from the strength condition; f_2, f_4 - the deflections in the loading sections (in section 2 between supports, in section 4 at the end of the cantilever), the section is the one obtained from the strength condition; f_a - maximum imposed deflection; m_{ns0} - the beam mass imposed by rigidity in reference 0 variant (beam on ideal supports without own weight).

Table 1 - Application for:

$$F=4000 \text{ daN}, Q=2000 \text{ daN}, a=b=c=200 \text{ cm}, \sigma_a=2000 \text{ daN/cm}^2$$

Parameter	VARIANT 0 q=0	VARIANT 1 q≠0	VARIANT 2 q≠0 δ=0,3 cm	Variant 3 k			
Diameter obtained from the strength condition d_n (cm)	12,7	12,9	12,9	12,9	12,9	12,9	12,9
Diameter obtained from the deflection condition $f_a=0,8$ cm	17,9	18,1	20,4	16,4	16,9	17,3	17,7
Masses ratio(%) $e=m_{ns}/m_n$	199	197	239	162	171	180	189
Masses ratio (%) $e=m_{ns0}/m_n$	100	103	131	84	89	94	98
Deflections ratio (%) $\varepsilon_2=f_2/f_a$	66	74	70	67	68	70	72
Deflections ratio (%) $\varepsilon_2=f_2/f_a$	395	387	357	261	293	324	356

From the numerical results analysis, there can be observed similar phenomena with the ones previously shown (the general ones), in this way:

1. the own weight has negligible on the necessary material quantity (almost 3% higher); so there can be made calculations with a better precision taking into account only the exterior loadings (concentrated).
2. the own weight must be take into account if there are compactions in supports
3. the stiffening to the supports spinning lead to material saving in a significant quantity, but not a huge one. This fact also recommends studying the consumptions for rigidity before a final conclusion
4. the high length of the cantilever imposes its decisive influence, especially in the case of rigidity condition; this fact is mostly shown by ratio ε_4 that gives the deflection on the cantilever and four times higher than the admissible one (with section from the strength condition). The leading character of the cantilever is also shown by the fact that, if the strength condition is imposed, the section is not influenced by the supports rigidity
5. spin rigidity of the supports has negligible influence on the deflection between the supports, but it can decrease de cantilever arrow with significant values (maximum 30%)

An essential conclusion, generally true for the present study, is the one referred to the structure strains that have a very big importance in structural element strength-metallic beam. Because the imposed strain leads to great material consumptions, we must not exaggerate in this conditioning; when it is possible, we would the responsibility of the beam maximum loading to be transferred on the mechanic stress conditions (strength ones).

REFERENCES

1. Ilincioiu, D., Rezistența Materialelor, ediția a-III-a, Editura ROM TPT, Craiova, 2008
2. Ilincioiu, D., Petrescu, G., Rezistența Susținerilor Miniere, Editura ROM TPT, Craiova, 2003
3. Dalbanu, C., Dima, S., Chesaru, E., Șerbescu, C., Construcții cu structură metalică, Editura Didactică și Pedagogică, București, 1997

EXPERIMENTALLY RESULTS ABOUT THE VIBRATIONS OF A LINEAR VISCOELASTIC CINEMATIC ELEMENT OF A CRANK AND CONNECTING ROD ASSEMBLY WORKING AT HIGHER SPEEDS

Raluca MALCIU¹, Mădălina CĂLBUREANU¹, Lucian SEPCU²

¹University of Craiova, Faculty of Mechanics

²Faculty of Automatics, Computers and Electronics

Abstract: This work presents the vibrational displacements for a viscoelastic cinematic element of crank and connecting rod assembly working at higher speeds. The movement equations of the linear-elastic straight kinematic elements in plan-parallel motion are presented by using the Hamilton's variational principle. Finally, for a concrete case, the plotting of the displacements is given in theoretical and experimental way.

Keywords: viscoelastic material, spectral analysis, acceleration of vibration, crank and connecting rod assembly.

1. THE ANALYTIC DETERMINATION OF THE DISPLACEMENTS FIELD FOR A VISCOELASTIC CINEMATIC ELEMENT OF A CRANK AND CONNECTING ROD ASSEMBLY

By applying in the movement's mathematical model of a linear elastic cinematic element bar type [1], the Laplace one-sided transform proportional to time and replacing the E modulus with $\tilde{E}(s)$ the matriceal equation of the first aproximation in Laplace images is obtained for the vibrations of the viscoelastic connecting rod of the R(RRT) mechanism figured in Fig. 1, as follows:

$$[L_0(s)]\{\tilde{u}^{(1)}\} + [M_4]\{\tilde{a}_0\} + \{\tilde{V}_1\} = \{0\} \quad (1)$$

where:

$$[L_0(s)] = [M_1(s)] \frac{\partial \bullet}{\partial x^4} + [M_8(s)] \frac{\partial \bullet}{\partial x^2} + [M_4(s)] \bullet; [M_1(s)] = \tilde{E}(s) \cdot I \cdot \begin{bmatrix} 0 & 0 \\ 0 & 1 \end{bmatrix}$$

$$[M_8(s)] = \begin{bmatrix} \tilde{E}(s)A & 0 \\ 0 & -\rho \cdot I \cdot s^2 \end{bmatrix}; [M_4(s)] = s^2 [M_4] \{ \tilde{a}_0 \} = \{ \tilde{a}_{01}(s), \tilde{a}_{02}(s) \}^T;$$

$$\{ \tilde{V}_1 \} = \rho A x \{ \tilde{g}(s), \tilde{\varepsilon}(s) \}^T; \omega^2(t) = g(t), \{ \tilde{u}^{(1)} \} = \{ \tilde{u}_1^{(1)}(x, s), \tilde{u}_2^{(1)}(x, s) \}^T;$$

$$\tilde{E}(s) = \frac{a_0 s}{b_0 s + b_1}; a_0 = 9GK; b_0 = 3K + G; b_1 = \frac{3KG}{\eta};$$

$$K = \frac{\nu E}{(1 + \nu)(1 - 2\nu)} + \frac{2}{3}G;$$

$\tilde{E}(s)$ - is the mathematical expression of Maxwell mechanical model for solid state polymers;

G – Transversal elasticity modulus;

K – compressibility modulus;

ν - Poisson's transversal elasticity coefficient;

η - Maxwell's model newtonian component constant.

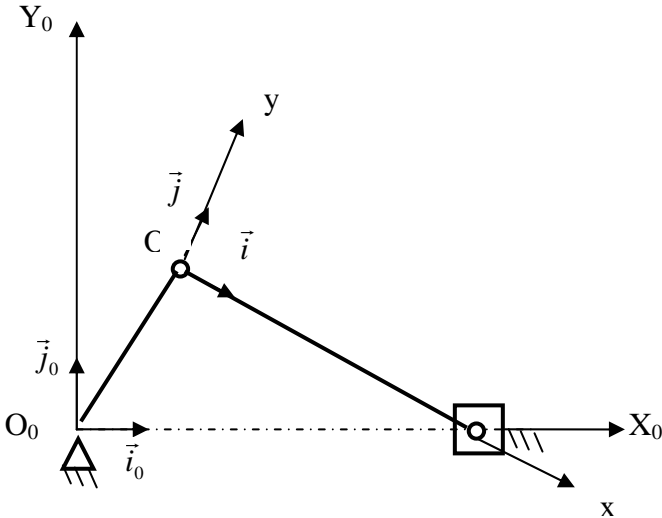


Fig. 1. The crank and connecting rod mechanism

Applying in (1) the finite Fourier transforms in cosine and sine, to the first and respectively to the second equation, there are obtained uncoupled algebraic systems having as unknowns the displacements $u_{1,c}^{(1)}(n, s)$ and $u_{2,s}^{(1)}(n, s)$ in Laplace and Fourier images in cosine,

respectively in sine. Then, by inverting the Laplace and Fourier transforms, there results the solution in the first approximation $\{u^{(1)}(x, t)\}$. With $\{u^{(1)}(x, t)\}$ it is calculated, in a first approximation, the vector $\{F^{(1)}\}$ which is introduced into the equation (1'), resulting the mathematical model in the second approximation, whose resolution can be obtained with the help of the integral transforms, finally having the solution $\{u^{(2)}(x, t)\}$ in the second approximation. Continuing the iterative process, results the mathematical model in the approximation „j”.

$$[L_0]\{u^{(j)}(x, t)\} + [M_4]\{a_0\} + \{V\}_1 + \{F^{(j-1)}\} = \{0\} \quad (2)$$

where:

$$\{F^{(j-1)}\} = [M_6]\{u^{(j-1)}(x, t)\}, \quad j=1,2,\dots,n; \quad \{F^{(0)}\} = \{0\};$$

$$\{u^{(j)}\} = \{u_1^{(j)}(x, t), u_2^{(j)}(x, t)\}^T;$$

$$\{u^{(j-1)}\} = \{u_1^{(j-1)}(x, t), u_2^{(j-1)}(x, t)\}^T$$

The solution in „j” approximation will be:

$$u_1^{(j)}(x, t) = \frac{1}{L} \cdot u_{1,c}^{(j)}(0, t) + \frac{2}{L} \sum_{n=1}^{n=\infty} u_{1,c}^{(j)}(n, t) \cdot \cos(\alpha_n \cdot x) \quad (3)$$

$$u_2^{(j)}(x, t) = \frac{2}{L} \sum_{n=1}^{n=\infty} u_{2,s}^{(j)}(n, t) \cdot \sin(\alpha_n \cdot x), \quad (4)$$

Where:

$u_{1,c}^{(j)}(n, t)$ și $u_{2,s}^{(j)}(n, t)$ are the finite Fourier transforms in cosine, respectively in sinus of the elastic longitudinal and transversal displacement.

The process of the successive approximation is considered complete when $\forall n, \|\{u^{(j)}\} - \{u^{(j-1)}\}\| \leq \varepsilon$, , where:

$\varepsilon > 0$ and low enough depending on the precision of the required operation;

And:

$$\{u^{(j)}\} = \{u_1^{(j)}(x, t), u_2^{(j)}(x, t)\}^T; \quad (5)$$

$$\{u^{(j-1)}\} = \{u_1^{(j-1)}(x, t), u_2^{(j-1)}(x, t)\}^T. \quad (6)$$

The connecting rod OA being double-articulated, the just on the line conditions which allowed the application of the two Fourier transforms, for initial functions and for their Laplace images, were:

$$\begin{aligned} \frac{\partial u_1(0,t)}{\partial x} = \frac{\partial u_1(L,t)}{\partial x} = 0; u_2(0,t) = u_2(L,t) = 0; \frac{\partial^2 u_2(0,t)}{\partial x^2} = \frac{\partial^2 u_2(L,t)}{\partial x^2} = 0, \\ \frac{\partial u_1(0,s)}{\partial x} = \frac{\partial u_1(L,s)}{\partial x} = 0; u_2(0,s) = u_2(L,s) = 0; \frac{\partial^2 u_2(0,s)}{\partial x^2} = \frac{\partial^2 u_2(L,s)}{\partial x^2} = 0. \end{aligned} \quad (7)$$

The initial conditions have been admitted:

$$u_1(x,0) = 0; \frac{\partial u_1(x,0)}{\partial t} = 0; u_2(x,0) = 0; \frac{\partial u_2(x,0)}{\partial t} = 0.$$

The displacements fields, in the first approximation, in the case of free vibrations of the connecting rod OA belonging to the mechanism R(RRT) in figure 1, represented by the equations (3) and (4), will be supplied, as a result of the application of the preceding algorithm of integration, by the function:

$$u_1^{(1)}(x,t) = \frac{1}{L} \cdot u_{1,c}^{(1)}(0,t) + \frac{2}{L} \sum_{n=1}^{n=\infty} u_{1,c}^{(1)}(n,t) \cdot \cos(\alpha_n \cdot x) \quad (8)$$

$$u_2^{(1)}(x,t) = \frac{2}{L} \sum_{n=1}^{n=\infty} u_{2,s}^{(1)}(n,t) \cdot \sin(\alpha_n \cdot x), \quad (9)$$

where $u_{1,c}^{(1)}(n,t)$ and $u_{2,s}^{(1)}(n,t)$ are determined as it is showed in [4].

2. NUMERICAL APPLICATION FOR A REAL RRT MECHANISM

It is considered a numerical application of RRT mechanism as follows:

$$\begin{aligned} L=1[m]; \quad r=0,07[m]; \quad \omega_0=29,45[s^{-1}]; \quad b=0,011[m]; \quad h=0,011[m]; \\ \rho=1213,3[kg/m^3]; \quad G=0,0118979 \cdot 10^{11}[N/m^2]; \quad \eta=4,5 \cdot 3600 \cdot 10^{13}[N \cdot s/m^2]; \\ K=0,02424455 \cdot 10^{11}[N/m^2]. \end{aligned}$$

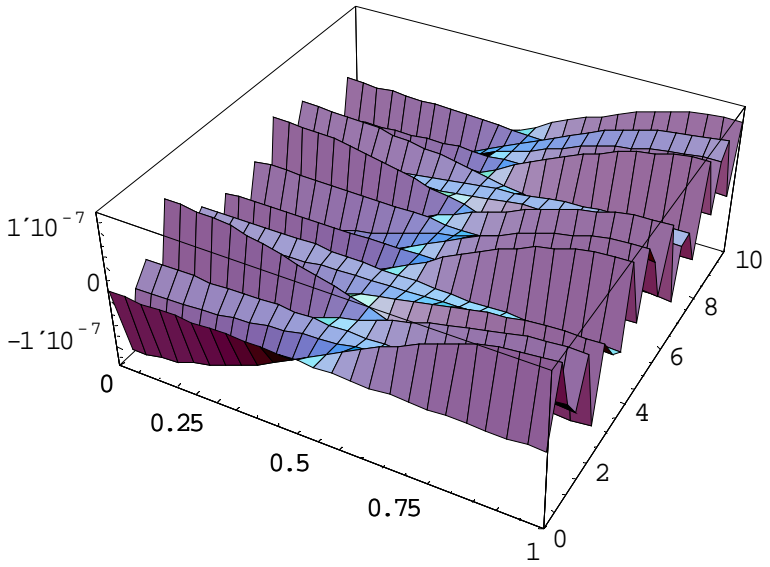


Fig.2 The longitudinal displacement $u_1 = u_1^{(1)}(x, t)$

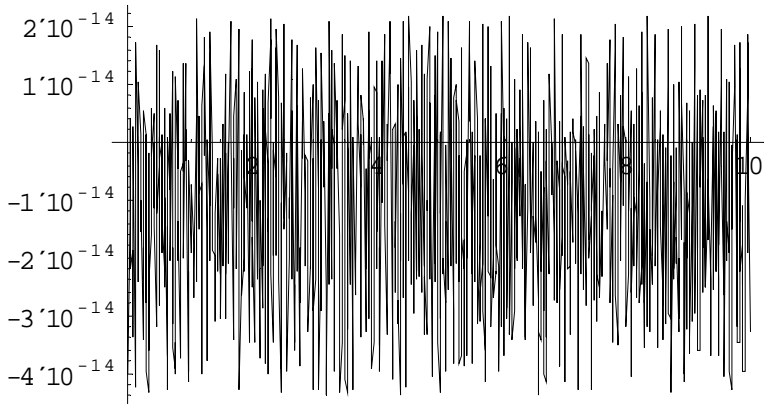


Fig.3 The longitudinal displacement variation at $x=L/2$: $u_1 = u_1^{(1)}\left(\frac{L}{2}, t\right)$

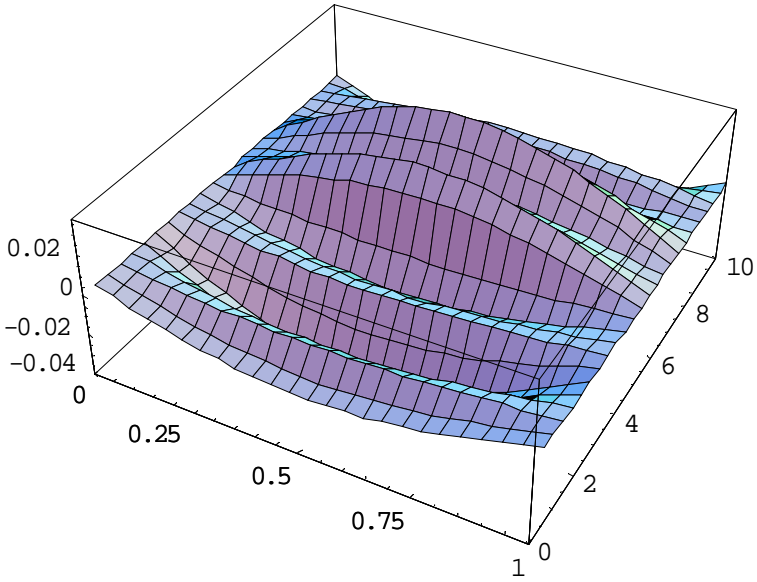


Fig.4 The transversal displacement $u_2 = u_2^{(1)}(x, t)$

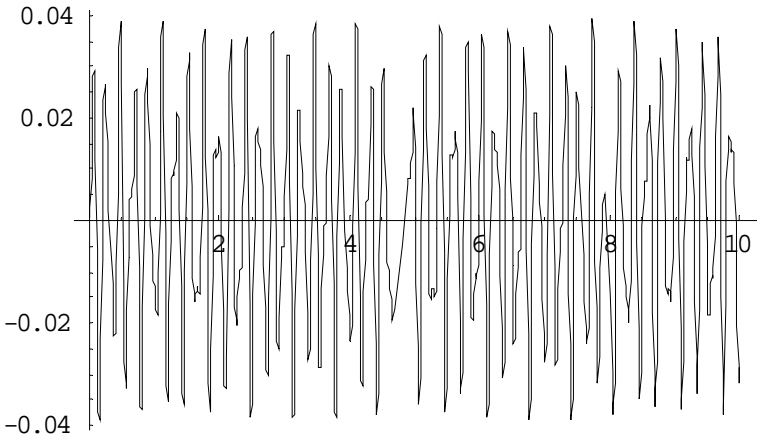


Fig.5 The transversal displacement variation at $x=L/2$: $u_2 = u_2^{(1)}\left(\frac{L}{2}, t\right)$

The experiment took place in the Mechanisms Laboratory of The Faculty of Mechanics from Craiova.

The experimental determination of the acceleration of vibration for the OA element, made of PVC-U, at higher speed is represented in Fig.6 and the spectral analysis is given by Fig. 7.

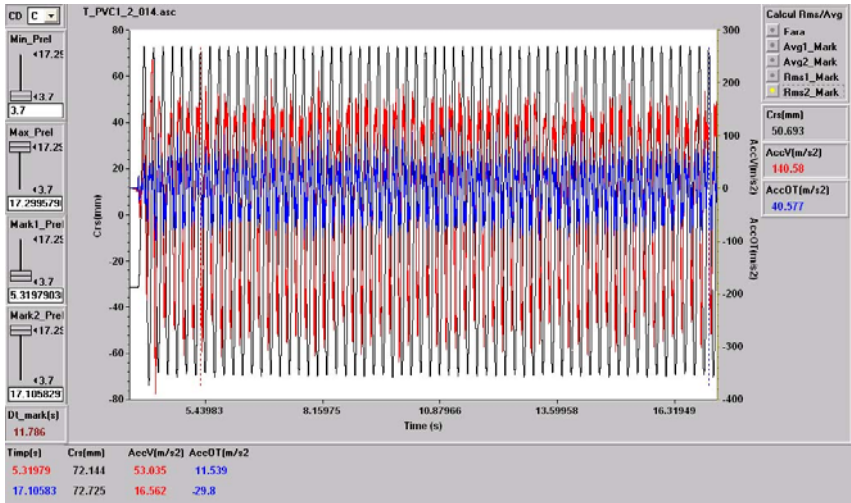


Fig.6. The acceleration of vibration at $x=L/2$, higher speed

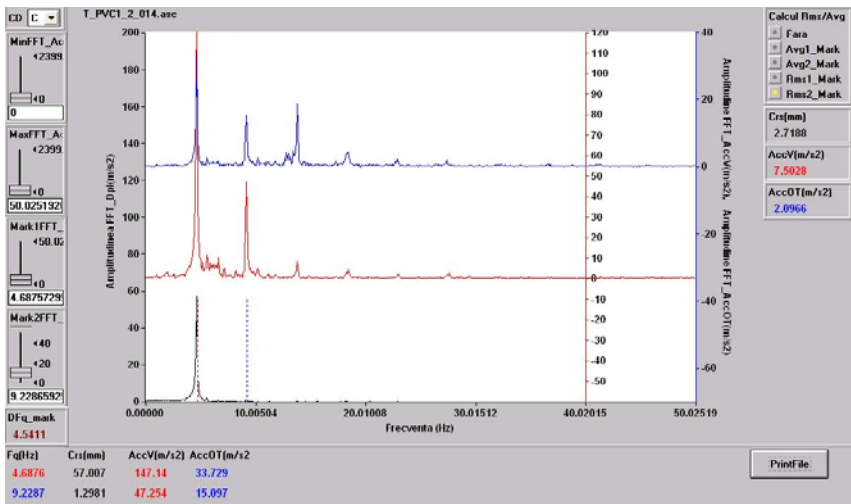


Fig.7 The spectral analysis at $x=L/2$, higher speed

3. CONCLUSIONS

The vibrations of the viscoelastic cinematic element from the crank and connecting rod assembly on the horizontal and vertical directions at higher speeds shows that the behaviour of the material is relatively good. The vibrations are measured at the half length of the element. The Mathematica program and the algorithm used in calculus of the acceleration of vibration is accurate. The experimental acceleration for vertical direction is 140.58 m/s^2 at maximum value and the theoretical maximum value is 138.49 m/s^2 .

REFERENCES

1. Băgnaru, D., *Vibrațiile elementelor cinematice*, Editura SITECH, Craiova, 2005, ISBN 973-657-854-2.
2. Bolcu, D., Băgnaru, D., *Aplicații ale transformărilor integrale în mecanică*, Editura Universitaria, Craiova, 2004, ISBN 973-8043-568-X.
3. Băgnaru, D., Marghitu, D.B., *Linear vibrations of viscoelastic links*, 20-th Southeastern Conference on Theoretical and Applied Mechanics, April 16–18, 2000, Callaway Gardens and Resort, Georgia, USA, pag. 1–7.
4. Băgnaru, D., Cătăneanu, A., *Calculus methods in dynamics of cinematic chains with linear viscoelastic elements*, International Conference Beyond 2000, Engineering Research Strategies, 25 – 26 nov. 1999, Sibiu, pag. 225 – 228.

NUMERICAL EVALUATIONS AND EXPERIMENTAL TESTS IN THE STUDY OF THE CRACK GROWTH

Vălcu ROȘCA¹, Nicolae CRĂCIUNOIU²
^{1,2}*University of Craiova, Faculty of Mechanics*

Abstract: This work is aimed to assess a numerical procedure for MSD crack propagation simulation of 2D pre-notched specimens (plates) undergoing a traction fatigue load, as defined by a general load spectrum. Experimental analyses on a fatigue machine were carried out in order to validate the numerical results and to provide the necessary material fatigue data for the aluminium plates. By means of a non-linear regression analysis, applied on in house obtained experimental data, a propagation law was defined, capable to effectively keep in account the threshold effect and the unstable final propagation. A satisfactory agreement between numerical and experimental crack growth rates was obtained even starting from a complex MSD test.

Keywords: crack growth, Multiple Site Damage (MSD), fracture mechanics, Stress Intensity Factors (SIF), crack length, fatigue, crack growth rate.

1. INTRODUCTION

With reference to fatigue and MSD (Multiple Site Damage) fracture mechanics, experimental fatigue tests were performed on a complex geometry notched plate undergoing cyclic axial load. The crack initiation process and crack propagation were monitored on a specimen undergoing a given traction load spectrum. Experimental crack growth rate and crack path were compared with those obtained with a numerical procedure and the correct simulation of the load introduction to the specimen was checked by strain gauge measurements. The fatigue data necessary for the numerical analysis were previously obtained by experimental crack growth tests on simple geometry specimen. The propagating crack lengths were monitored on both sides of the specimen in order to check the correctness of load introduction to the specimen.

2. EXPERIMENTAL ANALYSIS ON SIMPLE GEOMETRY CRACKED PLATES

The first part of the fatigue experimental test was carried out on 3 simple notched (hole/slot) aluminium specimens, in such a way to work out, with statistical significance, the material fatigue parameters for crack growth simulation. The plate geometry (Fig.1) as well as the whole testing procedure was consistent with ASTM E 647 specification. A constant amplitude fatigue traction load ($P_{max}=14\text{ kN}$, $R=P_{min}/P_{max}=0.1$) was applied by a servo-hydraulic machine, with a frequency $f=5\text{Hz}$, at ambient temperature.

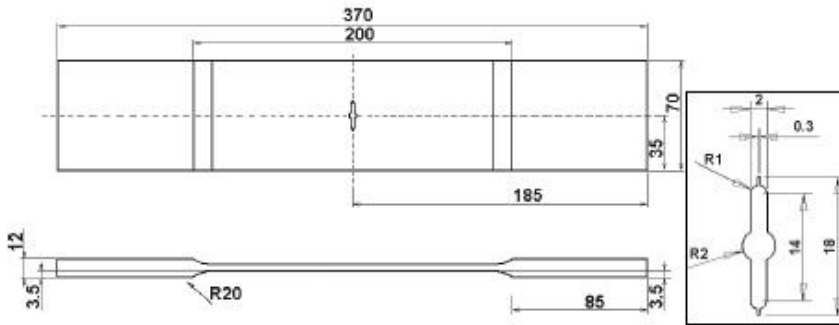


Fig.1. Specimen geometry adopted for fatigue strain

During the experimental fatigue test on simple specimens, figure 1, crack length data, measured by optical systems, were recorded and used to work out, by analytical formula, the corresponding SIF's (Stress Intensity Factors) and crack growth rates. The observed rectilinear crack propagation path turned out to be consistent with symmetric boundary conditions but, whenever out of tolerance deviations from the ideal rectilinear path came out, the corresponding specimens were discarded from the analysis. For each valid specimen, according to the mentioned standard, a chart with crack length against the number of cycles was plotted, in order to assess crack growth rates da/dN , calculated by the secant method, while SIF's were calculated by analytical formulas. Crack growth rate values were then plotted against ΔK in a bilogarithmic chart and a linear regression was performed to estimate the Paris law material constants C and m , figure 2.

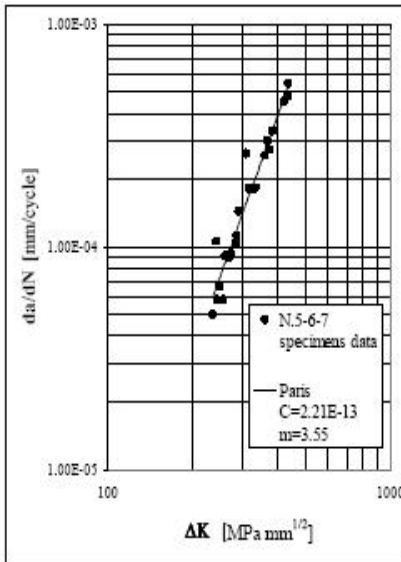


Fig.2. Interpolation curve using Paris law

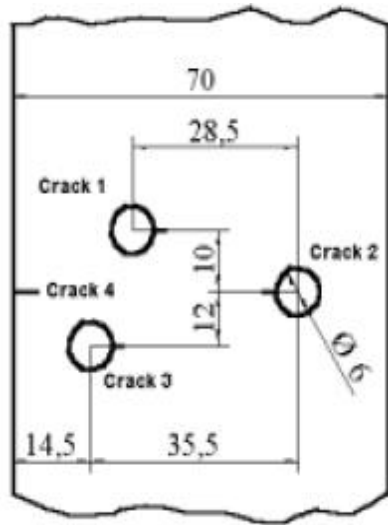


Fig. 3. Notched specimen, (dimensions mm)

3. NUMERICAL-EXPERIMENTAL ANALYSIS FOR MSD COMPLEX GEOMETRY CRACKED PLATES

The material fatigue parameters, obtained by the experimental analysis previously described, are useful to perform an MSD crack growth simulation on a complex geometry specimen made of the same material, figure 3. In our case the results of such numerical analysis were compared with those from the experimental tests, in order to validate and improve the numerical procedure. Two loading conditions were considered on different specimens:

1. Cyclic load with constant amplitude ($P_{max}-P_{min}=12.6$ KN) and stress ratio ($R=0.1$), the same values were used for the simple notched specimens, with Paris law adopted for numerical crack growth assessment. Crack paths and propagation times, figure 4 ÷ figure 7, were compared with the experimental ones from specimen N.1, getting a satisfactory agreement;

2. Cyclic load with variable amplitude and stress ratio with NASGRO law, equation (1), adopted for numerical crack growth assessment (in this case the Paris law did not give satisfactory results).

The crack paths are the same as for the previous case and the propagation times figure 4 ÷ figure 7, were compared with the

experimental ones from specimen N°2, getting a satisfactory agreement especially in the first part of the propagation. The differences (however limited) in the final part suggest improving the correlation by increasing the experimental data.

$$\frac{da}{dN} = \frac{C \cdot (\Delta K)^m \cdot \left(1 - \frac{\Delta K_{th}}{\Delta K}\right)^p}{\left(1 - \frac{\Delta K}{(1-R) \cdot K_c}\right)^q}; \Rightarrow C = 4.26E - 11, m = 2.69 \quad (1)$$

For that concern the specimen N°2, with the same experimental data (coming from simple notched specimens) a non-linear regression was attempted in order to model the threshold phenomena and the fracture toughness for the final unstable crack propagation. Such parameters were extracted from the NASGRO, equation (1), in order to get the unknowns C and m from the non-linear regression (made with MATHEMATICA).

From figure 4, related to crack 1, which is the first appearing, it is possible to note the little difference between initiation times for the two complex geometry specimens.

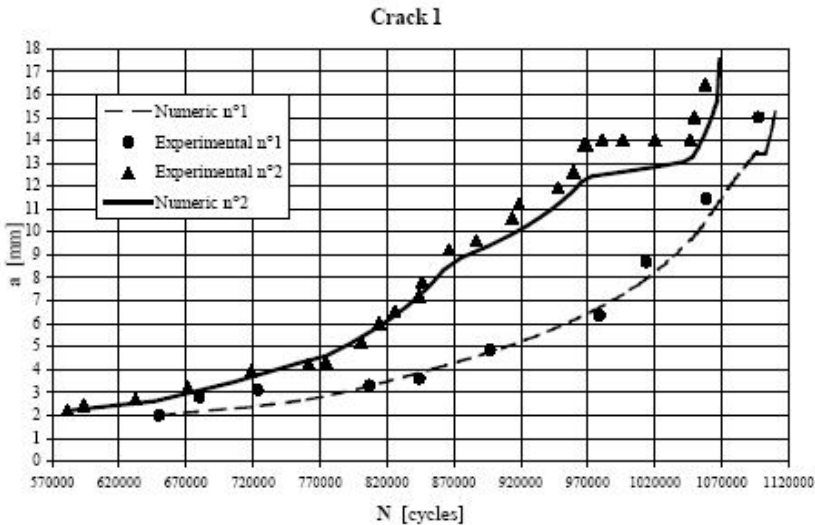


Fig. 4. Crack length versus number of cycles, as obtained by numerical simulation with Paris (specimen 1) and NASGRO (specimen 2) laws and by experimental tests

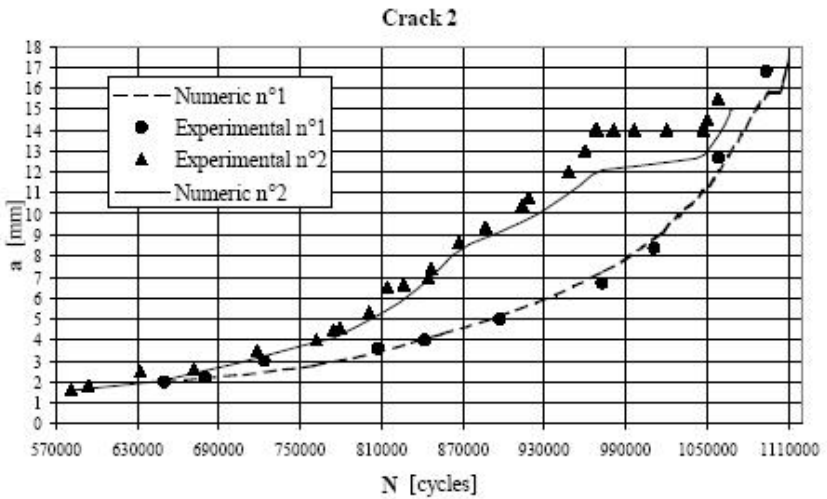


Fig.5. Crack length versus number of cycles, as obtained by numerical simulation with Paris (specimen 1) and NASGRO(specimen 2) laws and by experimental tests

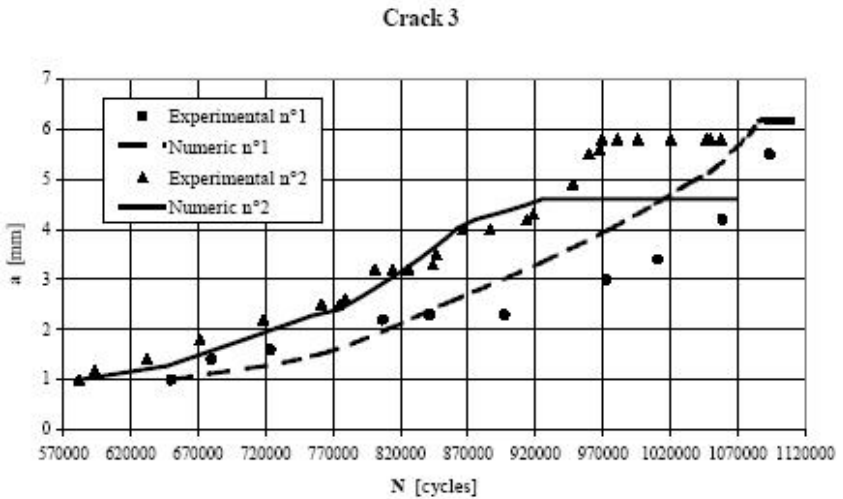


Fig.6. Crack length versus number of cycles, as obtained by numerical simulation with Paris (specimen 1) and NASGRO(specimen 2) laws and by experimental tests

Crack 4

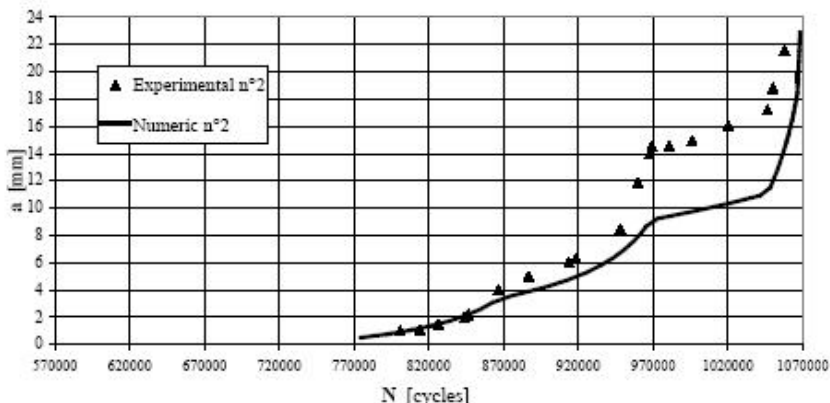


Fig.7. Crack length versus number of cycles, as obtained by numerical simulation with Paris (specimen 1) and NASGRO(specimen 2) laws and by experimental tests

4. CONCLUSIONS

Satisfactory agreement was obtained between numerical and experimental crack propagation rates on specimen 1 when using the Paris formula, with the related constants provided by in house made experimental tests. Such formula was not anymore accurate for variable amplitude load cycles (as applied to specimen 2) because unable to keep in account the load ratio variability. That is why a more complex correlation based on the same experimental data and on information from NASGRO database (without the need to model crack closure effect), was attempted with a satisfactory agreement between numerical and experimental results. The later approach could be improved by increasing the experimental data by cycling some simple notched specimen with different R values (at this stage only data with $R=0.1$ were available). Another possibility would be to use also the experimental data coming from the specimen N°1 in order to set up a propagation law to be tested with results coming from specimen N°2.

REFERENCES

1. "Standard Test Method for Measurement of Fatigue Crack Growth Rates", normative ASTM E 647-91;
2. Pană, T., The Mechanics of Fracture Materials, Bucharest, 1992;
3. Rusu, O., a. o., Fatigue of Metals, tomes 1 and 2, Technics' Publishing House, Bucharest, 1992.

THE COMPUTATIONAL ANALYSIS OF THE INFLUENCE OF VIBRATIONS ON THE SPEED AND ACCELERATION FIELDS OF THE LINEAR ELASTIC ROD OF AN R (RRT) MECHANISM

Dan Gheorghe BĂGNARU¹, Andrei Gheorghe NANU¹,
Gheorghe NANU¹

¹ University of Craiova, Faculty of Mechanics

Summary: In the paper it is presented, firstly, the influence of the kinematic parameters on the longitudinal and transversal displacement fields of the linear elastic rod of a slider-crank mechanism. After determining the displacements caused by vibrations, there are determined the speed and acceleration fields. Calling on a numerical application, it is considered only the vertical component of the acceleration, as the amplitudes of the longitudinal vibrations are of nonessential size. Finally, the theoretical and experimental results are compared.

Keywords: rod, vibrations, mechanism, speeds, accelerations.

1. INTRODUCTION

Let there be the linear elastic rod of the slider-crank mechanism given in figure 1.

Taking into account only the influence of the kinematic parameters, the mathematical model of the vibrations of the connecting rod OA [1] is:

$$\begin{aligned}
 & [L_o]\{u\} + \rho \cdot A \cdot \begin{bmatrix} -1 & 0 \\ 0 & 1 \end{bmatrix} \{a_o\} + \rho Ax \{\omega^2; \varepsilon\}^T + \\
 & + \begin{bmatrix} 1 & 0 \\ 0 & -1 \end{bmatrix} \{f\} + \left\{ 0; \frac{\partial m}{\partial x} \right\}^T + \{F\} = \{0\}
 \end{aligned} \tag{1}$$

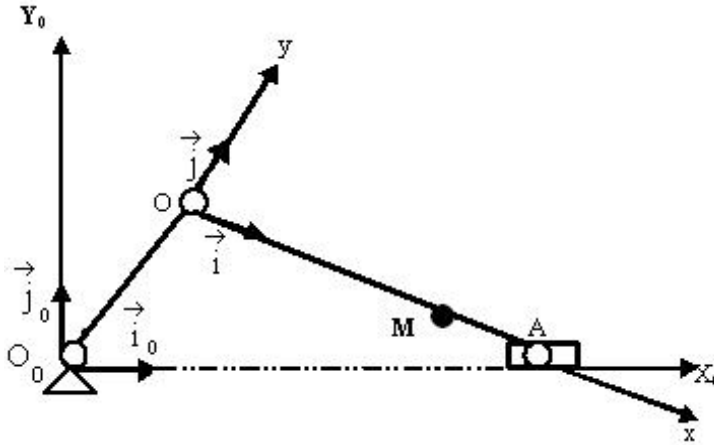


Fig. 1. R (RRT) Mechanism

where:

$$\{F\} = \{F_1, F_2\} = [L_l]\{u\};$$

$$[L_l]\bullet = [M_5] \frac{\partial \bullet}{\partial t} + [M_6]\bullet;$$

$$[L_0]\bullet = EI \begin{bmatrix} 0 & 0 \\ 0 & 1 \end{bmatrix} \frac{\partial^4 \bullet}{\partial x^4} + \rho I \begin{bmatrix} 0 & 0 \\ 0 & -1 \end{bmatrix} \frac{\partial^4 \bullet}{\partial x^2 \partial t^2} +$$

$$+ EA \begin{bmatrix} 1 & 0 \\ 0 & 1 \end{bmatrix} \frac{\partial^2 \bullet}{\partial x^2} + \rho A \begin{bmatrix} -1 & 0 \\ 0 & 1 \end{bmatrix} \frac{\partial^2 \bullet}{\partial t^2}$$

Disregarding the vector $\{F\}$ in the matrix equation (1), it results the particular form of this model:

$$[L_0]\{u\} + \rho \cdot A \cdot \begin{bmatrix} -1 & 0 \\ 0 & 1 \end{bmatrix} \{a_0\} + \rho Ax \{\omega^2; \varepsilon\}^T +$$

$$+ \begin{bmatrix} 1 & 0 \\ 0 & -1 \end{bmatrix} \{f\} + \left\{ 0; \frac{\partial m}{\partial x} \right\}^T = \{0\} \quad (1^{(1)})$$

which is a detached, linear model, with constant coefficients in a first approximation.

With $m = 0$ and $\{f\} = \{0\}$, in (1), it results the mathematical model of free vibrations as follows:

$$[L_0]\{u\} + \rho \cdot A \cdot \begin{bmatrix} -1 & 0 \\ 0 & 1 \end{bmatrix} \{a_0\} + \rho Ax \{\omega^2; \varepsilon\}^T + \{F\} = \{0\}, \quad (1^{(2)})$$

and with $\{F\} = \{0\}$, in (1⁽²⁾), it results the mathematical model of free vibrations in a first approximation as follows:

$$[L_0]\{u\} + \rho \cdot A \cdot \begin{bmatrix} -1 & 0 \\ 0 & 1 \end{bmatrix} \{a_0\} + \rho Ax \{\omega^2; \varepsilon\}^T = \{0\} \quad (1^{(3)})$$

2. DISPLACEMENT FIELDS

The longitudinal and, respectively, transversal displacement fields, in the first approximation, in the case of free vibrations of the connecting rod OA of the R (RRT) mechanism given in figure 1, represented by the equation (1⁽³⁾), will be given, following the application of the Laplace and Fourier transforms finite in sine and cosine, by the functions:

$$u_l^{(1)}(x, t) = a_1 + a_2 \cdot \cos^2(\omega_0 t) + a_3 \cdot \cos(\omega_0 t) + \frac{2}{L} \cdot \sum_{n=1}^{\infty} \left[a_{1,n} + a_{2,n} \cdot \cos^2(\omega_0 t) + a_{3,n} \cdot \cos(\omega_0 t) + a_{4,n} \cdot \cos(\omega_{n,l} t) \right] \cdot \cos(\alpha_n x) \quad (2)$$

$$u_2^{(I)}(x,t) = \frac{2b}{L} \cdot \sum_{n=1}^{\infty} \frac{1}{b_n} \left[\left(\sum_{j=1}^4 b_{j,n} \right) \sin(\omega_0 t) + (b_{5,n} + b_{6,n}) \sin(2\omega_0 t) + \left(\sum_{j=1}^4 c_{j,n} \right) \sin(\omega_{n,2} t) \right] \cdot \sin(\alpha_n x) \quad (3)$$

where:

$$a_1 = \frac{r(3r+4L)}{4}; a_2 = -\frac{3r^2}{4}; a_3 = -Lr; b = -Ar\rho\omega_0^2;$$

$$\omega_{n,1} = \alpha_n \sqrt{\frac{E}{\rho}}; \omega_{n,2} = \alpha_n^2 \sqrt{\frac{EI}{\rho A}};$$

$$\alpha_n = \frac{n\pi}{L}; a_{3,n} = -\frac{\rho\omega_0^2 r}{\alpha_n(\rho\omega_0^2 - E\alpha_n^2)} \cdot \sin(L\alpha_n);$$

$$a_{1,n} = \frac{\rho^2 \omega_0^2 r^2 (\omega_0^2 - \omega_{n,1}^2)}{\omega_{n,1}^2 L^2 \alpha_n^2 (\rho\omega_0^2 - E\alpha_n^2) (4\rho\omega_0^2 - E\alpha_n^2)} \cdot \left\{ L\alpha_n (\omega_{n,1}^2 - 4\omega_0^2) \sin(L\alpha_n) + 2\omega_0^2 [1 - \cos(L\alpha_n)] \right\};$$

$$a_{2,n} = -\frac{\rho^2 \omega_0^2 r^2 (\omega_0^2 - \omega_{n,1}^2)}{L^2 \alpha_n^2 (\rho\omega_0^2 - E\alpha_n^2) (4\rho\omega_0^2 - E\alpha_n^2)} \cdot [2L\alpha_n \sin(L\alpha_n) + \cos(L\alpha_n) - 1];$$

$$a_{4,n} = -a_{3,n} + \frac{\rho^2 \omega_0^2 r^2 (\omega_0^2 - \omega_{n,1}^2)}{\omega_{n,1}^2 L^2 \alpha_n^2 (\rho\omega_0^2 - E\alpha_n^2) (4\rho\omega_0^2 - E\alpha_n^2)} \cdot \left\{ \omega_{n,1}^2 L\alpha_n \sin(L\alpha_n) + (2\omega_0^2 - \omega_{n,1}^2) [1 - \cos(L\alpha_n)] \right\}$$

$$b_n = L\sqrt{EI} \cdot \alpha_n^4 \left(E^2 I^2 \alpha_n^8 - 5AEI \rho \alpha_n^4 \omega_0^2 + 4A^2 \rho^2 \omega_0^2 \right);$$

$$b_{1,n} = \sqrt{E^3 I^3} \alpha_n^6 \sin(L\alpha_n);$$

$$b_{2,n} = -\sqrt{E^3 I^3} \alpha_n^7;$$

$$b_{3,n} = -4A\rho\sqrt{EI} \cdot \alpha_n^2 \omega_0^2 \sin(L\alpha_n);$$

$$b_{4,n} = 4LA\rho\sqrt{EI} \cdot \alpha_n^3 \omega_0^2;$$

$$b_{5,n} = -\frac{1}{2}\sqrt{E^3 I^3} \alpha_n^7 r \left[1 - \cos(L\alpha_n) \right];$$

$$b_{6,n} = \frac{1}{2}A\rho r\sqrt{EI} \cdot \alpha_n^3 \omega_0^2 \left[1 - \cos(L\alpha_n) \right];$$

$$c_{1,n} = EI\sqrt{A\rho} \cdot \alpha_n^4 \omega_0 \sin(L\alpha_n);$$

$$c_{2,n} = EI\sqrt{A\rho} \cdot \alpha_n^5 \omega_0 \left[L + r - r \cos(L\alpha_n) \right];$$

$$c_{3,n} = 4\sqrt{A^3 \rho^3} \omega_0^3 \sin(L\alpha_n);$$

$$c_{4,n} = -\sqrt{A^3 \rho^3} \alpha_n \omega_0^3 \left[4L + r - r \cos(L\alpha_n) \right].$$

In the actual case in which: $L=1$ [m], $b=0,04$ [m], $h=0,005$ [m], $r=0,075$ [m], we obtain the graphic representations given in figures 2

and 3 of the functions $u_1 = u_1^{(1)}(x,t)$ and $u_2 = u_2^{(1)}(x,t)$. It can be noticed that the field of longitudinal displacements has a negligible influence. That is why we have continued the iterative process only for transversal displacements. With the transversal displacement function $u_2 = u_2^{(1)}(x,t)$ given the relation (3) it has been computed $\{F^{(1)}\}$, in a first approximation, which has been inputted in the second equation of the system given in (1⁽³⁾). Following the integration of this equation, it is obtained the solution in the second approximation $u_2^{(2)}(x,t)$. By stopping the iterative process at the third approximation, it results the

graphical representation of the transversal displacement function

$u_2 = u_2\left(\frac{L}{3}, t\right)$ given in figure 4.

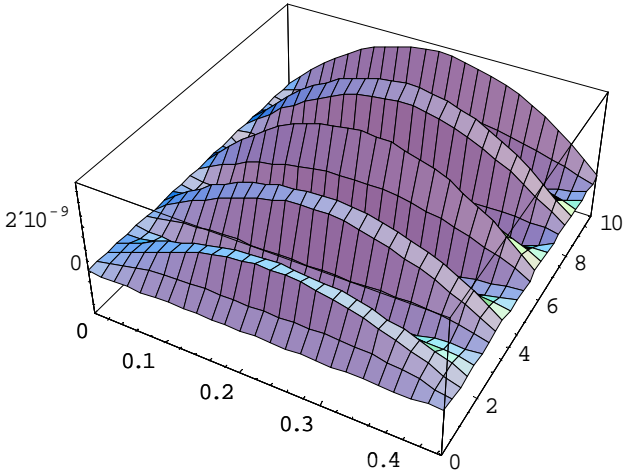


Fig. 2. $u_1 = u_1^{(1)}(x, t)$

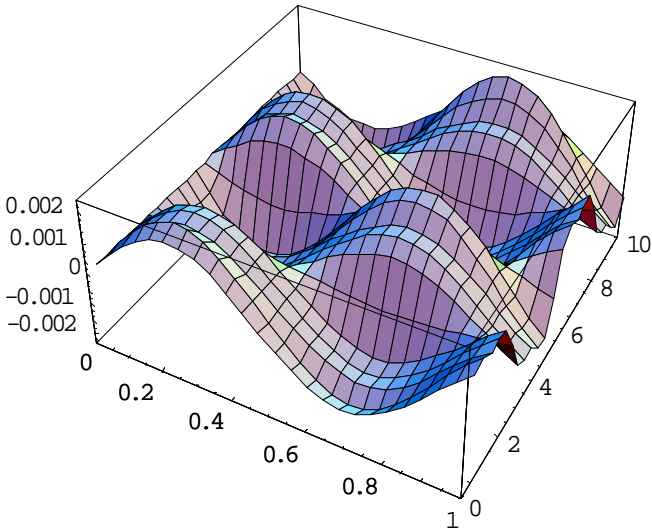


Fig. 3. $u_2 = u_2^{(1)}(x, t)$

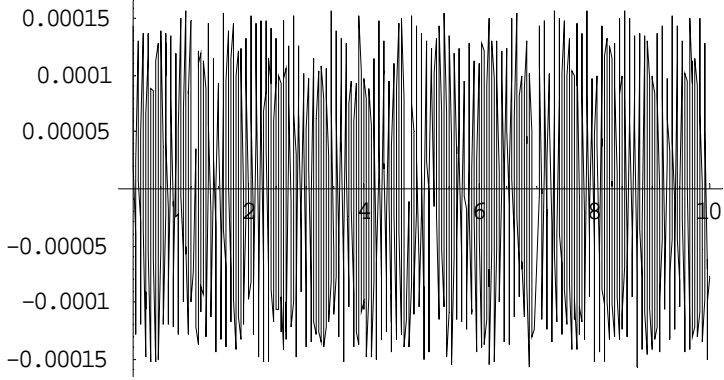


Fig. 4. The transversal displacement

3. THE SPEED AND ACCELERATION FIELDS

In [4] there are given the expressions for the speed and acceleration fields, which, in our case, become:

$$\begin{aligned} \vec{v}_M(x,t) &= \left\{ \vec{i}; \vec{j} \right\} \begin{pmatrix} v_{x,M} \\ v_{y,M} \end{pmatrix} = \\ &= \left\{ \vec{i}; \vec{j} \right\} \begin{pmatrix} v_{o_1} + \frac{\partial u_1(x,t)}{\partial t} - \omega u_2(x,t) \\ v_{o_2} + \omega x + \frac{\partial u_2(x,t)}{\partial t} + \omega u_1(x,t) \end{pmatrix}, \end{aligned} \quad (4)$$

$$\begin{aligned} \vec{a}_M &= \left(\vec{i}, \vec{j} \right) \begin{pmatrix} a_{x,M} \\ a_{y,M} \end{pmatrix} = \\ &= \left(\vec{i}; \vec{j} \right) \begin{pmatrix} a_{o_1} - \omega^2 x + \frac{\partial^2 u_1}{\partial t^2} - 2\omega \frac{\partial u_2}{\partial t} - \varepsilon u_2 - \omega^2 u_1 \\ a_{o_2} - \varepsilon x + \frac{\partial^2 u_2}{\partial t^2} + 2\omega \frac{\partial u_1}{\partial t} + \varepsilon u_1 - \omega^2 u_2 \end{pmatrix} \end{aligned} \quad (5)$$

in which the displacement u_1 and u_2 are given by the relations (2) and (3), and the kinematic parameters are given by the relations:

$$\{v_o\} = \left\{ -\omega_0^2 r \left[\sin(\omega_0 t) + \frac{r}{2L} \sin(2\omega_0 t) \right]; \omega_0 r \left[\cos(\omega_0 t) - \frac{r}{L} \sin^2(\omega_0 t) \right] \right\}^T \quad (6)$$

$$\{a_o\} = \left\{ \omega_0^2 r \left[\frac{r}{L} \sin^2(\omega_0 t) - \cos(\omega_0 t) \right]; -\omega_0^2 r \left[\sin(\omega_0 t) + \frac{r}{2L} \sin(2\omega_0 t) \right] \right\}^T ;$$

$$\omega = -\frac{r}{L} \omega_0 \cos(\omega_0 t); \varepsilon = \frac{\omega_0^2 r}{L} \sin(\omega_0 t), \quad (7)$$

In the end, there result the speed and acceleration fields as given below:

$$v_{x,M} = -\omega_0^2 r \left[\sin(\omega_0 t) + \frac{r}{2L} \sin(2\omega_0 t) \right] - a_2 \omega_0 \sin(2\omega_0 t) - a_3 \omega_0 \sin(\omega_0 t) +$$

$$+ \frac{2}{L} \cdot \sum_{n=1}^{\infty} \left[-a_{2,n} \omega_0 \sin(2\omega_0 t) - a_{3,n} \omega_0 \sin(\omega_0 t) - a_{4,n} \omega_{n,1} \sin(\omega_{n,1} t) \right] \cdot$$

$$\cdot \cos(\alpha_n x) + \cos(\omega_0 t) \cdot \frac{2br\omega_0}{L^2} \cdot$$

$$\cdot \sum_{n=1}^{\infty} \frac{1}{b_n} \left[\left(\sum_{j=1}^4 b_{j,n} \right) \sin(\omega_0 t) + (b_{5,n} + b_{6,n}) \sin(2\omega_0 t) + \left(\sum_{j=1}^4 c_{j,n} \right) \sin(\omega_{n,2} t) \right] \cdot$$

$$\cdot \sin(\alpha_n x),$$

$$v_{y,M} = \omega_0 r \left[\cos(\omega_0 t) - \frac{r}{L} \sin^2(\omega_0 t) \right] - \frac{r}{L} \omega_0 \cos(\omega_0 t) x + \frac{2b}{L} \cdot$$

$$\cdot \sum_{n=1}^{\infty} \frac{1}{b_n} \left[\left(\sum_{j=1}^4 b_{j,n} \right) \omega_0 \cos(\omega_0 t) + 2\omega_0 (b_{5,n} + b_{6,n}) \cos(2\omega_0 t) + \left(\sum_{j=1}^4 c_{j,n} \right) \omega_{n,2} \cos(\omega_{n,2} t) \right] \cdot$$

$$\cdot \sin(\alpha_n x) - \frac{r}{L} \omega_0 \cos(\omega_0 t) \left\{ a_1 + a_2 \cdot \cos^2(\omega_0 t) + a_3 \cdot \cos(\omega_0 t) + \right.$$

$$\left. + \frac{2}{L} \cdot \sum_{n=1}^{\infty} \left[a_{1,n} + a_{2,n} \cdot \cos^2(\omega_0 t) + a_{3,n} \cdot \cos(\omega_0 t) + a_{4,n} \cdot \cos(\omega_{n,1} t) \right] \cdot \cos(\alpha_n x) \right\};$$

$$\begin{aligned}
a_{x,M} = & \omega_0^2 r \left[\frac{r}{L} \sin^2(\omega_0 t) - \cos(\omega_0 t) \right] - x \frac{r^2}{L^2} \omega_0^2 \cos^2(\omega_0 t) - 2a_2 \omega_0^2 \cos(2\omega_0 t) - \\
& - a_3 \omega_0^2 \cos(\omega_0 t) + \frac{2}{L} \cdot \sum_{n=1}^{\infty} \left[-2\omega_0 a_{2,n} \cos(2\omega_0 t) - a_{3,n} \omega_0^2 \sin(\omega_0 t) - a_{4,n} \omega_{n,1}^2 \cos(\omega_{n,1} t) \right] \cdot \\
& \cdot \cos(\alpha_n x) + \frac{4br}{L^2} \omega_0 \cos(\omega_0 t) \cdot \\
& \cdot \sum_{n=1}^{\infty} \frac{1}{b_n} \left[\left(\sum_{j=1}^4 b_{j,n} \right) \omega_0 \cos(\omega_0 t) + 2\omega_0 (b_{5,n} + b_{6,n}) \cos(2\omega_0 t) + \left(\sum_{j=1}^4 c_{j,n} \right) \omega_{n,2} \cos(\omega_{n,2} t) \right] \cdot \\
& \cdot \sin(\alpha_n x) - \left[\frac{2br}{L^2} \omega_0^2 \sin(\omega_0 t) \right] \cdot \\
& \cdot \sum_{n=1}^{\infty} \frac{1}{b_n} \left[\left(\sum_{j=1}^4 b_{j,n} \right) \sin(\omega_0 t) + (b_{5,n} + b_{6,n}) \sin(2\omega_0 t) + \left(\sum_{j=1}^4 c_{j,n} \right) \sin(\omega_{n,2} t) \right] \cdot \\
& \cdot \sin(\alpha_n x) - \left[\frac{r^2}{L^2} \omega_0^2 \cos^2(\omega_0 t) \right] \cdot \left\{ a_1 + a_2 \cdot \cos^2(\omega_0 t) + a_3 \cdot \cos(\omega_0 t) + \right. \\
& \left. + \frac{2}{L} \cdot \sum_{n=1}^{\infty} \left[a_{1,n} + a_{2,n} \cdot \cos^2(\omega_0 t) + a_{3,n} \cdot \cos(\omega_0 t) + a_{4,n} \cdot \cos(\omega_{n,1} t) \right] \cdot \cos(\alpha_n x) \right\},
\end{aligned}$$

$$\begin{aligned}
a_{y,M} = & -\omega_0^2 r \left[\sin(\omega_0 t) + \frac{r}{2L} \sin(2\omega_0 t) \right] - x \frac{\omega_0^2 r}{L} \sin(\omega_0 t) + \frac{2b}{L} \sum_{n=1}^{\infty} \frac{1}{b_n} \cdot \\
& \cdot \left[- \left(\sum_{j=1}^4 b_{j,n} \right) \omega_0^2 \sin(\omega_0 t) - 4 \omega_0^2 (b_{5,n} + b_{6,n}) \sin(2\omega_0 t) - \left(\sum_{j=1}^4 c_{j,n} \right) \omega_{n,2}^2 \sin(\omega_{n,2} t) \right] \cdot \\
& \cdot \sin(\alpha_n x) + 2 \left[-\frac{r}{L} \omega_0 \cos(\omega_0 t) \right] \cdot \left\{ -a_2 \omega_0 \sin(2\omega_0 t) - a_3 \omega_0 \sin(\omega_0 t) + \right. \\
& \left. + \frac{2}{L} \sum_{n=1}^{\infty} \left[-a_{2,n} \sin(2\omega_0 t) - a_{3,n} \omega_0 \sin(\omega_0 t) - a_{4,n} \omega_{n,1} \sin(\omega_{n,1} t) \right] \cdot \cos(\alpha_n x) \right\} + \\
& + \left[\frac{\omega_0^2 r}{L} \sin(\omega_0 t) \right] \cdot \left\{ a_1 + a_2 \cdot \cos^2(\omega_0 t) + a_3 \cdot \cos(\omega_0 t) + \right. \\
& \left. + \frac{2}{L} \sum_{n=1}^{\infty} \left[a_{1,n} + a_{2,n} \cdot \cos^2(\omega_0 t) + a_{3,n} \cdot \cos(\omega_0 t) + a_{4,n} \cdot \cos(\omega_{n,1} t) \right] \cdot \cos(\alpha_n x) \right\} - \\
& - \frac{2br^2}{L^3} \omega_0^2 \cos^2(\omega_0 t) \cdot \\
& \cdot \sum_{n=1}^{\infty} \frac{1}{b_n} \left[\left(\sum_{j=1}^4 b_{j,n} \right) \sin(\omega_0 t) + (b_{5,n} + b_{6,n}) \sin(2\omega_0 t) + \left(\sum_{j=1}^4 c_{j,n} \right) \sin(\omega_{n,2} t) \right] \sin(\alpha_n x).
\end{aligned} \tag{8}$$

If we stop the iterative process for displacements at the third approximation and we are in the numerical case described above, we obtain the variation diagram of the vertical component of the acceleration given by the relation (8), as it appears in figure 5.

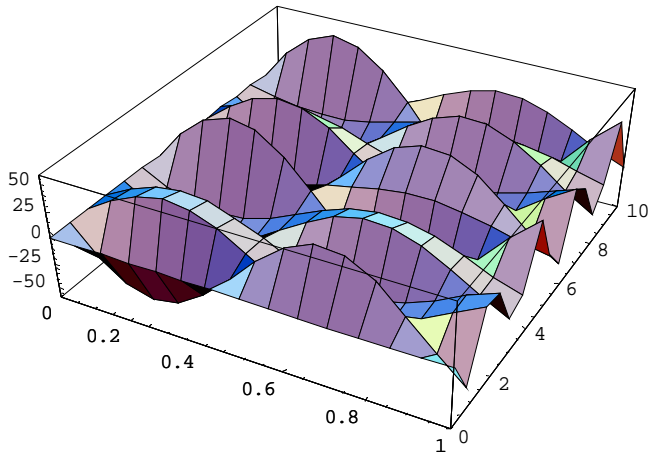


Fig. 5. The variation diagram of the vertical component

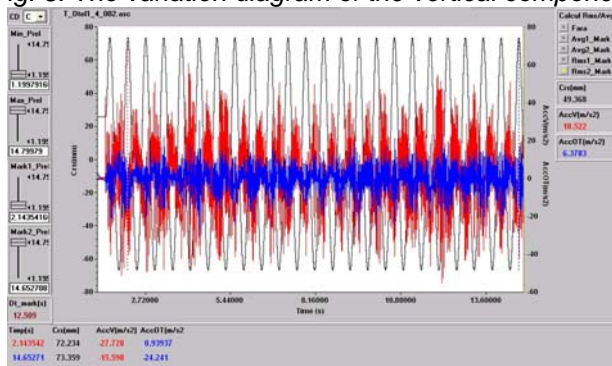


Fig. 6. The accelerations of different points of the connecting rod

4. EXPERIMENTAL TESTS

The accelerometers used to measure the vibrations were installed on the surface of the installation, on vertical and longitudinally horizontal directions (along the vibration direction on the horizontal). Tests were performed to determine the vibratory answer of the installation, on vertical direction, for different percussion frequencies of irritation. The sampling frequency, at acquisition, was of 40000Hz. The numerical integration of answers in acceleration was effectuated, determining the vibration speed of the installation mass. The numerical integration of answers in speed was performed, determining the vibration displacement of the installation mass. By Rapid Fourier Transform of the answer acceleration, it was determined the frequency spectrum of vibratory answer of the installation using a resolution of

0.1532 Hz. In figure 6 it is given the vertical component of the experimentally obtained acceleration.

4. CONCLUSIONS

The amplitude of longitudinal vibrations is much smaller than the amplitude of transversal vibrations and for this reason the longitudinal vibrations can be neglected. The apparition of buckling phenomenon where appear significant longitudinal deformations is done with transversal deformation that have much bigger values. Therefore they determined only bar transversal vibration. The amplitudes of transversal vibrations have minimum values when the connecting rod is perpendicular on the lug and maximum when the connecting rod and the lug are aligned.

REFERENCES

1. Băgnaru, D., *Vibrațiile elementelor cinematice*, Editura SITECH, Craiova, 2005, ISBN 973-657-854-2.
2. Băgnaru, D., Cătăneanu, A., Cătăneanu, M., About an approximately method to determinate the displacements field in case of a vibrating kinematical element, *Monograph of the Faculty of Technical Sciences, University of Novi Sad*, 2008, pag. 177-180, ISBN 978-86-7892-105-6.
3. Băgnaru, D., Cuță, P., Approximate method in order to determine the displacement fields for the kinematic elements standing in vibration, *Analele Universității din Craiova, Seria Mecanică*, 2007, pag. 1-6.
4. Buculei, M., Băgnaru, D., Nanu, Gh., Marghitu, D., *Metode de calcul în analiza mecanismelor cu bare*, Editura Scrisul Românesc, Craiova, 1986.

THE COMPUTATIONAL ANALYSIS OF THE INFLUENCE OF VIBRATIONS ON THE SPEED AND ACCELERATION FIELDS OF A THIN PLANE PLATE WHICH IS A CONSTITUTIVE ELEMENT OF A KINEMATIC CHAIN

Dan Gheorghe BĂGNARU¹, Andrei Gheorghe NANU¹,
Gheorghe NANU¹

¹ *University of Craiova, Faculty of Mechanics*

Summary: In the paper there are firstly presented the mathematical models of the vibrations of thin linear plates with linear elastic and, respectively, linear viscoelastic behavior, determined using Hamilton's variational principle and, in the case of the viscoelastic plate, using also the Alfrey-Lee correspondence. Then there are presented the displacements obtained after the integration of the mathematical models using Laplace and Fourier transforms finite in sine and cosine. Finally, there are determined the speed and acceleration fields as functions of position and time and, also, the speeds and accelerations in different points of the plate.

Keywords: plate, vibrations, mechanism, speed, acceleration.

1. INTRODUCTION

In figure 1 it is considered a thin plane plate which undergoes a rototranslation movement around the axis Ox_3 with a constant angular speed and which is subjected to free transversal vibrations along this axis.

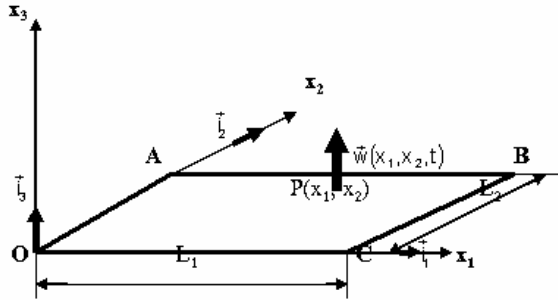


Fig. 1. The thin plane plate in rototranslation

The mathematical model of the transversal vibrations is:

$$\frac{\partial^4 w}{\partial x_1^4} + 2 \frac{\partial^4 w}{\partial x_1^2 \partial x_2^2} + \frac{\partial^4 w}{\partial x_2^4} + c^2 \frac{\partial^2 w}{\partial t^2} - c^2 \omega^2 w + c^2 a_0 = 0 \quad (1)$$

where:

$\vec{w} = w(x_1, x_2, t) \cdot \vec{i}_3$ - the transversal displacement; $\vec{\omega} = \omega \cdot \vec{i}_3$

$\vec{a}_0 = a_{03} \cdot \vec{i}_3 = a_0 \cdot \vec{i}_3$ - the elements of the rototranslation; h - the thickness of the plate; ρ - the specific superficial mass; ν - Poisson's

ratio; E - Young's modulus; $c^2 = \frac{12 \cdot \rho \cdot (1 - \nu^2)}{E \cdot h^2}$.

2. THE DISPLACEMENT FIELDS

In [5] there were obtained the displacement fields of a linear elastic and, respectively, viscoelastic plane plate, subjected to transversal vibrations, as follows:

$$\begin{aligned}
w(x_1, x_2, t) = & \frac{4}{L_1 L_2 \pi^2} \cdot \sum_{n=1}^{\infty} \sum_{m=1}^{\infty} \frac{1}{nm} \left\{ \frac{\pi^2 c n m g_s^{**}(n, m)}{\sqrt{(\alpha_n^2 + \beta_m^2)^2 - c^2 \omega^2}} \cdot \right. \\
& \cdot \sin \left[\frac{1}{c} \sqrt{(\alpha_n^2 + \beta_m^2)^2 - c^2 \omega^2} \cdot t \right] + \\
& \left. \frac{\pi^2 n m f_s^{**}(n, m) \left[(\alpha_n^2 + \beta_m^2)^2 - c^2 \omega^2 \right] + c^2 L_1 L_2 a_0 \left[1 + (-1)^{n+1} \right] \left[1 + (-1)^{m+1} \right]}{(\alpha_n^2 + \beta_m^2)^2 - c^2 \omega^2} \right. \\
& \cdot \cos \left[\frac{1}{c} \sqrt{(\alpha_n^2 + \beta_m^2)^2 - c^2 \omega^2} \cdot t \right] - \frac{c^2 L_1 L_2 a_0 \left[1 + (-1)^{n+1} \right] \left[1 + (-1)^{m+1} \right]}{(\alpha_n^2 + \beta_m^2)^2 - c^2 \omega^2} H(t) \left. \right\} \cdot \\
& \cdot \sin(\alpha_n x_1) \sin(\beta_m x_2),
\end{aligned} \tag{1}$$

$$\begin{aligned}
w(x_1, x_2, t) = & \frac{4}{L_1 L_2 \pi^2} \cdot \\
& \cdot \sum_{n=1}^{\infty} \sum_{m=1}^{\infty} \frac{2 \cdot b_{1,1}}{nm} \left\{ B_{1, nm} + \frac{B_{2, nm}}{B_{3, nm}} \left[\cosh(\Omega_{nm} t) - \sinh(\Omega_{nm} t) \right] + \right. \\
& \left. + \frac{B_{4, nm}}{B_{5, nm}} \cdot \left[\cosh(\Omega_{nm}^I t) - \sinh(\Omega_{nm}^I t) \right] \right\} \sin(\alpha_n x_1) \sin(\beta_m x_2)
\end{aligned} \tag{2}$$

In the actual case in which:

$$c^2 = 0,148; \rho = 1213,3 \left[\text{Kg} / \text{m}^3 \right]; v = 0,4; h = 3 \cdot 10^{-3} \left[\text{m} \right];$$

$$L_1 = 2,34 \left[\text{m} \right]; L_2 = 1,315 \left[\text{m} \right]; \eta = 4,5 \cdot 10^{13} \cdot 3600 \left[\text{Ns} / \text{m}^2 \right]; \omega = 0;$$

$$G = 0,0118979 \cdot 10^{11} \left[\text{N} / \text{m}^2 \right]; a_{03} = 0,2 \left[\text{m} / \text{s}^2 \right];$$

$$K = 0,02424455 \cdot 10^{11} \left[\text{N} / \text{m}^2 \right]$$

the function (2) has the graphic representations given in figures 2 and 3.

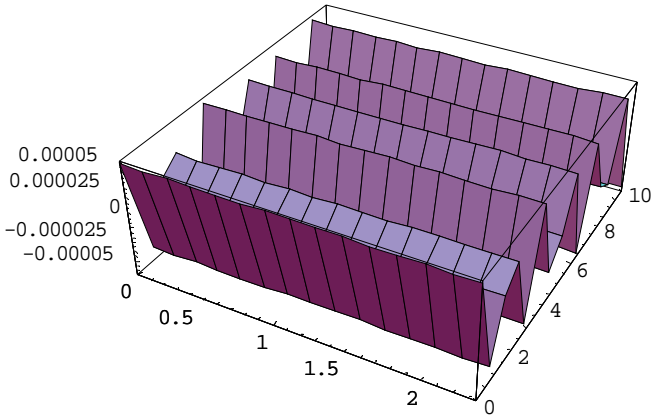


Fig.2. $w = w(x_1, L_2/2, t)$

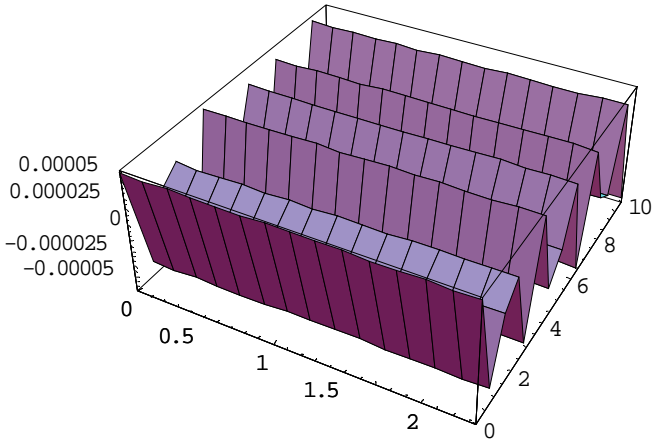


Fig.3. $w = w(L_1/2, x_2, t)$

3. THE SPEED AND ACCELERATION FIELDS

The expressions of the speed and acceleration fields obtained in [4] in the case of the linear elastic plate, with the displacements given in (1), give us the speed and acceleration fields as the functions given

below, in homogeneous and, respectively, inhomogeneous initial conditions.

$$v_P(x_1, x_2, t) = v_O + \frac{4}{L_1 L_2 \pi^2} \cdot \sum_{n=1}^{\infty} \sum_{m=1}^{\infty} \frac{1}{nm} \left\{ - \frac{c L_1 L_2 a_0 \left[1 + (-1)^{n+1} \right] \cdot \left[1 + (-1)^{m+1} \right]}{\sqrt{\left(\alpha_n^2 + \beta_m^2 \right)^2 - c^2 \omega^2}} \right. \\ \left. \cdot \sin \left[\frac{1}{c} \sqrt{\left(\alpha_n^2 + \beta_m^2 \right)^2 - c^2 \omega^2} \cdot t \right] \right\} \sin(\alpha_n x_1) \sin(\beta_m x_2) + v_O,$$

$$v_P(x_1, x_2, t) = v_O + \frac{4}{L_1 L_2 \pi^2} \sum_{n=1}^{\infty} \sum_{m=1}^{\infty} \frac{1}{nm} \left\{ \frac{\pi^2 c n m g_s^{**}(n, m)}{c} \cos \left[\frac{1}{c} \sqrt{\left(\alpha_n^2 + \beta_m^2 \right)^2 - c^2 \omega^2} \cdot t \right] - \frac{\pi^2 n m f_s^{**}(n, m) \left[\left(\alpha_n^2 + \beta_m^2 \right)^2 - c^2 \omega^2 \right] + c^2 L_1 L_2 a_0 \left[1 + (-1)^{n+1} \right] \cdot \left[1 + (-1)^{m+1} \right]}{c \sqrt{\left(\alpha_n^2 + \beta_m^2 \right)^2 - c^2 \omega^2}} \right. \\ \left. \cdot \sin \left[\frac{1}{c} \sqrt{\left(\alpha_n^2 + \beta_m^2 \right)^2 - c^2 \omega^2} \cdot t \right] \right\} \sin(\alpha_n x_1) \sin(\beta_m x_2) + v_O,$$

$$v\left(\frac{L_1}{2}, \frac{L_2}{2}, t\right) = v_O -$$

$$\frac{16ca_0 \sqrt{-c^2 \omega^2 + \frac{\pi^4}{L_1^4 L_2^4} (L_1^2 + L_2^2)^2}}{\pi^2 \left[\left(\frac{\pi^2}{L_1^2} + \frac{\pi^2}{L_2^2} \right)^2 - c^2 \omega^2 \right]} \sin \left[\frac{1}{c} \sqrt{-c^2 \omega^2 + \frac{\pi^4}{L_1^4 L_2^4} (L_1^2 + L_2^2)^2} \cdot t \right] +$$

$$+ \frac{16ca_0 \left[\sqrt{-c^2 \omega^2 + \frac{\pi^4}{L_1^4 L_2^4} (9L_1^2 + L_2^2)^2} t \right]}{3\pi^2 \left[\left(\frac{\pi^2}{L_1^2} + \frac{9\pi^2}{L_2^2} \right)^2 - c^2 \omega^2 \right]} \sin \left[\frac{1}{c} \sqrt{-c^2 \omega^2 + \frac{\pi^4}{L_1^4 L_2^4} (9L_1^2 + L_2^2)^2} t \right],$$

$$v\left(\frac{L_1}{4}, \frac{L_2}{4}, t\right) = v_O -$$

$$\frac{8ca_0 \sqrt{-c^2 \omega^2 + \frac{\pi^4}{L_1^4 L_2^4} (L_1^2 + L_2^2)^2}}{\pi^2 \left[\left(\frac{\pi^2}{L_1^2} + \frac{\pi^2}{L_2^2} \right)^2 - c^2 \omega^2 \right]} \sin \left[\frac{1}{c} \sqrt{-c^2 \omega^2 + \frac{\pi^4}{L_1^4 L_2^4} (L_1^2 + L_2^2)^2} \cdot t \right] -$$

$$\frac{8ca_0 \sqrt{-c^2 \omega^2 + \frac{\pi^4}{L_1^4 L_2^4} (9L_1^2 + 9L_2^2)^2}}{9\pi^2 \left[\left(\frac{9\pi^2}{L_1^2} + \frac{9\pi^2}{L_2^2} \right)^2 - c^2 \omega^2 \right]} \sin \left[\frac{1}{c} \sqrt{-c^2 \omega^2 + \frac{\pi^4}{L_1^4 L_2^4} (9L_1^2 + 9L_2^2)^2} t \right],$$

$$a_P(x_I, x_2, t) = a_O + \frac{4}{L_1 L_2 \pi^2} \cdot$$

$$\cdot \sum_{n=1}^{\infty} \sum_{m=1}^{\infty} \frac{1}{nm} \left\{ \frac{\pi^2 c n m g_s^{**}(n, m) \sqrt{(\alpha_n^2 + \beta_m^2)^2 - c^2 \omega^2}}{c^2} \cdot \right.$$

$$\cdot \sin \left[\frac{1}{c} \sqrt{(\alpha_n^2 + \beta_m^2)^2 - c^2 \omega^2} \cdot t \right] - \cos \left[\frac{1}{c} \sqrt{(\alpha_n^2 + \beta_m^2)^2 - c^2 \omega^2} \cdot t \right] \cdot$$

$$\left. \frac{\pi^2 n m f_s^{**}(n, m) \left[(\alpha_n^2 + \beta_m^2)^2 - c^2 \omega^2 \right] + c^2 L_1 L_2 a_0 \left[1 + (-1)^{n+1} \right] \cdot \left[1 + (-1)^{m+1} \right]}{c^2} \right\}$$

$$\cdot \sin(\alpha_n x_I) \sin(\beta_m x_2),$$

$$a_P(x_I, x_2, t) = a_O + \frac{4}{L_1 L_2 \pi^2} \cdot$$

$$\cdot \sum_{n=1}^{\infty} \sum_{m=1}^{\infty} \frac{1}{nm} \left\{ -L_1 L_2 a_0 \left[1 + (-1)^{n+1} \right] \cdot \left[1 + (-1)^{m+1} \right] \cdot \right.$$

$$\left. \cos \left[\frac{1}{c} \sqrt{(\alpha_n^2 + \beta_m^2)^2 - c^2 \omega^2} \cdot t \right] \right\} \cdot \sin(\alpha_n x_I) \sin(\beta_m x_2),$$

$$\begin{aligned}
a\left(\frac{L_1}{2}, \frac{L_2}{2}, t\right) &= a_O - \frac{16a_0}{\pi^2 \left[\left(\frac{\pi^2}{L_1^2} + \frac{\pi^2}{L_2^2} \right)^2 - c^2 \omega^2 \right]} \left[-c^2 \omega^2 + \frac{\pi^4}{L_1^4 L_2^4} (L_1^2 + L_2^2)^2 \right] \\
&\cdot \cos \left[\frac{1}{c} \sqrt{-c^2 \omega^2 + \frac{\pi^4}{L_1^4 L_2^4} (L_1^2 + L_2^2)^2} \cdot t \right] + \frac{16a_0}{3\pi^2 \left[\left(\frac{\pi^2}{L_1^2} + \frac{9\pi^2}{L_2^2} \right)^2 - c^2 \omega^2 \right]} \\
&\cdot \left[-c^2 \omega^2 + \frac{\pi^4}{L_1^4 L_2^4} (9L_1^2 + L_2^2)^2 \right] \cos \left[\frac{1}{c} \sqrt{-c^2 \omega^2 + \frac{\pi^4}{L_1^4 L_2^4} (9L_1^2 + L_2^2)^2} \cdot t \right], \\
a\left(\frac{L_1}{4}, \frac{L_2}{4}, t\right) &= a_O - \frac{8a_0}{\pi^2 \left[\left(\frac{\pi^2}{L_1^2} + \frac{\pi^2}{L_2^2} \right)^2 - c^2 \omega^2 \right]} \left[-c^2 \omega^2 + \frac{\pi^4}{L_1^4 L_2^4} (L_1^2 + L_2^2)^2 \right] \\
&\cdot \cos \left[\frac{1}{c} \sqrt{-c^2 \omega^2 + \frac{\pi^4}{L_1^4 L_2^4} (L_1^2 + L_2^2)^2} \cdot t \right] + \frac{8a_0}{9\pi^2 \left[\left(\frac{9\pi^2}{L_1^2} + \frac{9\pi^2}{L_2^2} \right)^2 - c^2 \cdot \omega^2 \right]} \\
&\cdot \left[-c^2 \omega^2 + \frac{\pi^4}{L_1^4 L_2^4} (9L_1^2 + 9L_2^2)^2 \right] \cos \left[\frac{1}{c} \sqrt{-c^2 \omega^2 + \frac{\pi^4}{L_1^4 L_2^4} (9L_1^2 + 9L_2^2)^2} \cdot t \right]
\end{aligned}$$

The expressions of the speed and acceleration fields obtained in [4] in the case of the linear viscoelastic plate, with the displacements given in (2), give us the speed and acceleration fields as the functions given below.

$$v_{3,M} = v_O + \frac{4}{L_1 L_2 \pi^2} \sum_{n=1}^{\infty} \sum_{m=1}^{\infty} \frac{A_{1,nm} \Omega_{nm}}{nm A_{5,nm}} [\sinh(\Omega_{nm} t) - \cosh(\Omega_{nm} t)].$$

$$\cdot \left\{ \omega_{nm} \left[\sinh(\omega_{nm}t) + \cosh(\omega_{nm}t) \right] \left[-2A_{3,nm} \Omega_{nm} \left(\sinh(\Omega_{nm}t) + \cos(\Omega_{nm}t) \right) + A_{4,nm} \omega_{nm} \left(\sinh(\omega_{nm}t) + \cosh(\omega_{nm}t) \right) \right] \right\} \cdot \sin(\alpha_n x_1) \cdot \sin(\beta_m x_2)$$

$$a_{3,M}(x_1, x_2, t) = a_O + \frac{4}{L_1 L_2 \pi^2} \cdot$$

$$\cdot \sum_{n=1}^{\infty} \sum_{m=1}^{\infty} \frac{1}{nm A_{5,nm}} \left\{ \operatorname{ch} \left[\frac{1}{2} t (\omega_{nm} - 2\Omega_{nm}) \right] + \operatorname{sh} \left[\frac{1}{2} t (\omega_{nm} - 2\Omega_{nm}) \right] \right\} \cdot$$

$$\cdot \left\{ \left[\operatorname{ch} \left(\frac{\omega_{nm}}{2} t \right) + \operatorname{sh} \left(\frac{\omega_{nm}}{2} t \right) \right] \cdot \omega_{nm}^2 (A_{1,nm} + A_{2,nm} A_{4,nm}) - 2 \left[\operatorname{ch} \left(\frac{\omega_{nm}}{2} t \right) + \operatorname{sh} \left(\frac{\omega_{nm}}{2} t \right) \right] \right\} \cdot$$

$$\cdot \omega_{nm} \Omega_{nm} (A_{1,nm} + A_{2,nm} A_{4,nm}) + 2 \Omega_{nm}^2 \left[A_{2,nm} A_{4,nm} \operatorname{ch} \left(\frac{\omega_{nm}}{2} t \right) + A_{1,nm} \operatorname{sh} \left(\frac{\omega_{nm}}{2} t \right) \right] \right\} \cdot$$

$$\cdot \sin(\alpha_n x_1) \cdot \sin(\beta_m x_2)$$

4. CONCLUSIONS

There were of interest the particular cases referring especially to the vibrations of car bodies. The solutions of the equations with partial derivatives and, implicitly, the speed and acceleration fields correspond to the dynamic response following the action of the kinematic parameters of the movement, movement which is assimilated to the "hopping" movement of a vehicle. Those presented find their use in the study of the vibrations of car bodies, which can be assimilated to the mechanical and mathematical models presented in this paper. In the design activity it is essential to determine the displacements caused by vibrations, as function of the kinematic parameters of the movement. This precedes the determination of the components of the specific deformations tensor and the tensions tensor, as well as the speed and acceleration fields. We should also remark the very small displacements in the case of plates with viscoelastic behavior.

REFERENCES

1. Băgnaru, D., About the vibrations of the vehicles, *Analele Universității din Craiova, Seria Mecanică*, Nr. 1, 2004, pag. 7-14, ISSN 1223-5296.
2. Băgnaru, D., Cătăneanu, A., Cătăneanu, M., About the influence of the vibrations of the stress and strain states in case of a thin linear-elastic plane plate, *Monograph, Faculty of Technical Sciences, University of Novi Sad*, 2007, pag. 395-400.

3. Băgnaru, D., Cătăneanu, A., About the Determined Vibrations of the Vehicles, XVI International Conference on „MATERIAL FLOW, MACHINES AND DEVICES IN INDUSTRY”, University of Belgrade, Dec.7-8, 2000, pag.16-20.
4. Buculei, M.,Băgnaru, D., Nanu, Gh., Marghitu, D., Metode de calcul în analiza mecanismelor cu bare, Editura Scrisul Românesc, Craiova, 1986.
5. Băgnaru, D., Vibrațiile elementelor cinematice, Editura SITECH, Craiova, 2005, ISBN 973-657-854-2.
6. Christensen, R.M., Theory of Viscoelasticity: An Introduction, Ac. Press, New York, 1982.
7. Buvet, R., Theorie de la viscoelasticite lineaire, vol. I, Ed. Hermann, Paris, 1970.
8. Chevalier, Y., Beda, T., Bechir, H., Nonlinear Viscoelasticity - Modeling and tests, 9th National Congress on Theoretical and Applied Mechanics - Varna Bulgarie, pp 422-429, 2001.
9. Casimir, J., Chevalier, Y., Du Développement d'un élément continu de plaque et de son implémentation sur le code ETAPE I, DCN, 2001.
10. Cuță P., Băgnaru, D., VIBRATIONS INFLUENCE ON THE ACCELERATION FIELD OF A THIN PLANE PLATE WITH LINEAR ELASTIC BEHAVIOUR, Annals of the Oradea University. Fascicle of Management and Tehnological Engineering, 2009, ISSN, 6 pag.
11. Potapov, V. D., Investigation of dynamical stability of viscoelastic systems with help of Lyapunov exponent. Reports of Russian Academy of Sciences, Mechanics of Solids 6, pp. 82–90, 2000.
12. Sadok, S., Thomas, M., Laville, F., Dynamic Response Obtained by Direct Numerical Integration of Pre-deformed Rectangular Plates Subjected to In-plane Loading, Journal of Sound and Vibration, 197(1), pp 67-83, 1996.

ESTIMATION OF MEAN IN PRESENCE OF NON RESPONSE USING EXPONENTIAL ESTIMATOR

Rajesh SINGH¹, Mukesh KUMAR², Manoj K. CHAUDHARY³,
Florentin SMARANDACHE⁴

^{1,2,3}*Department of Statistics, B.H.U., Varanasi (U.P.)-India*

⁴*Chair of Department of Mathematics, University of New Mexico,
Gallup, USA*

Abstract: This paper considers the problem of estimating the population mean using information on auxiliary variable in presence of non response. Exponential ratio and exponential product type estimators have been suggested and their properties are studied. An empirical study is carried out to support the theoretical results.

Keywords: population mean, study variable, auxiliary variable, exponential ratio, exponential, product estimator, Bias, MSE.

1. INTRODUCTION

In surveys covering human populations, information is in most cases not obtained from all the units in the survey even after some call-backs. Hansen and Hurwitz (1946) considered the problem of non response while estimating the population mean by taking a sub sample from the non respondent group with the help of some extra efforts and an estimator was proposed by combining the information available from response and non response groups. In estimating population parameters like the mean, total or ratio, sample survey experts sometimes use auxiliary information to improve precision of the estimates. When the population mean \bar{X} of the auxiliary variable x is known and in presence of non response, the problem of estimation of population mean \bar{Y} of the study variable y has been discussed by Cochran (1977), Rao (1986), Khare and Srivastava (1997) and Singh and Kumar (2008). In Hansen and Hurwitz (1946) method, questionnaires are mailed to all the respondents included in a sample and a list of non respondents is prepared after the deadline is over.

Then a sub sample is drawn from the set of non respondents and a direct interview is conducted with the selected respondents and the necessary information is collected.

Assume that the population is divided into two groups, those who will not respond called non-response class. Let N_1 and N_2 be the number of units in the population that belong to the response class and the non-response class respectively ($N_1+N_2=N$). Let n_1 be the number of units responding in a simple random sample of size n drawn from the population and n_2 the number of units not responding in the sample. We may regard the sample of n_1 respondents as a simple random sample from the response class and the sample of n_2 as a simple random sample from the non-response class. Let h_2 denote the size of the sub sample from n_2 non-respondents to be interviewed

and $f = \frac{n_2}{h_2}$. Let \bar{y}_1 and \bar{y}_{h_2} denote the sample means of y character

based on n_1 and h_2 units respectively. The estimator proposed by Hansen and Hurwitz (1946) is given by-

$$\bar{y}^* = \frac{n_1\bar{y}_1 + n_2\bar{y}_{h_2}}{n} \quad (1.1)$$

The estimator \bar{y}^* is unbiased and has variance

$$V(\bar{y}^*) = \left(\frac{1}{n} - \frac{1}{N}\right)S_y^2 + (f-1)\frac{N_2}{N} \cdot \frac{S_{y_2}^2}{n} \quad (1.2)$$

The population mean square of the character y is denoted by S_y^2 and the population mean square of y for N_2 non-response units of the population is denoted by $S_{y_2}^2$.

Bahl and Tuteja (1991) introduced an exponential ratio-type estimator for population mean as given by

$$\bar{y}_{er} = \bar{y} \exp \left[\frac{\bar{X} - \bar{x}}{\bar{X} + \bar{x}} \right] \quad (1.3)$$

and exponential product-type estimator as

$$\bar{y}_{ep} = \bar{y} \exp \left[\frac{\bar{X} - \bar{x}}{\bar{X} + \bar{x}} \right] \quad (1.4)$$

The objective of this paper is to study Bahl and Tuteja (1991) exponential ratio- type and product- type estimators in presence of non-response.

2. SUGGESTED ESTIMATOR

First we assume that the non response is only on study variable. The estimator \bar{y}_{er} under non response will take the form

$$\bar{y}_{er}^* = \bar{y}^* \exp \left[\frac{\bar{X} - \bar{x}}{\bar{X} + \bar{x}} \right] \quad (2.1)$$

To obtain the bias and MSE of the estimator \bar{y}_{er}^* we write

$$\bar{y}^* = \bar{Y}(1 + e_0^*), \quad \bar{x} = \bar{X}(1 + e_1)$$

Such that

$$E(e_0^*) = E(e_1) = 0,$$

and

$$\left. \begin{aligned} E(e_0^2) &= \frac{V(\bar{y}^*)}{\bar{Y}^2} \\ E(e_1^2) &= \frac{V(\bar{x})}{\bar{X}^2} = \left(\frac{1}{n} - \frac{1}{N} \right) \frac{S_x^2}{\bar{X}^2} \\ E(e_0^* e_1) &= \frac{\text{cov}(\bar{y}^*, \bar{x})}{\bar{Y}\bar{X}} = \left(\frac{1}{n} - \frac{1}{N} \right) \frac{S_{XY}}{\bar{Y}\bar{X}} \end{aligned} \right\} \quad (2.2)$$

$$\text{where } S_{xy} = \frac{1}{(N-1)} \sum_{j=1}^N (x_j - \bar{X})(y_j - \bar{Y}).$$

Now expressing \bar{y}_{er}^* in terms of e's we have

$$\bar{y}_{er}^* = \bar{Y}(1 + e_0) \exp \left\{ \frac{-e_1}{2(1 + \frac{e_1}{2})} \right\} \quad (2.3)$$

Expanding the right hand side of (2.3) and neglecting the terms involving powers of e's greater than two we have

$$\bar{y}_{er}^* = \bar{Y}(1 + e_0 - \frac{e_1}{2} - \frac{e_0 e_1}{2} + \frac{3e_1^2}{8}) \quad (2.4)$$

Taking expectations of both sides of (2.4), we get the bias of \bar{y}_{er}^* to the first degree of approximation, as

$$B(\bar{y}_{er}^*) = \left(\frac{1}{n} - \frac{1}{N}\right)\bar{Y} \left[\frac{3C_x^2}{8} - \frac{\rho C_y C_x}{2} \right] \quad (2.5)$$

Squaring both sides of (2.4) and neglecting terms of e's involving powers greater than two we have

$$(\bar{y}_{er}^* - \bar{Y})^2 = \bar{Y}^2 \{e_0^2 + \frac{e_1^2}{4} - e_0 e_1\} \quad (2.6)$$

Taking expectations of both sides of (2.6) we get the MSE (to the first degree of approximation) as

$$MSE(\bar{y}_{er}^*) = \left(\frac{1}{n} - \frac{1}{N}\right)\bar{Y}^2 \left[C_y^2 + \frac{C_x^2}{4} - \rho C_y C_x \right] + \frac{(f-1)N_2}{nN} S_{y^2}^2 \quad (2.7)$$

3. EXPONENTIAL PRODUCT TYPE ESTIMATOR

The estimator \bar{y}_{ep} under non response (only on study variable) will take the form

$$\bar{y}_{ep}^* = \bar{y}^* \exp \left[\frac{\bar{x} - \bar{X}}{\bar{x} + \bar{X}} \right] \quad (3.1)$$

Following the procedure of section 2, we get the bias and MSE of \bar{y}_{ep}^* as

$$\text{Bias}(\bar{y}_{ep}^*) = \left(\frac{1}{n} - \frac{1}{N}\right) \bar{Y} \left[\frac{-C_x^2}{8} + \frac{\rho C_x C_y}{2} \right] \quad (3.2)$$

and

$$\begin{aligned} \text{MSE}(\bar{y}_{er}^*) = & \left(\frac{1}{n} - \frac{1}{N}\right) \bar{Y}^2 \left[C_y^2 + \frac{C_x^2}{4} + \right. \\ & \left. C_y C_x \right] + \frac{(f-1)N_2}{nN} S_{y^2}^2 \end{aligned} \quad (3.3)$$

4. NON RESPONSE ON BOTH Y AND X

We assume that the non response is both on study and auxiliary variable. The estimator \bar{y}_{er} and \bar{y}_{ep} under non response on both the variables takes the following form respectively-

$$\bar{y}_{er}^{**} = \bar{y}^* \exp \left[\frac{\bar{X} - \bar{x}^*}{\bar{X} + \bar{x}^*} \right] \quad (4.1)$$

$$\bar{y}_{ep}^{**} = \bar{y}^* \exp \left[\frac{\bar{x}^* + \bar{X}}{\bar{x}^* + \bar{X}} \right] \quad (4.2)$$

To obtain the bias and MSE of the estimator \bar{y}_{er}^{**} and \bar{y}_{ep}^{**} we write

$$\bar{y}^* = \bar{Y}(1 + e_0), \quad \bar{x}^* = \bar{X}(1 + e_1^*), \quad \bar{x} = \bar{X}(1 + e_1)$$

Such that
 $E(e_0) = E(e_1^*) = 0$

$$\left. \begin{aligned}
 E(e_1^{*2}) &= \frac{v(\bar{x}^*)}{\bar{X}^2} = \left(\frac{1}{n} - \frac{1}{N} \right) S_x^2 + (f-1) \frac{N_2}{N} \cdot \frac{S_{x2}^2}{n} \\
 E(e_0 e_2) &= \frac{\text{cov}(\bar{y}^*, \bar{x}^*)}{\bar{Y}\bar{X}} \\
 &= \frac{1}{\bar{Y}\bar{X}} \left[\left(\frac{1}{n} - \frac{1}{N} \right) S_{xy} + (f-1) \frac{N_2}{N} \cdot \frac{S_{xy}}{n} \right]
 \end{aligned} \right\} \quad (4.3)$$

The population mean square of the character x is denoted by S_x^2 and the population mean square of x for N_2 non response units of the population is denoted by S_{x2}^2 .

The biases and MSE of the estimators \bar{y}_{er}^{**} and \bar{y}_{ep}^{**} are given by \bar{y}_{er}^{**} and \bar{y}_{ep}^{**}

$$\begin{aligned}
 B(\bar{y}_{er}^{**}) &= \left(\frac{1}{n} - \frac{1}{N} \right) \bar{Y} \left[\frac{3}{8} \cdot \frac{S_x^2}{\bar{X}^2} - \frac{S_{xy}}{2\bar{Y}\bar{X}} \right] + \bar{Y} \frac{(f-1)}{n} \cdot \frac{N_2}{N} \left[\frac{3}{8} \cdot \frac{S_{x2}^2}{\bar{X}^2} - \frac{S_{xy2}}{2\bar{Y}\bar{X}} \right] \\
 &= \left(\frac{1}{n} - \frac{1}{N} \right) \bar{Y} \left[\frac{3}{8} \cdot C_x^2 - \frac{\rho C_x C_y}{2} \right] + \bar{Y} \frac{(f-1)}{n} \cdot \frac{N_2}{N} \\
 &\quad \left[\frac{3}{8} \cdot C_x'^2 - \frac{\rho_2 C_x' C_y'}{2} \right] \quad (4.4)
 \end{aligned}$$

where $C_x' = \frac{S_{x2}^2}{\bar{X}^2}$, $C_y' = \frac{S_{y2}^2}{\bar{Y}^2}$.

$$\begin{aligned}
 B(\bar{y}_{ep}^{**}) &= \left(\frac{1}{n} - \frac{1}{N} \right) \bar{Y} \left[\frac{-1}{8} \cdot \frac{S_x^2}{\bar{X}^2} + \frac{S_{xy}}{2\bar{Y}\bar{X}} \right] + \bar{Y} \frac{(f-1)}{n} \cdot \frac{N_2}{N} \left[\frac{-1}{8} \cdot \frac{S_{x2}^2}{\bar{X}^2} + \frac{S_{xy2}}{2\bar{Y}\bar{X}} \right] \\
 &= \left(\frac{1}{n} - \frac{1}{N} \right) \bar{Y} \left[\frac{-1}{8} \cdot C_x^2 + \frac{\rho C_x C_y}{2} \right] + \bar{Y} \frac{(f-1)}{n} \cdot \frac{N_2}{N} \\
 &\quad \left[\frac{-1}{8} \cdot C_x'^2 + \frac{\rho_2 C_x' C_y'}{2} \right] \quad (4.5)
 \end{aligned}$$

$$\begin{aligned} \text{MSE}(\bar{y}_{er}^{**}) &= \left(\frac{1}{n} - \frac{1}{N}\right) \bar{Y}^2 \left[C_y^2 + \frac{C_x^2}{4} - \rho C_x C_y \right] + \\ &\bar{Y}^2 \frac{(f-1)}{n} \cdot \frac{N_2}{N} \left[C_y'^2 + \frac{C_x'}{4} - \rho_2 C_x' C_y' \right] \end{aligned} \quad (4.6)$$

$$\begin{aligned} \text{MSE}(\bar{y}_{ep}^{**}) &= \left(\frac{1}{n} - \frac{1}{N}\right) \bar{Y}^2 \left[C_y^2 + \frac{C_x^2}{4} + \rho C_x C_y \right] + \\ &\bar{Y}^2 \frac{(f-1)}{n} \cdot \frac{N_2}{N} \left[C_y'^2 + \frac{C_x'}{4} + \rho_2 C_x' C_y' \right] \end{aligned} \quad (4.7)$$

From expressions (2.7),(3.3),(4.6),(4.7), we observe that the MSE expressions of suggested estimators have an additional term (which depends on non-response)as compared to the estimator proposed by Bahl and Tuteja (1991- without non response).

5. EFFICIENCY COMPARISONS:

From (1.2), (2.7), (3.3), (4.6) and (4.7), we have

First we compare the efficiencies of \bar{y}_{er}^* and \bar{y}^*

$$\text{MSE}(\bar{y}_{er}^*) - V(\bar{y}^*) \leq 0$$

$$\frac{C_x^2}{4} - \rho C_x C_y \leq 0$$

$$\rho \geq \frac{C_x}{4C_y} \quad (5.1)$$

When this condition is satisfied \bar{y}_{er}^* will be better estimator than \bar{y}^* .

Next we compare the efficiencies of \bar{y}_{ep}^* and \bar{y}^*

$$\text{MSE}(\bar{y}_{ep}^*) - V(\bar{y}^*) \leq 0$$

$$\frac{C_x^2}{4} + \rho C_x C_y \leq 0$$

$$\rho \leq -\frac{C_x}{4C_y} \tag{5.2}$$

When this condition is satisfied \bar{y}_{ep}^{**} will be better estimator than \bar{y}^* .

Next, we compare the efficiencies of \bar{y}_{er}^{**} and \bar{y}^*

$$MSE(\bar{y}_{er}^{**}) - V(\bar{y}^*) \leq 0$$

$$(N - n)\alpha \leq (1 - f)N_2\alpha'$$

$$\frac{\alpha}{\alpha'} \leq \frac{(1 - f)N_2}{N - n} \tag{5.3}$$

$$\text{where } \alpha = \frac{C_x^2}{4} - \rho C_y C_x, \quad \alpha' = \frac{C_x^2}{4} - \rho C_y' C_x'$$

When this condition is satisfied \bar{y}_{er}^{**} will be better estimator than \bar{y}^* .

Finally we compare the efficiencies of \bar{y}_{ep}^{**} and \bar{y}^*

$$MSE(\bar{y}_{ep}^{**}) - V(\bar{y}^*) \leq 0$$

$$(N - n)\lambda \leq (1 - f)N_2\lambda'$$

$$\frac{\lambda}{\lambda'} \leq \frac{(1 - f)N_2}{N - n} \tag{5.4}$$

$$\text{where } \lambda = \frac{C_x^2}{4} + \rho C_y C_x, \quad \lambda' = \frac{C_x^2}{4} + \rho C_y' C_x'$$

When this condition is satisfied \bar{y}_{ep}^{**} will be better estimator than \bar{y}^* .

6. EMPIRICAL STUDY

For numerical illustration we consider the data used by Khare and Sinha (2004,p.53). The values of the parameters related to the study

variate y (the weight in kg) and the auxiliary variate x (the chest circumference in cm) have been given below.

$$\bar{Y} = 19.50$$

$$\bar{X} = 55.86$$

$$S_y = 3.04$$

$$S_x = 3.2735$$

$$S_{y^2} = 2.3552$$

$$S_{x^2} = 2.51$$

$$\rho = 0.85$$

$$\rho_2 = 0.7290$$

$$N_1 = 71$$

$$N_2 = 24$$

$$N = 95$$

$$n = 35$$

Here, we have computed the percent relative efficiencies (PRE) of different suggested estimators with respect to usual unbiased estimator \bar{y}^* for different values of f .

Table 5.1: PRE of different proposed estimators

Values of w	f values	\bar{y}^*	\bar{y}_{er}^*	\bar{y}_{ep}^*	\bar{y}_{er}^{**}	\bar{y}_{ep}^{**}
0.10	1.50	100	263.64	45.47	263.65	45.47
	2.00	100	263.62	45.47	263.65	45.47
	2.50	100	263.61	45.48	263.65	45.47
	3.00	100	263.59	45.48	263.64	45.47
0.20	1.50	100	263.62	45.47	263.65	45.47
	2.00	100	263.59	45.48	263.64	45.47
	2.50	100	263.56	45.48	263.64	45.47
	3.00	100	263.52	45.48	263.63	45.47
0.30	1.50	100	263.61	45.48	263.65	45.47
	2.00	100	263.56	45.48	263.64	45.47
	2.50	100	263.51	45.48	263.63	45.47
	3.00	100	263.46	45.48	263.62	45.47

From table 5.1, we conclude that the estimators which use auxiliary information performs better than Hansen and Hurwitz (1946) estimators \bar{y}^* . Also when non response rate increases, the efficiencies of suggested estimators decreases.

REFERENCES

1. Bahl. S. and Tuteja, R.K. (1991): Ratio and product type exponential estimator. *Infrm. and Optim.Sci.*,XII,I,159-163.
2. Cochran, W.G. (1977): *Sampling techniques*, 3rd edn. Wiley, New York.
3. Hansen, M.H. and Hurwitz, W.N. (1946): The problem of non-response in sample surveys. *J. Am. Stat. Assoc.* 41:517–529.
4. Khare B.B. and Srivastava, S. (1997): Transformed ratio type estimators for the population mean in the presence of non-response. *Commun. Stat. Theory Methods* 26(7):1779–1791.
5. Khare, B.B. and Sinha, R.R. (2004): Estimation of finite population ratio using two-phase sampling scheme in the presence of non-response. *Aligarh J Stat*, 24:43–56.
6. Rao, P.S.R.S.(1986): Ratio estimation with sub-sampling the non-respondents. *Surv Methodol* 12(2):217–230.
7. Singh, H.P. and Kumar, S. (2008): Estimation of mean in presence of non-response using two phase sampling scheme. *Statistical Papers*.

ANALYSIS METHODS OF A CIRCULAR PULL BROADCH STRENGTH

Cosmin MIRIȚOIU¹

¹University of Craiova, Faculty of Mechanics

Abstract: A very big importance in a pull broadch designing is represented by its mechanic computation, which tots put the pull broadch strength on various blank tooling, pull broadch productivity and also the loadings which is subdued to and the stresses that appear during the chipping process. The pull broadch geometric complexity leads to one difficulty concerning the strength computing methods application (and implicitly, simplifying assumptions application). This present study presents a strength computing of a pull broadch which dresses a circular hole trotting out more methods which can be used in this computing, and the theoretic aspects are then trotted out by an example of a numerical computation for a particular case.

Keywords: pull broadches, mechanical strength, mechanical stress, finite-elements analysis, circular plate.

1. INTRODUCTION

The pull broadches are tools of high-levelled productivity, which are used at chipping processing of circular holes, various inner channels, and also at simple or profiled plane outer surface processing.

The pull-broadches are high-levelled, constructive and operational complexity tools which leads to a high-cost price. From this reason, it is only used in big production or in operations found in lots of adjusting strips (e.g.: for quoin channel tooling).

An important chapter in pull broadch designing is represented by its strength computing. The high geometrical complexity of the pull broadch leads to difficulties in picking the best computing method which has to ensure its strength during the chipping operation, and to trot out the best phenomenon which takes place during the tooling process.

The present study presents a strength computing of a circular pull broadch which processes a circular hole, possible stresses on which the

pull broach is subdued during the tooling process, being studied. There are approached more mathematics computing simplifying methods and also finite elements analysis methods.

The pull broaches are generally made of high steels. For this present study the high steel HS-18-01 STAS SR EN ISO 4957 is chosen as material. It is considered that the pull broach works on a dragging broached machine.

In a general case, a circular pull broach which processes a circular hole has a form presented in figure 1.

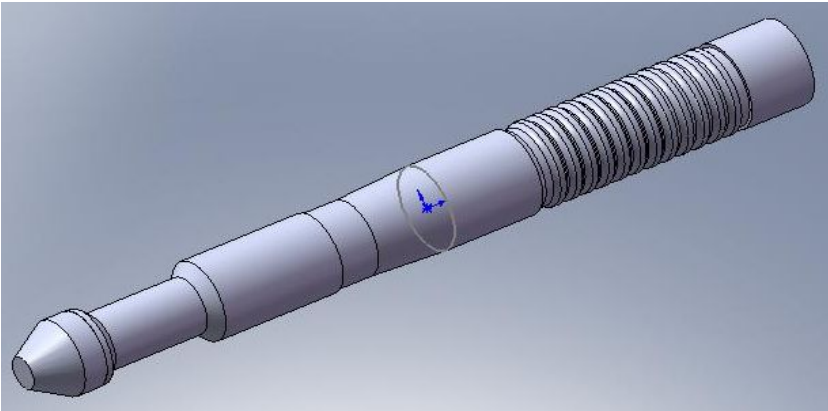


Fig.1. Pull broach

2. THE STRENGTH COMPUTING OF THE PULL BROACH COGS

The circular pull broach is a tool which has, in general, its cutting part made of three parts: roughing, finishing and calibrating parts.

The strength computing will be made for the first roughing cog that contacts the material and parts the addition processing, which is the most intensively sollicitated.

2.1. THE COG IS SUBDUED TO BENDING

Two cases are taken into consideration: variant 1- the cog is a bar with a fixed end; variant 2- the cog is a circular plate.

2.1.1. VARIANT 1

This method considers the pull broach cog as a bar with a fixed end and is actuated at the other end by the chipping force according to

the figure 3, using the notations: h - the height of the cog, F - the chipping force, M_2 and V_2 reactions (the unknown introduced by constraint).

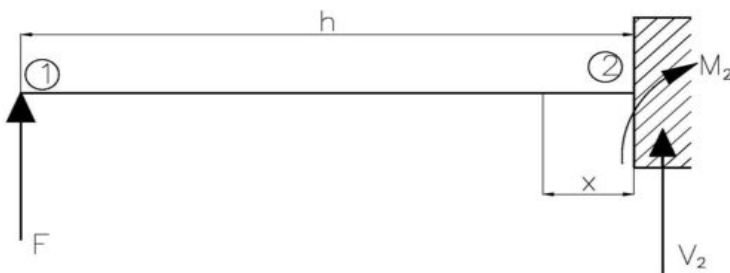


Fig.2. Bar with a fixed end

According to the upper schematization, the cog is subdued only to bending. The bending stress is determined by the relation (1):

$$\sigma_{il} = \frac{M_{i\max}}{W}, M_{i\max} = F \cdot h \quad (1)$$

where: $M_{i\max}$ – maximum bending moment, W - axial strength modulus.

So that the pull broach would not be broken during the tooling process, the condition $\sigma_{il} < \sigma_{ai}$ has to be fulfilled, where σ_{ai} is the stress admissible to the bending of the material of which is made the pull broach (in our case there is HS-18-01 STAS SR EN ISO 4957).

To demonstrate the upper announced theoretical relations, this method is used for a chosen particular case, in this way: $F= 2400\text{N}$; $h= 3,5 \text{ mm}$; $f_1= 3\text{mm}$; $W= 4,5\text{mm}^3$, $\sigma_{ai}= 1000 \text{ N/mm}^2$ (3), where f_1 is the width of the cog.

$$\text{The results are: } M_{i\max}= 8400 \text{ N}\cdot\text{mm}, \sigma_{i1}= 1867 \text{ N/mm}^2 \quad (4)$$

We observe that $\sigma_{i1} > \sigma_{ai}$ which means that the cog doesn't resist at the bending stress. In this case, so that the cog would resist, the next measures have to be taken: changing the chosen material with a more resistant one to bending; increasing the axial strength modulus which leads to a smaller bending stress; decreasing the height of the cog which leads to the decreasing of the bending moment.

2.1.2. VARIANT 2

In this case, the cog is also subdued to bending, but it is taken into consideration the fact that the cog is a plate, the action of the chipping force won't be in a point, but on the all exterior contour.

Because of the geometrical complexity the cog has, it is considered that the pull broach cog has the same width on all its height

(practically, the most inimical case is considered because the section of the cog base decreases). This is presented in figures 3, 4 and 5.

According to the considerations that were made, axial chipping force actuates the cog just like in figure 6.

To make this computing, the cog will be considered as a circular plate, constrained on the interior contour and actuated on the exterior contour. According to [7], the maximum stress that makes the bending is computed with the relation:

$$\sigma_{\text{imax}} = (2 \cdot F \cdot k) / (f_1)^2 \quad (5)$$

where k is a factor that heeds the a/b ratio with the values given in table 1.

Table 1

a/b	1,25	1,5	2
K	0,227	0,428	0,753

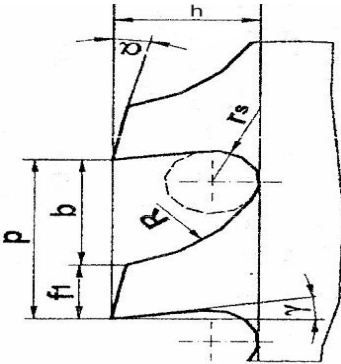


Fig.3. Real pull broach cog [6]

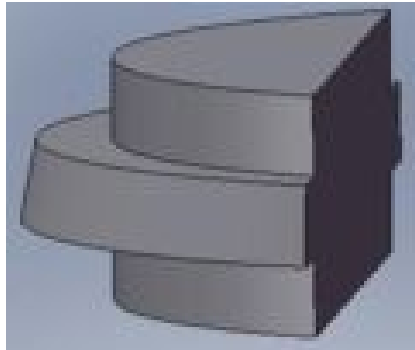


Fig.4. Simplified pull broach cog; 3D sectional representation

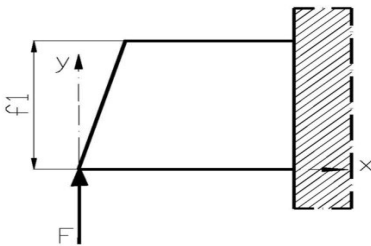


Fig.6. Chipping force action

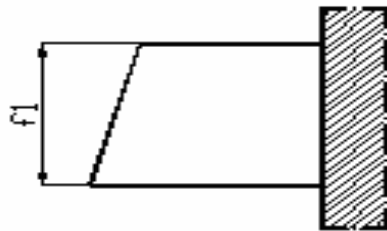


Fig.5. Simplified pull broach cog 2D representation

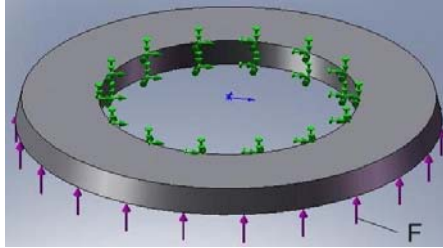


Fig.7. The cog is a circular plate constrained on the interior contour, and actuated on the exterior contour

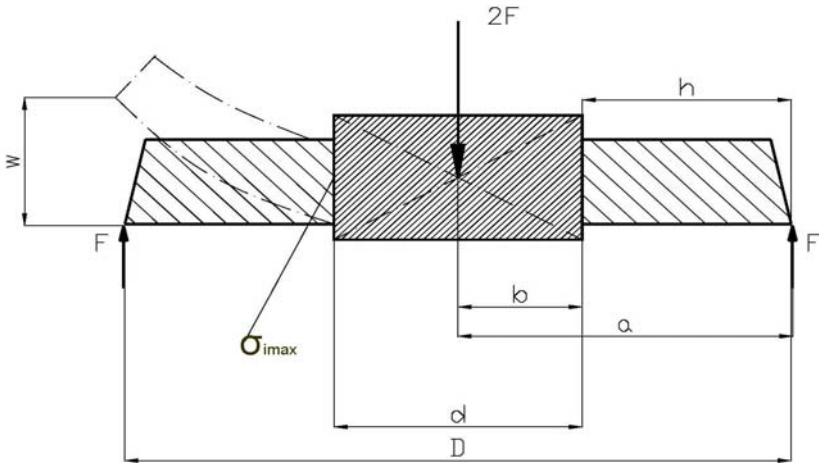


Fig.8. Cog loading schematization [7]

If the a/b ratio values is found in table 1, σ_{imax} is directly computed and the next condition must be fulfilled: $\sigma_{imax} < \sigma_{ai}$ (6), so that the cog resists bending. If the a/b ratio is not found in table 1, the interpolation is used to find out the value of k , following the next steps:

- the function $y(x) = mx^2 + nx + p$
- the values are consecutively given to x and three unknown equations system is made:

$$\begin{cases} m \cdot 1,25^2 + n \cdot 1,25 + p = 0,227 \\ m \cdot 1,5^2 + n \cdot 1,5 + p = 0,248 \\ m \cdot 2^2 + n \cdot 2 + p = 0,753 \end{cases} \quad (6)$$

- the unknown 3 equations system is solved and then the values m, n, p are obtained resulting that all the parameters of the function $y(x)$ are known
- $x=a/b$ is inserted in the function $y(x)$ resulting $k=y(a/b)$
- σ_{imax} will result by computing the value of k
- the strength condition (6) is checked

To demonstrate the upper theoretical relations, this method is used for a particular case, the same from 2.1.1 subitem:

$$F=2400 \text{ N}; h=3,5\text{mm}; f_1=3\text{mm}; \sigma_{\text{ai}}= 1000\text{N/mm}^2; D=45\text{mm}; d=44,5 \text{ mm} \quad (7)$$

The steps showed at 2.1.2 subitem are followed and there are obtained next results (it is mentioned that is the case where k is not directly chosen from the table):

$$\begin{aligned} a &= 22,5 \text{ mm}; b = 19,25\text{mm}; m = 1,253; n = -3,311; p = 2,437; \\ y(x) &= 1,235x^2 - 3,311x + 2,437; \\ x = a/b &= 1,184; k = y(1,184) = 0,247; \sigma_{\text{imax}} = 131,8\text{N/mm}^2 < \sigma_{\text{ai}}. \end{aligned} \quad (8)$$

The strength condition at the bending of the cog is checked by having $\sigma_{\text{imax}} = 131,8\text{N/mm}^2 < \sigma_{\text{ai}} = 1000\text{N/mm}^2$.

2.2. THE COG IS SUBDUED TO BENDING IMPACT

It is considered that the cog enters the material with impact. There are considered two cases: variant 3- the cog is a bar with a fixed end and actuated at the other end by chipping force; variant 4- the cog is a circular plate actuated by the chipping force on the entire exterior contour.

2.2.1. VARIANT 3

It is considered the same case as the one at the subitem 2.1.1. The static deflection is computed with the relation (9):

$$v = (F \cdot h^3) / (3 \cdot E \cdot I_z) \quad (9)$$

where E - longitudinal elastic modulus, I_z - inertia moment.

Then, the impact intensifier ψ is computed with relation (10):

$$\psi = 1 + \sqrt{1 + \frac{2 \cdot h_c}{v}} \quad (10)$$

where h_c - the height between the force F and the cog until they make contact. If the chipping force is suddenly applied, then $h_c=0$.

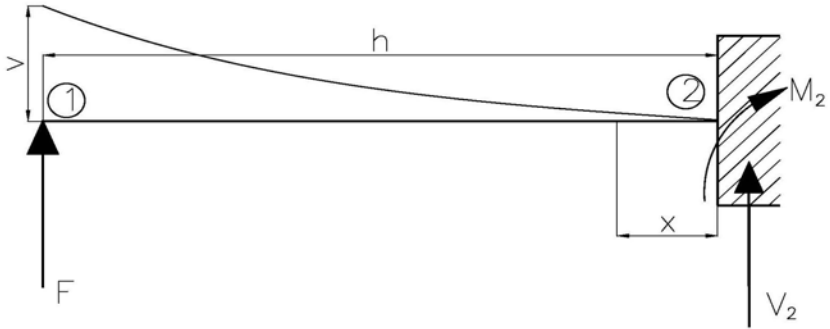


Fig.9. Variant 3 computing scheme

The maximum stress produced to impact will be: $\sigma_{soc} = \sigma_{st} \cdot \psi$ (11), where σ_{st} – the maximum stress produced at the static application of the chipping force (it is identical with the stress σ_{i1} produced at the bending case presented at the subitem 2.1.1).

The condition $\sigma_{soc} < \sigma_a$ (12) must be fulfilled, where σ_a is the impact admissible stress of the material of which the pull broach is made. The dynamic deflection is computed with the relation: $f = \psi \cdot v$ (13)

To demonstrate the upper defined theoretical relations, this method is used for a particular case (the same treated as the one from the item 2.1) defined this way:

$$F=2400\text{N}; h=3,5\text{mm}; f_1=3\text{mm}; l_2= 6,75\text{mm}^3; \sigma_a= 1000\text{N/mm}^2; E=2,1 \cdot 10^6 \text{ N/mm}^2; h_c=0. \quad (14)$$

Numerically replacing, we obtain:

$$v= 2,42 \cdot 10^{-3} \text{mm}; \psi=2; \sigma_{soc}= 3733\text{N/mm}^2; f=4,84 \cdot 10^{-3} \text{mm} \quad (15)$$

It is noticed that $\sigma_{soc} > \sigma_a$, the condition (12) is not respected and the cog does not resist to impact.

2.2.2. VARIANT 4

It is used the scheme from figure 8. According to [7], the deflection is computed with the next relation:

$$w = k_1 \cdot \frac{F \cdot a^2}{E \cdot f_1^3} \quad (16)$$

where k_1 is a factor that caters for a/b ratio with the values given in the table 2.

Table 2

a/b	1,25	1,5	2
k_1	0,0051	0,0249	0,0877

If the a/b value is found in table 2, w is directly computed and then the impact intensifier, ψ , is computed with relation (10). The maximum stress produced at impact is computed with relation (11), the strength condition (12) is checked and the dynamic deflection is computed with relation (13). If the a/b value is not found in table 2, the interpolation is used to find out the value of k_1 following the methodology described at 2.1.2 subitem.

To demonstrate the upper defined theoretical relations, this method is used for a particular case (the same treated at subitem 2.2.1).

The described steps from 2.2.1 are followed and there are obtained the next results (it is mentioned that it is the case where k_1 is not directly chosen from the table 2):

$$\begin{aligned}
 a &= 22,5\text{mm}; b = 19,25\text{mm}; m = 0,062; n = -0,091; p = 0,022; \\
 y(x) &= 0,062x^2 - 0,091x + 0,022; \\
 x = a/b &= 1,184; k_1 = y(1,184) = 1,175 \cdot 10^{-3}.
 \end{aligned}
 \tag{16}$$

The deflection is computed with relation (16): $w = 2,517 \cdot 10^{-5}\text{mm}$.
(17)

$$\begin{aligned}
 \text{Then, the other elements are computed, obtaining:} \\
 \Psi = 2; \sigma_{\text{soc}} = 263,6 \text{ N/mm}^2; f = 5,035 \cdot 10^{-5}\text{mm}.
 \end{aligned}
 \tag{18}$$

It is noticed that $\sigma_{\text{soc}} < \sigma_a$, the strength condition is fulfilled and the cog resists at impact.

2.3. FINITE ELEMENT ANALYSIS

It is considered that the pull broach cog, which according to figure 10, is fixed on the interior contour and actuated on the exterior contour by the force F, the chopping force. It is used the same particular case defined at the previous items.

After the finite element analysis, the stress map from figure 10 resulted. It is noticed that the maximum stress produce by force F is $\sigma_{\text{max}} = 68,6\text{N/mm}^2 < \sigma_{\text{al}} = 1000\text{N/mm}^2$, so the cog resist to bending.

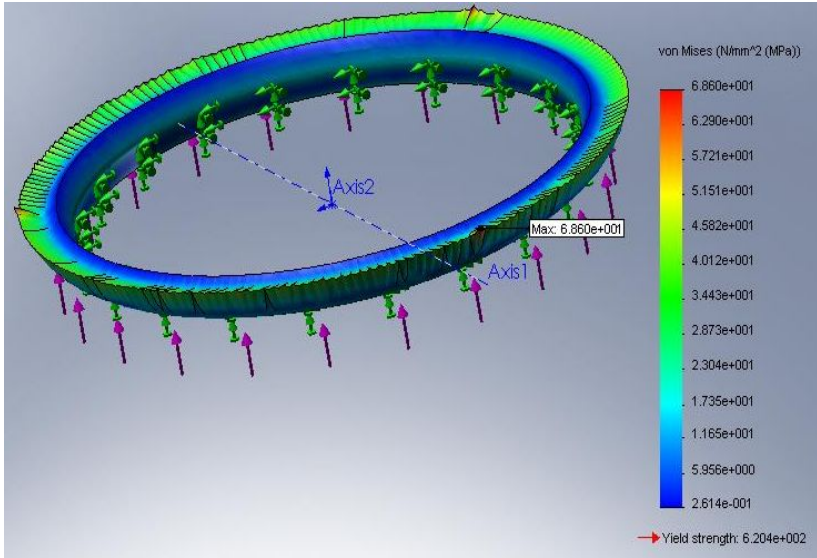


Fig.10. Finite element analysis cog

3. THE TENSILE CHECK OF THE PULL BROACH

The pull broach works on dragging, so it is subdued to tensile too. A strength complete computing means also the checking of the pull broach to this sollicitation. According to [6], the total force that actuates on the pull broach is dependent on the maximum number of cogs that simultaneously are in chipping at a moment of the tooling process and the force is computed with the relation (19):

$$F_{\text{tot}} = F \cdot z_{\text{sim}} \quad (19)$$

where: F - chipping force distributed to a cog; z_{sim} - the number of the pull broach cogs that are simultaneously in chipping.

3.1. ANALYTICAL METHOD

The strength computing is made on the supposition that the pull broach is a fixed bar actuated on the other side by the force defined at relation (19). We use the relation: $\sigma_t = F_{\text{tot}}/A_{\text{min}}$ (20), where A_{min} is the minimum section of the pull broach, F_{tot} is the total chipping force that actuates on the pull broach.

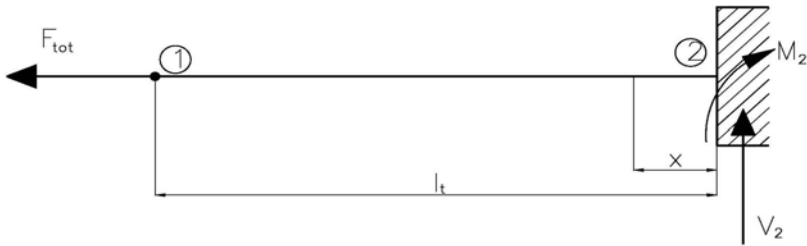


Fig.11. Pull broach solicitation scheme

The strength condition must be checked: $\sigma_t < \sigma_{at}$ (21), where σ_{at} is the tensile admissible stress of the material of which the pull broach is made. If the inequality (21) is not fulfilled, the pull broach breaks, and the minimum section of the pull broach must be increased or is must be chosen a new material with a higher admissible tensile stress.

To demonstrate the upper defined theoretical relations, this method is used for a particular case (the same presented in the subitems 2.1 and 2.2).

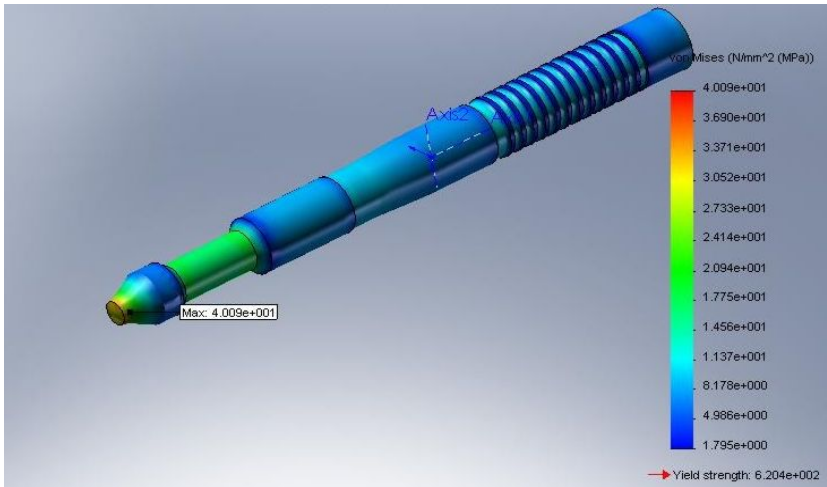
$$F=2400\text{N}; h=3,5\text{mm}; f_1= 3\text{mm}; \sigma_{at}= 150\text{N/mm}^2; z_{sim}=5; D_{min}=16\text{mm}.$$

$$\text{Numerically replacing in the relations (19),(20) and (21) we obtain:} \\ F_{tot}= 1,2 \cdot 10^4 \text{N}; A_{min}= 201,062\text{mm}^2; \sigma_t= 59,683\text{N/mm}^2. \quad (22)$$

The strength condition (21) is fulfilled, so the pull broach resists to tensile.

3.2. FINITE ELEMENT ANALYSIS

The pull broach is considered to be fix ended to one side, and at the other side actuated by the total chipping force. It is used the same example presented before. After the finite element analysis, it resulted the map with stresses from figure 12. We can observe that the tensile maximum stress is $\sigma_t= 40,09\text{N/mm}^2$, so the strength condition (21) is checked.



4. CONCLUSIONS

4.1. THE STRENGTH COMPUTING OF THE PULL BROACH COGS

The results are presented in the table 3.

Table 3

The adopted method	Method 1- fix ended bar	Method 2 - circular plate	Method 3 - finite element analysis
The maximum bending stress (N/mm ²)	$\sigma_{i1} = 1867$	$\sigma_{imax} = 131,8$	$\sigma_{max} = 68,6$
The maximum impact stress (N/mm ²)	$\sigma_{soc1} = 3733$	$\sigma_{soc2} = 263,6$	

We can extract the following conclusions:

- the using of the first method (the one from 2.1 subitem) leads to implausible results because it is noticed that the cog does not resist to the bending solicitation, the bending stress being too big than the one really produced; same conclusions can be made from the impact solicitation too.

- the using of the first method leads to implausible results also because of the adopted simplifying assumption, that is: the cog is a fix ended bar, because this assumption is adopted only for the bodies that have a bigger length in comparison with the width and thickness
- the results obtained with the second assumption are sustained by the finite element analysis (in this cases, similar values are obtained), the bigger bending stress obtained with the second method resulted from the fact that the most inimical case was chosen (which is: the width of the cog is constant on all its height)
- the second variant gives satisfying results also for bending impact computing, a solicitation to which the cog resists
- for a complete strength computing, it is recommended to use the methods presented at the subitems 2.1.2, 2.2.2 and 2.3.

4.2. THE TENSILE CHECK OF THE PULL BROACH

It is noticed that both methods lead to similar results: the stresses are nearly equal ($59,683\text{N/mm}^2$ with the analytical method and $40,09\text{N/mm}^2$ with the finite elements analysis variant); both methods can be used to the pull broach tensile check.

REFERENCES

1. Beleaev, N.,M., Rezistența Materialelor, vol.2, traducere din limba rusă,Editura Tehnică, București, 1956
2. Ilincioiu, D., Rezistența Materialelor, Editura ROM TPT, Craiova, 2002
3. Ilincioiu, D., Rezistența Materialelor, Editura ROM TPT, Craiova, 2003
4. Ilincioiu, D., Rezistența Materialelor, Editura ROM TPT, Ediția a-2-a, Craiova, 2007
5. Stoian, A., Proiectarea Sculelor Așchietoare, Reprografia Universității din Craiova, Craiova, 2001
6. Stoian, A., Proiectarea Broșelor, Editura Universitaria, Craiova, 2004
7. Timoshenko,S., Woionowsky-Krigev,S., Teoria Plăcilor Plane și Curbe, Editura Tehnică, București, 1968

CONTRIBUTIONS ABOUT HANDLING THERMAL BRIDGES FOR CIVIL BUILDINGS

Mădălina CĂLBUREANU¹, Raluca MALCIU¹, Lucian SEPCU²

¹*University of Craiova, Faculty of Mechanics*

²*Faculty of Automatics, Computers and Electronics*

Abstract: Within the context of an energy performance regulation, it is essential to take the transmission losses into account. If building details are not well designed or carried out, thermal bridges can substantially increase the transmission losses. Though, the physical principles for evaluating thermal bridges are well known and covered by European standards. However, the practical application of these calculation rules is not that evident and may be very time consuming.

Keywords: thermal bridges, heat losses, energy performance

1. INTRODUCTION

The internal thermal insulation systems are an unusual solution in Romanian residential buildings, despite the several advantages that justify their use when compared to external systems, like lowest cost, highest durability, increased airborne sound insulation (limitation of flanking transmission via facade, and also higher external noise insulation, specially when there are no windows), possibility to integrate several equipments (ex. water supply pipes) without damaging the masonry, and maintenance of facade appearance in ancient buildings rehabilitation interventions, among others.

On the other hand, some common disadvantages referred in literature are hygrothermal-related defects on the building envelope originated by interstitial condensations, thermal bridges and high temperature amplitudes on external wall, and also indoor thermal discomfort related with the risk of overheating during summer months.

Since the middle of the 1990 decade the Romanian construction sector has been gradually changing the traditional construction technique of the residential buildings façade – masonry cavity wall partially filled with a thermal insulation material – to a single leaf wall insulated (almost always) with an external thermal insulation system.

The growth foreseen in Romania for the rehabilitation sector when compared with the new construction market, along with more demanding building thermal regulations, motivated a quantitative research analysis on internal thermal insulation system behavior using computer simulation methods, both for the above-mentioned hygrothermal facade requirements, and also for the indoor thermal comfort conditions.

2. THERMAL BRIDGES AND TRANSMISSION LOSSES

Transmission losses mostly represent the largest part of the heat losses of a building. The calculation of transmission losses is covered by a range of European standards.

Thermal bridges can substantially increase the transmission losses (in some cases up to 10 to 20% of one-dimensional heat losses).

In the figure 1 there are presented the way it can be modeled the thermal bridges using finite element method and an adequate software.

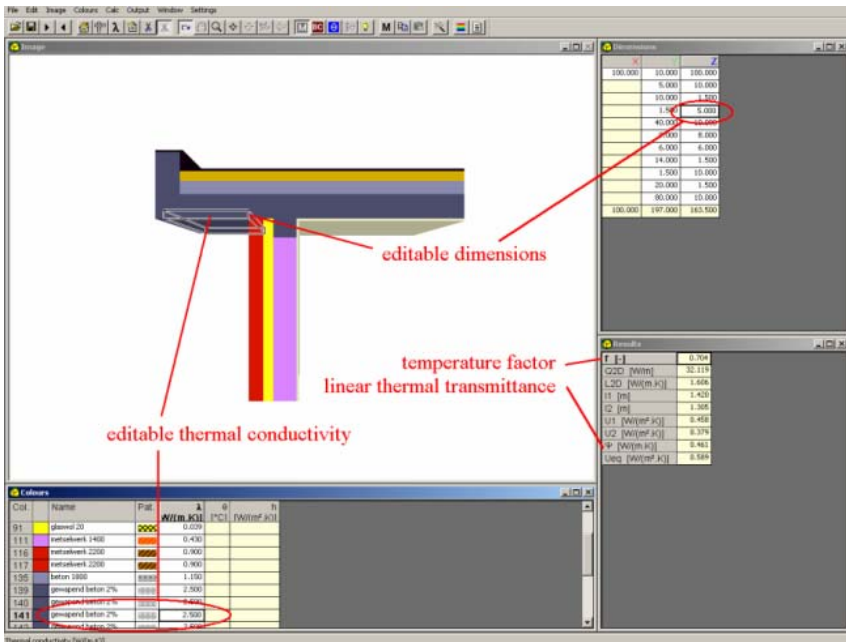


Fig. 1 The example of the thermal bridges at the intersection of the different walls

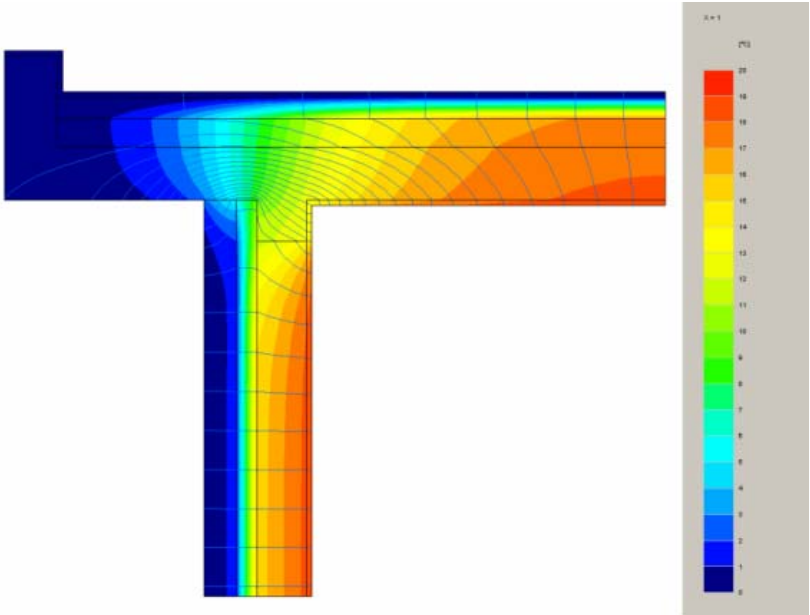


Fig. 2: Example of a thermal bridge with detail heat flow and temperature distribution

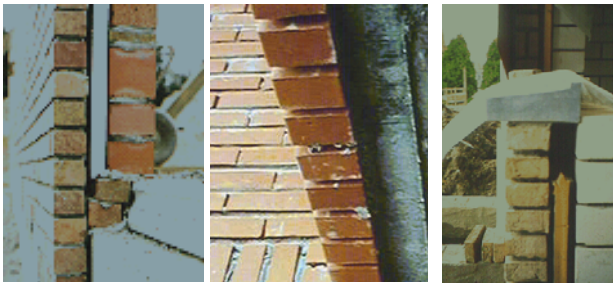


Fig. 3. Example of a thermal bridges in the different locations from civil buildings

A quantitative analysis on internal thermal insulation system is done based on three hygrothermal facade requirements: interstitial condensations, thermal bridges, and temperature variations across the external wall.

Computer simulation was used as research tool. The selected software applications were in compliance with the available European standards, particularly for the interstitial condensations and thermal bridges.

The effect of distinct external climate conditions was evaluated, taking also into account the typical indoor hygrothermal characteristics of Romanian residential buildings, namely temperature and ventilation rate.

3. CONCLUSIONS

In the framework of the goal of energy performance for civil buildings in Romania a specific concept for handling thermal bridges in daily practice is under development.

If good building details are used, a detailed calculation of thermal bridging effects is in most cases not required if good building details are used. In such cases building professionals can use default values in order to take thermal bridging into account.

In addition, the use of internal thermal insulation system may contribute to a lower thermal insulation cost in residential buildings with an expected higher durability when compared to external ones, thus assuring the solution sustainability.

When using internal system the internal thermal conditions will also change, with thermal inertia playing a decisive role to prevent overheating.

REFERENCES

1. Calbureanu, M. – Metode numerice în transferul de căldură, Ed. Universitaria, 2004
2. Schwab, H. Thermal Bridges in Vacuum-insulated Building Façades, Journal of Thermal Envelope and Building Science, Vol. 28, No. 4, 345-355 (2005)
3. EN ISO 10211-1. 1995. "Thermal Bridges in Building Construction. Heat Flows and Surface Temperatures. Part 1: General Calculation Methods".
4. EN ISO 10211-2. 2001. "Thermal Bridges in Building Construction. Heat Flows and Surface Temperatures. Part 2: Linear Thermal Bridges".
5. **NORMATIV PENTRU CALCULUL COEFICIENTULUI Ψ GLOBAL DE IZOLARE TERMICĂ LA CLĂDIRI CU ALTĂ DESTINAȚIE DECÂT CELE DE LOCUIT INDICATIV C107/2-97.**

SOME CONSIDERATIONS CONCERNING INCOMPRESSIBLE FLUID FLOW THROUGH INHOMOGENEOUS POROUS MEDIA

Ștefan ȚĂLU¹, Mihai ȚĂLU²

¹*Technical University of Cluj-Napoca, Faculty of Mechanics,
Department of Descriptive Geometry and Engineering Graphics*

²*University of Craiova, Faculty of Mechanics,
Department of Applied Mechanics*

Abstract: In this paper the authors present a particular mathematical model for determination of relations that characterize the flow of the incompressible fluids through inhomogeneous porous media.

Keywords: incompressible fluids, porous media.

1. THEORETICAL CONSIDERATIONS

The interest in the mathematical and numerical fluid flow and transport in porous media has been the subject of numerous researches during the past few decades [1, 2, 3]. Depending on the physical nature of the phenomena and due to complex geometry of fluid /solid systems and nonlinearity of processes, different mathematical procedures and schemes have been constructed to solve these problems [4, 5].

2. MATHEMATICAL MODELLING

In general, the flow through inhomogeneous porous media has the particularity of permeability dependency as a function of the point.

If we consider the flow with incompressible fluids and constant viscosity, which Darcy's law is expressed as [1]:

$$v_i = k \frac{\partial \varphi}{\partial x_i}; \quad \varphi = -\frac{1}{\mu}(p + U) \quad (1)$$

where: k - permeability, μ - viscosity; p - pressure and U - potential.

The speed rotor tensor is antisymmetrical with next components:

$$\omega_{jk} = \frac{\partial v_k}{\partial x_j} - \frac{\partial v_j}{\partial x_k} = \left(\frac{\partial k}{\partial x_j} \frac{\partial \varphi}{\partial x_k} - \frac{\partial k}{\partial x_k} \frac{\partial \varphi}{\partial x_j} \right); \quad \omega_{jk} = -\omega_{kj} \quad (2)$$

The rotor vector also has the components:

$$\omega_i = \delta_{ijk} \frac{\partial v_k}{\partial x_j} = \delta_{ijk} \left(\frac{\partial k}{\partial x_j} \frac{\partial \varphi}{\partial x_k} + k \frac{\partial^2 \varphi}{\partial x_j \partial x_k} \right) \quad (3)$$

where: $\bar{\delta}_{ijk} = 0$, if two indices are equals; $\bar{\delta}_{ijk} = + 1$, if i, j, k are in cyclic order; $\bar{\delta}_{ijk} = - 1$, otherwise.

If we consider the filter speed rotor to be null, it is obtained the particular solutions of the equation for incompressible fluid flow through inhomogeneous porous media [1].

For $\varphi = \varphi(k)$, the solutions of next equation:

$$\frac{\partial}{\partial x_i} \left(\frac{\partial \varphi}{\partial k} k \frac{\partial k}{\partial x_i} \right) = 0 \quad (4)$$

are appropriate laws of permeability variation.

Let's consider next relation between function φ and permeability k as:

$$\varphi = \lambda k^\beta + \lambda_0 \quad (5)$$

with real arbitrary constants $\lambda, \lambda_0, \beta$. By replacing φ in next equation:

$$\frac{\partial}{\partial x_i} \left(k^{j_i} \frac{\partial \varphi}{\partial x_i} \right) = 0 \quad (6)$$

it is obtained next relation:

$$\frac{\partial}{\partial x_i} \left(k^\beta \frac{\partial k}{\partial x_i} \right) = 0 \quad (7)$$

where:

$$\frac{\partial^2 k^{1+\beta}}{\partial x_i \partial x_i} = 0 \quad (8)$$

with harmonic function $k^{1+\beta}$. For $\beta = - 1$ function $\ln k$ is also harmonic.

According with relation (5), k could be expressed as:

$$k = \left(\frac{\varphi - \lambda_0}{\lambda} \right)^{1/\beta} \quad (9)$$

By replacing relation (9) in relation (6) and after some calculations it is obtained that:

$$\frac{\partial^2 (\varphi - \lambda_0)^{\frac{1+\beta}{\beta}}}{\partial x_i \partial x_i} = 0 \quad (10)$$

According with this result, function $(\varphi - \lambda_0)^q$ is harmonic, if $(\beta \in \mathbb{R}, \beta \neq -1 \text{ and } 0)$ and it is verified relation:

$$q = \frac{1 + \beta}{\beta} \quad (11)$$

For $\beta = 0$, the relationship between φ and k is:

$$\varphi = a \ln k + b \quad (12)$$

By replacing k for relation (12) in next relation:

$$\frac{\partial}{\partial x_i} \left(k \frac{\partial \varphi}{\partial x_i} \right) = 0 \quad (13)$$

it is obtained:

$$\frac{\partial^2 e^{\frac{\varphi-b}{a}}}{\partial x_i \partial x_i} = 0 \quad (14)$$

with harmonic function $\log(\varphi - \lambda_0)$.

If the relation between function φ and permeability k is:

$$k = v\varphi^\alpha + v_0 \quad (15)$$

and when $v_0 = 0$, v and α are arbitrary, from relation (13) results:

$$\frac{\partial^2 \varphi^{1+\alpha}}{\partial x_i \partial x_i} = 0 \quad (16)$$

with harmonic function $\varphi^{1+\alpha}$.

3. THE PARTICULAR APPLICATION: PLANE FLOW

Let's consider the plane flow in an area between two concentric circles, centered at the origin and having radii: r_c and r_s ($r_c > r_s$).

The mathematical model describing the plane fluid flow can be written in terms of the following equations. According with relation:

$$(\varphi - \lambda_0)^{\frac{1+\beta}{\beta}} = \lambda^{\frac{1+\beta}{\beta}} k^{1+\beta} \quad (17)$$

and limit conditions: $r = r_c, \varphi = \varphi_c, r = r_s, \varphi = \varphi_s$, it is obtained after some calculations:

$$(\varphi - \lambda_0)^{\frac{1+\beta}{\beta}} = \lambda^{\frac{1+\beta}{\beta}} (a_0 \ln r + \alpha_0) \quad (18)$$

$$\lambda = \frac{\varphi_c - \varphi_s}{(a_0 \ln r_c + \alpha_0)^{\frac{\beta}{1+\beta}} - (a_0 \ln r_s + \alpha_0)^{\frac{\beta}{1+\beta}}} \quad (19)$$

$$\lambda_0 = \varphi_s - \frac{\varphi_c - \varphi_s}{(a_0 \ln r_c + \alpha_0)^{\frac{\beta}{1+\beta}} - (a_0 \ln r_s + \alpha_0)^{\frac{\beta}{1+\beta}}} (a_0 \ln r_s + \alpha_0)^{\frac{\beta}{1+\beta}} \quad (20)$$

$$\varphi = \varphi_s + \frac{(\varphi_c - \varphi_s) \left[(a_0 \ln r + \alpha_0)^{\frac{\beta}{1+\beta}} - (a_0 \ln r_s + \alpha_0)^{\frac{\beta}{1+\beta}} \right]}{(a_0 \ln r_c + \alpha_0)^{\frac{\beta}{1+\beta}} - (a_0 \ln r_s + \alpha_0)^{\frac{\beta}{1+\beta}}} \quad (21)$$

The filter speed is:

$$v = a_0 \frac{\beta}{1 + \beta} \frac{(\varphi_c - \varphi_s)}{(a_0 \ln r_c + \alpha_0)^{\frac{\beta}{1+\beta}} - (a_0 \ln r_s + \alpha_0)^{\frac{\beta}{1+\beta}}} \frac{1}{r} \quad (22)$$

The pressure expression is:

$$p = p_s + \frac{(p_c - p_s) \left[(a_0 \ln r + \alpha_0)^{\frac{\beta}{1+\beta}} - (a_0 \ln r_s + \alpha_0)^{\frac{\beta}{1+\beta}} \right]}{(a_0 \ln r_c + \alpha_0)^{\frac{\beta}{1+\beta}} - (a_0 \ln r_s + \alpha_0)^{\frac{\beta}{1+\beta}}} \quad (23)$$

4. CONCLUSIONS

The proposed mathematical model of calculus is useful for the determining of the incompressible fluids flow to the probe units.

Mathematical modeling of these systems using porous media theory has proved to be beneficial in the design of experiments and equipments as well as gaining better insight about multiphysics phenomenon such as fluid flow and solid deformation.

REFERENCES

1. T. Oroveanu, Scurgerea fluidelor prin medii poroase neomogene, Editura Academiei, București, 1963.
2. J. Bear, Dynamics of fluids in porous media, Elsevier, 1972.
3. P. Plessis (Editor), Fluid Transport in Porous Media, Computational Mechanics Publications, UK, 1997.
4. Z. Chen, R. Ewing, Fluid flow and transport in porous media, mathematical and numerical treatment, American Mathematical Society, 2002.
5. M. Țălu, Ș. Țălu, Calculul căderilor de presiune în conducte hidraulice. Regim de curgere stabilizat și nestabilizat. Teorie, aplicații și programe computaționale, Craiova, Editura Universitaria, 2006.

THE PERFORMANCE OF BIODIESEL FROM ANIMAL FATS IN DIESEL ENGINES

Dragos TUTUNEA¹, George GHERGHINA¹, Dragos POPA¹

¹*The University of Craiova, Faculty of Mechanics*

Abstract: The limitation of available sources for petroleum exploration is a strong motivation to focus on renewable energy. An alternative to fossil diesel is the production of environmentally friendly biodiesel. According to European Commission regulations, by 2010 at least 5.75 percent of the annual fuel consumption in Europe will have to be substituted by renewable fuels like biodiesel. Biofuels have a great potential to decrease environmental pollution and improve emission behavior of engines. We study the performance of biodiesel from pig animal fat in a monocylindrical diesel engine and we compare his performance with classic petrodiesel.

Keywords: biodiesel, diesel engine, animal fat, petrodiesel.

1. INTRODUCTION

In Europe, biodiesel seems to be synonymous for RME. Only a small, well-informed public realizes that this alternative fuel can also be produced from other feed stocks, such as non-edible oils (or seed oils), used cooking oils, and animal fats. This aspect will become more and more important when seen in context with the latest developments on food- and feeding-stuff safety. The fact is that the usage of biodiesel produced from used cooking oils is well-known to the public and its advantageous emission behavior compared to fossil diesel or even RME could be pointed out sufficiently. What is less known is the fact that biodiesel can also be produced from 100 percent animal fats and fulfills the current EN 14214 for fatty acid methyl esters, as long as state-of-the-art process technology is applied.

2. PROPERTIES OF DIFFERENT ANIMAL FATS COMPARED WITH BIODIESEL FROM VEGETABLE OIL

When chemical properties of various feedstock materials for biodiesel production are compared, the main difference between vegetable oils like rapeseed oil and animal fats can be found in the diverse fatty acid composition as shown in Table 1. While rapeseed oil and soybean oil have a high content of unsaturated fatty acids, mainly oleic acid and linoleic acid, animal fats like tallow or lard have a major content of saturated fatty acids (e.g., palmitic and stearic acid). The increased amount of saturated fatty acids shows a reversed trend for two main fuel properties. While the oxidation stability of biodiesel derived from animal fats increases, the cold temperature performance decreases with a rising content of saturated fatty acids. We show the dependence of the content of saturated fatty acids in biodiesel – without additives – on its cold filter plugging point (CFPP). The cetane number of biodiesel is also positively affected by an increased amount of saturated fatty acids.

Table 1. Properties of biodiesel

Saturated fatty acids	Rapeseed oil			Soybean Oil			Beef Tallow		
	Min.	Avg	Max	Min.	Avg	Max	Min.	Avg	Max
Lauric	0.0	0.0	0.0	0.0	0.0	0.0	0.0	0.0	0.0
Myristic	0.0	0.0	0.0	0.0	0.3	0.5	2.0	3.0	4.0
Palmitic	3.0	4.5	6.0	8.0	10.0	12.0	23.0	26.0	29.0
Stearic	1.0	1.8	2.5	3.0	4.0	5.0	20.0	27.5	35.0
Arachidic	0.0	0.5	1.0	0.0	0.3	0.5	0.0	0.3	0.5
Behenic	0.0	0.3	0.5	0.0	0.0	0.0	0.0	0.0	0.0
Total	4.0	7.0	10.0	11.0	14.5	18.0	45.0	56.8	68.5
Unsaturated fatty acids	Min.	Avg	Max	Min.	Avg	Max	Min.	Avg	Max
Myristoleic	0.0	0.0	0.0	0.0	0.0	0.0	0.5	0.5	0.5
Palmitoleic	0.1	0.3	0.5	0.0	0.0	0.0	2.0	3.0	4.0
Oleic	52.0	59.0	66.0	18	21.5	25	26	35.5	45
Linoleic	17.0	21.0	25.0	49.0	53.0	57.0	2.0	4.0	6.0
Linolenic	8.0	9.5	11.0	6.0	8.5	11.0	1.0	1.0	1.0
Gadoleic	1.5	2.5	3.5	0.0	0.3	0.5	0.0	0.3	0.5
Erucic	0.0	1.3	2.5	0.0	0.0	0.0	0.0	0.0	0.0
Total	78.6	93.6	108.6	73.0	83.3	93.5	32.0	44.7	57.5
Iodine Number	96	115	134	116	133	149	30	43	56

Tallow-derived biodiesel can reach cetane numbers of up to 74, which leads to a much better performance in diesel engines regarding engine efficiency and subsequently reduced exhaust emissions. 4,5 .

Compared to conventional fossil diesel, the noise level of diesel engines – an often underestimated environmental pollution concern – is also reduced when AFME is used. The lubricity behavior of biodiesel was also investigated 7,8.

Compared to soybean oil- and rapeseed oil derived biodiesel, a superior performance of tallow-derived biodiesel could be found.

For High Frequency Reciprocating Rig (HFRR) 60C test, the limit for lubricity according to European diesel fuel standard EN 590 is below 460 μm (micrometer).

Biodiesel derived from tallow showed best performance as a lubricity enhancer for low-sulfur diesel and fulfills the prescribed limit already at a percentage of 0.5 percent added to diesel fuel. 8 certainly, due to the differences in composition and quality of the raw material (e.g., content of free fatty acids, content of impurities, etc.), the production of high-quality biodiesel from used animal material needs a more sophisticated production technology and specific know how concerning the pre-treatment of the feedstock.

3. LIFE CYCLE ANALYSIS FOR BIODIESEL

In a life cycle analysis study, ecological effects of the production of biodiesel (“from well to wheel”) derived from rapeseed oil or animal fat (with and without synergy effects of a rendering plant for animal by-products) were investigated and compared with the production of fossil diesel fuel.

Seven criteria for assessment of fuel production were pointed out:

1. Carcinogenic risk due to fuel components like benzene;
2. Particulate matter (PM 10, dust particles < 10 μm) content in exhaust gas;
3. Eutrophication rate of environment (soil, ground water, etc.);
4. Photosmog – breakdown rate of ozone layer due to photochemical oxidants;
5. Amount of resources consumed for production (fertilizer, catalysts, primary energy, etc.);
6. Greenhouse effect of relevant gases (carbon dioxide, laughing gas, and methane);
7. Potential of acidification due to noxious gases (e.g., sulfur dioxide);

Also, carbon dioxide balance is neutral for biodiesel from animal fat, thus no major contribution to the greenhouse effect could be stated.

4. EXPERIMENTAL DATA

We use for the experiment a slow turning a 5 kw diesel engine with the following characteristics given in table 2.

To measure the performance of biodiesel fats we compare the emission fuel with classic biodiesel. For the animal fats we use animal fat from pig and we blend it with Euro L diesel. The experimental researches on the engine focused on the influence of modifying the biodiesel percent in petrodiesel on the emissions of pollutants gases of a mono-cylindrical engine with direct injection.

Table 2 Technical data for diesel engine

Type	Direct Injection
Displacement	408 cc
Oil Capacity	1.7 Qts.
Cylinders	1
Cylinder Block	Aluminum w / Cast Iron Sleeve
Bore & Stroke	3.38 "x 2.83"
Exhaust Outlet	1-1/2 "OD Muffler Outlet
Fuel	No. 2 Diesel
Starting System	Electric

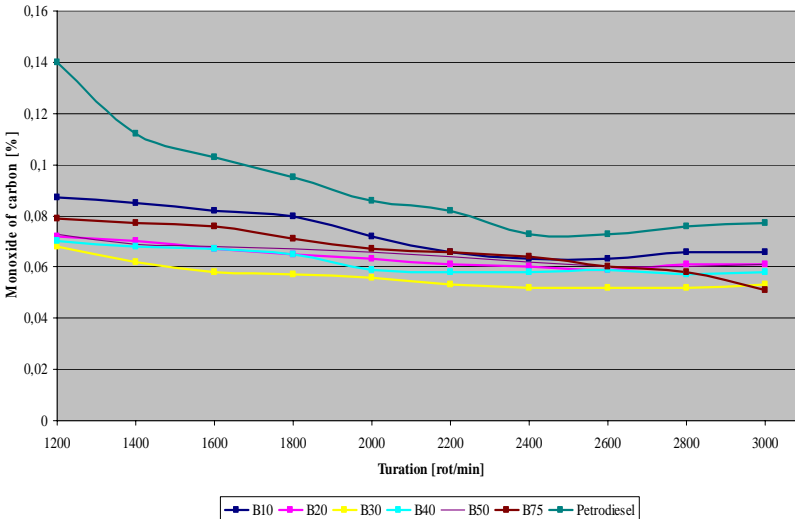


Fig. 1. The variation of carbon monoxide function of speed for different blends of biodiesel of animal pig and Euro L Diesel

The test consisted in lifting the turation (speed) characteristics of engine without load in forced regime with registration of the following parameters (carbon monoxide, carbon dioxide) for 10 speed regimes.

In the tests we gradually increased the percentage of biodiesel in order to observe its effects on performance of diesel engines with direct injection and to allow their evaluation compared with classic petrodiesel.

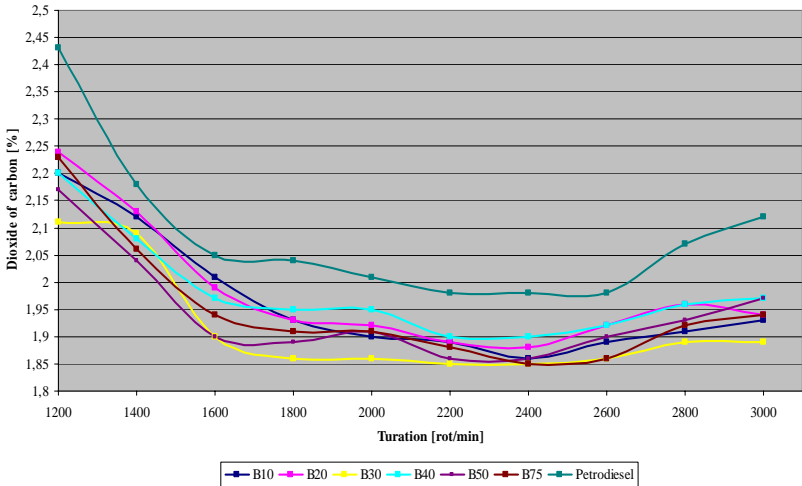


Fig.2. The variation of carbon dioxide function of speed for different blends of biodiesel of animal pig and Euro L Diesel Auxiliary construction

5. CONCLUSIONS

Based on the analysis of functional parameters of the engine fueled with biodiesel fuel, it can be affirmed that the alimentation with biofuels can provide performance comparable to those achieved with diesel on the characteristic of speed and load.

It was been analyzed different blends of biodiesel of rapeseed tested in separate two monocylindrical engines with load and no load. In general, combustion is more efficient for the use of these biofuels compared to diesel, because of the presence of the oxygen in molecule of ester.

The results depend on the type of engine (with direct injection or indirect, with normal or admission surcharge), the operating conditions (load, speed), fuel quality, but shows a decrease in overall emissions of CO, CO₂.

REFERENCES

1. Mittelbach, M and P. Tritthart 1988. DIESEL FUEL DERIVED FROM VEGETAL OILS, III: Emission Tests Using Methyl Esters of Used Frying Oil.
2. Van Carpen , J. 1996. CETAN NUMBER TESTING OF BIODIESEL, Conference Proceedings, 3rd Liquid Fuel Conference, September 15-19, 1996, Nashville
3. Andreas, C. M., H. Linder, A. Hansen, and F. Tack. 2003. OKOBILANZ FUR DIE BIODIESELHERESTELUN AUS TIERISHEN FETTEN, ecoMotion GmbH, Lunen, Germany
4. Thomas Hilber, M. M. and Eberhard Schmidt. ANIMAL FATS PERFORM WELL IN BIODIESEL. 5th International Coloquium FUELS in Germany January 12-13 2005
5. Anghel Chiru, Nicolae Ispas, Corneliu Cofariu, Dorin Dumitrescu, THE ANALYZE OF DIESEL FUEL AND BIODIESEL MIXTURE COMBUSTION IN DI DIESEL ENGINES, EAEC 2007, 11th European Automotive Congress, 30 May-1 June 2007, Budapest.
6. Istvan Barabas, Adrian Todorut, Doru Baldean, Florin Suci, EXPERIMENTAL STUDY ON THE SPRAY CHARACTERISTICS FOR DIESEL FUEL AND BIODIESEL-DIESEL FUEL-BIOETHANOL BLENDS, EAEC 2009, 12th European Automotive Congress, 29 June-02 July 2009, Bratislava.
7. L.de Simio, M. Gambino, S. Iannaccone, ENVIRONMENTAL ADVANTAGES FROM BIOFUELS EMPLOYMENT, EAEC 2009, 12th European Automotive Congress, 29 June-02 July 2009, Bratislava.

SOME CONSIDERATIONS CONCERNING COMPRESSIBLE FLUID FLOW THROUGH INHOMOGENEOUS POROUS MEDIA WITH CONSTANT POROSITY

Mihai ȚĂLU¹, Ștefan ȚĂLU²

¹University of Craiova, Faculty of Mechanics,
Department of Applied Mechanics

²Technical University of Cluj-Napoca, Faculty of Mechanics,
Department of Descriptive Geometry and Engineering Graphics

Abstract: In this paper the authors present a particular mathematical model for determination of relations that characterize the flow of the compressible fluids through inhomogeneous porous media with constant porosity.

Keywords: compressible fluid flow, inhomogeneous porous media, constant porosity.

1. THEORETICAL CONSIDERATIONS

The mathematical and numerical fluid flow in inhomogeneous porous media has been studied by numerous researchers during the last decades [1, 2, 3]. Because of the mathematical complexity the exact mathematical solutions of this process is difficult to obtain [4, 5].

2. MATHEMATICAL MODELLING

The differential equation of compressible fluids flow through inhomogeneous porous media could be expressed as [1]

$$\frac{\partial}{\partial x_i} \left(k \frac{\partial p}{\partial x_i} \right) = \beta_i \cdot \mu \cdot m \frac{\partial p}{\partial t} \quad (1)$$

where: k - permeability, μ – viscosity; p – pressure; m – porosity and β_i – compressibility coefficient.

If we consider the dimensionless permeability expression as:

$$\chi = k / k^{(0)} \quad (2)$$

$k^{(0)}$ being a constant reference value, and a^2 expression as:

$$a^2 = k^{(0)} \cdot (\beta_i \cdot \mu \cdot m)^{-1} \quad (3)$$

equation (1) could be written as:

$$a^2 \left[\frac{\partial}{\partial x_i} \left(\chi \frac{\partial p}{\partial x_i} \right) \right] = \frac{\partial p}{\partial t} \quad (4)$$

If we consider the specific case when the flow is one-dimensional, and the expression of permeability is:

$$\chi = (\alpha_0 + \alpha_1 x_1)^\delta \quad (5)$$

where α_0 , α_1 and δ are constant; the reference value corresponds to this case at $x_1 = x_1^{(0)}$. The equation (4) can be written as:

$$a^2 \left[\frac{\partial}{\partial x_1} \left((\alpha_0 + \alpha_1 x_1)^\delta \frac{\partial p}{\partial x_1} \right) \right] = \frac{\partial p}{\partial t} \quad (6)$$

and if we make substitutions:

$$\xi_1 = (\alpha_0 + \alpha_1 x_1); \quad \tau = (a\alpha_1)^2 t; \quad \pi = p / p_0 \quad (7)$$

it is obtained an equation in which all quantities are dimensionless:

$$\frac{\partial}{\partial \xi_1} \left(\xi_1^\delta \frac{\partial \pi}{\partial \xi_1} \right) = \frac{\partial \pi}{\partial \tau} \quad (8)$$

3. THE PARTICULAR APPLICATION: THE FLOW IS GIVEN ON BOTH BORDERS

Let's consider the case when the flow is given on both borders.

The proposed problem is solved by individual solutions, π_1 , π_2 , π_3 that satisfying next conditions:

$$(\pi_1, \pi_2, \pi_3) = \begin{cases} (1,0,0) & \text{for } \xi_1 = \xi_1^{(1)} \\ (0,1,0) & \text{for } \xi_1 = \xi_1^{(2)} \\ [0,0, g(\xi_1)] & \text{for } \tau = 0 \end{cases} \quad (9)$$

having an expression by a general form as:

$$\pi(\xi_1, \tau) = \pi_3(\xi_1, \tau) + \int_0^\tau \left[f_1(\lambda) \frac{\partial}{\partial \tau} \pi_1(\xi_1, \tau - \lambda) + f_2(\lambda) \frac{\partial}{\partial \tau} \pi_2(\xi_1, \tau - \lambda) \right] d\lambda \quad (10)$$

For a solution expressed as:

$$\pi = T(t) \cdot U(\xi_1) \quad (11)$$

and for the separation constant α_n^2 , are obtained next equations:

$$\frac{dT}{d\tau} + \alpha_n^2 T = 0 \quad (12)$$

$$\frac{dT}{d\xi_1} \left(\xi_1^\delta \frac{dU}{d\xi_1} \right) + \alpha_n^2 U = 0 \quad (13)$$

Equation (12) has a solution expressed as:

$$T = C e^{-\alpha_n^2 \tau} \quad (14)$$

For equation (13) are made next substitutions:

$$\xi_1 = X_1^s; \quad s = \frac{2}{2-\delta}; \quad U = X_1^{\frac{s(1-\delta)}{2}} Z; \quad q = \frac{1-\delta}{2-\delta}; \quad \zeta_1 = s \cdot \alpha_n \cdot X_1 \quad (15)$$

and after some calculations is obtained the equation normal form as:

$$\frac{d^2 Z}{d\zeta_1^2} + \frac{1}{\zeta_1} \frac{dZ}{d\zeta_1} + \left(1 - \frac{q^2}{\zeta_1^2} \right) Z = 0 \quad (16)$$

With an usual notation, the solution for equation (16) is:

$$Z_q(\zeta_1) = \begin{cases} AJ_q(\zeta_1) + BY_q(\zeta_1) & \text{for } q \text{ integer} \\ AJ_q(\zeta_1) + BJ_{-q}(\zeta_1) & \text{for } q \text{ noninteger} \end{cases} \quad (17)$$

So, if the return to function U and variable ξ_1 , the solution of equation (13) can be expressed as:

$$U = \xi_1^{\frac{1-\delta}{2}} Z_q \left(\frac{2\alpha_n}{2-\delta} \xi_1^{\frac{2-\delta}{2}} \right) \quad (18)$$

or the same solution (18) can be written as:

$$U(\xi_1, \alpha_n) = \xi_1^{\frac{1-\delta}{2}} \left[J_q \left(\frac{2\alpha_n}{2-\delta} \xi_1^{\frac{2-\delta}{2}} \right) Y_q \left(\frac{2\alpha_n}{2-\delta} (\xi_1^{(2)})^{\frac{2-\delta}{2}} \right) - J_q \left(\frac{2\alpha_n}{2-\delta} (\xi_1^{(2)})^{\frac{2-\delta}{2}} \right) Y_q \left(\frac{2\alpha_n}{2-\delta} \xi_1^{\frac{2-\delta}{2}} \right) \right] \quad (19)$$

where constants d^n are the roots of the equation:

$$U(\xi_1^{(1)}, \alpha_n) = 0 \quad (20)$$

The solutions are:

$$\pi_1(\xi_1, \tau) = \varphi_1(\xi_1) + \sum_{n=1}^{\infty} A_n \cdot U(\xi_1, \alpha_n) \cdot e^{-\alpha_n^2 \tau} \quad (21)$$

$$\pi_2(\xi_1, \tau) = \varphi_2(\xi_1) + \sum_{n=1}^{\infty} B_n \cdot U(\xi_1, \alpha_n) \cdot e^{-\alpha_n^2 \tau} \quad (22)$$

$$\pi_3(\xi_1, \tau) = \sum_{n=1}^{\infty} C_n \cdot U(\xi_1, \alpha_n) \cdot e^{-\alpha_n^2 \tau} \quad (23)$$

The constants expressions are:

$$A_n = -\alpha_n^2 \left[\int_{\xi_1^{(1)}}^{\xi_1^{(2)}} \varphi_1(\xi_1) \cdot U(\xi_1, \alpha_n) d\xi_1 \right] \cdot \left[\int_{\xi_1^{(1)}}^{\xi_1^{(2)}} \xi_1 \delta \left[\frac{dU(\xi_1, \alpha_n)}{d\xi_1} \right]^2 d\xi_1 \right]^{-1} \quad (24)$$

$$B_n = -\alpha_n^2 \left[\int_{\xi_1^{(1)}}^{\xi_1^{(2)}} \varphi_2(\xi_1) \cdot U(\xi_1, \alpha_n) d\xi_1 \right] \cdot \left[\int_{\xi_1^{(1)}}^{\xi_1^{(2)}} \xi_1 \delta \left[\frac{dU(\xi_1, \alpha_n)}{d\xi_1} \right]^2 d\xi_1 \right]^{-1} \quad (25)$$

$$C_n = \alpha_n^2 \left[\int_{\xi_1^{(1)}}^{\xi_1^{(2)}} g(\xi_1) \cdot U(\xi_1, \alpha_n) d\xi_1 \right] \cdot \left[\int_{\xi_1^{(1)}}^{\xi_1^{(2)}} \xi_1 \delta \left[\frac{dU(\xi_1, \alpha_n)}{d\xi_1} \right]^2 d\xi_1 \right]^{-1} \quad (26)$$

Therefore formula (10) can be written as:

$$\pi(\xi_1, \tau) = \sum_{n=1}^{\infty} \frac{\alpha_n^2 e^{-\alpha_n^2 \tau} \cdot U(\xi_1, \alpha_n)}{\int_{\xi_1^{(1)}}^{\xi_1^{(2)}} \xi_1 \delta \left[\frac{dU(\xi_1, \alpha_n)}{d\xi_1} \right]^2 d\xi_1} \left\{ \int_{\xi_1^{(1)}}^{\xi_1^{(2)}} g(\xi_1) \cdot U(\xi_1, \alpha_n) d\xi_1 + \alpha_n^2 \left[\int_{\xi_1^{(1)}}^{\xi_1^{(2)}} \varphi_1(\xi_1) \cdot U(\xi_1, \alpha_n) d\xi_1 \right] \right. \\ \left. \cdot U(\xi_1, \alpha_n) d\xi_1 \int_0^{\tau} f_1(\lambda) \cdot e^{\alpha_n^2 \lambda} d\lambda + \int_{\xi_1^{(1)}}^{\xi_1^{(2)}} \varphi_2(\xi_1) \cdot U(\xi_1, \alpha_n) d\xi_1 \int_0^{\tau} f_2(\lambda) \cdot e^{\alpha_n^2 \lambda} d\lambda \right\}$$

4. CONCLUSIONS

The proposed mathematical model of calculus is useful for the numerical procedures in problems of flow of the compressible fluids through inhomogeneous porous media with constant porosity.

REFERENCES

1. T. Oroveanu, Scurgerea fluidelor prin medii poroase neomogene, Editura Academiei, București, 1963.
2. J. Bear, Dynamics of fluids in porous media, Elsevier, 1972.
3. P. Plessis (Editor), Fluid Transport in Porous Media, Computational Mechanics Publications, UK, 1997.
4. Z. Chen, R. Ewing, Fluid flow and transport in porous media, mathematical and numerical treatment, American Mathematical Society, 2002.
5. M. Țălu, Ș. Țălu, Calculul căderilor de presiune în conducte hidraulice. Regim de curgere stabilizat și nestabilizat. Teorie, aplicații și programe computaționale, Craiova, Editura Universitaria, 2006.

THE INFLUENCES OF GAS COMBUSTION PARAMETERS ON RUNNING ELECTRO-FILTERS

Marin BICĂ¹, Marian ENACHE², Corina CERNĂIANU³
^{1,3}*University of Craiova, Faculty of Mechanics*
²*C.E.T.Craiova*

Abstract: Coating charged particles, into an electric field and on an adequate collecting surface, into an electro-filter, may seem like an easy process. In reality, this proves to be very complex, since basic phenomena depend on probabilistic elements rather than simple determinism. Given, for instance, the basic case of a single particle passing through the electro-filter, it is impossible to predict whether that particle will be collected or not. From theory, one can only foresee the probability that the particle will reach the collecting electrode. In practice, where there are billions of particles per gas unit volume, the distinction between probability and certainty is entirely blurred. However, when we deal with only a few particles, the distinction can be made, but the complete understanding of the electric separation principles, further on presented, is not possible without the acceptance of a probabilistic basis of the particle collecting phenomena.

1. INTRODUCTION

Particle separation in industrial equipment can be made even more difficult due to the repositioning effect of the particles, the perturbation of corona discharge by breakthrough or inverse corona, or because of the faulty gas leakage. These effects can manifest themselves through the loss of the already collected particles or even by interfering in the primary coating process.

The basic theory of particle collection is developed without disturbing the primary coating process. A more comprehensive theory would be undoubtedly much more complicated for general use. It appears to be more useful to apply basic knowledge in order to eliminate, or at least minimize these effects. Yet, the adjustment of the

particle collecting parameters has been proved possible and is frequently practiced, so that some of the disturbance effects can be properly addressed.

The most advantageous approximations for particle collection theory are:

- Theoretical performance calculus, neglecting the disturbance factors. The result of the calculus represents the peak performances that can be reached and, at the same time, a reference number through which experimental results can be compared.

- Applying basic principles or other technical knowledge for lowering or, if possible, eliminating the repositioning of particles and other disadvantageous effects.

- Modifying theoretical parameters of coating in order to control the losses triggered by the multiple factors that influence gas dedusting. The methods employed are mostly empirical, but represent a synthetic instrument for introducing and applying data and practical results. This semi empirical approximation may be deceiving or dangerous if applied without discrimination, but it is useful and enlightening when used in an intelligent manner.

Based on these principles and the direct observation of a few running electro-filters, several model studies, concerning the functioning of electrostatic precipitators, have been carried out. A number of simple theoretical models created in the past have been used for more than half a century in the field of electro-filter designing and dimensioning. Following the development of calculus instruments, more refined models have been elaborated, taking into account more of the phenomena existent in the electrostatic filtering process.

Under the circumstances, it can be said that the dedusting efficiency of an electro-filter is influenced by multiple factors, which can be divided into three groups:

- The first group includes the geometrical dimensions of the electro-filter's electric field and the gas flow capacity of the equipment that has to be cleaned.

- The second group consists of the gas-dust system parameters.

- The third group consists of electrical factors (the electric field distribution, the density and ionic charge repartition in the space between electrodes) – which determine, to a large extent, another essential measure involved in the electrostatic separation process, namely the electric charge stored by the particles while running inside the electro-filter.

In light of what was stated above, a couple of important observations can be made, which will be given careful consideration throughout this paper:

- Electrostatic precipitators combine electrical, aerodynamic and mechanical phenomena in close relation to one another.
- The simulation of a running electro-filter requires the creation of models which allow for the calculation of electrical and aerodynamic measures.

2. THE NON-UNIFORMITY INFLUENCE OF GAS FLOW ON A RUNNING ELECTRO-FILTER

The functioning efficiency of an electro-filter is directly influenced by the non-uniform distribution of velocities and dust concentrations. The electrical part of the electro-filter, by default, conditions the achieving of the imposed separation degree. Irrespective of the quality of conception and execution of the electro-filter, this will not be able to achieve the imposed limits if the gas flow requiring dedusting and the dust concentration are non-uniform.

The non-uniform distribution of velocities in the electro-filter diminishes performance in two ways:

- First, non-uniform treatment of the gas lowers the efficiency in areas with high velocity to a greater extent than the compensation which occurs in low velocity areas.
- Secondly, we have to deal with the repositioning or even the particle displacement from the electrodes, in areas with high gas velocity.

Both effects are important, but the second one usually prevails where the distribution is non-uniform. This can lower efficiency up to 60%.

When raising the velocity, the efficiency drops slightly at first and, upon exceedance of the repositioning velocity, the electro-filter runs faulty.

Deutsch's equation (1) is correct only when the electro-filter runs with a gas flow capacity that is evenly distributed throughout the active area of the electro-filter. This means that the gas velocity remains constant in every point "i" of the electro-filter field:

$$\eta = 1 - e^{-n} = 1 - e^{-\frac{WC_E}{V}} \quad (1)$$

where: C_E stands for the electro-filter constant ($C_E = L/h$), L is the length of the field in [m], h is the distance between the emission-deposit electrodes, [m], V is the gas velocity inside the electro-filter, [m/s] and W is the deposit velocity of a particle, [m/s].

In reality, the distribution of the gases that pass through the electro-filter is characterized by a certain degree of non-uniformity.

Therefore, the use of the aforementioned equation will not lead to correct results.

The influence of the velocities' non-uniformity on the values obtained by means of Deutsch's method is shown by the formula below.

To this end, section A of the electro-filter is divided into a series of elementary surfaces dA , in which gases flow at a constant velocity.

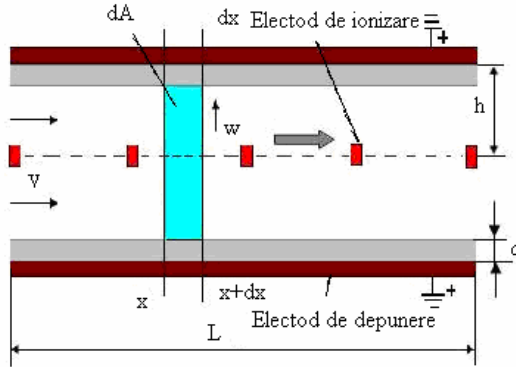


Fig.1- Simplified schema of an electro-filter plan

In this case, formula 1 can be written as follows:

$$\eta = \frac{\int \left(1 - e^{-\frac{WC_E}{V}} \right) \times V \times dA}{\int V dA} \quad (2)$$

This formula can be used if the distribution of the gas velocity inside the electro-filter is known and if the migration velocity remains constant, independently of the gas velocity.

Given that $W \square C_E$ has different values for every considered electro-filter, as well as for every charge and velocity distribution, the formula cannot actually determine the efficiency of the electro-filter. Thus, a characteristic of the velocity distribution that does not contain the $W \square C_E$ element must be found.

Dividing the circle into very small units, we approximate the circle arch with a segment tangent to the curve. After analyzing the dedusting efficiency graphic, with respect to the velocity shown in figure 2, we can write the following formula, which holds true for the contact point:

$$1 - e^{-\frac{WC_E}{V}} = A + BV \quad (3)$$

In this case, we get the formula for efficiency:

$$\eta = A + BV_y \quad (4)$$

where: $V_y = \frac{\int V^2 dA}{\int V dA}$

V_y is the equivalent velocity that takes into account the non-uniformity of the velocity repartition.

Substituting in Deutsch's formula we obtain:

$$\eta = 1 - e^{-\frac{WC_E}{V_y}} \quad (5)$$

Since the non-uniformity of velocity distribution triggers a decrease in efficiency, it follows that: $V_y \geq V_{med}$. The ratio of these two measures is m and it is known as the degree of used section from the point of view of velocity uniformity.

$$m = \frac{V_{med}}{V_y} = \frac{\left[\int V dA \right]^2}{A \int V^2 dA} \quad (6)$$

For a field of non-uniform velocities, the determined section for the electro-filter A_N is:

$$A_N = A_{teor.} / m \quad (7)$$

The following reasoning ensues:

Let us suppose that an evenly distributed gas flow passes through the electro-filter. For $WC_E/V = 0,3$, the dedusting efficiency $\eta = f(k.V)$ will be 96,5%, considering figure 2.

If the same gas flow is non-uniformly distributed, so that in some areas the velocity will increase with ΔV_1 and in others will drop with ΔV_2 , the dedusting efficiency will change. In the first area, the efficiency will decrease with η_1 and in the second it will increase with η_2 . In this case, by substituting "V" for the average velocity in formula (1), we get increased values for the dedusting efficiency. The error can be reduced by substituting V for V_y . K. Remmers suggests a modified procedure in order to address the velocities non-uniformity.

Based on the measured velocity of the gases V_i , we can determine the mean error corresponding to the mean velocity of the gases:

$$\Delta V'_{med} = \frac{\sqrt{\sum_{i=1}^n (V_i - V_{med})^2}}{n} \quad \text{for } n \geq 1 \quad (8)$$

where: n - number of points for velocity measuring, V_i - gas velocity measured at point "i" [m/s], V_{med} - the arithmetic mean of gas velocity [m/s]

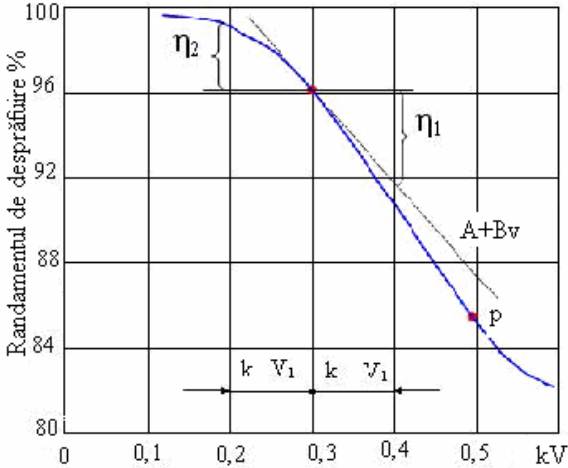


Fig. 2-The dedusting efficiency of the electro-filter according to the gas velocity.

The $\Delta\eta$ decrease due to velocities non-uniformity can be determined by means of the following formula:

$$\Delta\eta = \pm \frac{-WF}{e^{AV_{med}} F \Delta V'_{med} \ln e^{-W}} \quad (9)$$

where F is the depositing surface measured in $[m^2]$.

The efficiency achieved by the electro-filter will then be:

$$\eta = \eta_{teor.} - \Delta\eta \quad (10)$$

Experiments proved that by increasing the velocity non-uniformity, the efficiency decreases correspondingly.

I. E. Idelcik analyzed the influence of the velocity distribution on the dedusting efficiency, in an electro-filter. He used the coefficient M_k , namely the ratio between the energy impulse of the gas flow capacity calculated in two ways. In the former, the impulse energy was calculated using the real velocities of the gas in the desired points, whereas the latter resulted from the mean velocity of the gases [3].

$$M_K = \frac{\sum_{i=1}^n V_i^2 \Delta A}{V_{med}^2 A} = \frac{1}{A} \int \left(\frac{V}{V_{med}} \right)^2 dA \quad (11)$$

Velocity repartition can also be determined through the coefficient that characterizes the kinetic energy of the gas flow.

$$N_K = \frac{\sum_{i=1}^n V_i^3 \Delta A}{V_{med}^3 A} = \frac{1}{A} \int \left(\frac{V}{V_{med}} \right)^3 dA \quad (12)$$

M_K and N_K coefficients can be greater or equal to the unit. The more their value increases, the greater will be the degree of the velocities' non-uniformity and the lower the dedusting efficiency.

We introduce in Deutsch's formula the V_{med} term, so that we are able to account for the field of velocities non-uniformity.

$$V'_{med} = V_{med} M_K \quad (13)$$

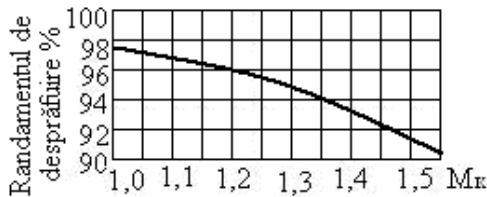


Fig.3 -The dedusting efficiency of the electro-filter according to the non-uniformity coefficient M_K of the velocity field, experimentally determined by Indelcik

The majority of researchers in the field concur that a uniform flow in the transverse section of the electro-filter, within both the In and Out areas of the electro-filter, has to meet the following criteria:

- the incorporation of 85% of the local velocity values, measured within the limit of 20% with respect to the mean velocity value;
- 99% of the local velocity values must fall within the limit of 40% with respect to the mean velocity value.

In figure 3 we have rendered the variation of the dedusting efficiency according to the non-uniformity coefficient M_K , corresponding to the velocities field, as shown in (11).

The dedusting efficiency is determined using the formula:

$$\eta = 1 - e^{-\frac{1}{K_1 M_K V_K}} \quad (14)$$

This formula shows that the higher the term M_K , the lower the dedusting efficiency.

Figure 4 shows the influence of the dedusting efficiency of an electro-filter that removes dust from gases, as a consequence of lignite coal burning. The process takes place in boilers of 1035t/h and uses equipment that has been placed internally at 400mm distance, in two ways:

- when the electro-filter is equipped with a smoothing system of the flowing gases- curve 1;
- when the electro-filter is not equipped with such a smoothing system – curve 2;

It can be seen that the results obtained are in accord with the theoretical conclusions regarding the influence of the non-uniformity in velocities field on the dedusting efficiency.

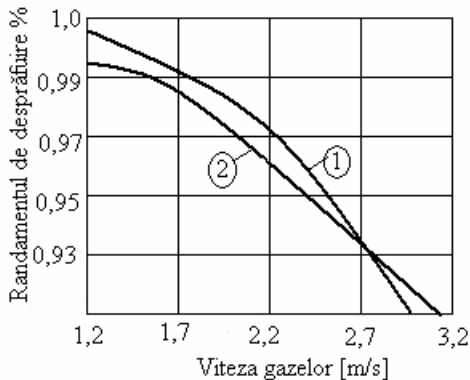


Fig. 4 Dedusting efficiency function of gas velocity for horizontal electro-filters with $2h=400\text{mm}$

A very important cause of efficiency decrease is represented by the repositioning in the areas with high gas velocity. Repositioning losses become important where maximum gas velocity exceeds the critical dedusting speed of the particles from the electrodes.

Beside the nonuniform flow and the repositioning of the dust particles, other disadvantageous effects may appear. The most important are particle loss from bunkers, because of the bunkers sweep and turbulences inside them. Also, the low pressure formed along the electro-filter tends to push a part of the gases underneath the depositing plates. It's necessary for the bunkers to be equipped with a system that avoids dust repositioning.

Gas leakage on the top part of the depositing electrodes, fake intake, leads to decreasing the dedusting efficiency, because of the misfit gas circulation in active area. For example, if 5% from the gas

flow passes through the active area (corona discharge areas), the dedusting efficiency cannot be higher than 95%.

Nonuniform repartition of velocities directly affects the dedusting efficiency of the electro-filter.

Besides that, it generates an indirect and negative effect over the efficiency in the electrostatic process of dedusting. A permanent, reduced content of dust is kept in active spaces, where gas velocity is low. Also, in this spaces, a high degree of ionized gas exists. This leads to an intense current, that reduces the dielectrical rigidity of the entire area connected to a high voltage grid.

The electro-filter is running ill, with discharges, that requires the lowering of the input voltage, meaning the reducing of the efficiency. Similar phenomena appear in the gas current. This undesired phenomena appear frequently in the technique of electrostatic dedusting, with direct impact over the efficiency and environment pollution.

3. THE EFFECT OF THE PARTICLE CONCENTRATION ON THE RUNNING ELECTRO-FILTER.

In this paragraph, the effects with particular importance on the running electro-filter are studied. These effects are produced by the pending particles and by the particle coating on the collecting electrodes.

This effects appear in every electro-filter and in some cases they prevails over the other factors; thus making the electro-filter becoming inefficient because of the perturbation of corona discharge and the modified repartition of the electric field between the 2 electrodes.

A high concentration of particles can have negative effect over the performance of an electro-filter.

As long as the particles from the electro-filter are getting chared, they move between the electrodes and an electric current appears. The mobility of these solid particles is 100 times smaller than of ions. Because of that, increasing the particle concentration leads to a spatial charge much less mobile than the space between electrodes. The mentioned phenomena can be practical formulated as a diminish of ion mobility.

$$k_{ef} = k_e \left(\frac{J}{200J_{part} + J} \right), \quad (15)$$

where: J_i - density of ionic current; J_{part} - density of particular current; k_e - ion mobility in air; k_{ef} - equivalent mobility in the presence of particles.

Thus, the filtering performance will be lower for the same value of the electrical voltage applied to the electrodes. For constant current, it's necessary to increase the voltage by ΔV_p [8,6]:

$$\Delta V_p = \frac{\rho_{\text{part}} k_e^2}{2\epsilon_0}, \quad (16)$$

with ρ_{part} - particular spatial charge.

As long as the particle concentration is high, the ionization current is low, leading sometimes to the cancellation of corona discharge [6]. Maintaining an electrical field strong enough, requires a voltage increase. A high concentration can favor the breakthrough between the electrodes (risks of explosion can appear if particle concentration in gas is between 20-100gm⁻³).

For higher concentrations, with an important percentage of small particles, the electro-filter is divided into several dedusting areas, electrically independent. This leads to the possibility of using adaptive voltage and intensity, accordingly to the particle concentration.

4. FACTORS THAT AFFECT RESISTIVITY

With the formula below electrical resistivity of dust can be calculated:

$$\rho = R \cdot \frac{A}{\delta}$$

where: R - is the probe resistivity [Ω], A - the surface on which the dust sets [cm²], δ - the thickness of the dust coating.

The concept of surface conductivity is related to the surface field between points on surface. Though, electrically, the dust coating is represented by a serial-parallel system of the volume density.

The equivalent circuit of resistances, representing a dust coating is presented in the next figure.

There are 3 resistances : volume, contact and surface. The volume resistance depends on the chemical component, but changes with temperature.

The contact resistance depends on the superficial conformation of the dust particle and the grouping density. The surface resistance is determined, as mentioned, by the particle surface and the absorption of liquid and gases.

When temperature changes, variations of particle state appear, meaning variations of superficial resistivity.

The total resistivity of the dust coating is the result of the volume, surface and contact resistances. Based on (15), the resistance of dry dust depends on temperature (fig. 14/1).

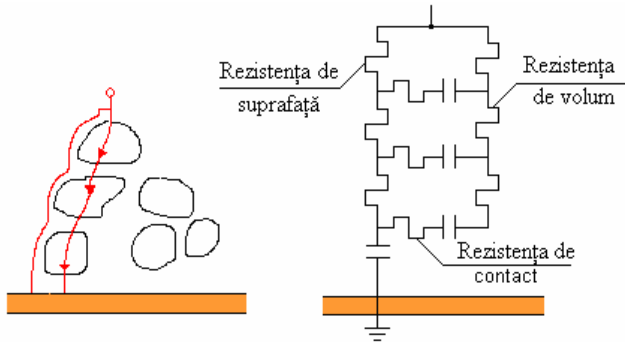


Fig. 5- Equivalent schema of the resistance for a dust coating

The factors that affect resistivity are: the amount of coal sulfur, temperature, humidity, and constituents of ash – sodium, potassium, carbon, iron oxide, etc.

In fig 6 is presented a typical curve presenting dust resistivity function of sulfur amount [1].

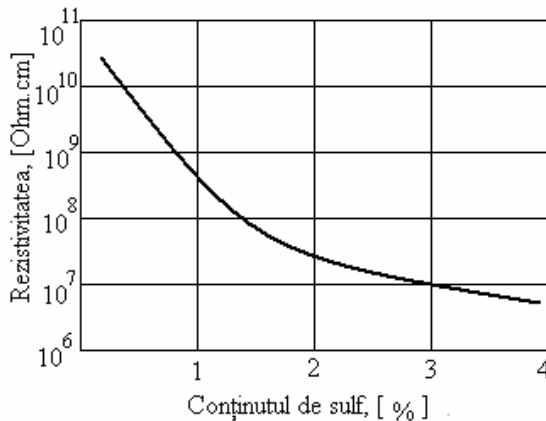


Fig. 6 - Sulfur influence on dust resistivity

Ash resistivity is inversely proportional with the SO_3 , water, potassium, sodium concentration in combustion gases and direct proportional with the amount of magnesium, calcium, etc.

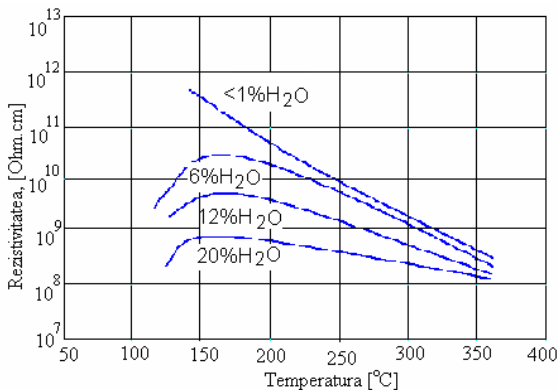


Fig. 7- Temperature influence on dust resistivity

In figure 7 is represented the typical curve of the temperature influence on the dust resistivity.

The resistivity peak for ash appears between 126°C and 210°C, depending on the ash characteristic and combustion gases. Ash resistivity over 232-288°C is inversely proportional with the absolute temperature, while below 126-149°C resistivity is direct proportional with the absolute temperature.

5. THE INFLUENCE OF GAS FLOW ON A RUNNING ELECTRO-FILTER.

The flowing velocity of gases is proportional to the purified gas flow, because of the constant section of the electro-filter. The flowing velocity must provide a sufficiently high time of the two-phase environment.

The repositioning of the collected particles is usually associated to the erosion phenomena. When speaking of electro-filters, five important effects can be distinguished:

- the direct interaction between gas flux and the particle coating on the electrodes;
- the repositioning of particles because of the gas flow. The particles are removed from electrodes and fall, due to gravity, in the bunkers from the lowest part of the electro-filter. The removing of particles is applied to avoid overloading the collecting plates and to reduce the anti-emission phenomena.
- the sweeping of the particles disposed in the dust bunker, because of an inadequate distribution of flowing;
- electrical breakthrough between the electrodes that can lead to the detachment of a coated area.

- anti-emission that modifies the coating and weakens it.

The repositioning phenomena is very complex and depends on the coating characteristic. The particles from the electrodes are exposed to Van der Waals forces and electrical forces, because of their residual charge. Particles loose sooner or later their electrical charge, in contact to the electrodes and because of their dielectrical properties.

The mass volume of particles plays an important role in purifying and repositioning the particles when hitting the electrodes. For particles with low density, it's necessary a reduced velocity of the gas (0.5m/s), which limits the electro-filter capacity. Repositioning also depends on the construction of the filter, gas flowing distribution, the shape of the electrodes and the manner they are cleaned.

Repositioning can diminish the efficiency of collecting, in practice, with about 40-50%.

Gas distribution must be improved for diminishing the repositioning phenomena, by using adequate shapes for the electrodes. Also using divided electrical sections leads to increased efficiency.

Repositioning is sensible to current and voltage. The industrial coatings usually have a resistivity of $10^8 - 10^{10} \Omega cm$, enough to determine important attraction forces. Coating adhesion is improved in this way by the ionic current that runs across the surface, as long as the current is high and well distributed.

Particle concentration in gas flowing is in many situations high enough, so that it will have an important effect on flowing. According to Eaton, a turbulence damping can be noticed, for a particle percentage greater than 10%. This damping is affected by different parameters like Stokes number, Reynolds number and ratio between particle diameter and the length scale characteristic to the turbulence.

Turbulence flowing is described by Reynolds formula and by the formula's of kinetic-energy transport along with ϵ scattering.

6. THE EFFECT OF PARTICLE COATING ON EMISSION ELECTRODES

The particles coating on emission electrodes can influence the corona emission in 2 ways:

Regions with intense local field can appear, for reduced coating, that produce corona emission at low voltage. The effect relays on reducing the voltage for the corona emission and displacing the current-voltage characteristic to lower voltages. If this phenomena appears, corona current increases and the voltage is lower than usual.

Massive coating on emission electrodes reduces the corona current due to increased diameter. Also, appears an additional voltage, created by the current that passes through the resistance caused by

dust coating. The coatings on these electrodes are usually nonuniform along the wires, so the corona current is also non-uniformly distributed. The result is a decrease in the dedusting efficiency.

The coatings on corona electrodes are usually more intense for tiny particles. Bigger particles tend to keep the electrodes clean because of the erosive action of these kind of particles.

Because of these causes, electro-filters must be equipped with systems for cleaning the emission and depositing electrodes.

7. CONCLUSIONS

The dedusting efficiency is heavily influenced by the gas velocity. Losses due to repositioning become important where the maximum gas velocity exceeds the critical velocity of electrodes cleaning. Because of nonuniform repartition of velocities, in the active area of the filter, another disadvantageous effects can appear. The most important are the particle losses from bunkers because of the bunkers sweep and turbulences inside them. Also the low pressure formed along the electro-filter tends to push a part of the gases underneath the depositing plates. That is why it is necessary for the bunkers to be equipped with a system that avoids dust repositioning. Gas leakage on the top part of the depositing electrodes, fake intake, leads to decreasing the dedusting efficiency because of the misfit gas circulation in active area. For example if 5% from the gas flow passes through the active area (corona discharge areas), the dedusting efficiency can't be higher than 95%. Nonuniform repartition of velocities directly affects the dedusting efficiency of the electro-filter.

Besides that, it generates an indirect and negative effect over the efficiency in the electrostatic process of dedusting. A permanent, reduced content of dust is kept in active spaces where gas velocity is low. Also, in this spaces, a high degree of ionized gas exists. This leads to an intense current, that reduces the dielectrical rigidity of the entire area connected to a high voltage grid. The electro-filter is running ill, with discharges, that requires the lowering of the input voltage, meaning the reducing of the efficiency. Similar phenomena appear in the gas current, which are mostly linked to the repartition of admission velocities. This undesired phenomena appear frequently in the technique of electrostatic dedusting with direct impact over the efficiency and environment pollution.

RESEARCH REGARDING THE ROUGHNESS OF THE SURFACES AT TURNING TITANIUM ALLOYS (TiAl₅Fe_{2.5})

Marius ZAMFIRACHE¹, Alexandru STANIMIR²
^{1,2}University of Craiova, Faculty of Mechanics

Abstract: This paper presents the results of some experimental research regarding the roughness of the surfaces for titanium alloys: TiAl₅Fe_{2.5} in the case of the turning process using tools carbide type K20.

Keywords: Titanium alloys, turning, roughness surfaces, non linear functions, analysis regression.

1. INTRODUCTION

Roughness, as a characteristic factor of surface is determined by the parameters of the cutting system, the geometry of the tool, the material structure, the rigidity of the technological system

The paper presents the study of the cutting system influence upon the roughness of the processed surfaces.

2. EXPERIMENTAL DATA

The chemical characteristics of the titanium alloys presented in table 1.

Table 1

Titanium alloys	Ti	Al	Fe
TiAl ₅ Fe _{2.5}	92,5	5	2.5

In table 2 there are presented mechanical properties of the researched material.

Table 2

Titanium alloys	Tensile strength (MPa)	Brinell Hardness(HB)
TiAl ₆ V ₄	920	300

The levels of the natural variants v , f , a_p , and are in geometric progression. Eighteen experiments were realized by using the special methodology of the planning of experiments.

The considered cutting tools were represented by carbon plates type: K20-ordinary tool and K20 without point tools.

The geometric parameters of the considered tools are characterized by: $\alpha = 6^\circ$, $\gamma = 5^\circ$, $\lambda_T = 0^\circ$, $\chi_r = 70^\circ$, $\chi_r = 10^\circ$ (ordinary tool) and $\alpha = 6^\circ$, $\gamma = -5^\circ$, $\lambda_T = -60^\circ$, $\chi_r = 70^\circ$ (without point tools, fig.1)

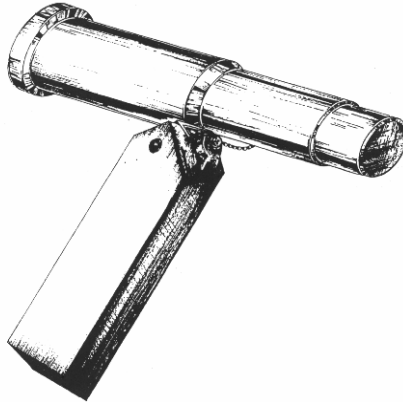


Fig. 1. Tools without point

The levels of the variables are presented in table 3.

Table 3

Symbol	Code	-1	0	+1
$V(m/min)$	X1	60	85	120
$f(mm/rot)$	X2	0.1	0.14	0.2
$a_p(mm)$	X3	0.5	0.9	1.5

The measurement results are shown in table 4.

Table 4

Type	Cod levels values			Roughness Ra(μm)	
	Xj	X1	X2	X3	TiAl5Fe2,5-K20 (ordinary tools)
1	-1	-1	-1	2.4	1.9
2	+1	-1	-1	2.45	1.9
3	-1	+1	-1	4.2	3.8
4	+1	+1	-1	4.1	3.7
5	-1	-1	+1	2.8	2.5
6	+1	-1	+1	2.9	2.5
7	-1	+1	+1	5.8	5.4
8	+1	+1	+1	5.7	5.2
9	0	0	0	3.7	3.2
10	0	0	0	3.6	3.1
11	0	0	0	3.7	3.2
12	0	0	0	3.7	3.2

During the cutting process, there was used a cutting emulsion liquid of the PE5EP type.

In order to determine the roughness of the considered Surf Test SJ 201.

3.ANALYZING THE EXPERMENTAL DATA

For example in the titanium alloys Ti Al6V4, the elements characterized by the Ra functions are presented regression indicators are shown in table 5 (turning tool without point) and in table 6 (turning tools ordinary).

Table 5

PROGRAM FOR DETERMINING THE REGRESION FUNCTIONS

STUDIEND PROCES : TURNING TOOLS WITHOUT POINT

Dependent variable $Y=Ra$

Non –dependent variables $X1=v$

Non –dependent variables $X2=f$

Non –dependent variables $X3=a$

Levels:
 for x1
 maximum level 120
 minimum level 60
 for x2
 maximum level 0.2
 minimum level 0.1
 for x3
 maximum level 1.5
 minimum level 0.5

RESULTS OF THE REGRESSION ANALYSIS

$R^* = 0.314 < 1$ == Adequate model.

Significant coefficients

$R_0 = 686.39 > 1$ == significant variable
 $R_1 = 0.10 < 1$ == non-significant variable
 $R_2 = 4.55 > 1$ == significant variable
 $R_3 = 0.16 < 1$ == non-significant variable

Table 5

No. exp	Measured values (Ra)	Calc. Values (Ra)	Abs. errors	Rel. errors
1	1.9	2.1	0.08	3.5
2	1.9	1.974	0.13	6.0
3	3.8	4.34	0.04	7.0
4	3.7	4.94	0.29	5.1
5	2.5	2.7	0.05	2.6
6	2.4	2.7	0.01	0.7
7	5.4	5.59	0.07	1.7
8	5.2	5.68	0.16	4.2
9	3.2	3.68	-0.38	-16.1
10	3.1	3.53	-0.39	-18.2
11	3.2	3.14	-0.27	-14.10
12	3.2	3.82	-0.83	-20.65

Using computing REGS programs, next functions non linear were determined:

$$Ra = 0.31v^{0.022} f^{0.78} a^{0.712} \quad (1)$$

(roughness surfaces without point turning)

PROGRAM FOR DETERMINING THE REGRESSION FUNCTIONS IN TURNING PROCES

Dependent variable $Y=R_a$
 Non –dependent variables $X_1=v$
 Non –dependent variables $X_2=f$
 Non –dependent variables $X_3=a$
 Levels:
 for x_1
 maximum level 120
 minimum level 60
 for x_2
 maximum level 0.2
 minimum level 0.1
 for x_3
 maximum level 1.5
 minimum level 0.5

RESULTS OF THE REGRESSION ANALYSIS

$R^2=0.236 < 1$ == Adequate model.

Significant coefficients

$R_0=542.22 > 1$ == significant variable
 $R_1=0.06 < 1$ == non-significant variable
 $R_2=7.25 > 1$ == significant variable
 $R_3=0.50 < 1$ == non significant variable

Table 6

No. exp	Meas. Values (R_a)	Calc. Values (R_a)	Abs. errors	Rel. errors
1	2.4	2.45	0.13	4.85
2	2.45	2.47	0.15	5.66
3	4.5	4.68	-0.18	-6.06
4	4.2	4.447	-0.25	-5.91
5	2.9	3.07	-0.17	-5.87
6	2.9	2.91	-0.11	-4.09
7	5.9	5.56	-0.33	5.66
8	5.8	5.51	0.28	4.85
9	3.7	3.69	0.01	0.14
10	3.6	3.64	-0.02	-2.63
11	3.7	3.66	0.05	0.14
12	3.7	3.61	0.04	0.14

Using computing REGS programs, the next non linear equations were determined:

$$Ra=0.212v^{-0.022}f^{0.578}a^{0.112} \quad (2)$$

(roughness surfaces tool ordinary turning)

4.CONCLUSIONS

Analysing the measurements, one can notice that when turning with a pointless tools, the roughness of the processed surface is lower than in the case of ordinary tools.

In most cases, every SA-MP couple and for every Ra value the f, v, a_p parameters are significant variables, the cutting depth a_p is determined and the cutting velocity has a minimum influence ($R2>R1>R3>R4$). The influence factors over the Ra values are: the advance, the cutting velocity, the cutting depth.

REFERENCES

1. Gheorghe, M., Stancescu, C., Draganescu, F., Algorithm and computer program to determine multiple variables regression functions, B.I.P., Bucharest., p.176-189, 1985.
2. Popescu, I., Optimization of cutting proceses, Romanien Writing, Craiova, 1987.
3. Strajescu E., Cutting Tools Desing, U.P. Bucharest, 1998.
4. Zamfirache, M., Machinability of titanium alloys by turning, University Publishing Craiova, 1996

THERMIC CALCULUS OF AIRCRAFT'S CABIN

Lucian SEPCU¹, Mihai LUNGU², Mădălina CĂLBUREANU³

¹University of Craiova, Faculty of Electrical Engineering

²University of Craiova, Faculty of Electrical Engineering

³University of Craiova, Faculty of Mechanics

Abstract: This paper presents the mathematical model for calculus of the heat of the cabin (the upper part of its casing). It goes from some experimental data and is an iterative calculation for variables E_{dir} , E_{dif1} , q_{inv} , q_{ext} , q_{rad} , T_{pint} , α_{rad} , q_{int} and so on.

Keywords: climatic conditions, heat calculus, flight, cabin.

1. INTRODUCTION

Eligibility for achieving thermal calculation of the cabin are: altitude conditions (ground, the maximum flight ceiling, at cruise altitude), velocity conditions, climate conditions.

The conditions of altitude and speed are shown in the below table.

Table 1

$H[m]$	$U_{\alpha min} [m/s]$	$U_{\alpha max} [m/s]$
0	47,82	119,95
500	49,38	120,49
1000	51,05	120,95
1500	52,90	121,25
2000	54,76	121,54
2500	56,62	121,78
3000	58,49	121,78
3500	60,42	120,94
4000	62,55	119,97
4500	64,78	118,96
5000	67,23	117,96
5500	70,15	116,76

In the above table H is the height of flight, $U_{\alpha min}$ - the minimum flight speed and $U_{\alpha max}$ - the maximum flight speed.

2. THERMICAL CALCULUS OF THE CABIN

Climatic conditions necessary to achieve these calculations heat of the cabin are:

1) maximum temperature for $H = 0 \div 6000m$ is

$$T_{ext} = 314,15 - \frac{H}{120} [K]; \quad (1)$$

2) minimum temperature for $0 \leq H \leq 1200m$ is

$$T_{ext} = 253,15 [K]; \quad (2)$$

3) minimum temperature for $1200m \leq H \leq 6000m$ is

$$T_{ext} = 253,15 - \frac{H - 1200}{192} [K]. \quad (3)$$

To apply the methodology of calculation of the upper cabin heat one must first determine the following parameters:

a) E_{dir} with approximate equation for $0 \leq H \leq 8000m$

$$E_{dir} = 500 + \frac{21}{400} H; \quad (4)$$

b) E_{dif1} with equation

$$E_{dif1} = \begin{cases} 280 - \frac{1}{40} H; 0 \leq H \leq 4000m \\ 170 - \frac{3}{400} (H - 4000); 4000m \leq H \leq 8000m \end{cases} \quad (5)$$

Knowing E_{dir} and E_{dif1} one obtains q_{us} as follows

$$q_{us} = 0,1E_{dir} + 0,98E_{dif1}. \quad (6)$$

The Mach number represents the raport $M = \frac{U_a}{a}$, where a is the thunder's speed; $a = \sqrt{401,8742 \cdot T_{ext}}$.

Further, thermal calculus is made through iterations as follows: one selects a value T_{pext} close to T_{ext} . The average temperature at which outside air properties are evaluated is calculated depending on Mach number for two different situations:

$$T_0 = \begin{cases} \frac{1}{2}(T_{ext} + T_{pext}); M < 0,3 \\ T_{ext} + 0,5[T_{pext} - T_{ext}] + 9,24 \cdot 10^{-5} U_a^2; M > 0,3. \end{cases} \quad (7)$$

The outside undisturbed air pressure or its density are important for calculations. The pressure is a function of height of flight of the aircraft.

$$P_{ext} = 101325 \left[1 - 22,55 \cdot 10^{-6} H \right]^{5,25} \quad (8)$$

and

$$\rho_{ext} = \frac{P_{ext}}{287,053 \cdot T_{ext}}. \quad (9)$$

Viscosity of the air shell is

$$\nu_0 = \frac{\eta_0}{\rho_{ext}}, \quad (10)$$

where η_0 is the dynamic viscosity of air and coating is calculated with relation

$$\eta_0 = 17,16 \cdot 10^{-6} \left[\frac{T_0}{273,15} \right]^{1,5} \cdot \frac{392,15}{T_0 + 119}. \quad (11)$$

Between outside air and the outer shell of the aircraft can be established (calculated) heat transfer coefficient by convection

$$\alpha_{ext} = 0,032 \left[\frac{U_{\alpha}}{\nu_0} \right]^{0,6} \frac{\lambda_0}{l_{cab}^2}, \quad (12)$$

where λ_0 is the thermal conductivity of coating $\lambda_0 = 1223,16 \cdot \eta_0$, and l_{cab} – the length of cylindrical part of the cabin.

Knowing α_{ext} , T_{ext} and T_{pext} one determines the unit of heat flow determined by convection between the outside air and the outer shell of the aircraft

$$q_{inv} = \alpha_{ext} (T_{ext} - T_{pext}), \quad (13)$$

and the total unit heat flow is

$$q_{ext} = q_{rs} + q_{inv} + q_{rad}, \quad (14)$$

where q_{rad} is determined by radiation flux between the outer shell of the aircraft and the outside air

$$q_{rad} = 4,5136 \left[\left(\frac{T_{pext}}{100} \right)^4 - \left(\frac{T_{ext}}{100} \right)^4 \right]. \quad (15)$$

The temperature T_{pint} will be

$$T_{pint} = T_{pext} - \left(\frac{\delta_{inv}}{\lambda_{inv}} + \frac{\delta_{iz}}{\lambda_{iz}} \right) q_{ext}, \quad (16)$$

where δ_{inv} is the thickness of coating, δ_{iz} – the thickness of the insulating coating, λ_{inv} – the coefficient of thermal conductivity and λ_{iz} – the coefficient of thermal conductivity coating of insulating coating.

According to the graph of variation of pressure in the cabin, the ratio of cabin pressure and cabin pressure in the soil is

$$\frac{P_{cab}}{P_0} = \begin{cases} 1, 0 \leq H \leq 2200m \\ \left(1 - 22,557 \cdot 10^{-6} H\right)^{5,25} + \frac{25100}{101325}, 2200 \leq H \leq 5500m \end{cases} \quad (17)$$

Total heat transfer coefficient has the expression

$$\alpha_{int} = \alpha_{conv} + \alpha_{rad}, \quad (18)$$

where α_{conv} is the transfer coefficient by convection

$$\alpha_{conv} = \frac{1,1434 \sqrt{|T_{pint} - T_{cab}|} \cdot \sqrt{\frac{P_{cab}}{P_0}}}{\sqrt[4]{\pi R}}, \quad (19)$$

R being the radius of the cylindrical casing,

$$\alpha_{rad} = \frac{4,5136}{T_{pint} - T_{cab}} \left[\left(\frac{T_{pext}}{100} \right)^4 - \left(\frac{T_{cab}}{100} \right)^4 \right], \quad (20)$$

and uniform flow of heat between air in the cabin and set its wall

$$q_{int} = \alpha_{int} [T_{pint} - T_{cab}]. \quad (21)$$

3. CONCLUSIONS

If the calculated flow q_{int} is different from q_{ext} one resumes the iteration choosing a new value for T_{pext} . When it was established equality $q_{ext} = q_{int} = q_{sup}$ the heat flow is calculated; this flow is determined by the upper panel $Q_{sup} = A_{sup} \cdot q_{sup}$; A_{sup} is the area of the upper casing.

REFERENCES

1. Tan, Chee-Fai, Chen, Wei, Rauterberg, Matthias „Design of an Aircraft Cabin Testbed for Stress-Free Air Travel Experiment”, International Conference on Planning and Design, 2009, NCKU, Tainan, Taiwan.
2. Douglas G. Macmartin „Collocated structural control for reduction of aircraft cabin noise”. Journal of Sound and Vibration (1996) 190(1), 105-119.
3. C. Müller, D. Scholz, T. Giese, „Dynamic simulation of innovative aircraft air conditioning”, CEAS – 2007 – 466.
4. “Avion de antrenament primar cu dubla utilizare – militara si civila – ALPHA” (contract de cercetare nr. 167387/2005).

ON A SOLUTION FOR PLANE-RADIAL FLOW OF A COMPRESSIBLE FLUID THROUGH INHOMOGENEOUS POROUS MEDIA

Ștefan ȚĂLU¹, Mihai ȚĂLU², Aurelian SIPOS³, Levente BOKOR⁴

¹*Technical University of Cluj-Napoca, Faculty of Mechanics,
Dept. of Descriptive Geometry and Engineering Graphics*

²*University of Craiova, Faculty of Mechanics,
Dept. of Applied Mechanics*

³*Croydon College, Dept. of Mathematics & Science, Croydon, UK*

⁴*Nivel Construct SRL, Cluj-Napoca*

Abstract: This paper presents a new class of solutions for plane-radial flow of compressible fluids through inhomogeneous porous media. On the basis of this solution class, a new model for interactions in inhomogeneous porous media is outlined.

Keywords: plane-radial flow, compressible fluids, inhomogeneous porous media.

1. THEORETICAL CONSIDERATIONS

The plane-radial flow of compressible fluids through inhomogeneous porous media is a complex process that has been studied by numerous researchers during the last decades, in various areas of engineering and physics [1, 2, 3, 4].

Generally, the mathematical models for solving these problems are derived from physical principles based on certain physical assumptions.

The mathematical formulations are composed of a system of mixed-type nonlinear partial differential equations. Numerical solution algorithms for solving such a system are difficult because the algorithms need to address the mathematical characteristics of both flow and deformation problems.

A very small number of exact mathematical solutions of this type are known [5, 6, 7]. Standard finite element methods have been used to solve these problems [8, 9, 10].

It is often desired to simulate the flow of fluids through inhomogeneous porous media to design processes or make decisions regarding operation and control. Such simulations require suitable mathematical models that relate various fluid states as well as various

inhomogeneous porous media properties that may be defined within the models. Also, the imaging methods and interpretations of image data are often complicated due to the effects that the solid matrix has on the fluid.

2. MATHEMATICAL MODELLING

The differential equation for plane-radial flow of the compressible fluids through inhomogeneous porous media could be expressed as [1]:

$$\frac{1}{r} \frac{\partial}{\partial r} \left(kr \frac{\partial \rho}{\partial r} \right) = \beta_l \cdot \mu \cdot m \frac{\partial \rho}{\partial t} \quad (1)$$

where: k - permeability, μ - viscosity; ρ - specific mass; m - porosity and β_l - compressibility coefficient.

If we consider next substitution:

$$F = \sqrt{k} \cdot \rho \quad (2)$$

equation (1) could be written as:

$$\frac{k}{r} \frac{\partial}{\partial r} \left(r \frac{\partial F}{\partial r} \right) + \frac{1}{2} \left[\frac{1}{2k} \left(\frac{dk}{dr} \right)^2 - \frac{1}{r} \frac{d}{dr} \left(r \frac{dk}{dr} \right) \right] F = \beta_l \cdot \mu \cdot m \frac{\partial F}{\partial t} \quad (3)$$

Because function $k(r)$ is known, it is introduced next notation:

$$K(r) = \frac{1}{2} \left[\frac{1}{2k} \left(\frac{dk}{dr} \right)^2 - \frac{1}{r} \frac{d}{dr} \left(r \frac{dk}{dr} \right) \right] \quad (4)$$

and with next substitution for function F :

$$F = R \cdot e^{\frac{K}{\beta_l \cdot \mu \cdot m} t} \quad (5)$$

equation (3) can be written as:

$$\frac{k}{r} \frac{\partial}{\partial r} \left(r \frac{\partial R}{\partial r} \right) = \beta_l \cdot \mu \cdot m \frac{\partial R}{\partial t} \quad (6)$$

If we make substitutions:

$$R = \sqrt{k} \cdot e^{-\frac{K \cdot t}{\beta_l \cdot \mu \cdot m}} \cdot \rho ; h(r) = k \cdot (\beta_l \cdot \mu \cdot m)^{-1} \quad (7)$$

equation (6) is expressed as:

$$h \left(\frac{\partial^2 R}{\partial r^2} + \frac{1}{r} \frac{\partial R}{\partial r} \right) = \frac{\partial R}{\partial t} \quad (8)$$

considering next simplifying assumptions: a) permeability varies quite a bit, so that the derivative dk/dr can be neglected; b) the porosity is constant; c) the coefficient h in equation (8) is constant.

3. THE PARTICULAR APPLICATION: THE SPECIFIC MASS IS GIVEN ON BOTH BORDERS

Let's consider the case when flow is considered to be in an area between two concentric circles having radii: r_i and r_e ($r_e > r_i$) and the specific mass (as a time function) is given on both borders.

The limits conditions are expressed as:

$$r = r_i ; R = \left(\sqrt{k^{(i)}} \right) \cdot e^{-\frac{K_i \cdot t}{\beta_i \cdot \mu \cdot m_i}} \cdot \rho_i \quad (9)$$

$$r = r_e ; R = \left(\sqrt{k^{(e)}} \right) \cdot e^{-\frac{K_e \cdot t}{\beta_e \cdot \mu \cdot m_e}} \cdot \rho_e \quad (10)$$

and initial conditions are:

$$t = 0 ; R = \sqrt{k} \cdot \rho(r) \quad (11)$$

The proposed problem is solved by individual solutions: R_1, R_2, R_3 that satisfying next conditions:

$$(R_1, R_2, R_3) = \begin{cases} (1, 0, 0) & \text{for } r = r_i \\ (0, 1, 0) & \text{for } r = r_e \\ [0, 0, R_0(r)] & \text{for } t = 0 \end{cases} \quad (12)$$

and Duhamel's theorem gives us next expression:

$$R = R_3(r, t) + \int_0^t \left[R_i(\lambda) \frac{\partial}{\partial t} R_1(r, t - \lambda) + R_e(\lambda) \frac{\partial}{\partial t} R_2(r, t - \lambda) \right] d\lambda \quad (13)$$

It can be observed that equation (8) admits elementary solution $C \cdot \ln r$, where C is a constant.

Further, we use the method of variables separation, considering the separation constant α_n^2 and the general solution is expressed as:

$$\left[A J_0(\alpha_n r) + B Y_0(\alpha_n r) \right] \cdot e^{-\alpha_n^2 h t} \quad (14)$$

If we introduce the function $U_0(\alpha_n r)$, expressed as:

$$U_0(\alpha_n r) = Y_0(\alpha_n r_e) J_0(\alpha_n r) - J_0(\alpha_n r_e) Y_0(\alpha_n r) \quad (15)$$

that is null for $r = r_e$ and the values α_n are considered to be roots of next equation:

$$U_0(\alpha_n r_i) = 0 \quad (16)$$

The solutions are:

$$R_1 = \left(\ln \frac{r}{r_e} \right) \left(\ln \frac{r_i}{r_e} \right)^{-1} + \sum_{n=1}^{\infty} A_n \cdot U_0(\alpha_n r) \cdot e^{-\alpha_n^2 h t} \quad (17)$$

$$R_2 = -\left(\ln \frac{r}{r_i}\right) \left(\ln \frac{r_i}{r_e}\right)^{-1} + \sum_{n=1}^{\infty} B_n \cdot U_0(\alpha_n r) \cdot e^{-\alpha_n^2 ht} \quad (18)$$

$$R_3 = \sum_{n=1}^{\infty} C_n \cdot U_0(\alpha_n r) \cdot e^{-\alpha_n^2 ht} \quad (19)$$

that satisfy the limits conditions (12), independent of constant values A_n , B_n and C_n - these ones being determined in order to respect the initial conditions.

Based on these assumptions are obtained next relations:

$$\sum_{n=1}^{\infty} A_n \cdot U_0(\alpha_n r) = -\left(\ln \frac{r}{r_e}\right) \left(\ln \frac{r_i}{r_e}\right)^{-1} \quad (20)$$

$$\sum_{n=1}^{\infty} B_n \cdot U_0(\alpha_n r) = \left(\ln \frac{r}{r_i}\right) \left(\ln \frac{r_i}{r_e}\right)^{-1} \quad (21)$$

$$\sum_{n=1}^{\infty} C_n \cdot U_0(\alpha_n r) = R_0(r) \quad (22)$$

To determine the coefficients A_n , B_n and C_n we use the Fourier-Bessel function. $U_0(\alpha_j r)$ is a solution of Bessel's equation.

After some calculations are obtained next relations:

$$rU_0(\alpha_j r) = -\frac{1}{\alpha_j^2} \frac{d}{dr} \left[r \frac{dU_0(\alpha_j r)}{dr} \right] \quad (23)$$

$$\frac{dU_0(\alpha_n r)}{dr} = -\alpha_n Y_0(\alpha_n r_e) J_1(\alpha_n r) + \alpha_n J_0(\alpha_n r_e) Y_1(\alpha_n r) \quad (24)$$

$$U_0'(\alpha_n r_e) = -\frac{2}{\pi \cdot r_e} \quad (25)$$

$$Y_0(\alpha_n r_e) J_0(\alpha_n r_i) = J_0(\alpha_n r_e) Y_0(\alpha_n r_i) \quad (26)$$

$$\frac{dU_0(\alpha_n r)}{dr} = \alpha_n \frac{J_0(\alpha_n r_e)}{J_0(\alpha_n r_i)} \left[J_0(\alpha_n r_i) Y_1(\alpha_n r) - Y_0(\alpha_n r_i) J_1(\alpha_n r) \right] \quad (27)$$

$$U_0'(\alpha_n r_i) = -\frac{2}{\pi \cdot r_i} \frac{J_0(\alpha_n r_e)}{J_0(\alpha_n r_i)} \quad (28)$$

The constants expressions are:

$$A_n = \pi \frac{J_0(\alpha_n r_e) J_0(\alpha_n r_i)}{J_0^2(\alpha_n r_i) - J_0^2(\alpha_n r_e)} \quad (29)$$

$$B_n = -\pi \frac{J_0^2(\alpha_n r_i)}{J_0^2(\alpha_n r_i) - J_0^2(\alpha_n r_e)} \quad (30)$$

$$C_n = \frac{\pi^2 \alpha_n^2}{2} \frac{J_0^2(\alpha_n r_i)}{J_0^2(\alpha_n r_i) - J_0^2(\alpha_n r_e)} \left[\int_{r_i}^{r_e} r \cdot U_0(\alpha_n r) R_0(r) dr \right] \quad (31)$$

So, the particular solutions are expressed as:

$$R_1 = \left(\ln \frac{r}{r_e} \right) \left(\ln \frac{r_i}{r_e} \right)^{-1} + \pi \sum_{n=1}^{\infty} \frac{J_0(\alpha_n r_e) J_0(\alpha_n r_i) \cdot U_0(\alpha_n r)}{J_0^2(\alpha_n r_i) - J_0^2(\alpha_n r_e)} e^{-\alpha_n^2 ht} \quad (32)$$

$$R_2 = - \left(\ln \frac{r}{r_i} \right) \left(\ln \frac{r_i}{r_e} \right)^{-1} - \pi \sum_{n=1}^{\infty} \frac{J_0^2(\alpha_n r_i) \cdot U_0(\alpha_n r)}{J_0^2(\alpha_n r_i) - J_0^2(\alpha_n r_e)} \cdot e^{-\alpha_n^2 ht} \quad (33)$$

$$R_3 = \frac{\pi^2}{2} \sum_{n=1}^{\infty} \frac{\alpha_n^2 J_0^2(\alpha_n r_i) U_0(\alpha_n r)}{J_0^2(\alpha_n r_i) - J_0^2(\alpha_n r_e)} e^{-\alpha_n^2 ht} \int_{r_i}^{r_e} r \cdot U_0(\alpha_n r) R_0(r) dr \quad (34)$$

Therefore formula (13) can be written as:

$$R = \pi \sum_{n=1}^{\infty} \frac{\alpha_n^2 J_0(\alpha_n r_i) U_0(\alpha_n r)}{J_0^2(\alpha_n r_i) - J_0^2(\alpha_n r_e)} e^{-\alpha_n^2 ht} \left[\frac{\pi}{2} J_0(\alpha_n r_i) \cdot \int_{r_i}^{r_e} r U_0(\alpha_n r) \cdot R_0(r) dr - h J_0(\alpha_n r_e) + \int_0^t R_i(\lambda) e^{\alpha_n^2 h \lambda} d\lambda + h J_0(\alpha_n r_i) \int_0^t R_e(\lambda) e^{\alpha_n^2 h \lambda} d\lambda \right] \quad (35)$$

Based on relation (35) the specific mass can be expressed as:

$$\rho = \frac{\pi}{\sqrt{k}} \cdot e^{\frac{Kt}{\beta_i \cdot \mu \cdot m}} \cdot \sum_{n=1}^{\infty} \frac{\alpha_n^2 J_0(\alpha_n r_i) U_0(\alpha_n r)}{J_0^2(\alpha_n r_i) - J_0^2(\alpha_n r_e)} e^{-\alpha_n^2 ht} \left[\frac{\pi}{2} J_0(\alpha_n r_i) \cdot \rho_0 \cdot \int_{r_i}^{r_e} r \sqrt{k}(r) U_0(\alpha_n r) \cdot dr - h J_0(\alpha_n r_e) (\sqrt{k}^{(i)}) \int_0^t e^{\left(\alpha_n^2 h \frac{K_i}{\beta_i \cdot \mu \cdot m_i} \right) \lambda} \cdot \rho_i(\lambda) d\lambda + \right. \\ \left. + h J_0(\alpha_n r_i) (\sqrt{k}^{(e)}) \int_0^t e^{\left(\alpha_n^2 h \frac{K_e}{\beta_i \cdot \mu \cdot m_e} \right) \lambda} \cdot \rho_e(\lambda) d\lambda \right] \quad (36)$$

The mass flow that crosses in a second the lateral surface of a cylinder of height equal to unity and having basic circle radius equal to r_i is determined with relation:

$$Q_m = 2\pi k^{(i)} \cdot (\beta_l \cdot \mu)^{-1} r_i \cdot \left(r \frac{\partial \rho}{\partial r} \right)_{r=r_i} \quad (37)$$

4. CONCLUSIONS

Modelling, simulation, and visualization of plane-radial flow of the compressible fluids through inhomogeneous porous media have practical applications in the petroleum and chemical industries.

Advances in modelling and simulation of inhomogeneous porous media can help in the understanding of processes in these areas.

The proposed mathematical model of calculus is useful for the numerical procedures in problems for plane-radial flow of the compressible fluids through inhomogeneous porous media.

REFERENCES

1. T. Oroveanu, Scurgerea fluidelor prin medii poroase neomogene, Editura Academiei, București, 1963.
2. J. Bear, Dynamics of fluids in porous media, Elsevier, 1972.
3. Dullien F. A. L., Porous media: Fluid transport and pore structure, Academic Press, New York, London, 1979.
4. Selyakov V.I., Kadet V.V., Percolation Models for Transport in Porous Media with Applications to Reservoir Engineering, Kluwer Academic Publishers, 1996.
5. P. Plessis (Editor), Fluid Transport in Porous Media, Computational Mechanics Publications, UK, 1997.
6. Chen Z., Ewing R.E., Shi Z., Numerical treatment of multiphase flows in porous media, Springer Verlag, Berlin, 2000.
7. Chen Z., Ewing R., Fluid flow and transport in porous media, mathematical and numerical treatment, American Mathematical Society, 2002.
8. Chen M., Rossen W.R., Yortsos Y.C., The flow and displacement in porous media of fluids with yield stress, Chemical Engineering Science, 60:4183-4202, 2005.
9. M. Țălu, Ș. Țălu, Calculul căderilor de presiune în conducte hidraulice. Regim de curgere stabilizat și nestabilizat. Teorie, aplicații și programe computaționale, Craiova, Editura Universitaria, 2006.
10. Sochi T.M., Pore-Scale Modeling of Non-Newtonian Flow in Porous Media, PhD thesis, Imperial College London, 2007.

TYPES OF LOCOMOTION SYSTEMS

Dumitru FILIP¹, Daniela TARNIȚĂ¹

¹University of Craiova, Faculty of Mechanics

Abstract: This paper includes the study of mechanical systems related locomotion. Mechanical motor with presenting several points of contact with the ground and a high stability, mechanical motor to two points of contact with the ground the biped to the settlement system, to get guidance is still studying bipedal position.

Keywords: locomotion, mechanism.

1. INTRODUCTION

The locomotion is one of the essential attributes of any animal, if it moves, is alive. Some animals hardly do more than that, but others have exploited the mechanisms to achieve performance locomotion phenomenal speed, agility, strength and gracious efficiency.

The locomotion mechanical systems can be classified in bipedal systems (encountered at humans) and systems with a great number of contact points (the case of insects), the difference between the two categories is, apart from the contact criteria, the stability criteria.

2. THE LOCOMOTOR MECHANISMS

In addition to the stability, the walking model must take into account the following properties:

- Ground reaction force over the is the always positive;
- Foot there is no slippage;
- Foot does not slide on the ground;
- Bipedal not upside down,
- Couples needed to support the motion falls within limits.

Most of the studies in this area have been focused on the design and control strategies for bipedal walking a steady including force, impedance control, torque control. Specialists have used balance and core stability movements to enlarge locomotion flesh of the robot. The gait is generated using the criterion of cost optimization and energy consumption. The movement is also caused by foot trajectory planning and the balance developed controllers for systems running stable planar biped. But none of these studies have addressed the problem of

generation analytic step, perhaps because of the complexity of human body from the kinematics and dynamics point of view.

3. TYPES OF MECHANISMS LOCOMOTOR

3.1. INSECT-INSPIRED, ACTIVELY COMPLIANT ROBOTIC HEXAPOD [1].

The robot shown in Figure 1. contains six points of contact with the soil and exhibits a high stability, even on rough terrain.

Should not be overlooked that the actuator 32 fails to reach a high point of freedom. Six feet notify the sensors located in contact with the ground and force distributed on each foot.

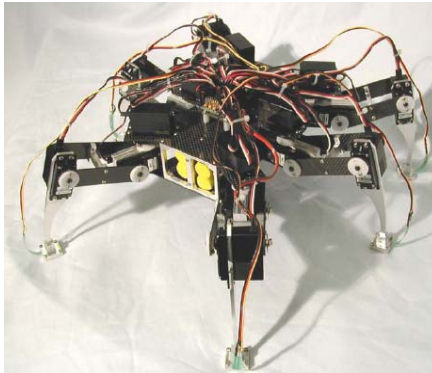


Fig. 1. BILL-Ant-p robot (without the neck, head, and mandibles)

The work shown in Figure 2. association with an insect robot aim pursued and during brain mechanism.

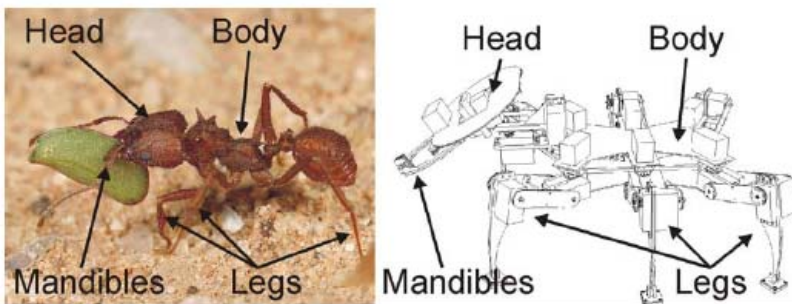


Fig. 2. The association between insects and a robot

Ultimately, it is the goal of this research is to develop a robot that is power and control autonomous; capable of navigating uneven terrain, manipulating objects within the environment, working together cooperatively, and employment of compliance with the environment and

other robots; very strong for its size; and is relatively inexpensive compared to other similar robots.

3.2. DIFFERENTIALLY FLAT BIPED ROBOTS [4].

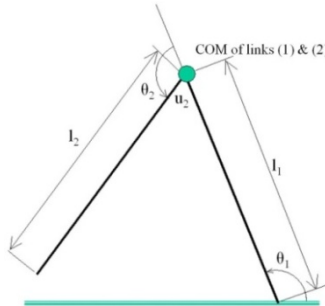


Fig. 3. Single DOF Biped. Hip joint is actuated and contact with ground is revolute and passive. Center of Mass of both the legs is at hip joint.

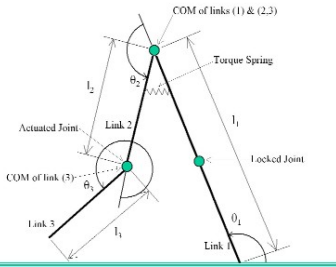


Fig. 4. DOF Biped. Hip and Knee joints are actuated and contact with ground is passive. COM of the shanks is at the knee joint and combined com of shank and thigh is at the knee joint.

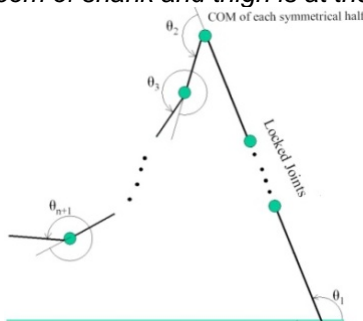


Fig. 5. A general bipedal structure with more than two segments in each limb. It follows the same recursive mass distribution as the previous two robots.

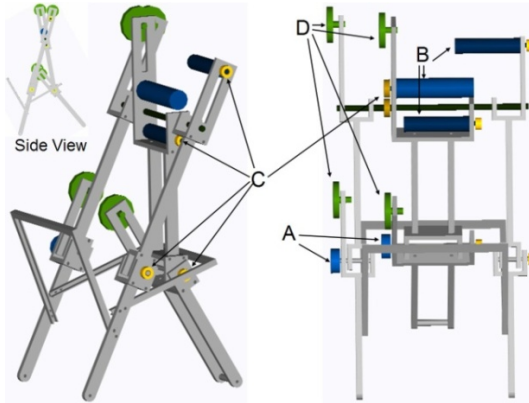


Fig. 6. Biped robots.

The knee joint has a stopper to avoid hyper-extension and there are latches (A) that lock the knee joint after the knee impact. Maxon motors (B) are placed at the hip and they drive the corresponding axis via a pulley (C) and belt arrangement. Counterweights (D) are used to place the center of mass at the respective joints. It is difficult to place encoders at the revolute ground contacts. To measure the inclination of the shank FAS-G, the inertial measurement unit from MicroStrain it is used.

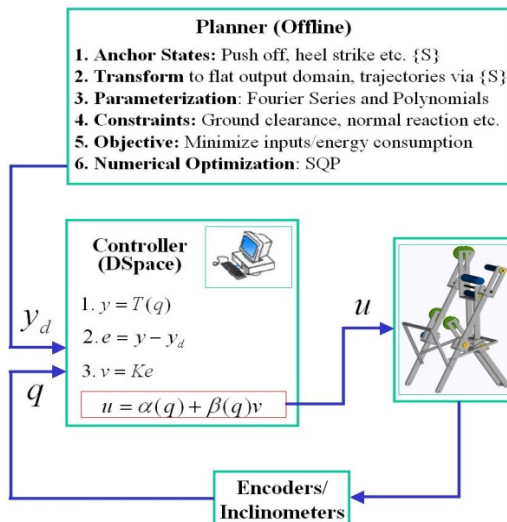


Fig. 7. Operating diagram.

3.3. WALKING CHAIR AS A WELFARE ROBOT [3].

The walking chair is a self-contained vehicle with legs that enables a person who cannot walk by himself / herself to move freely on the terrain in our life space such as horizontal planes, slopes and stairs with unevenness such as minute steps and undulations. For such a purpose of the walking chair, its mechanism and control algorithm should be constructed with consideration of simplicity, reliability, compactness and lightness. The authors have been studying about mechanisms and control of the walking chair as a welfare robot for more than fifteen years. The study was focused on the synthesis and control of the leg mechanism from the point of view of kinematics and statics, and their effectiveness was confirmed through experiments by means of some prototype walking chairs. After that, in order to realize a lightweight practical walking chair, we have been involved in the design of the leg through dynamics simulations, development of lightweight machine elements (a brake driven by a PZT actuator), design and manufacturing of the leg parts for lightening, and mechanism and control of power assisting system.

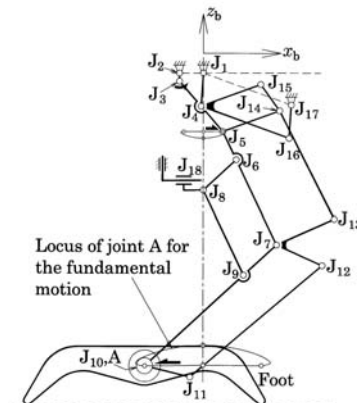


Fig. 8. Robot kinematics.

The composition of the synthesized leg mechanism of the walking chair is shown in Figure.8. Type and dimensional syntheses of the leg mechanism and design of the fundamental control system have been carried out with consideration of energy efficiency, adaptability to unevenness of the terrain, geometric and static condition during walking on stairs, etc (1). A planar closed-loop four-bar approximate-straight-line mechanism (J1J2J3J4J5) generates the fundamental leg motion by driving the crank J2 at a constant speed. Therefore, small input torque

and input energy is required at the crank J2 to propel the walking chair and the walking chair can keep stable posture even when the power source is break down. Adjusting motion with two degrees of freedom that is given at the Joint J8 is combined with this motion for generating other leg motions for slopes, large steps and stairs. The feet attached to the legs can swing around the ankle and passively adapt themselves to the unevenness of the terrain. For this adaptation, quite a simple control algorithm was developed and adopted which utilizes only the state (lock/free) control of the brake installed at each ankle according to the information of the contact state between the foot and the ground. By means of this composition of the leg mechanism, the power assisting system that is composed of the human arm and an actuator driven by a battery can be constructed by equipping a power transmission device with two inputs and one output in terms of the hardware composition.

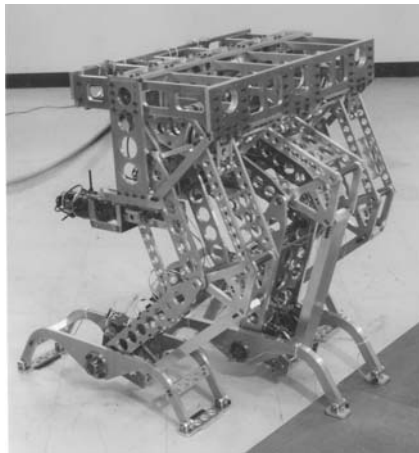


Fig. 9. Prototype.

The authors have investigated the minimum stiffness required to the leg for realizing stable walking through dynamics simulations evaluating the attitude angle of the main body, foot contact forces and driving torque of the leg mechanism. Based on the result, they designed and manufactured a prototype walking chair as shown in Figure.9. A lightweight brake driven by a PZT actuator that was originally designed and manufactured in our laboratory was installed in this prototype. The prototype weighs 88 kg and realized a stable walking at 30 steps/min (step length =300mm) on a floor with random steps whose height is 10mm while keeping the attitude angle of the main body within [-2,2] deg.

Though the prototype walking chair realized a stable walking, it was still heavy as a vehicle used in our life space. In order to lighten the walking chair, they tried to manufacture the leg parts by bending a thin sheet material, and designed and built a new prototype walking chair. The total result was a lighter (minus 37 kg) product.

3.4. BIOLOID-SERIES KONDO HUMANOID ROBOT [2].

Research has proven that they can achieve outstanding performance in the human body back to stability, control of bipedal robots. To control the robot in Figure 10. or using 18 actuators and 4 types of sensors.

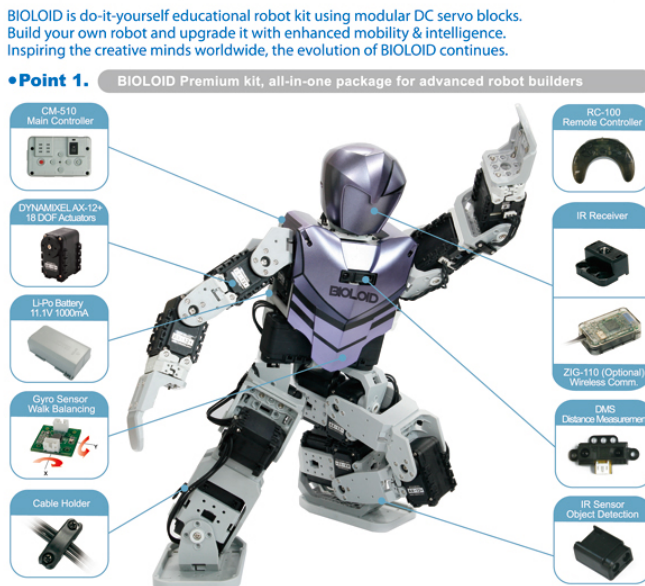


Fig. 10. Bioloid.

Oddly enough, the name has a lower version number than the previous version of the Bioloid series robot, the KHR-2HV. That aside, this new version sports 19 degrees of freedom, which enables the humanoid to rotate each leg independently at the hip. Additionally, each shoulder in the KHR-1HV are now equipped with KRS-4024SHV servos which are metal geared, and have greater range of rotation.

4. CONCLUSIONS

The locomotion devices had evaluate through time from the first locomotor devices in terms of mechanisms, actuation systems, control,

aesthetics, materials and overall performance. Some of the creations of the scientific community reach performances that came close to those of the human hand. Still, some of the abilities that the human possesses are unique and still untouchable.

REFERENCES

1. William, A. – Insect – inspired, Actively compliant robotic hexapod, For degree of master of science, Case Western Reserve University, 2005;
2. www.trossenrobotics.com.
3. www.jsme.or.jp/English/news03.html
4. http://mechsys4.me.udel.edu/research/biped_robots/
5. Starețu, I. – Elemente de robotică medicală și protezare, Editura Lux Libris, Brașov, 2004;
6. Starețu, I., Ionescu, M. – Modular design for two family of mechanical anthropomorphic grippers for robots, Proceedings of the International Conference Robotics'08, Brașov, Romania, Nov 13-14, 2008;
7. Jacobsen, S. C., Iversen, E. K., Knutti, D.F., Johnson, R.T., Biggers, K.B. – “Design of the Utah-MIT Dexterous Hand”, Proc. IEEE International Conference on Robotics and Automation, April 7-10, 1986;

AN OVERVIEW OF THE DESIGN AND IMPLEMENTATION OF VISUAL PROSTHESIS

Ștefan ȚĂLU¹

¹*Technical University of Cluj-Napoca, Faculty of Mechanics,
Department of Descriptive Geometry and Engineering Graphics*

Abstract: In this paper the author presents an overview on scientific researches concerning the design and implementation of human visual prosthesis.

Keywords: human visual system, visual prosthesis, retina models, visual image processing.

1. THEORETICAL CONSIDERATIONS

The impairments of profound blindness may have origins in degenerative retinal diseases or in brain injuries that affect the superior vision centers due to direct surgical intervention or to accidents.

The main causes of blindness in the world are: cataract, glaucoma, age-related macular degeneration, corneal opacity, trachoma, diabetic retinopathy, onchocerciasis, childhood blindness and others.

At the same time, as a demanding and challenging task, projects involving multidisciplinary research groups have been promoted to develop and demonstrate the importance of artificial vision systems.

The quest for developing artificial vision systems is refrained not due to technological issues, since with today's computers and electronics it is virtually possible to engineer any apparatus that the human kind can imagine [1, 2, 3].

2. BIOELECTRONIC VISION SYSTEM

The bioelectronic vision systems are supported on two main classes of visual neuroprosthesis:

a) retina neuroprosthesis are suitable when the front end of the retina is functioning properly;

b) a cortical neuroprosthesis when the retina, including the optic nerve, is not functional at all, and only the brain vision centers remain. In this case, the neuroprosthesis directly interfaces with the visual processing center in the brain, the area (V1) of the visual cortex. The components of a bioelectronic vision system supported on a complete

visual neuroprosthesis that directly interfaces with the brain are presented in Fig. 1 [1].

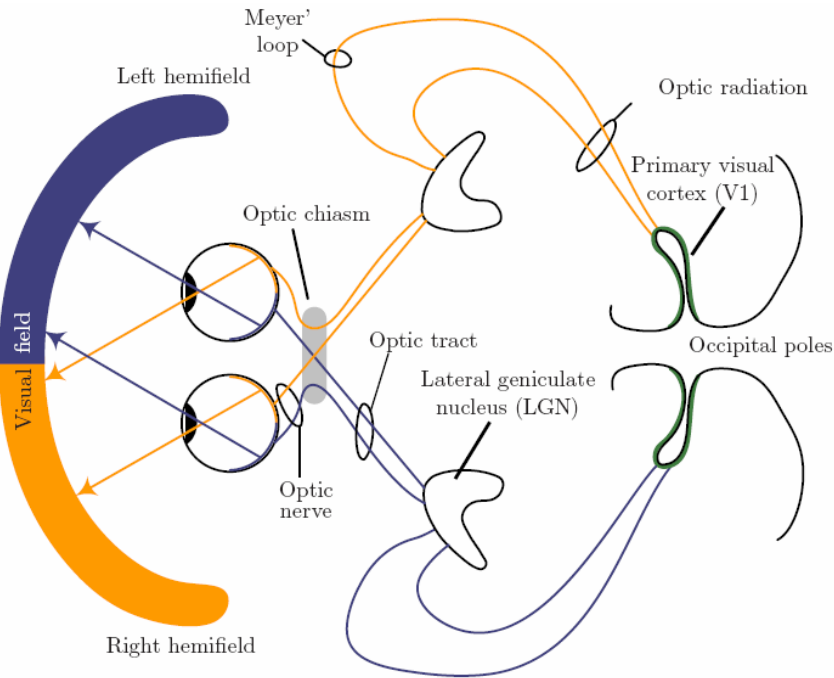


Fig. 1 - The scheme of a human visual system

A bioelectronic vision system includes a set of components which, depending on the class of visual neuroprosthesis, can be biological structures or their electronic circuit counterparts. Images in the visual field are mapped according to these models into a set of discrete signals that are then used to stimulate the visual cortex in the brain.

The digital signal processing system transforms the visual space image into a set of discrete signals, according to the retina model and taking into account the visuotopic organization of the target structure (retina or cerebral cortex).

3. RETINA MODELS

In the design of visual prosthesis is important the selection and evaluation of the adopted retina model.

Two different approaches have been proposed for these models:

a) the structural models try to mimic the biological systems based on knowledge about its physiological composition and operation;

b) the functional models attempt to replicate the functions performed by the retina but are not motivated by the characteristics of the biological systems themselves.

The most recent proposed retina models (that approximate the real neural retina response with good accuracy), belonging to distinct classes are: c) pseudo-deterministic model, where a given light stimulus produces always the same model output;

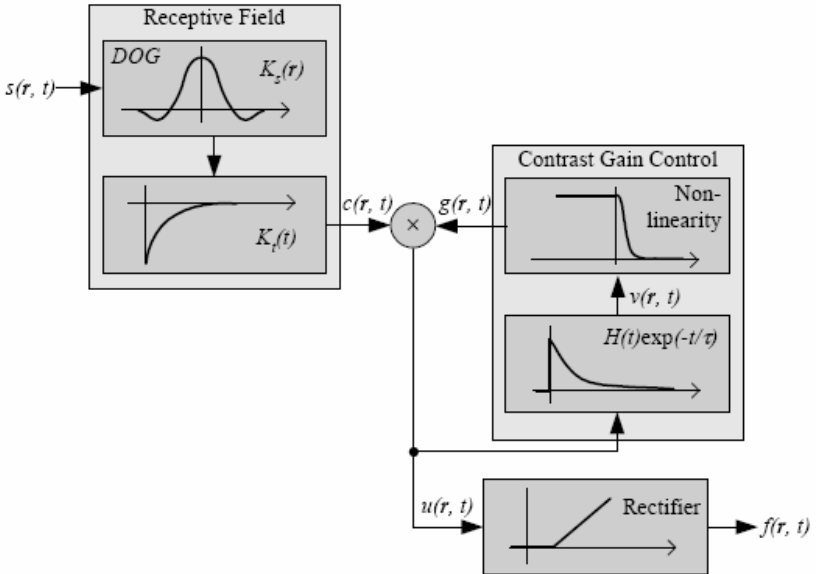


Fig. 2 - Diagram of the pseudo-deterministic retina model

d) stochastic model, where noise is introduced within the model to resemble the spike train variability.

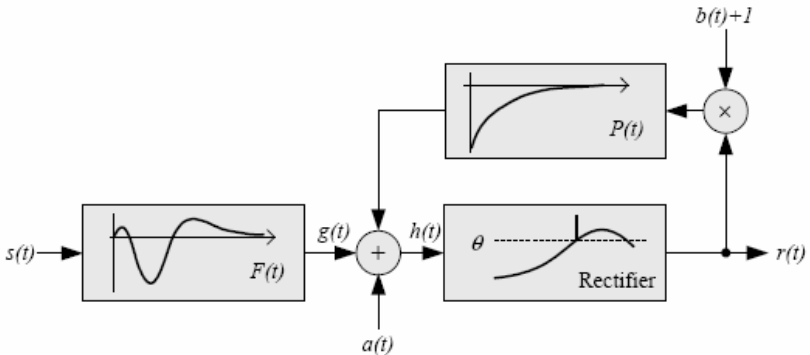


Fig. 3 - Diagram of the stochastic retina model

4. CLASSIFICATION OF VISUAL PROSTHESIS

Three types of prosthesis uses some part of the human visual system: retinal and optic nerve neuroprosthesis at the eye level, and cortical neuroprosthesis at the brain level.

a) The retinal neuroprosthesis use the remaining functioning parts of the retina to send the visual signals to the brain. Retinal neuroprosthesis require the presence of viable cells in the inner retina. There are the two kinds of retinal implants. In a subretinal implant, the prosthesis is placed between the pigment epithelial layer and the outer layer of the retina, which contains the photoreceptors cells. The epiretinal device is placed directly against the ganglion cells and their axon layer, bypassing the rods and cones, and directly stimulating the inner retina.

One of these prosthesis, named the "Bionic Eye", uses a new ceramic material to replace the retina's photoreceptors, which acts as an optic detector that transduces light into electrical impulses by means of the photoferroelectric effect. Another example of a retinal neuroprosthesis is the artificial silicon retina (ASR) microchip, which uses silicon technology. Also, there are other examples of subretinal implants.

b) the optic nerve neuroprosthesis stimulate what is left of the optic nerve;

c) the cortical neuroprosthesis inject the visual signals directly into the visual cortex. Cortical visual neuroprosthesis are bioelectronic systems that use the visual cortex in the brain as the interface between the electronics components and the biological visual pathway.

Different research projects have been conducted over the last few years to design and develop a complete visual neuroprosthesis.

5. CONCLUSIONS

Scientific research since at least the 1950s have promoted projects involving multidisciplinary research groups to design and implement the artificial vision systems.

REFERENCES

1. J. C. Martins, L. A. Sousa, Bioelectronic vision, World Scientific Publishing Co. Pte. Ltd., USA, 2009.
2. J. C. Martins, L. A. Sousa, Performance comparison of computational retina models, Proceedings of Visualization, Imaging, and Image Processing (VIIP 2005), July 9 – September 9, 2005, Benidorm, Spain.
3. K. T. Garrett, T. Kenyon, J. George, B. Travis, K. Blagoev, Models of the retina with application to the design of a visual prosthesis, Los Alamos Science 29, p. 110-123, 2005.

MODERN CONCEPTS IN THE CONSTRUCTION OF HIGH POWER ENERGY BOILERS WITH OPERATING ON COAL

Viorel TUDOR

Abstract: Coal remains a reliable energy source that can provide basic yet. Coal burning technologies and energy facility construction solutions are studied and developed so that a polluting fuel to obtain a clean electricity. Choosing a particular technology of combustion, a producer of electricity depends on a number of factors such as long-term existence of primary energy sources, can support a financial investment, the rules imposed by environmental legislation on emissions in the atmosphere, etc.

Keywords: Pulverized Coal (PC), burning coal in steam boilers overcritical parameters, Circulating Fluidized Bed (CFB), Pressurized Fluidized Bed Combustion (PFBC), Integrated Gasification Combined Cycle (IGCC).

1. INTRODUCTION

Currently coal is the primary energy source to fuel the planet as holds approx. 80% of existing fossil fuel reserves. He also is one of the key sources of electricity production in power stations.

Decade late '90's, internationally, was a period in which, due to low natural gas prices and increased efficiency gas turbine combined cycle, decreased development of new power generation capacity using coal.

Encourage the promotion and building blocks that use coal energy was sustained at the start of the new millennium, in Asia (especially India and China) because:

- uncontrollable increase in the price of natural gas;
- energy efficiency of boilers and steam turbines and
- development of advanced technologies more affordable, applicable in thermal power plants, emission in the apprehension.

Thus, only in China (using approx. 25% of coal exploited in the world), there is a strong program of implementation of thermal power

plants using coal as fuel and in parallel develop a whole-building power equipment industry.

During 2008-2014, estimated the development of new coal capacity of approx. 22 TW. It is notable to remember that in the U.S. in the last 10 years, there has been a growing interest on developing power generation capacity from coal due to continuous rise in the price of gas.

2. TECHNOLOGIES FOR CLEAN ELECTRICITY PRODUCTION FROM COAL

Clean production technologies in electricity most important international coal power plants are: burning conventional Pulverized Coal (PC), burning coal in steam boilers overcritical parameters, Circulating Fluidized Bed (CFB) Pressurized Fluidized Bed Combustion (PFBC), Integrated Gasification Combined Cycle (IGCC). Abbreviations listed in parentheses are the names abbreviated in English for the technology.

The advantages of innovative technologies for burning coal to conventional pulverized technology (PC) of coal are shown in the following table:

FEATURES	Pulverized coal combustion Classic (PC)	Burning coal in boilers with steam parameters overcritical	Burning coal in circulating fluidized layer (CFB)	Burning coal in Pressurized Fluidized Bed Combustion (PFBC)	Integrated coal gasification with steam-gas combined cycle (IGCC)
Technology Maturity	Demonstrated available commercially with guarantees	Demonstrated available commercially with guarantees	Demonstrated available commercially with guarantees	Demonstration plants using coal	In the research-development phase
Installed capacity of groups	Available commercial all levels of power including the power to 1300 MWe	Available commercial all levels of power including the power to 1300 MW	Capacities up to 460 MW	250 ÷ 300 MWe, in currently limited by high gas turbines available	Capacity proposed demonstration plant is approx. 90 MWe

Fuel flexibility	Use a wide range of fuels	Use a wide range of fuels	Use a wide range of fuels. The most suitable better for coal with high content of ash	Should use a wide range of fuels, but this has not been yet demonstrated; not suitable for inferior coal with high content of ash	Should use a wide range of fuels, designed to effective use of inferior coal with high content of ash
Net thermal efficiency of the cycle	Limited steam parameters; About 41% modern projects	Currently at least 45%, and in light of the development of performance materials, over 50%	Currently approx. 44%, but it may increase it in perspective and/or use of steam overcritical parameters	Currently approx. 43%, but possibly an efficiency of 50% with advanced gas turbines and after results of research - development	Currently approx. 43%, but possibly an efficiency of over 50% through its obtained from research - development and use of turbines advanced gas
Flexibility in operation	Low performance at low loads	Can operate at low loads but with low performance	Low performance at low loads	It can work only in the load curve	Studies suggest a satisfactory performance at low loads

Currently, the world, approx. 90% of power stations are using Pulverized Coal combustion technology (PC), approx. 10% technology in a Fluidized Bed Combustion (CFB) and a few technology in Pressurized Fluidized Bed Combustion (PFBC) and Integrated Gasification Combined Cycle (IGCC).

Technological development has enabled:

- increasing the net yield, the value of 35-37% (`70 years) to 40-41% between `90`s;
- increasing the net yield of plants with PC technology, the value of 42% (since `90`s) to 46-48% in the first 3 years of the 3`rd millennium;
- using technologies to reduce NOx emissions (by low NOx burners and catalytic installation or non-catalytic);
- using technologies to reduce SOx emissions (by installation of desulphurisation).

2.1. BURNING COAL IN BOILERS OVERCRITICAL PARAMETERS

Coordinates of the critical point are 221.2 bar and 373.2 °C (Fig. 2.3 - Section C). In this point the water turns sharply critical of the liquid vapor. Becoming "overcritical fluid" phase to a density converge

without passing through the vapor phase specific wet cycle with subcritical parameters.

The difference between these types of cycles is shown in the diagrams below TS.

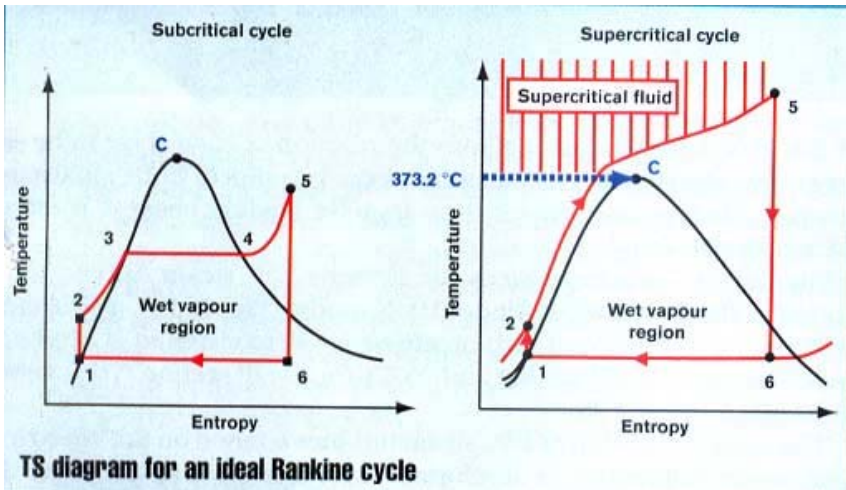


Fig. 1. TS diagram for the ideal Rankine cycle

The key difference between plants with the subcritical and overcritical parameters is given by way of boiler design.

In cycles with overcritical parameters due to the elimination phase stable vaporisation can use boilers with forced run with the package no longer separate:

- economizer;
- vaporizer;
- superheater.

The basic advantages of technology with the overcritical parameters are listed below:

- technology is tested, used and refined for a long time;
- the regime is more appropriate to use part load because:

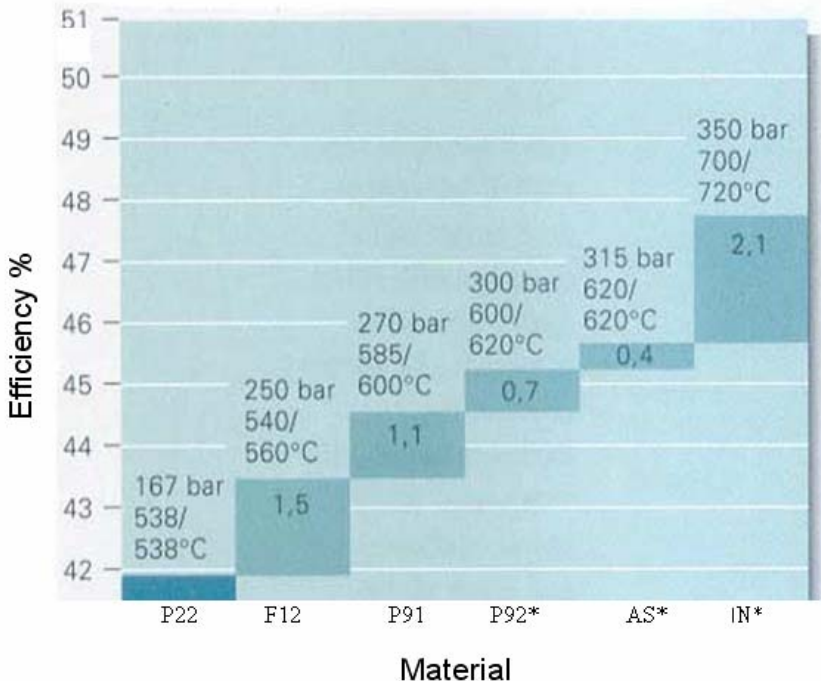
1) for a load about 50% yield decrease 6% in the case of overcritical systems to approx. 10% within the subcritical;

2) for a load about 75% yield decrease 2% in the case of overcritical systems to approx. 4% within the subcritical;

- is possible to thermal load in a very short time;
- lower fuel costs due to better thermal efficiency approx. 10% vs. subcritical cycle technology used at this time;
- reduction of pollutant emissions of particulate, NO_x, CO₂ and SO₂ due to lower amount of coal used;

The use of special materials for high temperature membrane for walls, mopping, etc.. is the main research area under the EU Thermie Program which takes into account parameters of 375 bar / 700 °C to obtain a power efficiency above 50%.

Below we present, in Figure 2.1.2, the evolution of the net yields coal with overcritical parameters and quality of materials needed in the area with high temperatures of steam.



* P92=NF616; AS= Austenitic steel; IN= inonel (Nickel Alloys)

Fig. 2. The evolution of plants with net yields parameters overcritical

Increasing energy efficiency of power stations with overcritical parameters is a major desire to promote these technologies. In this purpose have been applied some innovative concepts such as evacuation of combustion gases through the cooling tower, as shown in the diagram on the lignite power plant at Schwarze Pump, in Fig. 2.1.3.

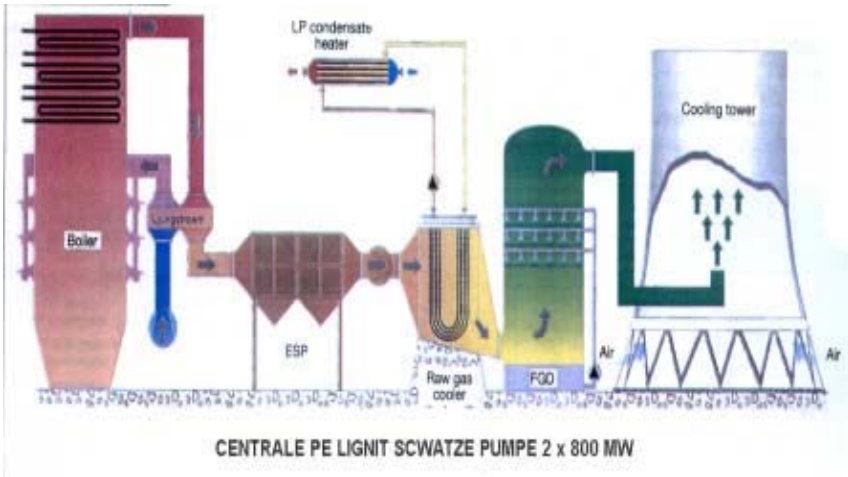


Fig. 3. Lignite Power Plant Schwartz Pumpe 2x 800 MWe

2.2. BURNING COAL IN CIRCULATING FLUIDIZED BED (CFB)

The technology of fluidized bed combustion (CFB) has distinct advantages for combustion of solid fuels and energy recovery to produce steam.

Feature process, consists of a mixture of particles suspended in an upward current of gas, leading to a fluid combination of good properties.

Combustion takes place in bed with a high heat transfer in the outbreak and low combustion temperatures.

The benefits of this process are:

- greater flexibility in burning various fuels and
- reducing emissions.

The CFB technology lists the following features:

- CFB boilers burning temperatures ($840 \div 900 \text{ }^{\circ}\text{C}$), much lower than in boilers burning pulverized ($1350 \div 1500 \text{ }^{\circ}\text{C}$), have the effect of reduced formation of NO_x and SO₂ capture possible outbreak, the injection of limestone;

- although the CFB combustion temperature is lower, while parking in the outbreak of the coal is longer than the PC so that yields two types of boilers are similar;

- experience has shown that the conditions to achieve the same effective retention of polluting emissions (SO₂, NO_x and particulate) recorded lower investment costs by approx. $8 \div 15\%$ and

- lower operating costs by approx. 5 ÷ 10% in CFB boilers than pulverized coal boilers equipped with flue gas desulphurisation plant (FGD) and catalytic treatment plant flue gases (SCR);

- CFB boilers allow a faster start than PC boilers, so cold and the hot, thereby reducing operating costs associated with fuel;

The following figure (Fig. 2.2.1) presents technological scheme of a boiler with coal in circulating fluidized bed, which is part of a 250 MW power block, Gardanne power plant, France.

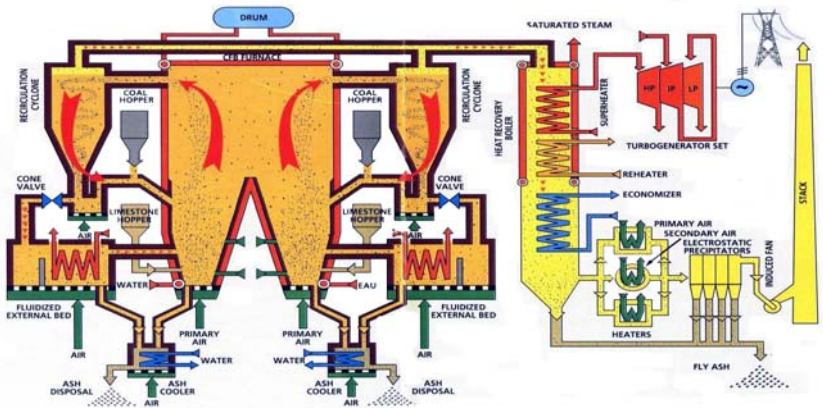


Fig. 4. Technological scheme of the boiler of 250 MW from Gardanne - France

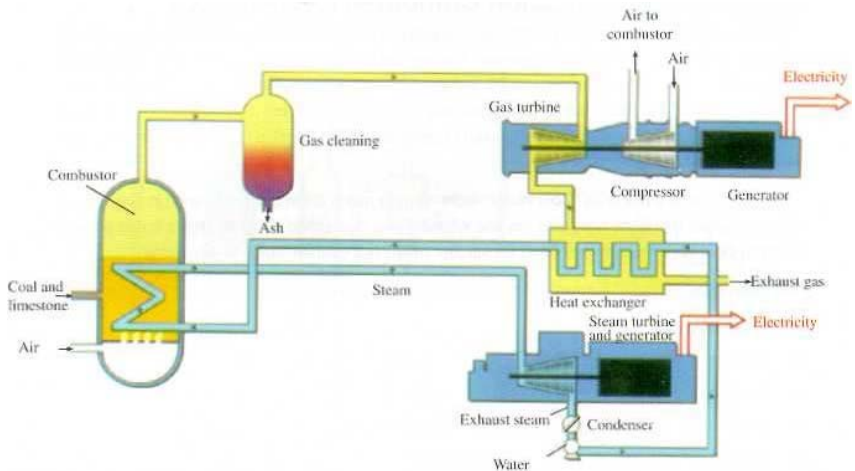


Fig. 5. The principle scheme of a PFBC power plants

2.3. BURNING COAL IN PRESSURIZED FLUIDIZED BED COMBUSTION (PFBC)

Plants using burning coal boiler technology in Pressurized Fluidized Bed Combustion (PFBC) combined cycle used to achieve greater efficiency.

Waste gases from gas turbine are used to heat water used in the generation of steam.

Figure 2.3.1 present the principle scheme for a power plant using PFBC technology.

2.4. INTEGRATED GASIFICATION COMBINED CYCLE (IGCC)

Coal IGCC technology is currently under demonstration projects varied in types of applications (in number, strength), higher than the PFBC system, but with a fairly high investment cost.

In terms of efficiency noted that IGCC technology for the gasification efficiency values of 80 ÷ 85% and combined cycle efficiency of 55 ÷ 56% to 1100 ÷ 1300 °C temperature of combustion gases from entering the gas turbine is can reach a value of overall efficiency of IGCC technology 44 ÷ 46%.

2.4.1. WORKING PRINCIPLE

IGCC technology type, at limit, can be treated as a combined cycle without post combustion, which was attached a coal gasification plant in which fuel prepare "clean" necessary for the installation of gas turbine.

Figure 2.4.1 is shown block diagram of such installations and is shown in Figure 2.4.2 scheme of principle of a power plant with IGCC.

This process occurs by partial oxidation with formation of carbon monoxide and hydrogen.

The IGCC technology lists the following features:

- gasification agents currently used are: air, oxygen, water vapor, carbon dioxide, hydrogen;
- gasification process takes place in gas-producing facility called;
- obtained is called gas-producing fuel gas (synthesis gas)
- there are a number of three types of gasification processes, which is today the commercial stage, namely:
 - a) fixed-bed;
 - b) fluidized bed and
 - c) by engagement.

Principle schemes of these types of gasification processes are shown in the Figure 2.4.3. Also, in the Figure 2.4.4. are presented the main developments in IGCC.

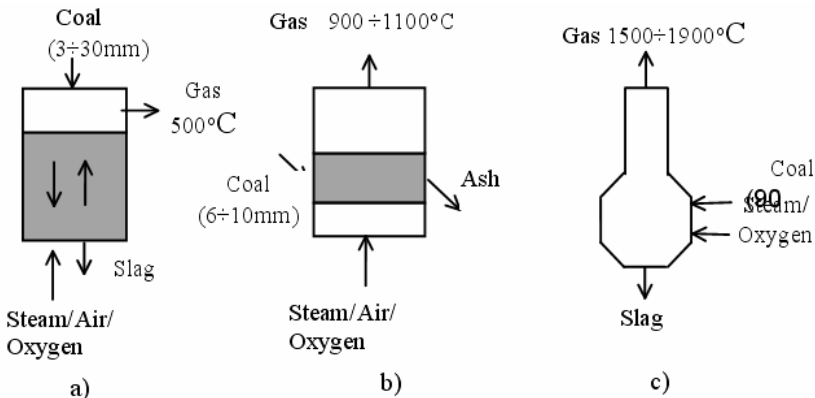


Fig. 6. Principle schemes of these types of gasification processes
 a) fixed-bed; b) fluidized bed; c) by engagement

Gasification is not a new technique, being used on relatively large scale since the interwar period.

Which brings IGCC technology is gasification plant coupling with a combined cycle gas - steam without post combustion.

Globally, at present, there are approx. 160 modern gasification facilities, medium and large (see Fig 2.4.4.) another 35 units are under development.

Of all the above facilities, ca. 20% use coal as fuel for production of electricity.

2.4.2. CONCLUSION ON IGCC

- IGCC is still in development phase demonstration. Business applications are provided to materialize after 2010.
- The current IGCC focused in particular on the use of high quality coal (except lignite).
- IGCC yield is low compared with the main competitor - the Conventional Steam Cycle (CSC) with parameters overcritical. Increased efficiency is conditional on the development of processes for cleaning high temperature gas-producing gas.
- IGCC is still characterized by low levels of availability. Increasing the availability can be obtained by reducing the level of integration of facilities, with a negative effect on yield.
- Investment costs are quite high. It is expected to decrease as they improve and standardize their IGCC components.
- Globally there is a reluctance of the central players in the team to IGCC.

It seems that, at least for the next 10 years, CSC with overcritical parameters will be first choice in the use of coal to produce electricity. IGCC can be a serious competitor for about only when the question will be central to achieving zero carbon emissions.

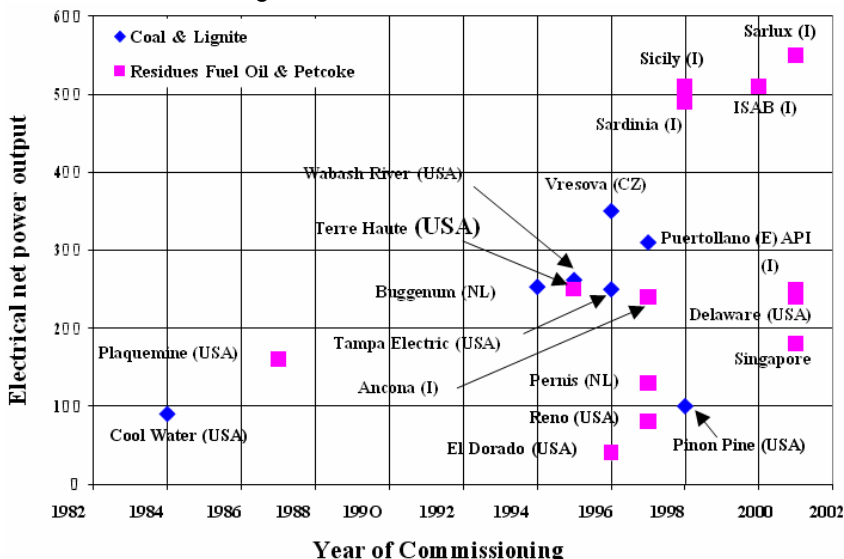


Fig. 2.4.4 Situation of IGCC Development

REFERENCES

1. „ Modern technologies for burning lignite in the context of liberalized electricity market ”, Energy Messenger, Year V1, No. 51, January 2006 — Constantin Bălășoiu, Corneliu Dițescu, Sorin Alecu, Ionel Ilie — Complexul Energetic Craiova
2. „The Advances of a Supercritical Circulating Fluidized Bed Boiler” Ragnar Lundqvist, Foster Wheeler Energia Oy — Finland, Rudolf Kral Siemens AG, PG W 731.
3. „Pulverized coal and IGCC Plant Cost and performance estimates” George Booras, Neville Holt, EPR1 - California
4. „The Implication of CFB Technology for Repowering of Old Pulverization Coal Boiler in Rusia”, G.A. Ryabov and I. Nadinov from VT1/ Moscow, 15th Conference for burning in fluidized bed, Georgia — USA
5. Technical prospectus, Gardanne, France

KINEMATICS AND DYNAMIC MODELLING OF A PLANE MANIPULATOR

Alexandru MARGINE, Gheorghe CATRINA
Ionuț GEONEA
Universitatea din Craiova, Facultatea de Mecanică

Abstract: The paper is structured in two parts. In the first part is presented the kinematics scheme of a plane manipulator and is described the mechanism functioning. In the second part is presented the kinematical and dynamical analysis for the plane manipulator mechanism. Using the Maple computer program we process the kinematics and dynamic model of the mechanism and we represent graphics of the kinematics and dynamic parameters variation laws.

Keywords: kinematics – dynamic - analyze – manipulator - modelling.

1. INTRODUCTION

The mechanism works sequentially, with a single motor element (the crank A_0A). The kinematics' scheme of the plane mechanism [2, 3, 4], with two degree of mobility, is presented in figure 1a.

The characteristics dimensions are, (in conformity with figure 1):

$$A_0G = e = 100mm; CG = l_6 = 680mm; CD = l'_6 = 380mm;$$

$$A_0A = l_1 = 220mm; AB = l_2 = 680mm; BC = l_3 = 240mm;$$

$$CF = l'_3 = 620mm; DE = l_4 = 540mm; EF = l_5 = 440mm; FH = l'_5 = 120mm.$$

The maximum rotation angle of the crank shaft 1 is:

$$\angle A_i A_0 A_f = 260^\circ.$$

We draw the kinematics' scheme, on scale, for the angle $(xA_0A_i) = \varphi_{1i}$, and the segment GCD is in vertical position, the points C and D are considered as fixed joints.

The initial position of the crank is A_0A_i when the elements 1 and 2 are in prolongation.

In the mechanism functioning we identify two phases [4]:

- The element 6 (with the points G, C and D) stays fixed until, trough the crank shaft rotation, the point B reach on the vertical part of the element 6, between the points C and G;

- All the kinematics elements of the mechanism are joining rigid, also continuing the crank shaft rotation until the end position A_0A_f , the mechanism become as a rigid body, which rotate upon the fixed joint A_0 . The trajectories of all mobile joints are circles with the centre in A_0 joint.

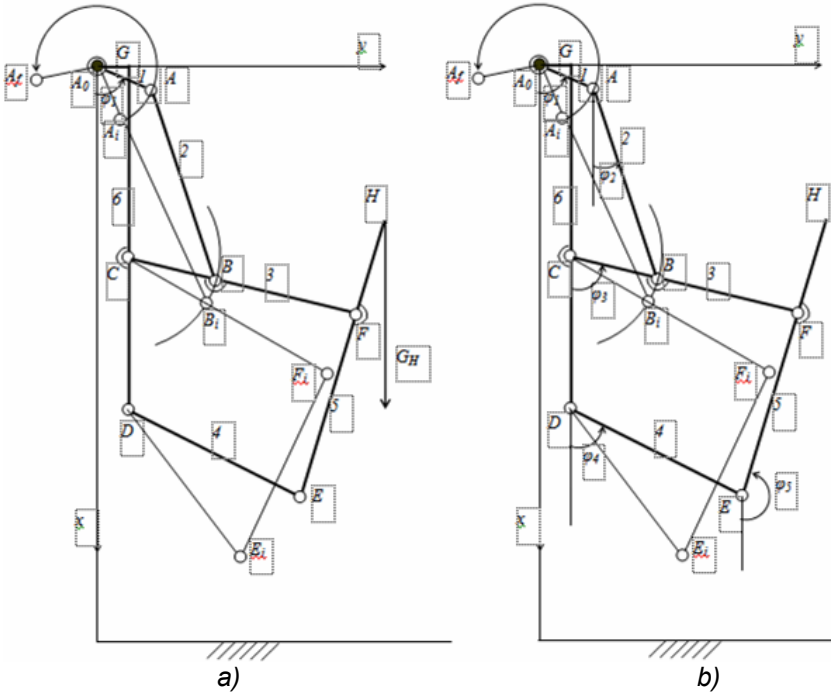


Fig. 1. The kinematics' scheme of the manipulator

2. THE KINEMATICAL ANALYSIS OF THE MANIPULATOR MECHANISM

The position of the point A^* (implicitly the angle $\angle A_i A_0 A^*$), for which the angle $\varphi_3=180^\circ$, is determined resolving the nonlinear system of scalar equations:

$$x^2 + y^2 = l_1^2; \tag{1}$$

$$(x - x_C + l_3)^2 + (y - e)^2 = l_2^2. \tag{2}$$

where: $l_1=220\text{mm}$; $l_2=680\text{mm}$; $l_3=240\text{mm}$; $x_C=CG=680\text{mm}$; $e=100\text{mm}$.

Resolving the system formed by the equations (1) and (2) we obtain the point A* coordinates, for which the angle $\varphi_3=180^0$. This are, $x= - 210,60 \text{ mm}$, $y= - 63,61 \text{ mm}$.

We consider the angular velocity of the crank shaft as being 1 rad/s. With that motion law for the motor element, we represent in figure 2, the time variation law of the angular position, in degrees, of the crank shaft.

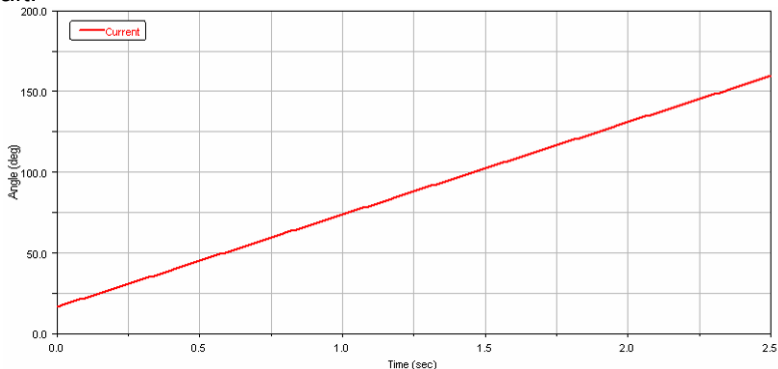


Fig. 2. Law of variation of the crank rotation angle, in degrees

The analytical calculus of the angles φ_2 and φ_3 , is made by solving the following scalar equations systems (fig. 1):

$$l_2 \cos \varphi_2 - l_3 \cos \varphi_3 = l_6 - l_1 \cos \varphi_1; \quad (3)$$

$$l_2 \sin \varphi_2 - l_3 \sin \varphi_3 = e - l_1 \sin \varphi_1. \quad (4)$$

where: $l_6=CG=680\text{mm}$; $e=100\text{mm}$.

In figures 3 and 4 we have represented the laws of variations in time for the angles φ_2 and φ_3 . We observe that the angle φ_2 starts from 16,47 degree and the angle φ_3 starts from 40 degree.

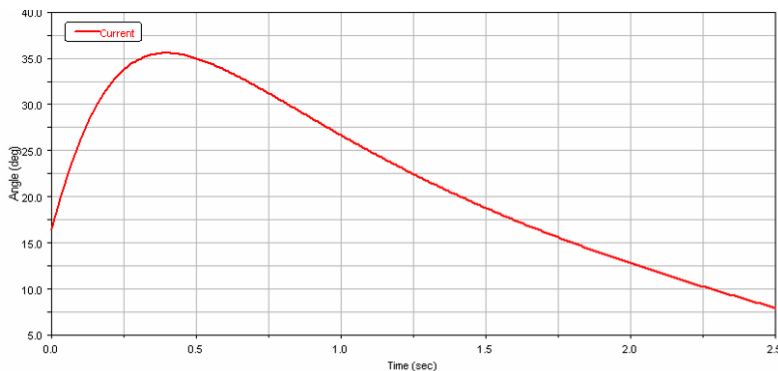


Fig. 3. Time variation law of the angle φ_2

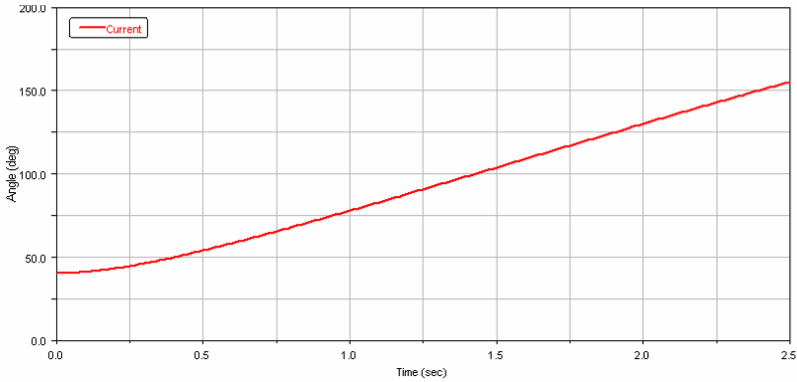


Fig. 4. Time variation law of the angle φ_3

The analytical calculus of the angles φ_4 and φ_5 (upon the angle φ_3) is made by solving the following scalar equations system (fig. 1):

$$l_4 \cos \varphi_4 + l_5 \cos \varphi_5 = l'_6 + l'_3 \cos \varphi_3; \quad (5)$$

$$l_4 \sin \varphi_4 + l_5 \sin \varphi_5 = l'_3 \sin \varphi_3. \quad (6)$$

where:

$$l'_6 = 380\text{mm}; l'_3 = 620\text{mm}; l_4 = EF = 440\text{mm}; l_5 = DE = 540\text{mm}.$$

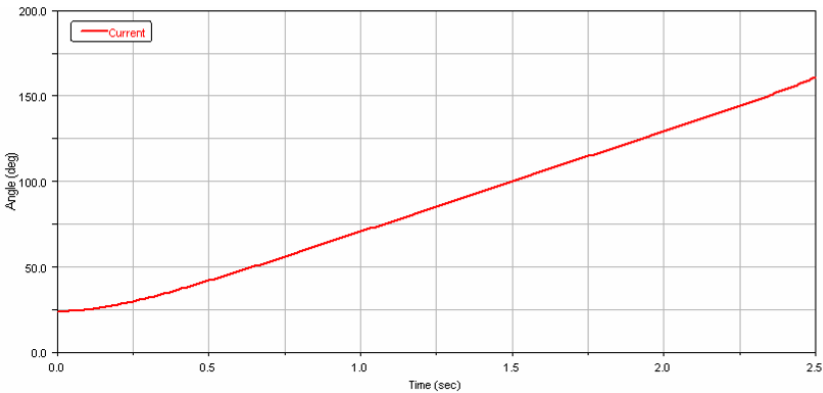


Fig. 5. Time variation law of the angle φ_4

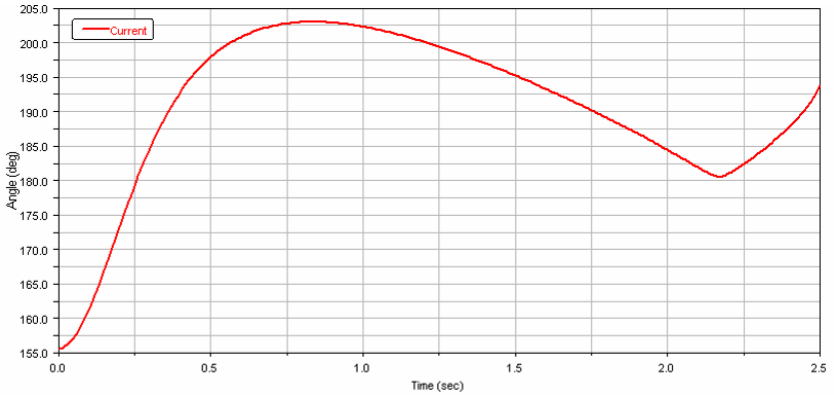


Fig. 6. Time variation law of the angle φ_5

We establish the Cartesian coordinates of the point H (figure 1), which depends by the point F coordinates and by the angle φ_5 , calculated previously [1]:

$$x_H = l_6 + l'_3 \cdot \cos \varphi_3 + l'_5 \cdot \cos \varphi_5; \quad (7)$$

$$y_H = e + l'_3 \cdot \sin \varphi_3 + l'_5 \cdot \sin \varphi_5. \quad (8)$$

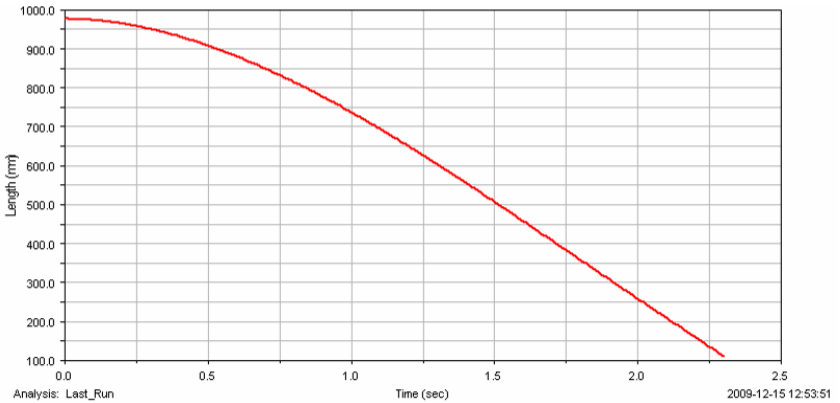


Fig. 7. Time variation of the coordinate x_H

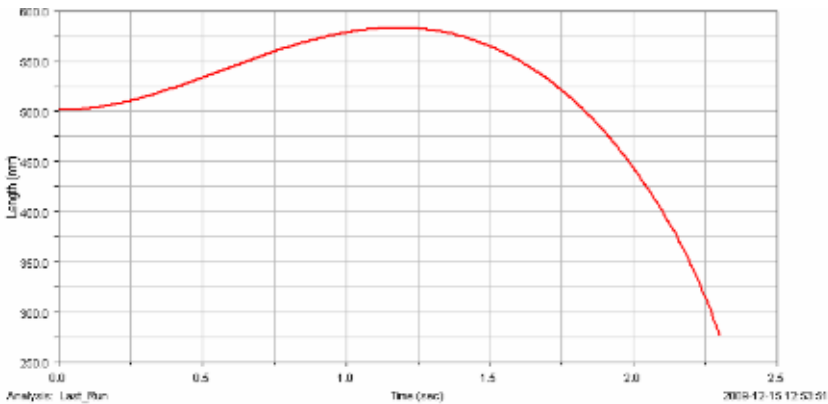


Fig. 8. Time variation of the coordinate y_H

We observe, from figure 7 and 8, that the coordinate x_H decrease from approximately 1000 mm to 100 mm, and the coordinate y_H varies from 580 mm to 275 mm. The curve described by the point H, is represented in figure 9. We also have represented, in figures 10 and 11, the components of the linear speed and acceleration of the point H.

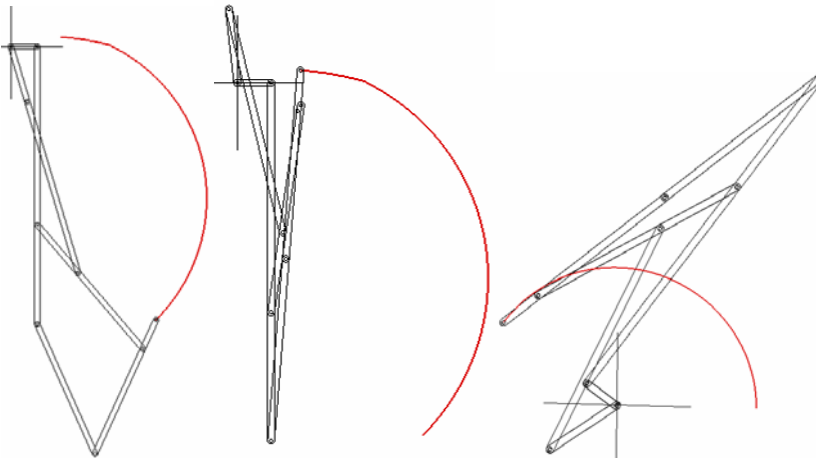


Fig. 9. The trajectory described by the point H

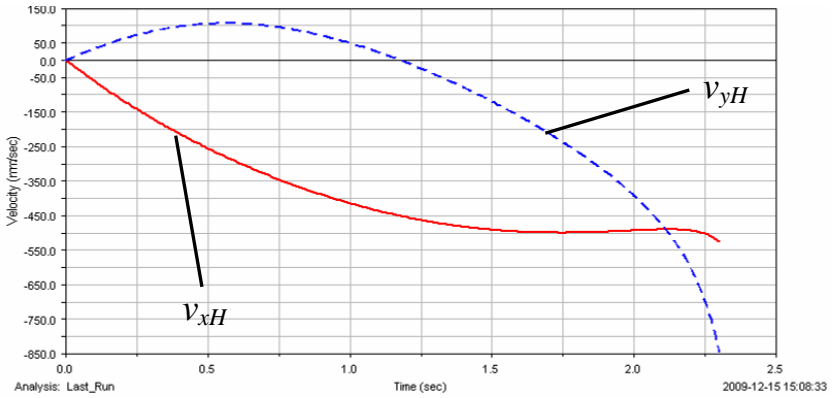


Fig. 10. The linear velocity components of the point H, in mm/s

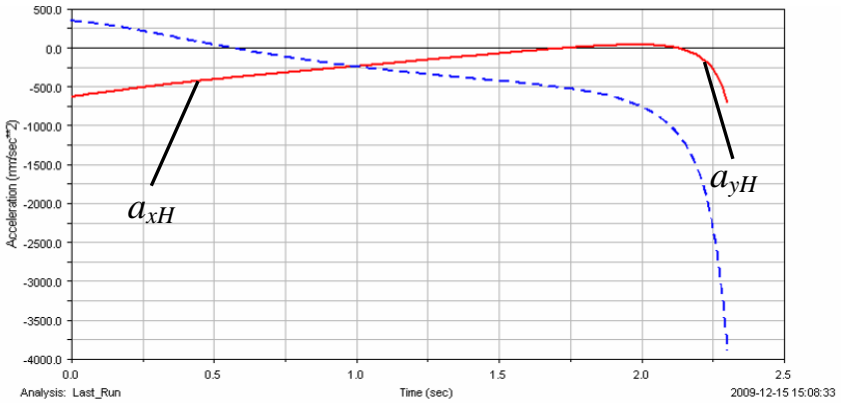


Fig. 11. The linear acceleration components of the point H, in mm/s²

The motor torque variation, $M_{m1} = M(\varphi_1)$, at the crank shaft 1, with a technological resistant force $F_r = G_H = 1000$ N (figure 1), is represented in figure 12.

The motor torque is obtained from the formula [1, 5]:

$$M_{m1} = F_r \frac{v_{xH}}{\omega_1} \quad (9)$$

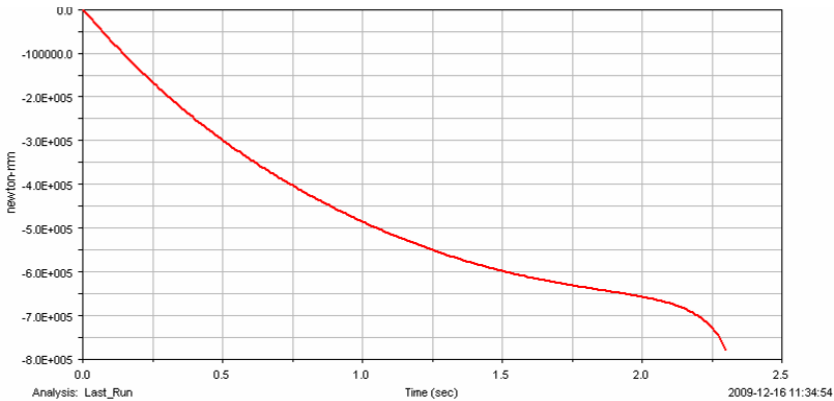


Fig. 12. The motor torque variation law, in Nmm

3. REFERENCES

1. Antonescu, P., *Mechanism and Machine Science*, Ed. Printech Bucharest, 2005.
2. Antonescu, O., Coltofeanu, R., Antonescu, P., *Geometria manipuloarelor pentru descărcarea recipientelor cu reziduuri gunoiere*, Revista Mecanisme și Manipuloare, Vol. 5, Nr. 2, p. 25-30, 2006.
3. Antonescu, O., Antonescu, P., Mihalache, D., *Geometry of lifting manipulators for green environment*, Rev. Robotica și Management, Vol., 11, Nr. 1, p. 35-40, 2006.
4. Antonescu, O., Mihalache, D., Antonescu, P., *Lifting manipulators for a green environment*, Twelfth world congress in Mechanism and Machine Science, Besancon – Franța, Poceedings vol. 3, p. 205-212, 2007.
5. Dumitru, N., Nanu, Gh., Vintilă D., *Mecanisme și transmisii mecanice - Tehnici de modelare clasice și moderne*, Editura Didactică și Pedagogică, București, 2008.

ON THE MODELS USED IN GEOMETRICAL REPRESENTATION OF HUMAN EXTRAOCULAR MUSCLES

Rajiv SHAH¹, Ștefan ȚĂLU²

¹*The University of Pittsburg, Faculty of Medicine,
Dept. of Ophthalmology, Pittsburg, Pennsylvania, USA*

²*Technical University of Cluj-Napoca, Faculty of Mechanics,
Dept. of Descriptive Geometry and Engineering Graphics*

Abstract: The objective of this paper is to present the models used in geometrical representation of human extraocular muscles. There are presented: the string model, the tape model and the Pulley model.

Keywords: human visual system, extraocular muscles models.

1. THEORETICAL CONSIDERATIONS

The human eye is suspended within the orbit by three pairs of agonist-antagonist extraocular muscles (Fig. 1) [1].

The superior rectus and inferior rectus muscles make up the first pair. They control the vertical rotations of the eye, and are attached just above and just below the periphery of the cornea respectively.

The second pair of muscles are the medial rectus and lateral rectus muscles which control the horizontal rotation of the eye. As suggested, they are attached to the medial and lateral sides of the eye respectively.

The superior oblique and inferior oblique muscles are the final pair of extraocular muscles. They are responsible for the torsional rotations of the eye. Both of these muscles are attached to the lateral side of the eye, with the superior oblique muscle coming over the top of the eye to the medial side of the orbit, and the inferior oblique muscle going under the bottom of the eye to the medial side of the orbit.

All of the rectus muscles run straight from their scleral attachment points to the posterior orbit near the optic nerve.

The obliques however have a different orientation. The angle between the plane of action and the plane of vision for the obliques is approximately 51°.

The superior oblique also runs through a pulley attached to the superior portion of the anterior orbit. This accounts for it being the longest of the extraocular muscles. All of the extraocular muscles are attached to eye, and their anchoring points at the posterior or anterior (inferior oblique only) orbit, with short lengths of tendon woven into the sclera tissue.

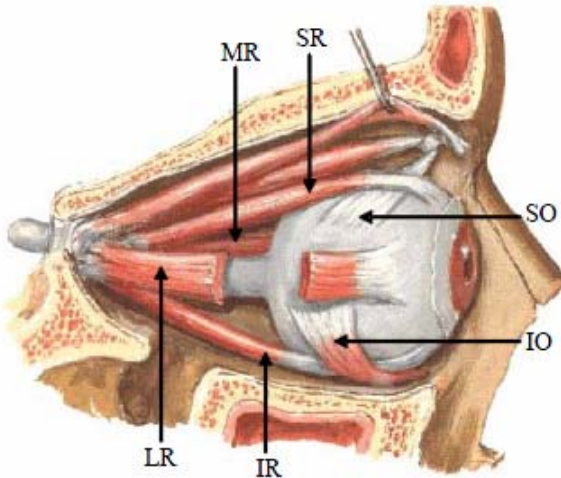


Fig. 1 - The extraocular muscles and their attachment points, shown on a right eye: (SR) superior rectus, (IR) inferior rectus, (MR) medial rectus, (LR) lateral rectus, (SO) superior oblique, and (IO) inferior oblique.

2. EXTRAOCULAR MUSCLES MODELS

In order to geometrically define the action of the extraocular muscles, specific landmark-points that describe the muscle path and the direction of pull are chosen for each muscle [2 – 6].

An extraocular muscle can geometrically be approximated by a straight line. Muscle force and deformation due to contraction or relaxation are not of primary interest in the geometrical model.

These properties are added by additional models of muscle force and dynamic visualization. The geometrical model predicts how a muscle can transfer its force into a rotation axis that affects eye position.

The requirements for a particular geometrical model of the extraocular muscles are the calculation of the following entities: the origin of each muscle, the point of tangency of each extraocular eye muscle, the insertion point, the muscle action circle, the arc of contact and the muscle rotation axis.

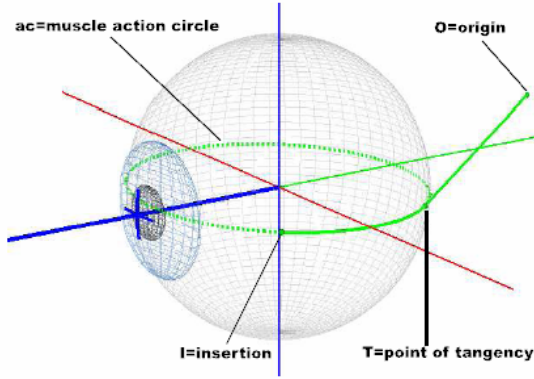


Fig. 2 - The geometrical abstraction of an eye muscle.

a) The string model

In this model the muscle strings are assumed to be always tight and therefore take the shortest possible connection between the insertion and the origin. The definition of the string model can be reduced to specifying the point of tangency as a function of gaze position.

Let \vec{I} the vector from the center of the coordinate system C to the insertion point of a muscle and \vec{I}' the vector to the insertion point in the actual eye position, such that,

$$\vec{I}' = Vect(Rot(\vec{I}, q)), \quad (1)$$

where the rotation quaternion q specifies the current eye position.

Let's note with \vec{O} the origin of an eye muscle and with \vec{R} a vector with length $r = |\vec{R}|$ that is perpendicular to the vector \vec{O} .

The angle between \vec{O} and \vec{R} is expressed as,

$$\delta = \cos^{-1}(l/r), \quad (2)$$

where l is the shortest path from origin to insertion by using,

$$l = \sqrt{|\vec{O}|^2 - |\vec{R}|^2}. \quad (3)$$

The rotation axis \overrightarrow{RM} of the muscle can be expressed as,

$$\overrightarrow{RM} = \frac{\vec{O} \times \vec{I}'}{|\vec{O} \times \vec{I}'|}. \quad (4)$$

The vector \overrightarrow{QN} , which points along the vector \overrightarrow{O} with length r is rotated around the muscle rotation axis \overrightarrow{RM} by the angle δ .

The vector \overrightarrow{QN} is expressed as:

$$\overrightarrow{QN} = \frac{\overrightarrow{O}}{|\overrightarrow{O}|} r. \quad (5)$$

Let's consider a rotation quaternion r_q by the form:

$$r_q = [\delta, (\overrightarrow{RM})]. \quad (6)$$

The vector \overrightarrow{QN} is rotated into the position of the point of tangency T by,

$$\vec{T} = Vect(Rot(\overrightarrow{QN}, r_q)), \quad (7)$$

Using string model, only in primary position, predictions for muscle path and muscle match clinical expectations.

b) The tape model

This model tries to reduce the side-slip of the muscles in secondary and tertiary positions. So, the side-slip of the point of tangency was limited with an empirical value depending on the extent of the rotation of the eye.

Let \overrightarrow{MP} a vector perpendicular to \vec{I} and \overrightarrow{O} , and \overrightarrow{TP} a tangential vector with respect to the arc of contact of the muscle such that,

$$\overrightarrow{MP} = \frac{\vec{I} \times \overrightarrow{O}}{|\vec{I} \times \overrightarrow{O}|}, \quad \overrightarrow{TP} = \frac{\overrightarrow{MP} \times \vec{I}}{|\overrightarrow{MP} \times \vec{I}|}, \quad (8)$$

These two base vectors are defined with respect to \vec{I} , the insertion point in primary position.

Let's define these two base vectors for the current gaze position, using the vector \vec{I}' from eqn. (1), as,

$$\overrightarrow{MP}' = \frac{\vec{I}' \times \overrightarrow{O}}{|\vec{I}' \times \overrightarrow{O}|}, \quad \overrightarrow{TP}' = \frac{\overrightarrow{MP}' \times \vec{I}'}{|\overrightarrow{MP}' \times \vec{I}'|}, \quad (9)$$

Let q be the quaternion that defines the current eye position; then q^{-1} is a backward rotation into the head-fixed coordinate space with,

$$\overrightarrow{MP}_h = Vect(Rot(\overrightarrow{MP}, q^{-1})), \quad \overrightarrow{TP}_h = Vect(Rot(\overrightarrow{TP}, q^{-1})), \quad (10)$$

that transform the vectors \overrightarrow{MP} and \overrightarrow{TP} into head-fixed vectors \overrightarrow{MP}_h and \overrightarrow{TP}_h respectively.

The maximum angle of deviation v_{max} of the muscle action circles between the primary position and the current gaze position with respect to the string model and is expressed as,

$$v_{max} = \text{sgn}(\overrightarrow{MP}' \cdot \overrightarrow{TP}_h) \cos^{-1}(\overrightarrow{MP}' \cdot \overrightarrow{MP}_h), \quad (11)$$

The actual deviation angle e with respect to the vector \overrightarrow{MP}_h is,

$$e = \cos^{-1}(\overrightarrow{MP}_h \cdot \vec{O}), \quad (12)$$

The reduced side-slip angle v is expressed as,

$$v = v_{max} |\cos(e)|, \quad (13)$$

Let's consider a rotation quaternion q_t by the form:

$$q_t = [v, (\vec{O})], \quad (14)$$

The definition of the point of tangency TT in the tape model is,

$$\overrightarrow{TT} = \text{Vect}(\text{Rot}(\vec{T}, q_t)), \quad (15)$$

c) The Pulley model

The pulley model lets the muscle slide through a fascial pulley which is elastically coupled to the orbital wall. The pulley model adapts the axis of rotation such that the primary direction of action of the muscle is preserved with respect to the current gaze position.

Let's define three vectors $\{\overrightarrow{SX}, \overrightarrow{SY}, \overrightarrow{SZ}\}$ based on the insertion in primary position I , the pulley location P and the center of the globe C .

The orientation of the eye is defined through a rotation quaternion q ; q is used for reorienting of three vectors $\{\overrightarrow{SX}, \overrightarrow{SY}, \overrightarrow{SZ}\}$, such that,

$$\begin{aligned} \overrightarrow{TX} &= \text{Vect}(\text{Rot}(\overrightarrow{SX}, q)), \\ \overrightarrow{TY} &= \text{Vect}(\text{Rot}(\overrightarrow{SY}, q)), \\ \overrightarrow{TZ} &= \text{Vect}(\text{Rot}(\overrightarrow{SZ}, q)), \end{aligned} \quad (16)$$

The resulting vectors $\{\overrightarrow{TX}, \overrightarrow{TY}, \overrightarrow{TZ}\}$ define the three base-vectors $\{\overrightarrow{SX}, \overrightarrow{SY}, \overrightarrow{SZ}\}$, in the current eye position.

The angle γ can be expressed as,

$$\gamma = 90^\circ - \sin^{-1}(r/l), \quad (17)$$

The angle between the insertion and the point of tangency at the center of the muscle action circle is $(\beta - \gamma)$. The point of tangency t can be determined by rotating the point \vec{I}' around an axis defined through the vector \vec{N} using a rotation quaternion r_q by the form:

$$r_q = [\beta - \gamma, (\vec{N})], \quad (18)$$

The rotation quaternion r_q is used to rotate the point \vec{I}' in the muscle's direction of pull by $(\beta - \gamma)$ degrees and the resulting quaternion is assigned to the point T ,

$$\vec{T} = Vect(Rot(\vec{I}', r_q)), \quad (19)$$

3. CONCLUSIONS

The string or tape model are not exact and the predictions of these one did not compare to clinical findings. These assume that the muscle tendon is coupled tightly to the globe. Also, these models tend to define a constant axis of rotation with respect to different gaze positions.

The pulley model redirects a muscle's main direction of pull towards the functional pulley point that permits a stabilization of the muscle path in the posterior area of the orbit as well as an adaption of the muscle rotation axis with respect to the current eye position. Also, the Pulley model affects the surgery techniques.

REFERENCES

1. Leigh, R.J., Zee, D.S., The neurology of eye movements, Third Edition, New York, Oxford, 1999.
2. Fetter, M., Haslwanter, T., Misslisch, H., Tweed, D., Three-Dimensional Kinematics of Eye, Head and Limb Movements, Harwood Academic Publishers, Amsterdam, The Netherlands, 1997.
3. Moore, S.T., Haslwanter, T., Curthoys, I.S., Smith, S.T., A geometric basis for measurement of three-dimensional eye position using image processing, Vision Res., no. 36, pp. 445 – 459, 1996.
4. Martin, C., Schovanec, L., The control and mechanics of human movement systems, Progress in Systems and Control Theory, no. 25, pp. 173 - 202, 1999.
5. Tweed, D., Vilis, T., Implications of rotational kinematics for the oculomotor system in three dimensions, J Neurophysiol., no. 58, pp. 823 - 849, 1987.
6. Kuipers, J.B., Quaternions and Rotation Sequences, Princeton University Press, 1999.

RESEARCH REGARDING THE ROUGHNESS OF THE SURFACES AT STAINLESS STEEL GRINDING

MARIUS ZAMFIRACHE

University of Craiova, Faculty of Mechanics

Abstract: This paper presents the results of some experimental research regarding the roughness of the surfaces for stainless steel in the case of the grinding process.

Keywords: Stainless steel, grinding, roughness surfaces, non linear functions, analysis regression.

1.INTRODUCTION

At present in technically literature a great number of scientific works appeared. On this way, diverse law and theories was completed or others were discovered. We refer here to these discoveries related to the part processing using different classical and modern technologies; all of this can conduct to the productivity augmentation, reducing the production cost, a high quality of the products and to the improvement of the work conditions.

The quantitative and qualitative development of the industry, as an base element of an strong economy, cannot be realize without to develop the processing method in a optimum industrial environment, with an adequate cutting tools and machine tools, and, also to qualify the specialized personnel, capable to assimilate the scientific and professional knowledge according to the actual science and technique.

The common effort of the researcher and the specialists tend to the obtaining of the competitive products that can easily come in the international changes. Today, on the world market win that one witch can realize in a shortest possible time, with minimum expenses, high quality products and with reduced retail costs.

In order to apply in production, to complete and improve, to contribute at the rise of the technical and scientific level of our enterprises, and to improve and modernise the applied technologies, all of this challenges must be known by the students and the actual and futures engineers.

The important development of the aero spatial constructions program, and the implants in medical technique has determinate and finally conducted to the whole series of the new materials with a high resistance, with a very good behaviour in use and with a great compatibility with a human body, with a high resistance to the salesman, and in the same time very easy.

The researcher Ewell R. J., show that the machinability of the material is established more by the thermal properties that the hardness and microstructure. This is the main conclusion after the laborious researches in the laboratories of General Dynamics from California.

Although the heat storage was recognized long time ago as a limitative factor for the cutting of the material, this limitation was usually associated with the hardness and microstructure of the materials.

It appears that even if the rhythm in witch the material disperses this heat is independently of the structure.

Although has a strong effect on his machinability. In the research studies was included the base operations like face milling, turning, drilling, threading and perforation, and the mechanical and physical properties of the materials.

Roughness, as a characteristic factor of surface is determined by the parameters of the cutting system, the geometry of the tool, the material structure, the rigidity of the technological system

The paper presents the study of the cutting system influence upon the roughness of the processed surfaces.

2. EXPERIMENTAL DATA

The chemical characteristics of the stainless steel presented in table 1.

Table 1

Stainless steel	C %	Mn %	Si %	Ni %	Cr %	Al %	Ti %	Fe %
10TiAlCrNi320	0,07	0,8	0,4	32	20,8	0,3	0,3	remainder

In table 2 there are presented mechanical properties of the researched material.

Table 2

Stainless steel	Brinell Hardness(HB)
10TiAlCrNi320	164

The levels of the natural variants v , f , a_p , and are in geometric progression. Eighteen experiments were realized by using the special methodology of the planning of experiments.

Table 3

Symbol	Code	-1	0	+1
v (m/sec)	X1	10	14	40
f (mm/rot)	X2	8	9.7	12
a_p (mm)	X3	0.04	0.06	0.08

The measurement results are shown in table 4.

Table 4

Type	Cod levels values			10TiAlCrNi320
X_j	X1	X2	X3	
1	-1	-1	-1	1.6
2	+1	-1	-1	1.40
3	-1	+1	-1	1.8
4	+1	+1	-1	1.55
5	-1	-1	+1	1.40
6	+1	-1	+1	1.40
7	-1	+1	+1	1.7
8	+1	+1	+1	1.30
9	0	0	0	1.20
10	0	0	0	1.22
11	0	0	0	1.3
12	0	0	0	1.3

During the cutting process, there was used a cutting emulsion liquid of the PE5EP type.

In order to determine the roughness of the considered Surf Test SJ 201.

3.ANALYZING THE EXPERIMENTAL DATA

For example in the titanium alloys 10T9iAlCrNi320, the elements characterized by the R_a functions are presented regression indicators are shown in table 5.

Table 5

RESULTS OF THE REGRESSION ANALYSIS

$R^* = 0.44 < 1$ == Adequate model.

Significant coefficients

$R_0 = 46.39 > 1$ == significant variable

$R_1 = 0.3 < 1$ == non-significant variable

$R_2 = 155 > 1$ == significant variable

$R_3 = 0.181$ == non-significant variable

Using computing REGS programs, next functions non linear were determined:

$$Ra = 0.12^{0.03} f^{0.850.82} \quad (1)$$

(grinding 10T9iAlCrNi320)

4.CONCLUSIONS

By analysing the measurements, one can notice that when grinding with a pointless tool, the roughness of the processed surface is lower than in the case of ordinary tools.

In most cases, every SA-MP couple and for every Ra value the f, v, a_p parameters are significant variables, the cutting depth a_p is determined and the cutting velocity has a minimum influence ($R_2 > R_1 > R_3 > R_4$).

The influence factors over the Ra values are: the advance, the cutting velocity, the cutting depth.

REFERENCES

1. Gheorghe, M., Stancescu, C., Draganescu, F., Algorithm and computer program to determine multiple variables regression functions, B.I.P., Bucharest., p.176-189, 1985.
2. Popescu, I., Optimization of cutting proceses, Scrisul Romanesc, Craiova, 1987.
3. Strajescu E., Cutting Tools Desing, U.P. Bucharest, 1998.
4. Zamfirache, M., Machinability of titanium alloys by turning, University Publishing

USING THE EFFECT OF THERMOCOOLING AT THE SEDIMENTING OF DUST PARTICLES INSIDE THE INDUSTRIAL ELECTROFILTERS

Dumitru STĂNCIOIU

School Group Industrial Energy Turceni

Abstract: Positioning under the deposition electrodes in the industrial electro filter chambers of mini bunkers, in a horizontal position perpendicularly to the direction of gas flow and cooling them with air from an external circuit to ensure that the effect of thermo cooling is applied for the sedimentation of dust particles, is removed the retraining from the bunkers of the dust and the filtration efficiency is increased.

Keywords: dust particles, thermo cooling effect, and sedimentation.

1. GENERAL CONSIDERATIONS

It was demonstrated that by applying the method to reduce the height of the existing bunkers at the industrial electro filters, the sedimentation yield increases substantially, what made us intend to mount the mini bunkers under the collection electrodes panels in each filter chamber as in Figure No.1, positioned horizontally and perpendicular to the direction of gas flow. The mini bunkers are placed equidistant with the step $p=0.6$ m, so that two consecutive walls of two mini bunkers attached through form a pyramidal tube of transversal section of triangular shape through which, if we produce a forced movement of atmospheric air using a network powered by a fan, the phenomenon of environmental thermo cooling of the decantation environment is produced, fact that will increase the sedimentation velocities but also particles sedimentation which, under normal operating circumstances of the electro filters, would have never sediment.

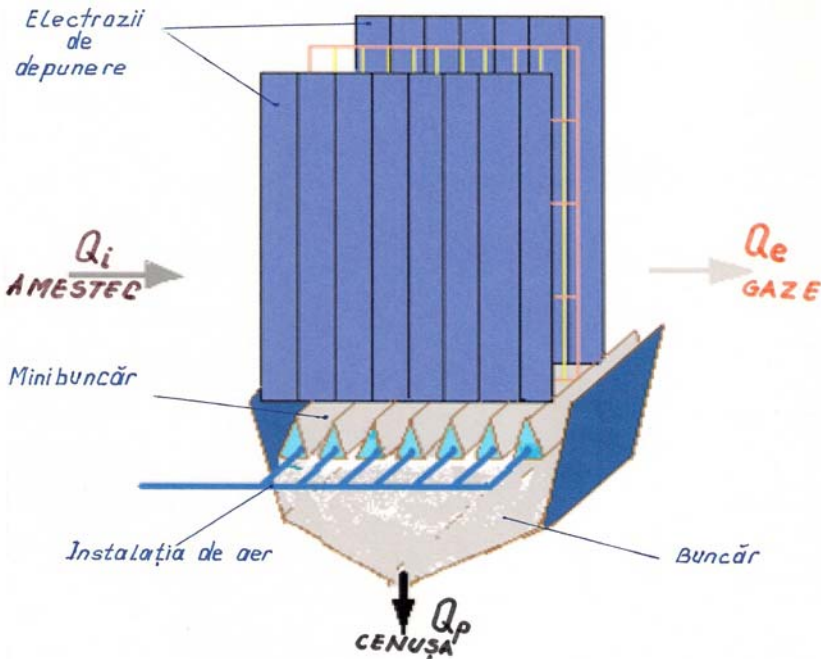


Fig.1. Positioning scheme of the sedimentation mini bunkers.

Particle separation of the two phases (gaseous and solid) will be made by transporting the solid substance by fluid, from the hot areas to cold walls of the mini bunkers, where they give a large amount of heat by free convection, the particles remain a short period on the cold surface, then, due to the high inclination of the walls of 75° , the particles will slide in the depth of the mini bunkers, creating the piston effect of large particles in the main bunker.

2. DETERMINING THE HEAT FLOW

The heat flow changed through convection is determined with Newton relation:

$$Q = \alpha \cdot S \cdot \Delta T \quad (1)$$

where: α - convection coefficient;

S - the size of the wall fluid contact surface;

ΔT - the difference of temperature between fluid and the wall.

The medium value of the convection coefficient α between the fluid and the wall is obtained with the relation:

$$\alpha = q / \Delta T \quad (2)$$

The values of the convection coefficient α are obtained according to the flow of combustion gases and the geometrical conditions with the following criteria relationship:

$$Nu = f(Re, Gr, Pr) \quad (3)$$

Determining the similarity criteria Re , Gr , Pr , the value of the Nusselt criteria is obtained, with which is obtained the medium value of the convection coefficient:

$$\alpha = Nu \frac{\lambda_f}{l} \quad [m / m^2 \cdot k] \quad (4)$$

So that the medium value of α along the surface S will be:

$$\alpha = \frac{1}{S} \int_S \alpha_x dS = C \cdot x^n \quad (5)$$

2.1 CHARACTERISTIC LENGTH OF THE CONVECTION PHENOMENA

For channels of any shape of the section, through which fluids are circulating, the characteristic length is the equivalent inside diameter:

$$d_{echiv} = \frac{4S}{P} \quad (6)$$

Where: S – mini bunker section;
 P – section perimeter.

In the case of triangular channels of isosceles triangle type:

$$d_{echiv} = \frac{2B \cdot i}{B + \sqrt{B^2 + 4i^2}} \quad (7)$$

where: S = section perimeter
 P = channel section perimeter
 B = channel base
 l = channel high

For $B = 0.45 \text{ m}$; $i = 0.9 \text{ m}$ we obtain $d_{echiv} = 0,35 \text{ m}$

2.2 FREE CONVECTION BETWEEN THE COMBUSTION GASES AND THE MINI BUNKER WALL UNDER LAMINAR (FREE) FLOW REGIME

The laminar flow happens for $10^{-5} < Gr \cdot Pr < 10^{-9}$. The element of which depends the value of the coefficient α is the equivalent diameter of the channel. For diameters equivalent for which: $10\text{mm} < d_{echiv} < 500\text{mm}$, the convection coefficient value α decreases along with the increase of the diameter, like in figure no.2,

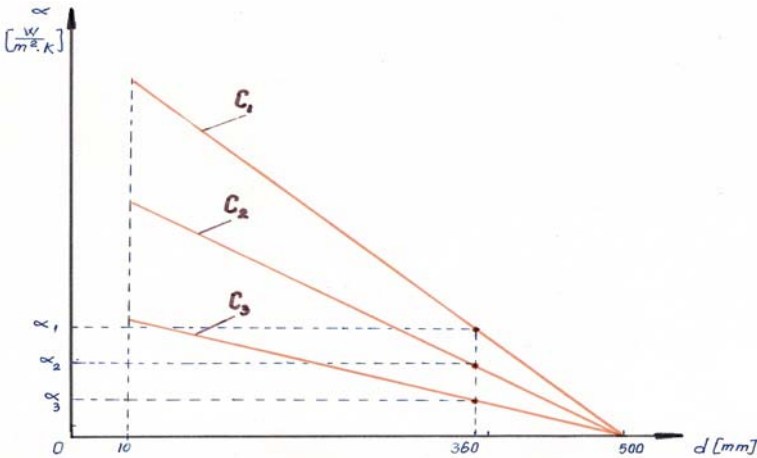


Fig. 2. The variation of the convection coefficient with the channel diameter.

the expression of the convection coefficient has the shape:

$$\alpha = \frac{Nu \cdot \lambda_f}{d_{echiv}} \quad (9)$$

The general calculus relation of the Nussle criteria is:

$$Nu = C(Pr \cdot Gr)^{0.25}$$

where: $C = 0,53$

To determine the unit vertical convection heat flow, transversal between the combustion gases mixed with ash particles and the

surface of a decantation mini bunker whose high is 0,9 m and whose perimeter of the sections: $P = 2.32 \text{ m}$

The gas temperature is of 160°C , the thermo phisic constants of the gases have the values:

- the kinematics viscosity

$$v = \frac{\eta}{\rho} = \frac{A \cdot T^n}{\rho} \quad (10)$$

where: $A = 2,49 \cdot 10^{-6}$; $n = 0,754$; a dimensional coefficients

$T_g = 433^\circ \text{K}$ – gases temperature

$T_p = 353^\circ \text{K}$ - wall temperature

$\rho = \rho(z)$; $z \in [0,2;h]$, $h = 1 \text{ m}$;

$\bar{\rho} = (\rho_i + \rho_{strat}) / 2$, medium density of the mix;

$\rho_i = 1,5 \div 5 \text{ Kg} / \text{m}^3$, the polifasic density at the bunker entrance;

$\rho_{strat} = 200 \div 1300 \text{ Kg} / \text{m}^3$, the density of the sedimentary layer.

$v_{160} = 16,4 \cdot 10^{-6} \text{ m}^2 / \text{s}$

$v_{80} = 82 \cdot 10^{-9} \text{ m}^2 / \text{s}$

- the Prandtl criteria has the following expression for gas:

$$\text{Pr} = \frac{\rho v c_p}{\lambda} \quad (11)$$

where: $c_p = 1,028 \text{ kJ/kg.k}$ - molar heat at the pressing $p = \text{ct.}$

ρ - gas density

v - gas kinematic viscosity

$\lambda = 0,034 \text{ w/m.k}$; thermal conductivity

Where we have that: $\text{Pr} = 0,71$; for temperatures of $80\text{-}160^\circ\text{C}$

- the Grashof criteria for gases at $t=160^\circ\text{C}$ will have the following relation :

$$\text{Gr} = \frac{g \cdot \beta \cdot \Delta t \cdot h^2}{v^2} \quad (12)$$

where: $h = 0,9 \text{ m}$; the height of the cooling channel.

$g = 9,81 \text{ m/s}^2$; gravity velocity

$\beta = 1 / T_g = 1/433 [1/^\circ\text{K}]$; T_g - gas temperature

Δt - difference of temperature between gases and the mini bunker wall

Replacing the given data's of the fiscal sizes, the Grashof criteria will be:

$$Gr = 1,624 \cdot 10^{-9}$$

$$\text{We will have that the product } (Gr \cdot Pr)_{gaz} = 1,153 \cdot 10^{-9}$$

Because the flow conditions are completed, in laminar regime, for which:

$$10^{-5} \triangleleft (Gr \cdot Pr)_{gaz} \triangleleft 10^9$$

We apply for calculating the Nussle criteria the following relation:

$$Nu = 0,53 \cdot (Gr \cdot Pr)^{0,125}$$

meaning: $Nu = 130$

the convection coefficient will be determined with the relation:

$$\alpha = Nu \cdot \frac{\lambda_{gaz}}{h} \quad (13)$$

It is noted that the convection coefficient is directly proportional to the Nusselt criteria and the heat conductivity of the polyphase mixture λ gas and inversely proportional to the height of the mini bunker h .

So: $\alpha = 4.911 \text{ w/m}^2 \cdot \text{K}$.

By replacing the known quantities in the relation (1) we have that $Q = 16.4 \text{ kw}$ is the permanent conductive heat flow that is carried out between the polyphase mixtures and a mini bunker walls that could be mounted in the space beneath the filing electrodes positioned perpendicular to the flow direction of gases in the industrial electro filters.

2.3 DETERMINATION OF THE HEAT QUANTITY ACCUMULATED BY THE DUST PARTICLES BEFORE SEDIMENTING

It is known that the average temperature of the polyphase mixtures of the industrial electro filters is 433°K and we want that the effect of thermo cooling produced by mounting sedimentation mini bunkers, the temperature of dust particles to drop to values of 353°K .

How the total flows of filtered particles with efficiencies exceeding 99.5 %, the entry debit $Q_i = 9.604 \text{ kg/s}$ - is distributed on the three filtering rooms bunkers successively placed on the flow direction of gas, thus' the flows collected on each room are:

$$Q_{n1} = 5,59 \text{ kg/s} ; Q_{n2} = 3,071 \text{ kg/s} ; Q_{n3} = 0,903 \text{ kg/s}$$

The heat quantity accumulated by the dust particles at 433°K that the cooling and sedimentation mini bunker give until 353°K is determined with the relation :

$$Q = m \cdot c \cdot \Delta T = m \cdot c \cdot (T_f - T_p) [\text{kJ}] \quad (14)$$

where: m - weight of the sedimenting particles; [kg]

c - specific heat of the dust particles; [kJ/kg·K]

$\Delta T = 80$; difference of temperature between which the heat transfer occurs. [°K]

Through the emplacement in the above relation of the fiscal known values we will have that:

- in the no. 1 chamber: $Q_1 = 416$ kJ

- in the no. 2 chamber: $Q_2 = 256$ kJ

- in the no. 3 chamber: $Q_3 = 74$ kJ

But as in every sedimentary room there are seven mini bunkers, we will have different amounts of heat that are transferred through mini bunkers.

It is given the condition that the heat fluxes density inside each mini bunker to be constant in the horizontal plane, at any point and in any time (t):

$$Q_s = Q / n \quad ; \text{ where } n = 7$$

So: $Q_{s1} = Q_1 / n = 59,4$ kJ

$$Q_{s2} = Q_2 / n = 36,57 \text{ kJ}$$

$$Q_{s3} = Q_3 / n = 10,54 \text{ KJ}$$

3. DETERMINATION OF THE SEDIMENTATION YIELD

Comparing the values of the flow taken through the thermo cooling effect by each mini bunker, with the initial heat quantity values in each filtering room is seen that the thermo cooling efficiency is:

$$\eta = \frac{Q}{Q_s} \cdot 100 \quad (15)$$

meaning: chamber no.1 - $\eta_1 = 27$ %

chamber no. 2 - $\eta_2 = 50$ %

chamber no.3 - $\eta_3 = 100$ %

4. CONCLUSIONS

From analyzing the yield on the three filtering rooms is found that the applied thermo cooling effect in the process of sedimentation of dust particles is particularly effective at the industrial electro filters if it will be applied as follows:

- In the chamber no. 1, the yield is only $\eta_1 = 27\%$ which is not advantageous to use the solution.

- In the chamber no. 2, the yield is 50%, we consider good to avoid large quantity of dust to be retained by the gas currents and sent to chamber no. 3

- In the chamber no. 3, the yield is maximum possible, which allows us to consider it exceptional, especially since there is still willingness to additional deposit, as follows from calculations.

- By applying this solution to accelerate the dust particles sedimentation especially in the exit chamber will substantially reduce the bunker dust particles retraining so the total yield will reach values below $25 \text{ mg} / \text{m}^3 \text{ N}$, that will reduce the emissions to half of existing particles to the electro filters operating.

- The mini bunker construction that produce sedimentation by thermo cooling are relatively simple constructions and will be connected to a cooling installation with air circulated by fans.

The costs of implementation will not be too high but the efficiency will be maximum.

REFERENCES

1. Apostolescu N., Taraza D., Experimental research bases of heat machines, Didactic and Teaching Editor, Bucharest, 1979.
2. Carabogdan ,Gh.,I. Thermo technician engineer guide .Ed.Technical 1986.
3. Florea J., Panaitescu V., Fluid mechanics, Didactic and Teaching Editor.
4. Neacsu R.M., Ciocănea A., Calculus, drafting and testing the fans, blowers and compressors pumps, Dacia Editure, Cluj-Napoca, 2000.
5. Oprean A., Tool machine hydraulic, Didactic and Teaching Editor, Bucharest.
6. Robescu N.D., s.a., Polizasic fluids , Technical Editor ,2000.
7. Robescu N.D., s.a., Molding and simulating the cleaning processes, Technical Editure, 2004.
8. Stefanescu D., ș.a., Heat transfer in techniques, Technical Editor, 1982.

MATHEMATICAL MODEL OF THE CABIN AND THE BOTTOM OF THE COATING CABIN'S HEAT CALCULUS

Lucian SEPCU¹, Mihai LUNGU², Raluca MALCIU³

¹University of Craiova, Faculty of Electrical Engineering

²University of Craiova, Faculty of Electrical Engineering

³University of Craiova, Faculty of Mechanics

Abstract: In the first part of this paper one presents the calculus methodology for air flow which passes through the "hot sewer" (m_c) and the mixture's temperature (the air introduced in the cabin). In the second part of the paper the calculus of the heat flow through the bottom of the cabin is presented.

Keywords: coating cabin, heat calculus, flight.

1. INTRODUCTION

To make the mathematical model of this subsystem one considers different values of pressure (P_s) and temperature (T_s) of the air turbine

$$\begin{aligned} p_s &= 1;1,2;1,4;...;2,8;3\text{ bar}; \\ T_s &= 273,15\text{ K}; 283,15\text{ K}; 293\text{ K}; ...; 393,15\text{ K}. \end{aligned} \quad (1)$$

2. MATHEMATICAL MODEL OF THE AIR TRANSFER SYSTEM

The circulated air flow is given by:

$$m_T = 45286 \frac{P_s}{T_s} \quad (2)$$

The cabin pressure at different levels of height

$$H = 0\text{m}, 1000\text{m}, 2000\text{m}, 3000\text{m}, 4000\text{m}, 5000\text{m}$$

is:

$$P_{cab} = \begin{cases} 101325\text{ N/m}^2; 0 \leq H \leq 2200\text{m} \\ P_{cab} = 101325 \left[1 - 22,55 \cdot 10^{-6} H \right]^{5,25} + 25100; 2200 \leq H \leq 5500\text{m} \end{cases} \quad (3)$$

T_6 (the air temperature at the exit of turbine) will be calculated next using equation

$$T_6 = T_5 \left\{ 1 - \eta_T \left[1 - \left(\frac{P_6}{P_5} \right)^{0,286} \right] \right\} \quad (4)$$

where

$$\eta_T = \begin{cases} 0,65; m_T \leq 3 \text{ kg/min}; \\ 0,70; m_T > 3 \text{ kg/min}. \end{cases} \quad (5)$$

In the below equation P_6 (the pressure from the downstream of the turbine) occurs

$$P_6 = \begin{cases} (p_{cab} + 20000) \cdot 10^{-5}; m_{c\text{lim}} = 7,75 \text{ kg/min}; \\ (p_{cab} + 30000) \cdot 10^{-5}; m_{c\text{lim}} = 10,8 \text{ kg/min}. \end{cases} \quad (6)$$

Knowing the values of T_6 , given by (4) and T_5 one can calculate the adiabatic temperature of the turbine and enthalpy drop. Adiabatic temperature is calculated by the relationship

$$\Delta T_{ad} = \frac{T_5 - T_6}{\eta_T} \quad (7)$$

and enthalpy drop with equation

$$\Delta i_{ad} = 0,24 \cdot \Delta T_{ad}. \quad (8)$$

At periphery the rotor has a peripheral speed u_T which is calculated as

$$u_T = 0,6 \cdot c_0, \quad (9)$$

where c_0 is the speed in the turbine

$$c_0 = 91,5 \sqrt{\Delta i_{ad}}. \quad (10)$$

Knowing the speed of turbo-cooler n , one can determine more peripheral speed compressor rotor c_u . The angular velocity of the compressor speed is given by equation

$$n = \frac{60 \cdot u_T}{\pi \cdot 0,076} \text{ rot/min}; \quad (11)$$

then

$$u_c = \frac{\pi \cdot 0,085 \cdot n}{60}. \quad (12)$$

For different values of T_3 (the air's temperature at the entrance of the compressor), $T_3 = 2900 \text{ K}, 3200 \text{ K}, 3500 \text{ K}, 3800 \text{ K}; 4100 \text{ K}; 4400 \text{ K}$, the compressor compression ratio value is given by the following equation

$$\pi_c = \left(1 + 0,001 \cdot \frac{l_{cad}}{T_3} \right)^{3,5}, \quad (13)$$

where l_{cad} is the work is specifically adiabatic compressor.

Specific work of compressor adiabatic value is:

$$l_{cad} = 0,55 \cdot u_c^2. \quad (14)$$

At the compressor exit the temperature T_4 is

$$T_4 = T_3 \left(1 + \frac{\pi^{0,286} - 1}{\eta_c} \right), \quad (15)$$

where $\eta_c = \eta_T$ - equation (5)

Loss of pressure in the two heat exchangers (main heat exchanger and the secondary heat exchanger) is

$$\Delta P_{sp} = \Delta P_{ss} = \frac{10600}{11} \cdot 10^{-5} \cdot m_T. \quad (16)$$

Upstream of the primary heat exchanger the pressure P_2 is

$$p_2 = p_3 + \Delta P_{sp}; \quad (17)$$

one notes that p_3 intervenes in equation (16); this parameter represents the input pressure in compressor

$$p_3 = \frac{P_4}{\pi_c} \quad (18)$$

with:

$$p_4 = p_5 + \Delta P_{ss}. \quad (19)$$

Taking into account that the air from the engine (air that goes on the "hot sewer") has temperatures in the field $375K \div 525K$ one will calculate the air temperature from the cabin as follows: first one calculates the flow of air that goes on the "hot sewer"

$$m_c = m_{c\lim} - m_T; \quad (20)$$

then the mixture temperature (blown air in the cabin) with equation

$$t_a = \frac{m_T T_6 + m_c T_c}{m_{c\lim}} - 273,15 \quad (21)$$

for different values of T_c such as $T_c = 5250K, 4750K, 4250K, 3750K$.

Cabin air temperature calculated with relation (15) represents the temperature of the environment in which the aircraft pilot lives. This temperature must not exceed $22^\circ C$; it may be manually or automatically using the temperature regulator from the cabin.

Knowing the air flow and temperature of the mixture air one desires to establish the mathematical calculation for the termical calculus of the bottom of the coating cabin.

In this situation E_{div} mustn't be calculated; only E_{dif2} must be obtained with equation

$$E_{dif2} = \begin{cases} 360 - \frac{1}{40}H; 0 \leq H \leq 4000m \\ 260 - \frac{3}{400}(H - 400); 4000 \leq H \leq 8000. \end{cases} \quad (22)$$

Knowing E_{dif2} one obtains the value of q_{rs}

$$q_{rs} = 0,98 \cdot E_{dif2}. \quad (23)$$

If one knows the values of the parameters: T_{int} – the temperature inside wall of the cab, T_{cab} – the cab's temperature, p_{cab} – the cab's pressure, p_0 – the cabin pressure ramp and R – the radius cylindrical casing one can determine the coefficient of transfer by convection of air in the cabin and the inner wall of the cab with equation

$$\alpha_{conv} = 1,7586 \cdot \frac{\sqrt{T_{pint} - T_{cab}} \cdot \sqrt{\frac{p_{cab}}{p_0}}}{\sqrt[4]{\pi R}}. \quad (24)$$

Using equality

$$q_{ext} = q_{inf} = q_{sup}, \quad (25)$$

the heat flow determined by the lower side is calculated as follows

$$Q_{inf} = A_{inf} \cdot q_{inf}, \quad (26)$$

where:

$$q_{inf} = \alpha_{inf} \cdot (T_{pint} - T_{cab}); A_{inf} = 48,818m^2, \quad (27)$$

$$\alpha_{int} = \alpha_{conv} + \alpha_{rad} \quad (28)$$

and

$$\alpha_{rad} = \frac{4,5136}{T_{pint} - T_{cab}} \cdot \left[\left(\frac{T_{pint}}{100} \right)^4 - \left(\frac{T_{cab}}{100} \right)^4 \right]. \quad (29)$$

REFERENCES

1. Tan, Chee-Fai, Chen, Wei, Rauterberg, Matthias „Design of an Aircraft Cabin Testbed for Stress-Free Air Travel Experiment”, International Conference on Planning and Design, 2009, NCKU, Tainan, Taiwan.
2. Douglas G. Macmartin „Collocated structural control for reduction of aircraft cabin noise”. Journal of Sound and Vibration (1996) 190(1), 105-119.
3. C. Müller, D. Scholz, T. Giese, „Dynamic simulation of innovative aircraft air conditioning”, CEAS – 2007 – 466.
4. “Avion de antrenament primar cu dubla utilizare – militara si civila – ALPHA” (contract de cercetare nr. 167387/2005).

A BALANCING FORCES MODEL FOR THE HUMAN EXTRAOCULAR MUSCLES

Rajiv SHAH¹, Ștefan ȚĂLU²

¹The University of Pittsburg, Faculty of Medicine,
Dept. of Ophthalmology, Pittsburg, Pennsylvania, USA

²Technical University of Cluj-Napoca, Faculty of Mechanics,
Dept. of Descriptive Geometry and Engineering Graphics

Abstract: The objective of this paper is to present a mathematical model of balancing forces for human extraocular muscles.

Keywords: human visual system, extraocular muscles models, balancing forces.

1. THEORETICAL CONSIDERATIONS

The human eye is tightly suspended within the orbita, surrounded by six extraocular muscles which are responsible for the movement of the globe. The four straight eye muscles (musculi recti) and the upper diagonal (superior oblique) eye muscle originate in the posterior part of the orbita. Only the lower diagonal (inferior oblique) muscle originates from the orbital plate of the maxilla [1].

Let's determine a geometrical model and the muscle force prediction model for all six extraocular eye muscles together with initial values for all parameters [2 – 6].

2. A MODEL OF BALANCING FORCES

Let's consider a mathematical model of a stable eye position.

The stable eye position is given, when all forces that act on the globe are in an equilibrium and it can be appreciated by a force balance equation, that derives a torque imbalance vector based on the current eye position and muscle forces.

The torque imbalance vector \vec{t} can be expressed using,

$$\vec{t} = \sum_{i=1}^6 F_{Ti} (dl_i, iv_i, e_{si}, c_{si}, t_{si}) \cdot \vec{n}_i, \quad (1)$$

where F_{Ti} denotes the total output force of a muscle i , and the vector \vec{n}_i is the unit moment vector.

A stable eye position can be expressed as the constraint,

$$|\vec{t}| \approx 0. \quad (2)$$

In the orbit besides of the torque, there are resistance from non-muscular elastic tissues that acts to restore the eye to primary position.

This resistance can be expressed using a passive moment vector $\vec{P}(P_\alpha, P_\beta, P_\gamma)$, where the components of the vector correspond to angular coordinates (α, β, γ) based on the angular coordinates of the current eye position.

In modelling the orbital restoring force, a simple nonlinear spring model was adopted.

The globe translation (the anteroposterior movement of the globe during eye movements) alters the relative position to the muscle origin and therefore also the stretch of each muscle, which in turn modifies output force and force balance. Also, when the globe translates during rotation, the center of rotation is shifted and thus, the axis of rotation is modified.

To measure globe translation, a new coordinate system is defined that describes the orbital cone through the definition of an apex point that lies midway between the origin point of the superior rectus (O_{sr}) and inferior rectus (O_{ir}) muscles.

The new apex coordinate system can then be defined by three base vectors $\{\vec{A}_x, \vec{A}_y, \vec{A}_z\}$, where the base vector \vec{A}_y represents the vector from the origin to the apex point, the vector \vec{A}_x is perpendicular to the head-fixed vertical axis and the vector \vec{A}_y and the vector \vec{A}_z is perpendicular to \vec{A}_x and \vec{A}_y .

Let's introduce the stiffness vector \vec{F}_a , that is linearly related to translation values.

The translation vector \vec{G}_{trans} can be found by first transforming the torque imbalance vector \vec{t} to the apex coordinate system, and then restrict the length of this vector using the stiffness values \vec{F}_a , which leads to,

$$\vec{G}_{trans} = \frac{Vect(Rot(\vec{t}, q_{apex}))}{2\vec{F}_a}. \quad (3)$$

The amount of globe translation gt along the axis \vec{A}_y for a given eye position can then be written as,

$$gt = \left| \vec{G}_{trans} \right|, \quad (4)$$

and the translation that affects ocular geometry can be expressed by a vector \vec{T}_{trans} , defined with respect to the head-fixed coordinate system using,

$$\vec{T}_{trans} = Vect(Rot(\vec{G}_{trans}, q_{head})). \quad (5)$$

The translation vector \vec{T}_{trans} can now reflect rotational changes. The refined torque imbalance equation can be expressed as,

$$\vec{T} = \vec{P} + \sum_{i=1}^6 F_{Ti} (dl_i, iv_i, e_{si}, c_{si}, t_{si}) \cdot G_i(\vec{trans}, \vec{ra}_i), \quad (6)$$

where the force of each eye muscle is multiplied by the unit moment vector that is determined with translated origin and pulley points (G_i), and \vec{P} is the orbital restoring force, that modifies the global rotational balance.

Each value for the torque imbalance vector \vec{T} in eqn. (6) is determined by six innervations (iv) and six length changes (dl). Each modification to the current eye position results in different length change values and thus also in a different torque imbalance vector.

Conversely, changing innervations give different force values and therefore also affect torque balance.

To rapidly control the value of \vec{T} is by defining an innervation vector \vec{I}_v and an eye position vector \vec{E}_p such that,

$$\vec{I}_v = \{iv_1, iv_2, iv_3, iv_4, iv_5, iv_6\}, \quad \vec{E}_p = \{e_x, e_y, e_z\}. \quad (7)$$

where the values $\{iv_1, iv_2, iv_3, iv_4, iv_5, iv_6\}$ contain the innervation values for each eye muscle and the values $\{e_x, e_y, e_z\}$ contains a rotation vector that describes an eye position based on a rotation quaternion by the form,

$$\vec{E}_p = \left(\frac{1}{2} \tan(\theta) \right) \cdot \vec{U}, \quad (8)$$

where the orientation vector \vec{U} is parallel to the axis of rotation and the length is given by half the tangens of the rotation angle in radians.

A stable eye position depends on the parameter vectors \vec{I}_v and \vec{E}_p where the model parameters i_x and e_x dictate the model function defined in eqn. (6).

To quantify the model parameter values in \vec{I}_v and \vec{E}_p approximate a stable eye position, eqn. (6) can be used such that the squared length L_T of the vector \vec{T} gives information about kinematic instability,

$$L_t(\vec{I}_v, \vec{E}_p) = \left| \vec{P} + \sum_{i=1}^6 F_{Ti}(dl_i, iv_i, e_{si}, c_{si}, t_{si}) \cdot G_i(\overrightarrow{Trans}, R\vec{A}_i) \right|^2 \quad (9)$$

The minimum of this function specifies the best approximation to a stable eye position. The desired objective is to minimize eqn. (9), that can be reached by finding values for \vec{I}_v and \vec{E}_p such that,

$$\min L_t(\vec{I}_v, \vec{E}_p). \quad (10)$$

3. CONCLUSIONS

The structure of the mathematical formulation guarantees that all components of the biomechanical model can independently be exchanged by other models without invalidating the model itself.

It is desirable to use a stable minimization approach in order to offer flexibility with respect to the proposed mathematical model.

REFERENCES

1. Leigh, R.J., Zee, D.S., The neurology of eye movements, Third Edition, New York, Oxford, 1999.
2. Fetter, M., Haslwanter, T., Misslisch, H., Tweed, D., Three-Dimensional Kinematics of Eye, Head and Limb Movements, Harwood Academic Publishers, Amsterdam, The Netherlands, 1997.
3. Moore, S.T., Haslwanter, T., Curthoys, I.S., Smith, S.T., A geometric basis for measurement of three-dimensional eye position using image processing, Vision Res., no. 36, pp. 445 – 459, 1996.
4. Martin, C., Schovanec, L., The control and mechanics of human movement systems, Progress in Systems and Control Theory, no. 25, pp. 173 - 202, 1999.
5. Tweed, D., Vilis, T., Implications of rotational kinematics for the oculomotor system in three dimensions, J Neurophysiol., no. 58, pp. 823 - 849, 1987.
6. Kuipers, J.B., Quaternions and Rotation Sequences, Princeton University Press, 1999.

THE STUDY OF THE PHYSIC PROCESSES OF SEPARATING THE FASES OF THE COMBUSTION GAS MIX – DUST PARTICLES IN SUSPENSION THROUGH SEDIMENTATION

Ioan AȘTEFANEI¹, Dumitru STĂNCIOIU²,

¹University of Craiova, Faculty of Mechanical Engineering

²School Group Industrial Energy Turceni

Abstract: The sedimentation process of dust particles from the combustion gases, which is carried out in the industrial electro filters is dependent on both the dynamics of gas flow in the filtration chambers and on the electric field intensity where the particles are sedimenting.

The increase of the filtration efficiency is proved that it is possible by reducing the height of sedimentation bunkers, reason for which is proposed to mount mini bunkers at the top side of the industrial electro filter bunkers that are running.

Keywords: Dust particles, sedimentation velocity, depth of the bunker; mini bunkers.

1. GENERAL CONSIDERATIONS

Separating through sedimentation of the dust particles in suspension in the combustion gases, resulted by evacuation from power boilers, furnaces or cement ovens is an essential process in ensuring the quality of the environment. In consequence, without an efficient sedimentation, so with maximum efficiency, the unreserved particles in the industrial electro filters will be discharged into the air along with the gases through the smoke furnaces. That is why is equally important to study the phenomenon of sedimentation as well as the phenomenon of collecting on the surface of filing electrodes.

The natural separation that takes place in the environment is of gravity type, also called sedimentation and decanting. In the industrial electro filters, the sedimentation phenomena are conducted almost

identical but with minor differences due to the existence of high temperatures and of some electrostatic fields created by each particle of dust in sedimentation, but which is charged partially electrostatic, because this in the collection process at the filing electrode doesn't give all the energy accumulated on its surface.

So the particles react with each other due to the electrostatic interaction forces whose resultant:

$$\vec{F}_e = \frac{q_0}{4\pi\epsilon_0} \sum_{i=1}^n \frac{q_i}{r_i^2} \vec{e}_{r_i} = \sum_{i=1}^n \vec{F}_i \quad (1)$$

Where: q_0 - load of the particle

q_i - load of the neighbor particles in the field

Or scalar:

$$F_e = q_o \cdot E \quad (2)$$

Where E - intensity of the electric field

F_e - electrostatic force that reduces the sedimentation effect by opposing with the Archimedes force and the dynamic pressure forces.

Sedimenting equation is:

$$\vec{G} + \vec{F}_i - \vec{F}_a - \vec{F}_{pd} - \vec{F}_e = 0 \quad (3)$$

2. GRAVITATIONAL SEDIMENTATION

The process ensures the reducing of the dust particles concentration from gases that are deposited by gravity in proportion of 50-70%. For the industrial electro filter, the sedimentation occurs continuously in all the filtration chambers, but the supply of particle process differs in the three chambers:

- In the first chamber the power is permanent and is due to the permanent shaking of the depositing electrodes;

- In the chamber no. 2 the shaking happens at 10-15 minutes interval;

- In the chamber no. 2 the shaking happens at 25-35 minutes.

The sedimentation time varies depending on the shape, size and density of the particle, of the temperature and pressure of the gas inside the electro filters and can be between 1 and 3 hours.

2.1. THEORY BASES OF THE SEDIMENTATION PROCESS

The sedimentation is characterized by the base-speed of sedimentation parameter, which is maximum at the entry in the bunker (upper side) and zero in sedimentary bed. Therefore, the space in the bunker can be split fictively into four areas of concentrations where the particulates sediment continuously.

a) layer no. 1 is the surface layer which exists only in the 1 and 2 chambers of filtration ;

b) layer no. 2 of sedimentation of floccs seen in all the filtration chambers ;

c) layer no. 3 of sedimentation in the mass where velocities are very small ;

d) layer forming the bed sediments.

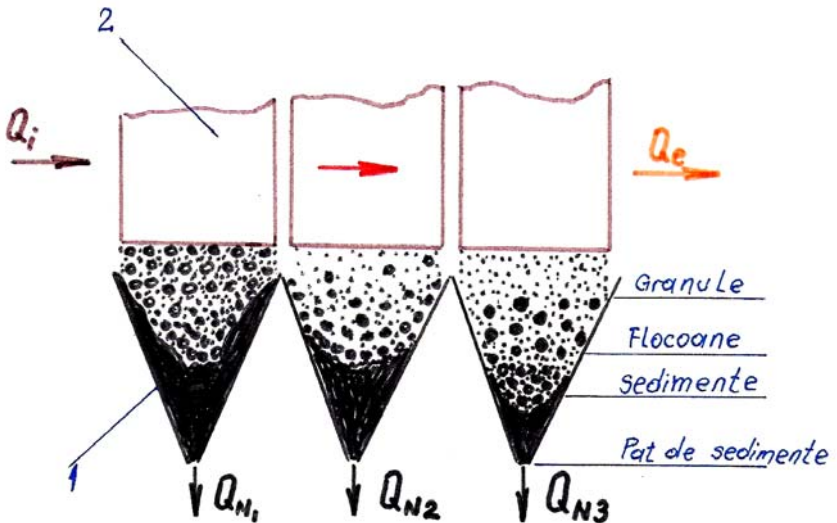


Fig. 1. Sedimentation of the particles in industrial electro filters:
1-sedimenting bunker; 2- electrodes deposit panel.

Briefly can be observed the phases of sedimentation in an electro filter in Figure No. 1

It is considered a sedimentation bunker as the one in fig. no. 1 in which, in the entrance, where the flow regime is turbulent turns at the entrance into the bunker in an uniform motion regime of piston type over the entire vertical section (longitudinal or transverse) so that we can consider that the entry concentration into the bunker is constant, so

the speed of decantation is the same at any point of the horizontal plane.

From the bed area of sedimentation is constantly discharged through the bottom side, the sediments to be transported as a slam at the ash pit.

2.1.1. GRANULAR PARTICLE SEDIMENTATION

The sedimentation can be considered in this volume as unimpeded, dependent by the gas properties and the intensity of the electrostatic field E , by the temperature and particle size.

Moving the particle is made on the direction shown in Figure. 2.

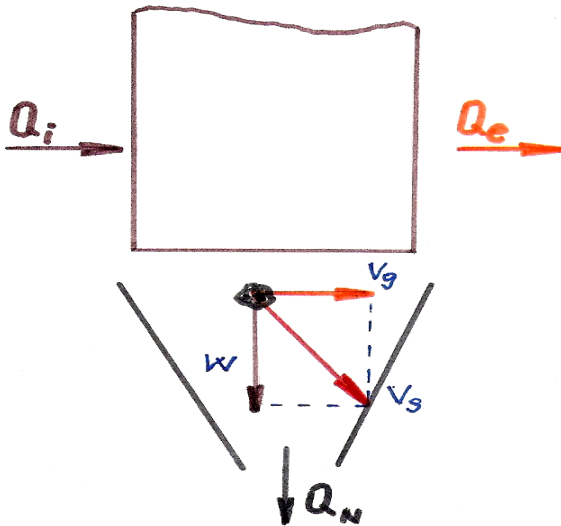


Fig.2. Determining the sedimentation velocity

To compose the gas flow velocity v_g with the sedimentation velocity w , meaning:

$$v = \sqrt{v_g^2 + w^2} ; \text{ where } v_g = \frac{Q}{\rho l H}$$

(4)

In which: ρ – particle density

L, h – length, height of the mini bunker in the electro filter;

Q – entry debit in the electro filter chamber

From the movement of the particle equation at sedimentation in accelerating regime:

$$m \frac{d\vec{v}}{dt} = \vec{G} - \vec{F}_a - \vec{F}_{pd} - \vec{F}_e \quad (5)$$

Where

1. Weight force $\vec{G} = m \cdot \vec{g}$

for $G = m \cdot g = \rho \cdot V \cdot g = \frac{\pi}{2} \rho \cdot g \cdot d^3$

In which ρ – particle density
 g – gravity acceleration
 d – particle diameter

2. Friction force in gas $\vec{F}_R = -k \cdot l \cdot \eta \cdot \vec{w}$; - Stokes Law.

In which $k = 6\pi$, for the sphere particle
 $l = R$, for the spheres of radius R
 η – dynamic viscosity
 w – sedimenting velocity

meaning $F_R = -k \cdot R \cdot \eta \cdot w$ - Stokes Law

3. Archimedes force $\vec{F}_a = -m_f \vec{g}$

In which m_f – fluid mass

4. Electrostatic force $\vec{F}_e = q_o \vec{E}$

In which q_o – electrical charge of the particle
 E – intensity of the electrostatic field

5. Inertia force $\vec{F}_i = m \frac{d\vec{w}}{dt}$

Replacing in the movement equation (4) we have:

$$m \frac{dw}{dt} = m \cdot g - m_f g - 6\pi \cdot \eta \cdot R \cdot w - q_o \cdot E \quad (6)$$

Considering that the fluid mass is zero, the dust particle movement equation is reduced to:

$$m \frac{dw}{dt} = m \cdot g - 6\pi \cdot \eta \cdot R \cdot w - q_0 \cdot E \quad (7)$$

Putting the initial conditions to the sedimenting start, meaning at $t = 0$, we have $v = 0$ the movement equation will be:

$$m \cdot g - 6\pi \cdot \eta \cdot R \cdot w - q_0 \cdot E = 0 \quad (7')$$

From which it results the hydraulic size of the radius particle $R = d/2$ is:

$$w_o = \frac{mg - q_0 E}{6\pi R \eta} = \frac{\rho_s g d^2}{6\eta} - \frac{q_0 E}{3\pi d \eta} \quad (8)$$

The time necessary to reach the regime velocity, uniform of particle fall, is obtained by multiplying with m the members of the equation (6)

$$\frac{dw}{dt} = g \left(1 - \frac{m_f}{m g} - \frac{6\pi \eta R w}{m g} - q_0 E \right) \quad (9)$$

Through dividing with g and expressing the masses according to densities and volume replaced by the dust particle

$$\Rightarrow \frac{1}{g} \frac{dw}{dt} = 1 - \frac{\rho_f}{\rho_s g} - \frac{6\eta w}{\rho_s g d^2} - q_0 E$$

And because the gases density is very small comparative with that of the dust particle meaning

$$\rho_f \ll \rho_s \Rightarrow \frac{1}{g} \frac{dw}{dt} = 1 - \frac{6\eta w}{\rho_s g d^2} - q_0 E \quad (10)$$

We note with: $A = g(1 - q_0 E)$ and $B = -\frac{6\eta}{\rho_s d^2}$ the differential equation (9) will transform in:

$$dw = (A + Bw)dt \quad \text{or} \quad dt = \frac{dw}{A + Bw}$$

Which we can integrate and obtain the solution:

$$t = \ln[A + Bw] \quad (11)$$

We will have through replacing A and B that:

$$t = \ln\left[g(1 - qE) - \frac{6\eta w}{\rho_s g d^2}\right]$$

Or written differently: $e^t = g(1 - q_0E) - \frac{6\eta w}{\rho_s g d^2}$

$$\Rightarrow \frac{6\eta w}{\rho_s g d^2} = g(1 - q_0E) - e^t \quad ;$$

from where we have that:

$$w = [g(1 - q_0E) - e^t] \frac{\rho_s g d^2}{6\eta} \quad (12)$$

3. DETERMINING THE BUNKER DEPTH

Known being the fact that the moving time Δt in the sedimentation space can be expressed according to velocity and space:

$$\Delta t = hw = v_g L \quad (13)$$

Where: h is the height of the bunker;
 L – length of the bunker;
 v_g – gas flow velocity;
 w - sedimentation velocity.

Medium sedimentation velocity can be expressed according to the decantation flow Q_n .

$$w = \frac{Q_N}{S} = \frac{Q_N}{Ll} \quad (14)$$

And replacing in the relation (13) we have: $v_g L = hQ_N / lL$

From where it results that the moving velocity of the mix

$$v_g = hQ_N / lL^2 \quad (15)$$

Equation that must be taken into consideration for obtaining of some big sediments yields.

The equation (15) can be written as $Q = Q(h)$ and we will have that the hydraulic surface charge:

$$Q_N = \frac{l L^2 v}{h} \quad (16)$$

For average flow velocities required of the gas mixed with the particles $v = 0,2-0,5$ m/s, we have that the relation is dependent of the sedimentation bunker dimensions depending on the flow of particles to be retrieved.

It is observed from the relation (16) that the sedimentation flow is directly proportional to the flat size of the bunker and inversely proportional with its height meaning h , by reducing the half height of the bunker will get a doubling of the decantation flow which should not be a neglected variable in sizing sedimentation bunkers of electro filters.

In the practice of particle sedimentation with diameters larger than 20 micron, the hydraulic loading varies between 180-200 kg/m². h in the chamber no. 1 of the industrial electro filter.

For diameters $d = 1-20$ microns the loading is between 120-130 kg/m². h in the chamber no. 2.

For diameters $d < 0.1 \mu\text{m}$ the loading is between 70 - 80 kg/m². h in the chamber no. 3.

4. CONCLUSIONS

1. The depth of decanting is less so the bunker efficiency is higher, reducing to 0.5 h of the bunker height existing the flow sedimentation is doubled.

2. The effect of dust particles retraining in bunkers will be canceled almost completely.

3. The effect of the electrostatic field will be canceled by its downloading in the mounted mini bunkers, and the electrostatic force from the general equation of sedimentation is canceled or substantially reduced.

5. MOUNTING MINIBUNKERS IN THE INDUSTRIAL ELECTROFILTERS

Starting from these findings the author proposes the performance and positioning of mini bunkers inside the existent electro filter bunkers equipping thermoelectric plants, at the top to 100 mm below the filing electrodes like in the figure no. 3. The mini bunkers are positioned horizontally, perpendicular to the direction of gas flow in electro filter and will have the role to increase substantially the sedimentation velocity and the bunker flow collection. Positioning mini bunkers with an angle of inclination of 75° and height $h = 1$ m at distances between

them (step) $p = 600$ mm would solve another urgent problem affecting the electro filter yield presently and the unfiltered gas movement through the bunker.

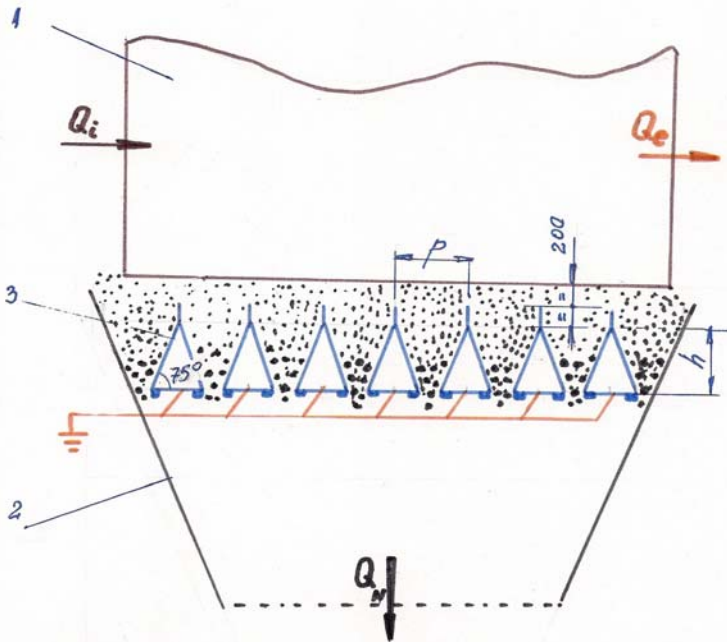


Fig. 3. Mounting the mini bunkers into the industrial electro filters:
1-electrode depositing panel; 2- bunker; 3- sedimentation mini bunkers

Using mini bunkers gives us the possibility to use other methods to increase the sedimentation velocity which may increase the effect of gravity previously studied with two methods that can be used independently from each other or combined, and that can eliminate the effect of retraining bunker particles.

The two processes which the author proposes are based:

- first, the effect of thermo cooling through forming two consecutive walls of mini bunkers of some channels of cooling with industrial air introduced through an additional air supply circuit from a fan which introduces air from the atmosphere.

- the electrostatic effect that some electrodes connected to the emission frame at the lower part whose configuration is identical to that used to encased electrodes, but so willing that electron emission flows to be directed towards the walls of the mini bunkers, would remove retraining of particles that do not sediment, again in filtering space.

REFERENCES

1. Apostolescu N., Taraza D., Experimental research bases of heat machines, Didactic and Teaching Editor, Bucharest, 1979.
2. Carabogdan ,Gh.,I. Thermo technician engineer guide .Ed. Technical, 1986.
3. Florea J., Panaitescu V., Fluid mechanics, Didactic and Teaching Editor.
4. Neacsu R.M., Ciocănea A., Calculus, drafting and testing the fans, blowers and compressors pumps, Dacia Editure, Cluj-Napoca, 2000.
5. Oprean A., Tool machine hydraulic, Didactic and Teaching Editor, Bucharest.
6. Robescu N.D., s.a., Polizasic fluids , Technical Editor ,2000.
7. Robescu N.D., s.a., Molding and simulating the cleaning processes, Technical Editure, 2004.

STUDIES AND RESEARCH REGARDING THE ROUGHNESS OF THE SURFACES GOT BY MILLING THE REFRACTAR STEEL

Marius ZAMFIRACHE, Luminita LAZAR

Abstract: This paper contains the method of establishing the workability functions related to the roughness of the surfaces got by milling the refractar steel.

Keywords: Refractar steel, milling, roughness surfaces, liniar functions, analysis regression.

1. INTRODUCTION

The roughness, regarded as a charectirizing factor of the surface quality is determined by the parameters of the cutting process, by the geometry of the cutting tool, the material, the rigidity of the tehnological system.

One of the factors influencing the exploitation of machine pieces is the roughness of the surface, which directy influences the wearing resistance as were as the character of the adjustment of the joint pieses and the corrosoion resistance.

To gen important saving of time, material and energy in this paperwork there was preferred the experiment statistic scheduling on identifying a process global optimum by two or more factors.

The experimentation strategy contains there successive working stages:scheduling, carrying out and analysing the data measured during the experiment.

There were defined the following stages:

-Establishing the problems (which the experimental program must answer), the variables (answers) dependent on the process and the independent ones (parameters);

-Choosing, amongn the possible variables, those, which, they considered could influence the experiment, answer. Generally speaking there were maintained more variables, those insignificant being subsequently cancelled by statistical analysis;

-Establishing the limits (put into practice) each chipping parameter of the could change;

- Choosing, within the stated limits, some values (experimentation points or levels) necessary to estimate the variables; usually, could be chosen three levels: a central one(reference), a lower and a higher level placed at equal distances to the central level;

- Closing the experimental program type;

- Measuring the experimental program error by repeating more experiences in the central point on independently, on the basis of the same previous experiences;

- Drawing up the experimental program;

- Setting up experimentation condition;

- The statistical analysis of the measured data, fixing the maths model coefficients and establishing the functional relations between the process answers and parameters;

- Interpretation, in practice, of the statistics analysis results.

The experiments statistical schedule together with the multiple regression and spreading analysis form the answer surfaces, method. Regarding this method in the dimensional space n of a process variables, the points cluster which represent the answers out of the process, form an answer surface. The above mentioned method allows the separate estimation of the process parameters effect and interaction, although within the experiment they are simultaneously changed.

The optimization of the fabrication process(material, geometry, tool, cutting parameters etc.) is possible only if the relations between different factors that appear during the cutting process are well known. These relations are determined, in general, by experiments.

2.EXPERIMENTAL DATA

The chemical characteristics stainless refractory steel presented in table 1 :

Tab. 1

O\elul	C%	Mn %	Si %	Cr %	Ni %	Al %	Ti %	Fe%
10TiAlCrNi3 20	0,0 7	0,8	0,4	20, 8	32	0,3	0,3	Rest ul

Mechanical properties of researched material are Brinell Hardness 192.

It was used the forward milling cutter type R245-0.63 P22-12H Coromant with $d=60\text{mm}$, $z=6$ teeth the plates being mechanically fixed. The metallic carbide plates are type SPUN 12 03 08 K20.

The geometric parameters of the considered tools are characterized by: $\alpha = 10^\circ$, $\gamma = 5^\circ$, $\lambda_T = 4^\circ$, $\chi_r = 75^\circ$, $\chi_r^i = 15^\circ$.

The levels of the natural variants v , f , a_p , r_n and τ are in geometric progression.

Eighteen experiments were realized by using the special methodology of the planning of experiments.

The levels of the variables are presented in table 2.

Tab.2

Leveis of the variables in the plan of experimens

Symbol	Code	-1	0	+1
$v(\text{m/min})$	X1	80	113	160
$f(\text{mm/d})$	X2	0.05	0.08	0.1
$r(\text{mm})$	X3	0.8	1.2	2

It is chosen as a model (to determine the roughness) a polithropical function dependent on the chipping parameters:

$$Ra = a_0 + a_1v + a_2f + a_3r + a_{11}v^2 + a_{22}f^2 + a_{33}r^2 + a_{12}vf + a_{13}vr + a_{23}fr \quad (1)$$

During the cutting process, there was used a cutting emulsion liquid of the PE5EP type

In order to measure the roughness of the turned surface, a TEST SURF 201 was used.

3.ANALYZING THE EXPERMENTAL DATA

The measurements are shown in table 3: $Ra(\mu\text{m})$ the roughness surfaces of refractar steel 10TiAlCrNi320 miling.

Tab. 3

No.exp/Xj	X1	X2	X3	$Ra(\mu\text{m})$
1	-1	-1	-1	2.2
2	+1	-1	-1	2.0
3	-1	+1	-1	2.4
4	+1	+1	-1	2.3
5	-1	-1	+1	2.1
6	+1	-1	+1	2.0
7	-1	+1	+1	2.5
8	+1	+1	+1	2.2
9	-1	0	0	2.5
10	+1	0	0	2.4
11	0	-1	0	2.3

12	0	+1	0	2.8.
13	0	0	-1	2.4
14	0	0	+1	2.2
15	0	0	0	2.4
16	0	0	0	2.4
17	0	0	0	2.5
18	0	0	0	2.5

For example, the elements characterized the Rc functions are presented regression indicators are shown in table 4.

Tab.4

PROGRAM FOR DETERMINING THE REGRESION FUNCTIONS

Initial data:

Studied process: milling

Non -dependent variables: $x_1=v$;

Non-dependent variables $x_2=f$;

Non-dependent variables $x_4=r$

Probabilities:

Fisher functions values:

Fprim=9.010

Fsec=5.320

Student functions values:

student=2.306

RESULTS OF THE REGRESSION ANALYSIS

$R^* = 0.659 < 1$ == Adequate model.

Significant coefficients

$R_0 = 22.03 > 1$ == significant variable

$R_1 = 0.08 < 1$ == non-significant variable

$R_2 = 2.38 > 1$ == significant non.variable

$R_3 = 0.05 < 1$ == non significant variable

$R_{11} = 1.99 > 1$ == significant variable

$R_{22} = 4.62 > 1$ == significant variable

$R_{33} = 2.95 > 1$ == significant variable

$R_{12} = 0.03 < 1$ == non-significant variable

$R_{13} = 0.01 < 1$ == non-significant variable

R23=0.01<1 ==non-significant variable

No. exp	Values(Ra)		Errors	
	Measured values	Calculated values.	Abs.	Rel.
1	2.2	2.181	0.02	1.53
2	2.0	2.038	-0.04	-3.79
3	2.4	2.233	0.17	6.96
4	2.3	2.228	0.37	16.18
5	2.1	2.406	0.29	16.18
6	2.0	2.303	0.10	6.96
7	2.5	2.802	-0.10	-3.79
8	2.2	2.462	0.04	1.53
9	2.5	2.709	-0.21	-13.70
10	2.4	2.709	-0.31	-21.82
11	2.3	2.709	-0.11	-6.60
12	2.7	2.928	-0.12	-6.61
13	2.4	2.709	-0.31	-21.82
14	2.2	2.181	0.02	1.53
15	2.4	2.708	-0.31	-21.82
16	2.4	2.708	-0.31	-21.82
17	2.5	2.709	-0.31	-21.82
18	2.5	2.709	-0.11	-6.60

5

Using computing REGS programs the following functions were determined:

$$Ra = -4.213 + 0.085v + 23.913f - 2.430r - 0.001v^2 - 12.762f^2 + 1.712r^2 + 0.059vf + 0.003vr - 1.300fr \quad (2)$$

4.CONCLUSIONS

The parameters of the cutting proces v, f, a, analysed using the R1, R2, R3 indicators influence the roughnes Ra values in a different way.

In most cases, every SA-MP couple advance is determined .

Thus, ane can notice that the main factors of influence upon the Ra, in the order of their importance to the studied stainless steel are: the advance, the cutting speed, the radius.

5.REFERENCES

1. Gheorghe, M., Stanescu, C., Draganescu, F.- Algorithm and computer program to determine multiple variables regression function,B.I.P., Bucharest., 1985.
2. Popescu, I.-Optimization of cutting proceses, Rominen Writing Craiova, 1987.
3. Zamfirache, M.- Machinability of titanium alloy by turning, University Publihing House, Craiova, 1996.

LIFE CYCLE ASSESMENT FOR RAPESEED METHYL ESTER AND BIODIESEL

TUTUNEA Dragos¹, BICA Marin¹, CERNAIANU Corina¹, STANCUT Adriana¹, DIMA Alexandru¹

¹*University of Craiova, Faculty of Mechanics*

Abstract: In this paper is presented a life cycle assessment for rapeseed oil methyl ester and petrodiesel. In the first part is analyzed the crop effect, nitrous oxide emissions, honey production and biogas generation from rapeseed meal. Then we present a life cycle analysis of biodiesel and diesel fuel for automotive industry and final conclusions.

Keywords: biodiesel, diesel, life cycle, pollutant emission.

1. INTRODUCTION

In recent years the popularity of biodiesel (rapeseed oil methyl ester, RME) has increased dramatically in Europe and recently in Romania. Since the beginning of the 1990s extensive research has compared the environmental impact of RME with conventional diesel fuel. The analysis [3] has resulted in a number of important conclusions, which have been confirmed by other institutions both in Romania and abroad: on balance, RME offers more positive outcomes relative to diesel fuel if the goal is to conserve fossil energy and reduce the greenhouse effect. However, if it is more important to reduce acidification, lower the nutrient input into soils and surface water, and to decrease ozone depletion, conventional diesel fuel offers more favorable outcomes. With this general result the discussion of the advantages and disadvantages of RME compared to diesel fuel has apparently reached an end and the system seems to be reliably assessable. Biodiesel also is an economically [4] viable solution to meet future emissions regulations. When reviewing the high costs associated with other alternative fuel systems, many fleet managers believe biodiesel is their least-cost-per-compliance mile option for cleaner air. Biodiesel doesn't require expensive modifications to engines or refueling facilities and mechanics do not have to be

retrained to work on your vehicle or vessel. The only thing that changes is air quality.

2. GENERAL LIFE CYCLE ANALYSIS OF BIODIESEL AND RAPESEED METYL ESTER

In recent years, further progress has been made in areas of agricultural research, such as the emission of greenhouse gases from agriculture or the preceding crop effect of rapeseed on the yields of the subsequent crop. Furthermore, the recent increase in rapeseed production has led to a rise in the availability of co-products (for example, rapeseed honey) and innovative new uses for these co-products (such as the fermentation of rapeseed meal to generate biogas) that may be economically viable. The analysis of these effects was the objective of a study conducted in this paper.

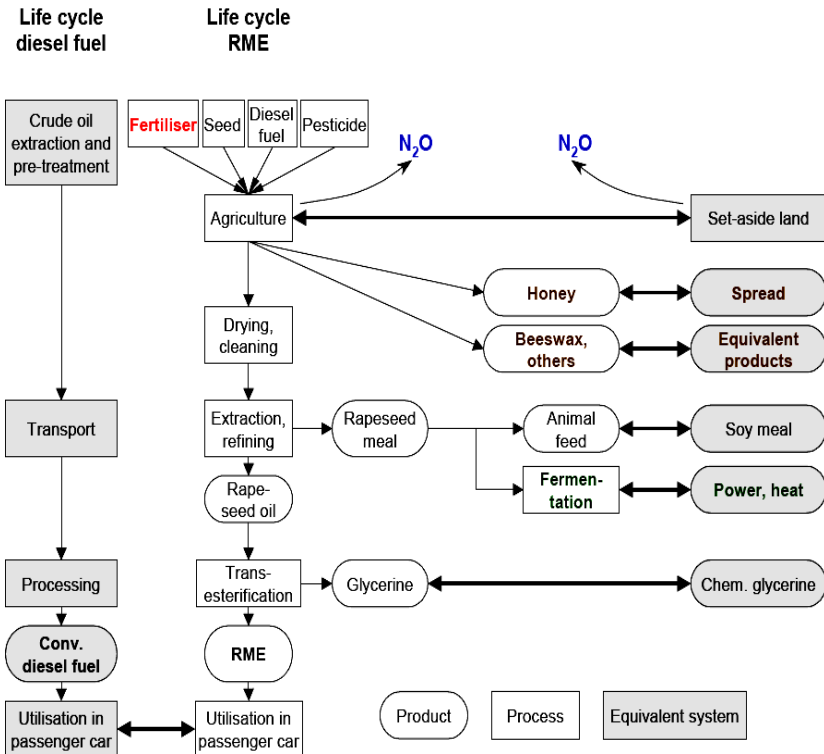


Fig.1 Life cycle of diesel and RME

The use of RME instead of fossil diesel fuel [1] produces environmental advantages as well as disadvantages. RME is beneficial with respect to the saving of fossil energy and to the greenhouse effect, but is detrimental regarding acidification, nutrient inputs and ozone depletion. No clear positive result for one or the other fuel is given within the impact category photo smog. An objective, scientifically [4] justified decision for one or the other fuel is therefore impossible. A comprehensive overall assessment can be achieved only if we draw on additional criteria. If for instance the protection of fossil energy resources and the greenhouse effect is given a higher priority than the other impact categories, a decision in favor of RME is justified. If other impact categories are valued higher the result may be different. In many life cycle assessments of agricultural products fertilizers often appear to be particularly relevant for the result. The same is true for the comparison between RME and diesel fuel. For that reason the derivation of the fertilizer balances, which have to be considered in the assessments, plays an exceedingly important role in the entire life cycle assessment. In this approach the quantity of fertilizer actually applied in the production process is considered. From that quantity the preceding crop effect, if any, is deducted.

The value [3] of the preceding crop comprises the soil improving properties of the crop (e.g. the fertilizing effect of the residues remaining on the field, serving as a nutrient source for the subsequent crop). As is generally known for rapeseed plants, this effect is very distinct. In the literature [4] the preceding crop effect of rapeseed is reported to contribute up to 60 kg of nitrogen per hectare originating from the straw, roots, and empty pods. Results originating from single investigations, in which measurements have been conducted for a number of different soil types, also fit into this range. As a matter of principle the nutrient removal approach underestimates the amount of fertilizer that has to be applied because the nutrients remaining on the field are not 100% available for the subsequent crop. Consequently the quantities of fertilizer calculated according to the nutrient removal approach tend to be lower than those calculated by the actual fertilizer application approach. On the other hand, for increased future rapeseed production for RME, a fertilizer regime optimized using good professional practices has to be assumed rather than the current average fertilizer practice. Comparing the data from both approaches, it becomes evident that the resulting differences of 10 to 20 kg N do not entail significantly different results. Therefore it can be concluded that the fertilizer quantities estimated in the calculations do not have to be altered.

Rotational set-aside land within a crop rotation is currently used as standard agricultural reference system for biodiesel rapeseed

production. However, according to expert assessments, in particular cases nitrous oxide emissions from set-aside land can actually be as large as those from areas under agricultural use due to the pronounced nitrogen dynamic of agricultural soils. In addition, according to expert judgments, nitrous oxide emissions are to a certain extent dependent on the nitrogen fertilizer rate. In addition, honey production yields the co-products pollen, beeswax, propolis, and royal jelly. Beeswax is mainly used in the cosmetics and pharmaceutical industry and is able to substitute various substances. In the current study we assume that it can be used as a coating material for dragees substituting camauba wax, a hard wax from the leaves of the camauba palm native to Brazil. As an example, propolis as a natural drug used to maintain human health is considered significant in preventing the application of chemical Pharmaceuticals.

Both environmental advantages and disadvantages result [4] from the different use of rapeseed meal. For that reason a scientifically justifiable, objective assessment is impossible. However, it is remarkable that the advantages and disadvantages are almost the same as for the comparison of RME with diesel fuel: advantages in the categories energy saving and greenhouse effect, disadvantages in the categories acidification and nutrient inputs. With regard to ozone depletion biogas generation has an additional advantage in comparison with the animal feed option. Therefore the following conclusion can be drawn: if a decision is made in favor of RME instead of diesel fuel based on ones own measure of value, then - as a consequence of the very same measure of value - biogas generation of rapeseed meal has clearly to be preferred to the use as animal feed.

3. THE EFFECT OF LIFE CYCLE ANALYSIS OF BIODIESEL AND DIESEL IN REDUCTION OF POLLUTION

Life cycle analyses [6] look at the whole picture of how a fuel is made, from "cradle to grave." The life cycles begin with the extraction of all raw materials to make petroleum diesel and biodiesel, and end with using the fuels in an urban bus. Examining global issues, such as CO₂ emissions, requires a comprehensive life cycle analysis. Understanding the benefits of biodiesel requires us to compare its life cycle emissions to those of petroleum diesel. This study examines biodiesel energy's balance, its effect on greenhouse gas emissions, and its effects on the generation of air, water, and solid waste pollutants for every operation needed to made biodiesel and diesel fuel. We made no attempt to quantify its domestic economic benefits.

Major operations within the boundary of the petroleum diesel system include:

- Extract crude oil from the ground;
- Transport crude oil to an oil refinery;
- Refine crude oil to diesel fuel;
- Transport diesel fuel to its point of use;
- Use the fuel in a diesel bus engine.

For the biodiesel system, major operations include:

- Produce culture;
- Transport rapeseed to a rape crushing facility;
- Recover rapeseed oil at the crusher;
- Transport rapeseed to a biodiesel manufacturing facility;
- Convert rapeseed oil to biodiesel;
- Transport biodiesel fuel to the point of use;
- Use the fuel in a diesel bus engine;

Life cycle analyses all have similar limitations. Incomplete data are the rule rather than the exception. The most reliable conclusions are for overall energy balance and CO₂ emissions. For these two measures, our data are the most complete.

3.1 REDUCTIONS IN PETROLEUM AND FOSSIL ENERGY COMSUMPTION

Biodiesel [6] offers tremendous potential as one component of a strategy for reducing petroleum oil dependence and minimizing fossil fuel consumption. The benefit of using biodiesel is proportionate to the blend level of biodiesel used. Substituting B100 for petroleum diesel in buses reduces the life cycle consumption of petroleum by 95%. A 20% blend of biodiesel and petroleum diesel (B20) causes the life cycle consumption of petroleum to drop 19%.

Biodiesel yields 3.2 units of fuel product energy for every unit of fossil energy consumed in its life cycle. The production of B20 yields 0.98 units of fuel product energy for every unit of fossil energy consumed.

3.2 REDUCTION IN CO₂ EMISSION

Because biodiesel production [5] requires such small amounts of fossil fuel, its CO₂ life cycle emissions are, not surprisingly, much lower than those of petroleum diesel. Displacing petroleum diesel with biodiesel in urban buses is an extremely effective strategy for reducing CO₂ emissions.

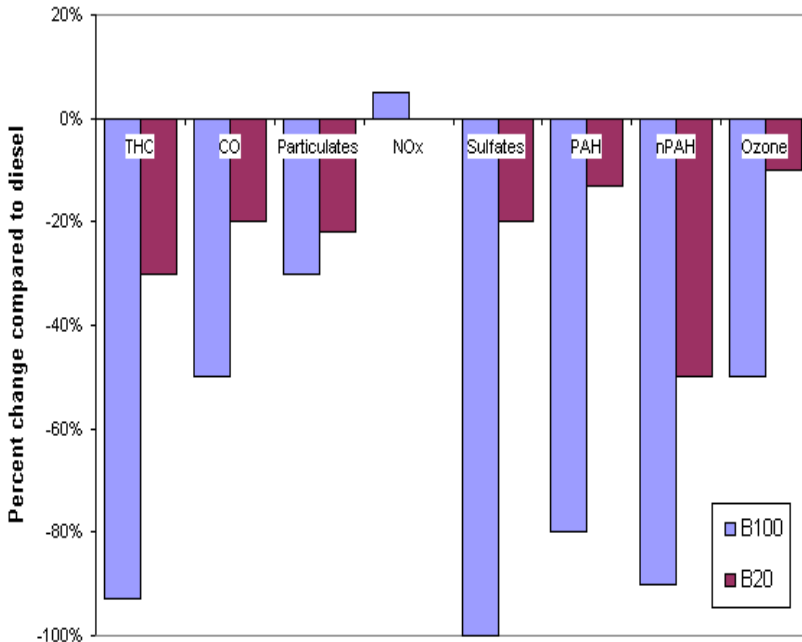


Fig.2 Emission of biodiesel compared to diesel fuel

3.3 CHANGES IN AIR POLLUANT EMISSIONS

The effect of biodiesel on air quality is complex and requires an understanding of the chemical interactions of air pollutants. To begin such an analysis, you need to know the amounts and type of air pollutants each fuel releases into the environment. Biodiesel, as it is available today, substantially reduces some air pollutants; it leads to increases in others. Using B100 in urban buses substantially reduces life cycle emissions of total particulate matter (32%), CO (35%), and SO_x (8%), relative to petroleum diesel's life cycle. Biodiesel reduces particulate, carbon monoxide, and sulfur dioxide emissions compared to diesel fuel. The EPA targets these three emissions because they pose public health risks, especially in urban areas where they can affect more people. Because transportation emissions contribute significantly to urban concentrations of these pollutants, reducing tailpipe emissions is a powerful tool for improving air quality. Using biodiesel in buses operating in urban areas significantly reduces these pollutants. Biodiesel helps to keep air clean and protect the environment. The use of biodiesel [6] in a conventional diesel engine

results in substantial reduction of unburned hydrocarbons, carbon monoxide, and particulate matter. Biodiesel is safer for people to breathe. Research conducted in the U.S. showed biodiesel emissions have decreased levels of all target polycyclic aromatic hydrocarbons (PAH) and nitrated PAH compounds, as compared to petroleum diesel exhaust. PAH and nPAH compounds have been identified as potential cancer causing compounds. Targeted PAH compounds were reduced by 75 to 85 percent, with the exception of benzo(a) anthracene, which was reduced by roughly 50 percent. Target NPAH compounds were also reduced dramatically with biodiesel fuel, with 2-nitrofluorene and 1-nitropyrene reduced by 90 percent, and the rest of the nPAH compounds reduced to only trace levels. All of these reductions are due to the fact the biodiesel fuel contains no aromatic compounds.

Biodiesel [5] offers fleets a cost-effective and simple solution to clean the air. Environmental concerns and energy security issues have prompted legislation and regulatory actions spurring demand for alternative fuels such as biodiesel. One of the largest roadblocks to the use of alternative fuels is the change of performance noticed by users. Biodiesel has many positive attributes associated with its use, but by far the most noted attribute highlighted by fleet managers is the similar operating performance to conventional diesel fuel and the lack of changes required in facilities and maintenance procedures. Biodiesel functions in the engine the same way as petroleum diesel, but is a fuel that fulfills all the environmental and energy security needs previously mentioned without sacrificing operating performance.

4. CONCLUSIONS

In conclusion RME in contrast to diesel fuel continues to save greenhouse gases and to release more nitrous oxide. For the comparison of animal feed, biogas generation, or direct combustion of rapeseed meal the following conclusion can be drawn: based on a measure of value that favours RME instead of diesel fuel because of the benefits regarding energy saving and greenhouse effect, the options can be classified as follows: the direct combustion of rapeseed meal is more favourable than fermentation to yield biogas, which in turn is more favourable than the use of rapeseed meal as animal feed. The production of honey and its co-products (beeswax, propolis, pollen, and royal jelly) from rapeseed fields was a part of the RME assessment. In automotive industry biodiesel present a reduction of emission gases compared with diesel fuel and offer a tremendous potential as one component of a strategy for reducing petroleum oil dependence and minimizing fossil fuel consumption.

5. REFERENCES

1. Anneliese Niederl, Michael Narodoslawsky Life Cycle Assessment – study of Biodiesel from Tallow and Used Vegetable Oil Graz, December 2004
2. Ben Lane Life Cycle Assessment of Vehicle Fuels and Technologies Ecolane Transport Consultancy on behalf of London Borough of Camden, March 2006.
3. Life Cycle Inventory of Biodiesel and Petroleum Diesel for Use in an Urban Bus by U.S. Department of Agriculture and U.S. Department of Energy Final Report, May 1998.
4. Life cycle assessment of biodiesel: Update and New Aspects, Project No. 530/025. Heilderberg May 2003
5. Paul R. Adler, Stephen J. Del Grosso, William J. Parton Life-Cycle Assessment Of Net Greenhouse-Gas Flux For Bioenergy Cropping Systems Ecological Applications, 17(3), 2007, pp. 675–691.
6. Rainer Zah, Heinz Böni, Marcel Gauch, Roland Hirschler, Martin Lehmann, Patrick Wäger Life Cycle Assessment of Energy Products: Environmental Assessment of Biofuels EMPA, Switzerland, 22 May 2007.

THE MODELLING OF THE SEDIMENTATION PROCESS OF THE DUST PARTICLES OF THE FLUE GASSES

Ioan AȘTEFANEI¹, Dumitru STĂNCIOIU²,

¹*The University of Craiova, The Faculty of Mechanics*

²*The Turceni Industrial Energetic Vocational School*

Abstract: The modelling of the sedimentation process offers the possibility to optimize the dimensions of the sedimentation chambers of the dust which was filtered from the flue gasses emitted by the existing industrial installations, which are sources of polluting substances. Through the modelling it is underlined that, in order to increase the gradient of the concentration of dust in the chamber, it is necessary to reduce the depth of sedimentation of the existing chambers.

For that purpose, in this paper we propose the installation, at the entry into the chambers of the existing electrofilters, of mini-chambers of sedimentation, placed horizontally and perpendicularly on the flowing direction of the flue gasses.

Keywords: dust concentration; depth of sedimentation; mini-chambers

1. GENERAL CONSIDERATIONS

In the modelling of the sedimentation process, the following aspects are taken into consideration:

- it appears in the process of transporting particles in gasses;
- the process is also accompanied by the diffusion of the particles, as a consequence of the difference in concentration between the various layers of the chamber;
- the sedimentation is accompanied by thermal convection between different areas as a consequence of the difference in temperature;
- the sedimentation is accompanied by electrostatic separation as an effect of the difference in electric potential between the potential of the particle and that of the field in which it is found;
- the particles are influencing each other as an effect of the interaction between them, in the sedimentation process;

- in the chamber, preferential currents appear, parasitical currents with substance density and bearing charges, acting in counter-current with the sedimentation, phenomenon not taken into account during the modelling.

The general equation of the dispersion process accompanying the sedimentation is:

$$\frac{\partial \bar{c}}{\partial t} + \frac{\partial}{\partial x}(\bar{u}\bar{c}) + \frac{\partial}{\partial y}(\bar{v}\bar{c}) + \frac{\partial}{\partial z}(\bar{w}\bar{c}) = \frac{\partial}{\partial x}\left(\varepsilon_x \frac{\partial \bar{c}}{\partial x}\right) + \frac{\partial}{\partial y}\left(\varepsilon_y \frac{\partial \bar{c}}{\partial y}\right) + \frac{\partial}{\partial z}\left(\varepsilon_z \frac{\partial \bar{c}}{\partial z}\right) + D_m\left(\frac{\partial^2 \bar{c}}{\partial x^2} + \frac{\partial^2 \bar{c}}{\partial y^2} + \frac{\partial^2 \bar{c}}{\partial z^2}\right) + S(x, y, z, t) \quad (1)$$

Where: $\varepsilon_x, \varepsilon_y, \varepsilon_z$ - dispersion coefficients on the Ox, Oy and Oz axes;
 \bar{c} - the average concentration of the disperse medium;

D_m - the molecular diffusibility;

$S(x, y, z, t)$ - the source introducing the substance;

$\bar{u}, \bar{v}, \bar{w}$ - the projections of the speed on Ox, Oy, Oz;

$x(t), y(t), z(t)$ – the position of the material point at the moment t

The solution of this equation, to which the continuity equations and the movement equation are added, is impossible to obtain, which is why simplifying hypotheses are used.

2. MODELLING THE DISPERSION OF DUST PARTICLES IN THE CHAMBERS OF THE ELECTROFILTERS

In order to study the issue, the general equation of the dispersion will be adapted to the physical conditions of the phenomenon taking place in the sedimentation chambers of the industrial electrofilters, the speed graphic of which is shown in figure no. 1.

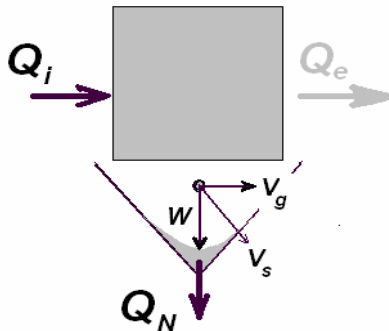


Fig. no.1 Determining the sedimentation speed

In order to accomplish the sedimentation of the particles from the gasses, one must create the gasdynamic conditions necessary for their independent movement, since they have a tendency to deposit.

The movement speed of the particle v_s is obtained by combining the two component speeds, the gas flow speed v_g and the hydraulic dimension w .

For determining the distribution of the concentration in a sedimentation chamber, the following simplifying hypotheses are made:

- a) There are no interactions between the dust particles and the gasses, which implies the annulment of the term of mass diffusion;

$$D_m \left(\frac{\partial^2 \bar{c}}{\partial x^2} + \frac{\partial^2 \bar{c}}{\partial y^2} + \frac{\partial^2 \bar{c}}{\partial z^2} \right) = 0$$

- b) The movement is axially symmetrical, since it takes place identically on the vertical and axial planes, like in fig. no. 1, on the direction Oy there are no variations, therefore:

$$\frac{\partial}{\partial y} (\bar{v} \bar{c}) = 0; \quad \frac{\partial}{\partial y} \left(\varepsilon_y \frac{\partial \bar{c}}{\partial y} \right) = 0$$

So the equation of the dispersion (1) is reduced to:

$$\begin{aligned} \frac{\partial \bar{c}}{\partial t} + \frac{\partial}{\partial x} (\bar{u} \bar{c}) + \frac{\partial}{\partial z} (\bar{w} \bar{c}) &= \frac{\partial}{\partial x} \left(\varepsilon_x \frac{\partial \bar{c}}{\partial x} \right) + \\ &+ \frac{\partial}{\partial z} \left(\varepsilon_z \frac{\partial \bar{c}}{\partial z} \right) + S(x, y, z, t) \end{aligned} \quad (2)$$

Since the dispersion coefficients ε_x , ε_y , ε_z are constant and the power source

$$S(x, y, t) = Q.C/v$$

The equation of the dispersion becomes:

$$\frac{\partial \bar{c}}{\partial t} + \frac{\partial}{\partial x} (\bar{u} \bar{c}) + \frac{\partial}{\partial z} (\bar{w} \bar{c}) = \varepsilon_x \frac{\partial^2 \bar{c}}{\partial x^2} + \varepsilon_z \frac{\partial^2 \bar{c}}{\partial z^2} + S(x, y, z, t)$$

Where: $\frac{\partial \bar{c}}{\partial t}$ - represents the moving character of the process;

$\frac{\partial}{\partial x}(\bar{u}\bar{c})$ - the transportation of the particles on the flowing direction of the gasses;

$\frac{\partial}{\partial z}(\bar{w}\bar{c})$ - represents the sedimentation process;

$\varepsilon_x \frac{\partial^2 \bar{c}}{\partial x^2} + \varepsilon_z \frac{\partial^2 \bar{c}}{\partial z^2}$ - represents the dispersion of the particles in the two directions.

3. ANALYTICAL SOLUTIONS FOR THE CONCENTRATION DISTRIBUTION IN THE MOTIONLESS DISPERSION MODEL

The motionless dispersion model in sedimentation is encountered in the filtration chambers no.2 and no.3 of the industrial eco filters, where the shaking is done intermittently, this causing the dust concentration to have a stationary flow regime at the entry into the chamber.

If the sedimentation process is motionless: $c=ct.$ and $\frac{\partial \bar{c}}{\partial t} = 0$, the equation of the dispersion

$$\frac{\partial}{\partial x}(\bar{u}\bar{c}) + \frac{\partial}{\partial z}(\bar{w}\bar{c}) = \varepsilon_x \frac{\partial^2 \bar{c}}{\partial x^2} + \varepsilon_z \frac{\partial^2 \bar{c}}{\partial z^2} \quad (3)$$

For the solving of which the following simplifying hypotheses are made:

- the dispersion of the dust on the direction Ox inside the chamber is negligible;
- the concentration variation on the direction Ox is negligible in

relation with the weight forces $\frac{\partial c}{\partial x} = 0$

- the speed of transportation of the fluid is small in comparison with the speed of sedimentation.

Thus, the equation (3) is transformed into:

$$\frac{\partial}{\partial z}(\bar{w}\bar{c}) = \varepsilon_z \frac{\partial^2 \bar{c}}{\partial z^2} \quad (4)$$

Which is equivalent to:
$$\frac{dc}{c} = \frac{w_0}{\varepsilon_z} dz \quad (5)$$

Which through integration in the limits (z-z₀) and (c-c₀):

$$\int_c^{c_0} \frac{dc}{c} = \int_{z_0}^z \frac{w_0}{\varepsilon_z} dz \quad (6)$$

The solution of the above one is: $\ln c - \ln c_0 = \frac{w_0}{\varepsilon_z} (z - z_0)$;

Or, written differently, the solution to the equation becomes:

$$\frac{c}{c_0} = e^{\frac{w_0}{\varepsilon_z}(z-z_0)} \quad \text{or} \quad c = c_0 e^{\frac{w_0}{\varepsilon_z}(z-z_0)} \quad (7)$$

where c – the concentration of dust at the moment t;

c₀ – the concentration of dust in the particle bed deposited in the chamber;

(z-z₀) = h – the height of the chamber;

ε_z - the vertical dispersion coefficient;

The hydraulic dimension of the particle

$$w_0 = \frac{\rho_s g d^2}{6 \eta} - \frac{q_0 E}{3 \pi d \eta}; \quad (8)$$

Which depends on: ρ – the density of the particle

g – the gravitational acceleration

d – the diameter of the particle

η – the dynamic viscosity

q₀ – the electric charge of the particle

E – the intensity of the electrostatic field

The graphic representation of the solution to the differential equation is shown in fig. no.2.

In order to obtain a family of curves showing the distribution of the concentration, one must determine the speed of depositing (the hydraulic dimension) of each particle with the variable diameter d. Yet, neglecting the variation of the speed of sedimentation with the concentration can cause significant variations of the theoretical results as compared to the experimental ones, so, going back to the sedimentation equation, we have:

$$\frac{\partial}{\partial z} \left(w_o \frac{\bar{c}}{1-\bar{c}} \right) = \varepsilon_z \frac{\partial^2 \bar{c}}{\partial z^2} \quad (9)$$

Which by integration becomes:

$$w_o \frac{\bar{c}}{1-\bar{c}} = \varepsilon_z \frac{d\bar{c}}{dz} \quad (10)$$

It results that

$$\frac{c}{1-c} dc = \frac{w_o}{\varepsilon_z} dz \quad (11)$$

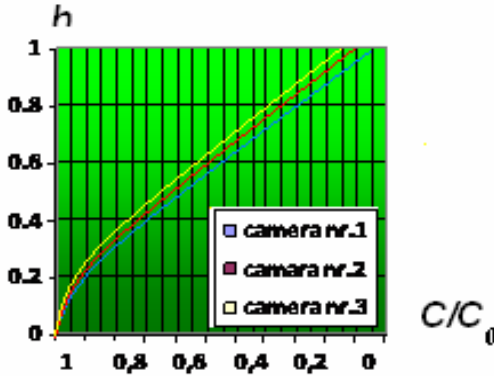


Fig.no.2 The variation of the concentration of dust in motionless sedimentation regime

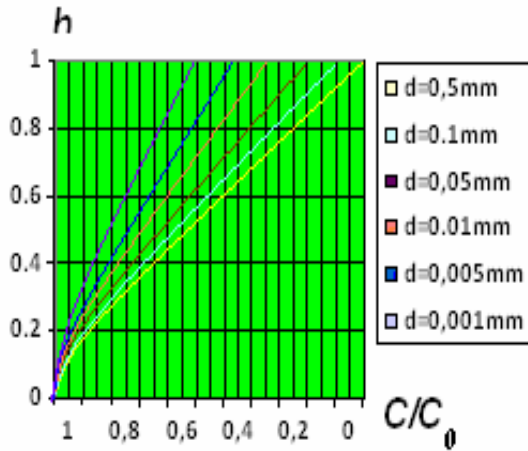
Which through integration becomes

$$\ln c - \ln c_o - (c - c_o) = \frac{w_o}{\varepsilon_z} (z - z_o) \quad (12)$$

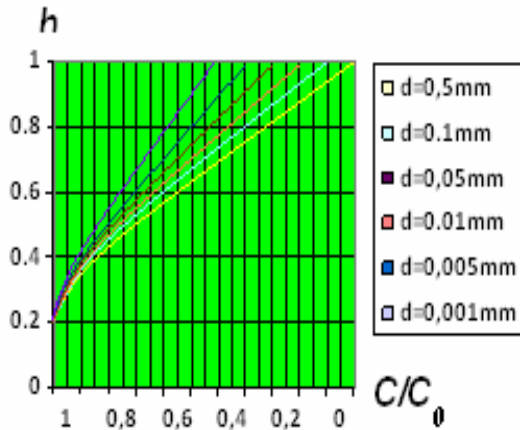
Differentially written

$$\frac{c}{c_o} = e^{\frac{2\bar{c} + \frac{w_o}{\varepsilon_z}(z-z_o)}{\varepsilon_z}} \Leftrightarrow c = c_o e^{\frac{2\bar{c} + \frac{w_o}{\varepsilon_z}(z-z_o)}{\varepsilon_z}} \quad (13)$$

The graphic representation of the solutions to the differential equation is:



a) at the start-up of the electrofilter;



b) in normal functioning

Fig.no.3 The variation of the concentration of dust with the length of the diameter of the particles:

The graphic is obtained through the variation $w=w_0(d)$, the speed of sedimentation depending on the diameter of the particle, the shape of which is the relation (8).

The graphical representation in fig. 3 of the solution to the equation (25) can show us the exponential increase of the concentration depending on the decrease of the height of sedimentation and the size of the dispersion coefficient of the dust particles which are deposited in the chamber of the electrofilter.

3. CONCLUSIONS

From the analysis of the solutions to the differential equations accompanying the sedimentation process in various situations, expressed in the relation (7), we can draw the conclusion that the gradient of the concentration of the depositing particles increases exponentially with the decrease of the depth of sedimentation, conclusion which demonstrates the efficiency of our proposition to install, on the upper side of the chambers found on the industrial ecofilters, mini-chambers, placed perpendicularly on the flowing direction of the gasses in the filtration space; the height $h=1m$ and wall inclination at 75° of the minichambers will create a piston effect of the particles in the main chamber, substantially increasing the speed of sedimentation.

Also, it can be noticed that for the chambers existing in the filtration installations of the functional energetic groups, the reduction of the sedimentation height can be made through the increase of the level of the sediment layer. By reducing to half the sedimentation height, we get a double increase of the sedimentation speed, which could solve many problems concerning the increase of the filtration efficiency at the present time.

BIBLIOGRAPHY

1. Apostolescu N., Taraza D., Foundations of the Experimental Research of Thermal Machines, Editura Didactică și Pedagogică, Bucharest, 1979.
2. Carabogdan, Gh., I. The Manual of the Thermo-technician Engineer, Ed. Tehnică, 1986.
3. Florea J., Panaitescu V., The Fluid Mechanics, Editura Didactică și Pedagogică.
4. Neacsu R.M., Ciocănea A., Calculating, Designing and Testing the Pumps of the Fans of Blowers and Compressors, Editura Dacia, Cluj-Napoca, 2000.
5. Oprean A., The Hydraulics of Machine Tools, Editura Didactică și Pedagogică, Bucharest.
6. Robescu N.D., et. al., Polyphase Fluids, Editura Tehnică, 2000.
7. Robescu N.D., et. al., The Modelling and the Simulation of the Purification Processes, Editura Tehnică, 2004

A MATHEMATICAL MODEL OF HUMAN RETINA

Rajiv SHAH¹, Ștefan ȚĂLU²

¹The University of Pittsburg, Faculty of Medicine,

Dept. of Ophthalmology, Pittsburg, Pennsylvania, USA

²Technical University of Cluj-Napoca, Faculty of Mechanics,

Dept. of Descriptive Geometry and Engineering Graphics

Abstract: The objective of this paper is to present a mathematical model of human retina.

Keywords: human visual system, retina, fovea.

1. THEORETICAL CONSIDERATIONS

The human eye has multiple discrete parts that must function together properly to produce a clear vision [1 - 9].

The retina is a thin tissue lining the innermost wall of the eye.

The retina responds to light rays hitting it and converts them to electrical signals carried by the optic nerve to the brain.

The outlying parts of the retina are responsible for peripheral vision while the center area, called the macula, is used for fine central vision and color vision (Fig. 1).

The very center of the macula is called the fovea, with a very high concentration of special cells (cones).

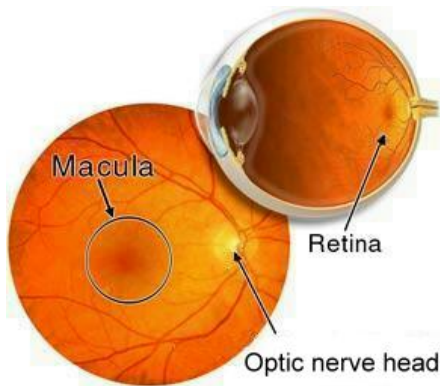


Fig. 1 - The retina.

2. MATHEMATICAL MODELLING OF RETINA

The human retina is formed by two concentric regions. The innermost region, named the fovea, can be approximated as a set of receptive fields hexagonally distributed in a maximal uniform packing density. The outer region can be approximated by receptive fields distributed hexagonally with an exponentially decreasing sampling density [10].

In the fovea, receptive fields have the same radius \hat{r} . As they are circular regions, to assure a complete sampling of the input image, each receptive field overlaps by a certain percentage $\hat{\delta}$ of its diameter with all of its neighbours.

A neighbourhood is defined as a set of rings ("hexagonal rings") surrounding a receptive field, and the position of a specific neighbour in a ring is given by an angular displacement. The hexagonal distribution of receptive fields can be viewed as a sequence of concentric rings in which each ring contains a multiple of six receptive fields.

Within this context, the whole fovea structure is composed of a central receptive field surrounded by a number of receptive field rings,

The number of receptive fields in a given ring n of the fovea is:

$$\hat{F}(n) = \begin{cases} 1 & \text{if } n = 0 \\ 6n & \text{if } 0 < n < \hat{N} \end{cases}, \quad (1)$$

where \hat{N} is the total number of rings in the fovea.

The local neighbour (n', s') of the receptive field (n, s) can be written in global coordinates by converting both coordinates to hexagonal ones, translating the neighbour coordinates by the central receptive field coordinates, and then converting the result back to polar coordinates. This operation can be expressed as,

$$\hat{G}(n', s', n, s) = \hat{H}^{-1}(\hat{H}(n', s') + \hat{H}(n, s)), \quad (2)$$

where $0 \leq n' < (\hat{N} - n)$ and $0 \leq s' < \hat{F}(n')$.

Receptive fields have been considered as points of infinitesimal area in a given coordinate system.

But, it is known that [10],

$$\hat{Q}(n, s) = \hat{C} \circ \hat{H}(n, s). \quad (3)$$

The radius of the ring that passes through the receptive field centres of a given ring n within the fovea is given by:

$$\hat{R}(n) = 2n\hat{r}(1 - \delta), \quad (4)$$

Three input parameters can be identified from the definition of the fovea structure: the radius of the receptive fields \hat{r} , the total number of rings \hat{N} and the overlap between adjacent receptive fields $\hat{\delta}$.

Outside the fovea, is easily to have receptive fields organised in an overlapping hexagonal structure which causes neighbours of a receptive field to be uniformly displaced.

To assure a complete sampling of the field of view, receptive fields overlap by a certain percentage of their diameter with both radial and angular (concentric) neighbours. We suppose this overlap will be identical to the one used in the fovea.

As a result, the radius of a ring n is a constant $B > 1$ times the radius of the previous ring.

$$\bar{R}(n) = B\bar{R}(n-1) = B(B\bar{R}(n-2)) = \dots = B^n \bar{R}(0). \quad (5)$$

The characteristic angle $\bar{\theta}$ defines an angle between their centres and the retina centre, for each pair of adjacent receptive fields in a specific ring and it can be expressed as:

$$\bar{\theta} = 2\pi / F. \quad (6)$$

To obtain the neighbour (n', s') of a receptive field (n, s) in global coordinates, it is necessary to convert (n, s) to the auxiliary coordinate system and (n', s') to displacements in the auxiliary coordinate system. The final output is the sum expressed as:

$$\bar{G}(n', s', n, s) = \bar{L}^{-1}(\bar{L}(n, s) + \bar{D}(n', s')), \quad (7)$$

where $0 \leq n' < \text{MIN}(n, \bar{N} - n)$ and $0 \leq s' < \hat{F}(n')$; MIN returns the minimum value amongst its arguments.

The Cartesian coordinates of a receptive field centre indexed by ring and sector (n, s) is a standard polar to Cartesian transformation of its ring radius and actual angle expressed as:

$$\bar{Q}(n, s) = (\bar{R}(n) \cos(s\bar{\theta}), \bar{R}(n) \sin(s\bar{\theta})). \quad (8)$$

Finally, for the entire retina a unified notation can be used. So, the number of receptive fields in a given ring n is:

$$F(n) = \begin{cases} 1 & \text{if } n = 0 \\ 6n & \text{if } n < \hat{N} \\ F(\hat{N} - 1) & \text{otherwise} \end{cases}, \quad (9)$$

The radius of a given ring n is given by:

$$R(n) = \begin{cases} 2 \hat{r} n (1 - o) & \text{if } n < \hat{N} \\ B^{n-\hat{N}} R(\hat{N} - 1) & \text{otherwise} \end{cases}, \quad (10)$$

The receptive field centre in Cartesian coordinates can be written as:

$$\bar{Q}(n, s) = \begin{cases} \hat{C} \circ \hat{H}(n, s) & \text{if } n < \hat{N} \\ (R(n) \cos(s\bar{\theta}), R(n) \sin(s\bar{\theta})) & \text{otherwise} \end{cases} \quad (11)$$

The receptive field radius of a given ring n is:

$$r(n) = \begin{cases} \hat{r} & \text{if } n < \hat{N} \\ r(n-1)B & \text{otherwise} \end{cases}, \quad (12)$$

The equations (2) and (7) can be unified as follows:

$$\hat{G}(n', s', n, s) = \begin{cases} \hat{H}^{-1}(\hat{H}(n', s') + \hat{H}(n, s)) & \text{if } n < \hat{N} \\ \bar{L}^{-1}(\bar{L}(n, s) + \bar{D}(n', s')) & \text{otherwise} \end{cases}, \quad (13)$$

The relationship between N and the previous parameter \bar{N} is:

$$N = \bar{N} + \hat{N} - 1. \quad (14)$$

3. CONCLUSIONS

This paper presented a mathematical model of the retina that can be used in biomechanical model of the human eye.

REFERENCES

1. Watt, R.J., Understanding Vision. Academic Press, 1991.
2. Wandell, B.A., Foundations of Vision. Sinauer Associates Inc., 1995.
3. Ullman, S., High-level vision: object recognition and visual cognition. MIT Press, Cambridge, Mass. London, 1996.
4. Zeki, S., A Vision of the Brain. Blackwell Scientific Publications, 1993.
5. Wilson, S.W., On the retino-cortical mapping. International Journal on Man-Machine Studies, 18:361–389, 1983
6. Leigh, R.J., Zee, D.S., The neurology of eye movements, Third Edition, New York, Oxford, 1999.
7. Lindberg, T., Scale-space theory in computer vision, Kluwer Academic, London, 1994.
8. Pardo, F., Development of a retinal image sensor based on cmos technology. Technical Report LIRA-TR 6/94, LIRA-Lab, DIST - University of Genova, 1994.
9. Rojer, A.S., Schwartz, E.L., Design considerations for a space-variant visual sensor with complex-logarithmic geometry. In Proceedings of the International Conference on Pattern Recognition, pp. 278–285, 1990.
10. Gomes, H.M., Fisher, R.B., Hallam, J., A retina-like image representation of primal sketch features extracted using a neural network approach. In Proceedings of Noblesse Workshop on Non-Linear Model Based Image Analysis, pp. 251 – 256, Glasgow, Scotland, July 1998.

ON THE APPLICATION OF LAMINOGRAPHY TO THE HUMAN EYE

Rajiv SHAH¹, Ștefan ȚĂLU²

¹*The University of Pittsburg, Faculty of Medicine,
Dept. of Ophthalmology, Pittsburg, Pennsylvania, USA*

²*Technical University of Cluj-Napoca, Faculty of Mechanics,
Dept. of Descriptive Geometry and Engineering Graphics*

Abstract: The objective of this paper is to present an application of the laminography to the human eye.

Keywords: human visual system, eye, laminography.

1. THEORETICAL CONSIDERATIONS

Laminography is a method that consists of a photo plate mechanically linked with a moveable source. This technique is based on the parallax of the different source positions [1 – 12].

By moving the combination of source and photo plate into different directions, in such a way that parts of the focal layer are always projected on the same spot of the photo plate with the same orientation and magnification, a clear image of the focal layer is obtained.

Parts of other layers, above and below the focal layer, will move during the motion of the source and their influence is spread out over a larger area, resulting in background intensity.

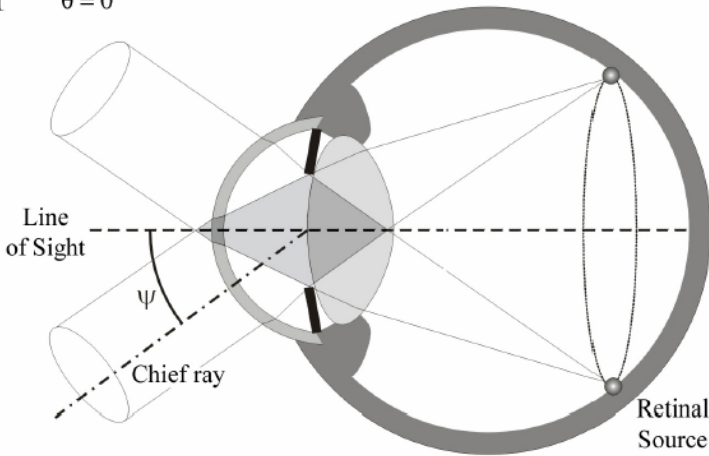
The application of laminography to the human eye provide information on the sources of aberration and also insight into the distribution of refractive index within the eye. This permit to an in-vivo method to determine the gradual changes in refractive index distribution within the crystalline lens that it is not entirely understood.

2. MATHEMATICAL MODELLING OF REFRACTIVE CORRECTION. TWO-DIMENSIONAL RAY TRACING

A light ray entering the eye is refracted four times before it reaches the retina. As each refraction changes the direction of the ray, the ray tracing going from the projection towards the secondary point source on the retina no longer encloses a 'tilted cone' as was the case in the non-refractive case. Instead it forms a more complex volume which may be estimated by means of ray tracing and an eye model.

The reversed ray tracing technique can easily be modified to include these refractive corrections.

T $\theta = 0^\circ$



N $\theta = 180^\circ$

Fig. 1 - The refraction of the projections in the right eye.

The angle of incidence ψ is defined between the optical axis and the chief ray, the line connecting the center of the projection and the pupil center.

Angle θ indicates the orientation of the projection, with $\theta = 0^\circ$ the horizontal hemi-meridian in the nasal direction and progressing in the counter-clockwise direction.

Let's consider a two-dimensional optical system shown in Fig. 2 formed by two optical interfaces m and $m + 1$.

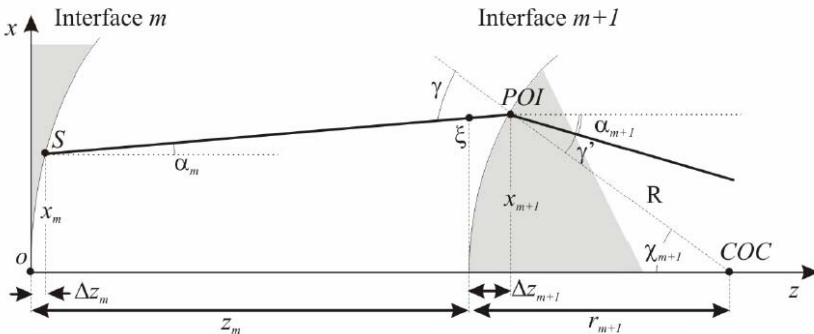


Fig. 2 - The diagram of the two-dimensional ray tracing through an optical system.

A light ray with the origine in source S, located on interface m and with an angle α_m with the optical axis can be traced through the system.

Let's determine the Point of Incidence (POI) on the $(m + 1)^{\text{th}}$ interface and the refracted angle α_{m+1} so the full path of the ray is known.

The coordinates can be expressed as:

$$\begin{cases} S = (x_m, \Delta z_m) \\ POI = (x_{m+1}, z_m + \Delta z_{m+1}), \\ COC = (0, z_m + r_{m+1}) \end{cases} \quad (1)$$

where Δz_{m+1} is the aspherical curvature of the $(m + 1)^{\text{th}}$ optical interface and r_{m+1} is its radius of curvature originating from the Center of Curvature (COC).

A ray leaving source S under an angle α_m intersect the $(m + 1)^{\text{th}}$ interface in POI, that is found by solving the next system:

$$\begin{cases} x_{m+1} = x_m + (z_m + \Delta z_{m+1} - \Delta z_m) \tan \alpha_m \\ \Delta z_{m+1} = \frac{c_{m+1} x_{m+1}^2}{1 + \sqrt{1 - (K_{m+1} + 1)c_{m+1}^2 x_{m+1}^2}} \end{cases} \quad (2)$$

By solving the previous system, the solution for Δz_{m+1} is:

$$\Delta z_{m+1} = \frac{A - \sqrt{A^2 - c_{m+1} B (x_m + (z_m - \Delta z_m) \tan \alpha_m)}}{B}, \quad (3)$$

where:

$$\begin{cases} A = 1 - c_m [x_m \tan \alpha_m + (z_m - \Delta z_m) \tan \alpha_m] \\ B = c_{m+1} (1 + K_{m+1} + \tan^2 \alpha_m) \end{cases} \quad (4)$$

The refraction of the ray on the $(m + 1)^{\text{th}}$ refractive surface can be determined by relation:

$$n_{m+1} \sin \gamma' = n_m \sin \gamma, \quad (5)$$

where the angles γ and γ' are calculated with respect to the normal vector on the refractive interface in POI.

For this point the local radius of curvature R_{m+1} is expressed as:

$$R_{m+1} = \sqrt{x_{m+1}^2 + (r_{m+1} - \Delta z_{m+1})^2}. \quad (6)$$

The angle χ_{m+1} between the optical axis and the normal vector in POI is expressed as:

$$\chi_{m+1} = \arcsin\left(\frac{x_{m+1}}{R}\right). \quad (7)$$

But: $\chi_{m+1} = \gamma' + \alpha_{m+1} = \gamma - \alpha_m$ (convex surface, $r_{m+1} > 0$)
 $\chi_{m+1} = \gamma' - \alpha_{m+1} = \gamma + \alpha_m$ (concave surface, $r_{m+1} < 0$).

Finally, are obtained next relations:

$$\left\{ \begin{array}{l} r_{m+1} > 0: \alpha_{m+1} = \chi_{m+1} - \arcsin\left(\frac{n_m}{n_{m+1}} \sin(\alpha_m + \chi_{m+1})\right) \\ r_{m+1} < 0: \alpha_{m+1} = -\chi_{m+1} + \arcsin\left(\frac{n_m}{n_{m+1}} \sin(\alpha_m - \chi_{m+1})\right) \end{array} \right. \quad (8)$$

3. CONCLUSIONS

This paper presented an application of the laminography to the human eye. The two-dimensional ray tracing calculation can only be used in situations in which both the rays and the optical axis remain within one single plane.

REFERENCES

1. Watt, R.J., Understanding Vision. Academic Press, 1991.
2. Wandell, B.A., Foundations of Vision. Sinauer Associates Inc., 1995.
3. Ullman, S., High-level vision: object recognition and visual cognition. MIT Press, Cambridge, Mass. London, 1996.
4. Zeki, S., A Vision of the Brain. Blackwell Scientific Publications, 1993.
5. Leigh, R.J., Zee, D.S., The neurology of eye movements, Third Edition, New York, Oxford, 1999.
6. Wilson, S.W., On the retino-cortical mapping. International Journal on Man-Machine Studies, 18:361–389, 1983
7. Jos J. Rozema, Dirk van Dyck, Frans J. Van de Velde, Phase Contrast Aberroscope, US patent, no. US 6002484, 1999.
8. Molebny, V., Pallikaris, I., Naoumidis, L., Chyzh, I., Molebny, S., Sokurenko, V., Retina ray-tracing technique for eye refraction mapping, SPIE proc. 2971, pp. 175-183, 1997.
9. Moreno-Barriuso, E., Laser Ray Tracing in the human eye: measurement and correction of the aberrations by means of phase plates, PhD thesis, University of Cantabria, p. 39, 2000.
10. Moreno-Barriuso, E., Navarro, R. Laser Ray Tracing versus Hartmann-Shack sensor for measuring optical aberrations in the human eye, J. Opt. Soc. Am. A, 17, pp. 974 – 985, 2000.
11. Chan, D.Y.C., Ennis, J.P., Pierscionek, B.K., Smith, G., Determination and modeling of the 3-D gradient refractive indices in crystalline lenses, Applied Optics, 27, pp. 926 – 931, 1988.
12. Barbero, S., Global Optimization Strategies in ray tracing deflection tomography: Accuracy and Possibilities for evaluating the Gradient Index in Crystalline lenses', Chapter VIII in 'Optical Quality of the Cornea and the Crystalline Lens: Implementation of Objective Technique and Clinical Applications', PhD thesis, University of Valladolid, Spain, 2003.

THE TRANSPORT OF THE ELECTROSTATICALLY CHARGED PARTICLES FROM THE FILTRATION SPACE – TO THE DEPOSITING ELECTRODES

Dumitru STĂNCIOIU

Turceni Industrial Vocational School

Abstract : The work presents the way to determine the trajectory of any electrostatically charged particle in the field E, formed inside the space between the electrodes of an industrial electro-filter and its purpose is determining the maximum axial filtration space in which any dust particle from the combustion gases is gathered.

Keywords : industrial electro-filter, inter-electrodes space, particle trajectory, gathering axial distance.

INTRODUCTION

The transport of the solid particles from the mixture of burnt gases – particles of ash is a permanent process which takes place through the evacuation circuit, as a consequence of the burning of the fuel in the boiler, towards the smoke chimney, passing through the electro-filter, whose role is the electrical separation in the field of the solid particles. So the final point of the transport of the particle is the surface of deposit of the electrodes.

From the trajectory described by the solid particle from the burning cauldron to the depositing electrode, we intend to analyse only the transport of the electrostatically charged particle in the field, that is from the reaching of the electrical

charge of saturation by the moving particle until the deposit in the layer on the electrodes, fig. 1

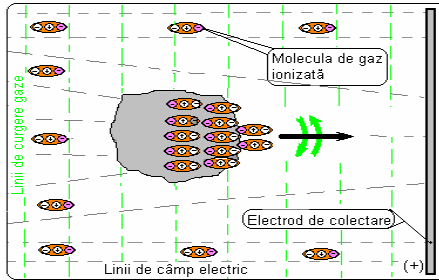


Fig. 1 The transport of the electrically charged particle

Since the movement of the biphasic mixture is turbulent, initially the solid particles have a non-defined trajectory because of the flowing turbulence, but after the charging, because of the influence of the field on it through Coulomb's force, we can determine the movement trajectory and the speed of the charged particles.

2. THE DETERMINING OF THE TRANSPORT SPEED OF THE CHARGED PARTICLE

We consider that the speed of the particle before the charge v_s is equal to the flow speed of the gases v_g . Form the vectorial composition of the two speeds at which the particle moves in the electrical field formed between the electrodes with different electrical signs, the electrical migration speed w and the flow speed of the gases, we get:

$$\vec{v}_T = \vec{v}_g + \vec{w} \quad (1)$$

Scalarly, the transport speed has the relationship:

$$v_T = \sqrt{v_g^2 + w^2} \quad (2)$$

And since $v_g = u_m \left(\frac{y}{0,5b} \right)^{\frac{1}{7}}$ is the relation of the speed

for the turbulent flow [6] a medium speed $u_m = 1-1.5m/s$, and $w = 6,652 \cdot 10^{-6} E$; for $E_0 = 5kv/cm$ at the limit of the zone the corona $\Rightarrow w = w_0 = 3,326 m/s$

$$\Rightarrow v_T = \sqrt{u_m \left(\frac{y}{0,5b} \right)^{\frac{2}{7}} + (6,652 \cdot 10^{-6} E)^2} \quad (3)$$

Since the electric field is similar to the field of particle concentration, we can consider that the solution of the equation of the dispersion of two phases (no matter their nature) is similar, that is:

$$E_y = E_0 \cdot e^{-\frac{w_0 y}{k}} = E_0 \cdot e^{-K \cdot y} \quad (4)$$

But the electric field E also has a linear variation alongside the filtration channel on the direction Ox as it results from the relation [rendering efficient]: $E_x = E_y (1 + 3.33x^2)$

So the variation of the electric field E in the xOy plane takes the form:

$$E = E_0 \cdot e^{-\frac{w_0 y}{k}} \sqrt{1 + (1 + 3.33x^2)^2} \quad (5)$$

By replacing the expression of the field E in the relation of the transport speed, it results that:

$$v_T = \sqrt{u_m \left(\frac{y}{0,5b} \right)^{\frac{2}{7}} + \left(6,652 \cdot 10^{-6} E_0 \cdot e^{-\frac{w_0 y}{k}} \sqrt{1 + (1 + 3.33x^2)^2} \right)^2} \quad (6)$$

Where: u_m is the medium flow speed of the gases;

b – Width of the flowing channel of the gases in the field;
 y – the projection of the trajectory on the Oy axis;
 x – the projection of the trajectory on the Ox axis;
 $k = 2,2 \text{ cm} / \text{s/V/cm}$ is the mobility of the gas ions on the field.

The graphical representation of the transport speed depending on the position of the particle in the sectioning plane of the electrostatic gathering channel can be seen in fig.2.

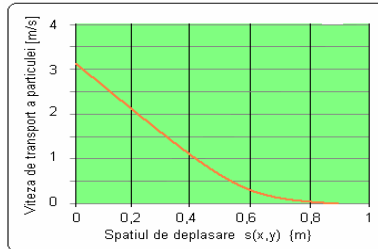


Fig.2 The variation of the transport speed depending on the position of the particle in the field

3. THE TRAJECTORY OF THE MOVEMENT OF THE PARTICLE

Since the movement of the particle on the two axes Ox and Oy takes place in the same amount of time or by applying the criterion of movement similitude of Strouhal on the two axes, that is $Sh = vt / l$, we get:

$$\frac{v_g t}{dx} = \frac{wt}{dy} \quad (7)$$

$$\Rightarrow dx = \frac{v_g dy}{w} = \frac{u_m \left(\frac{y}{0,5b} \right)^{\frac{1}{7}}}{6,652 \cdot 10^{-6} E} dy$$

Through the integration, we obtain the length of the trajectory projected on the Ox axis

$$\int \sqrt{1 + (1 + 3,33x^2)^2} dx = \int \frac{u_m \left(\frac{y}{0,5b} \right)^{\frac{1}{7}}}{6,652 \cdot 10^{-6} E_0 \cdot e^{-\frac{w_0 y}{k}}} dy \quad (8)$$

And by limiting the integration space we get:

$$\int_0^{0,5b} \frac{u_m \left(\frac{y}{0,5b} \right)^{\frac{1}{7}} e^{\frac{w_0 y}{k}}}{6,652 \cdot 10^{-6} E_0} dy = \frac{u_m \left(\frac{1}{0,5b} \right)^{\frac{1}{7}}}{6,652 \cdot 10^{-6} E_0} \int_0^{0,5b} y^{\frac{1}{7}} e^{\frac{w_0 y}{k}} dy$$

Which, by integration through parts, gives:

$$I_D = \frac{u_m \left(\frac{1}{0,5b} \right)^{\frac{1}{7}}}{6,652 \cdot 10^{-6} E_0 \cdot \frac{w_0}{k}} \left(y^{\frac{1}{7}} - \frac{k}{7w_0} \right) \Bigg|_0^{0,5b}$$

By replacing the values of the known physical dimensions: $u_m = 1 \text{ m/s}$; $b = 0.4 \text{ m}$; $w_0 = 3.326 \text{ m/s}$;

$k = 2.2 \text{ m/s/V/m}$; $E_0 = 5 \text{ kV/cm}$; $pe = 0.3 \text{ m}$; $ne = 1-14$ electrodes we get:

$$I_D = 0,25 e^{\frac{w_0 y}{k}} \left(y^{\frac{1}{7}} - 0,095 \right) ; y \in \left[0; \frac{b}{2} \right] \quad (9)$$

By integrating the left part

$$I_S = \int \sqrt{1 + (1 + 3,33x^2)^2} dx \approx \int (1 + 3,33x^2) dx = 1,11x^3 + x$$

But for determining the trajectory of the particle in an electrostatic field applied to the flowing channels, we get the equation of the trajectory of the particle $F(x,y) = I_S - I_D = 0$,

$$F(x,y) = 1,11x^3 + x - 0,25 e^{\frac{w_0 y}{k}} \left(y^{\frac{1}{7}} - 0,095 \right) = 0 \quad (10)$$

The solution of the equation is determined by establishing the conditions at the limit for y and by solving the equations of the II^{nd} degree we obtain the real solution of the equation, which delimits the trajectory of the particle. The relative point in which the electrostatic charge has been reached, being the starting point for the proposed study and the point of contact with the deposit layer, being the end point of the trajectory.

Therefore: -for $y = 0 \Rightarrow x \leq 0$;

-for $y = 0,5b = 0,2m \Rightarrow I_D = 1,86$ and $I_D = -0,023$;

$\Rightarrow I_D = 1,86 \Leftrightarrow I_S - 1,86 = 0 \Leftrightarrow 1,11x^3 + x - 1,86 = 0$; with a positive solution: $x = 0,97$

$\Rightarrow I_D = -0,023 \Leftrightarrow I_S + 0,023 = 0 \Leftrightarrow 1,11x^3 + x + 0,023 = 0$; with negative solutions which are not real in the process of electrostatic filtration.

We reach the conclusion that the only positive solution is $x = 0.97m$, so any electrostatically charged particle, found on the flow axis of the filtration channel, meaning on the plane of the electrodes of corona emission from where the migration begins towards one of the two deposit surfaces, found at 200 mm, will move along the channel in the flow sense 0.9m until the deposit in layer, with a uniformly slowed movement.

In view of the graphical representation of the relation (10) we will first express the dependency between the variables of the relation, $x = x(y)$, meaning:

$$x(1,11x^2 + 1) = 0,25 e^{\frac{y w_0}{k}} \left(y^{\frac{1}{7}} - 0,095 \right)$$

$$\Rightarrow x = 0,25 e^{\frac{y w_0}{k}} \left(y^{\frac{1}{7}} - 0,095 \right) \quad (11)$$

The graphical representation of the exponential function $x(y)$ is presented in fig..

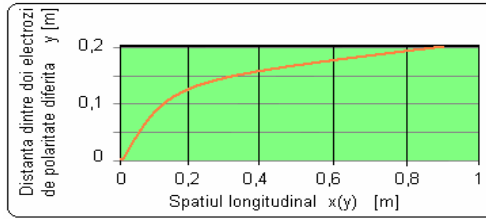


Fig. 3 The movement trajectory of the solid particle

For the particles which due to their spatial positions are not on the plane of the emission electrodes, but at a certain distance $y \leq 0.5b$ and who in their turn will be charged electrostatically in the field and consequentially will have a trajectory almost parallel with the trajectory of another particle which is placed on the same perpendicular at the gathering plane but on a starting point placed on the plane of the emission electrodes, as can be seen in fig.4.

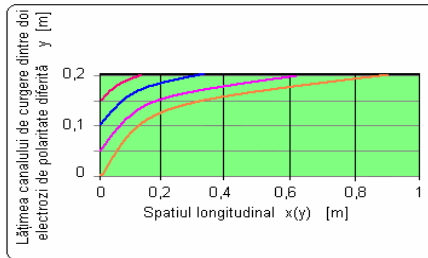


Fig. 4 The trajectories of the particles placed on the same transversal direction

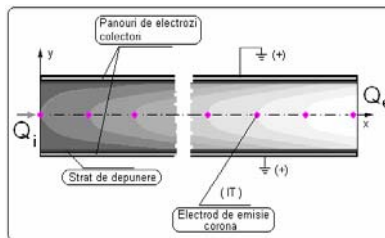


Fig.5 Filtration of the charged particles of the burning gases

By generalising the transport process of every electrostatically charged solid particle in the space between the electrodes we have a general image of the dust cloud found in a continuous filtration which will look like in fig.5.

CONCLUSIONS

From the analysis of the graphic of the determined equation we will notice the trajectory of the particle, which is curved and not linear, as it was first believed. The variation of the movement speed of the electrostatically charged particle proves that the movement is uniformly slowed. The maximum distance, alongside the flowing axis, Ox, from the moment of the electrical charging and until reaching the surface of the deposit electrodes, is of 0.9 m. The need to find the methods and the ways to increase the intensity of the electrostatic field E, so that they rapidly charge any dust particle in order to have at their disposal the gathering field on the deposit electrodes.

BIBLIOGRAPHY

1. Apostolescu N., Taraza D., The Basis of the Experimental Research of the thermal machines, Editura Didactică și Pedagogică, Bucharest, 1979.
2. Carabogdan, Gh., I. The Textbook of the thermo-technician Engineer, Ed. Tehnică 1986
3. Florea J., Panaitescu V., Fluid Mechanics, Editura Didactică și Pedagogică
4. Neacsu R.M., Ciocănea A., The Calculation, the Projecting and the Testing of the Pumps of the Blowers Fans and of the Superchargers, Editura Dacia, Cluj-Napoca, 2000.
5. Oprean A., The Machines-Tool Hydraulics, Editura Didactică și Pedagogică, București.
6. Robescu N.D., et. al., Poly-phased Fluids, Editura Tehnică, 2000.
7. Robescu N.D., ș.a., The Modeling and the Simulation of the Filtering Processes, Editura Tehnică, 2004
8. Spânulecu I., Electricity and magnetism, Editura Victor, 2001.

INDEX

A

AȘTEFANEI Ioan 181, 205

B

BĂGNARU Dan Gheorghe 31, 43

BICĂ Marin 93, 197

BOKOR Levente 117

C

CĂLBUREANU Mădălina 17, 75,
113

CATRINA Gheorghe 147

CERNĂIANU Corina 93, 197

CHAUDHARY Manoj K. 53

CRĂCIUNOIU Nicolae 25

D

DIMA Alexandru 197

E

ENACHE Marian 93

G

GEONEA Ionuț 147

GHERGHINA George 83

F

FILIP Dumitru 123

I

ILINCIOIU Dan 3

K

KUMAR Mukesh 53

L

LAZAR Luminita 191

LUNGU Mihai 113, 173

M

MALCIU Raluca 17, 75,
173

MARGINE Alexandru 147

MIRIȚOIU Cosmin 3, 63

N

NANU Andrei Gheorghe 31, 43

NANU Gheorghe 31, 43

P

POPA Dragos 83

R

ROȘCA Vălcu 25

S

SEPCU Lucian 17, 75,
113, 173

SHAH Rajiv 155, 177,
213, 217

SINGH Rajesh 53

SIPOS Aurelian 117

SMARANDACHE Florentin 53

STANIMIR Alexandru 107

STĂNCIOIU Dumitru 165, 181,
205, 221

STANCUT Adriana 197

T

ȚĂLU Mihai

79, 89,
117

ȚĂLU Ștefan

79, 89,
117, 131,
155, 177,
213, 217

TARNIȚĂ Daniela

123

TUDOR Viorel

135

TUTUNEA Dragos

83, 197

Z

ZAMFIRACHE Marius

107, 161,
191